TECHNISCHE UNIVERSITÄT MÜNCHEN
Institut für Energietechnik

Lehrstuhl für Thermodynamik

On the Formation of Nitrogen Oxides During the Combustion of Partially Pre-Vaporized Droplets

Klaus Georg Mösl

Vollständiger Abdruck der von der Fakultät für Maschinenwesen der Technischen Universität München zur Erlangung des akademischen Grades eines

DOKTOR – INGENIEURS

genehmigten Dissertation.

Vorsitzender:
Univ.-Prof. Dr.-Ing. Horst Baier
Prüfer der Dissertation:
1. Univ.-Prof. Dr.-Ing. Thomas Sattelmayer
2. Univ.-Prof. Dr.-Ing. Stefan Will
Friedrich-Alexander-Universität Erlangen-Nürnberg

Die Dissertation wurde am 25.09.2012 bei der Technischen Universität München eingereicht und durch die Fakultät für Maschinenwesen am 12.12.2012 angenommen.

That's one giant leap for a man, one small step for mankind.

– freely adapted from N.A. Armstrong

Vorwort

Die vorliegende Arbeit entstand am Lehrstuhl für Thermodynamik der Technischen Universität München während meiner Zeit als wissenschaftlicher Mitarbeiter. Sie wurde zunächst im Rahmen des Projekts “Combustion Properties of Partially Premixed Spray Systems (CPS)” durch die Europäische Raumfahrt Agentur (ESA) gefördert, im Weiteren aber wesentlich durch das Deutsche Zentrum für Luft- und Raumfahrt (DLR) finanziert.

Mein herzlicher Dank gilt meinem Doktorvater, Herrn Prof. Dr.-Ing. Thomas Sattelmayer, für die Betreuung der Arbeit, das mir entgegengebrachte Vertrauen und die stetige Unterstützung bei meiner wissenschaftlichen Tätigkeit. Sein waches Interesse an all den Dingen und seine reiche Erfahrung gepaart mit Geradlinigkeit und Pragmatismus begeisterten mich fortwährend neu für meine Arbeit und die Verbrennungsforschung. Herrn Prof. Dr.-Ing. Stefan Will danke ich für das Interesse an meiner Arbeit und die freundliche Übernahme des Co-Referats. Herrn Prof. Dr.-Ing. Horst Baier gilt mein Dank für die Abwicklung des Promotionsprozesses und den Vorsitz in der mündlichen Prüfung.

Bei allen Kolleginnen und Kollegen des Lehrstuhls für Thermodynamik möchte ich mich für die stets wohlwollende Unterstützung und die freundschaftliche Zusammenarbeit bedanken. Dies gilt insbesondere für die Werkstätten und das Sekretariat. Mein besonderer Dank kommt Herrn Dr.-Ing. Stefan Bäßler zu, der mich als seinen Nachfolger außerordentlich gut und sorgfältig in die Organisation des “Raumfahrtprojektes” sowie in die technischen und wissenschaftlichen Inhalte der Arbeit eingeführt hat und mir auch über die Anfangsphase hinaus stets beratend zur Seite stand. Ganz besonders hervorzuheben ist Herr Dr.-Ing. Ewald Freitag, auf dessen Unterstützung ich schon während meiner Studienzeit als Nachbar im Wohnheim zählen konnte. Die Weine seines elterlichen Hauses waren mir all die Jahre über ein Genuss und halfen bei der Korrektur der ein oder anderen schwer verdaulichen studentischen Arbeit. Bleibt nur zu hoffen, dass er bei der Durchsicht dieser Arbeit selbst nicht allzu sehr davon Gebrauch machen musste. Hervorheben möchte ich auch folgende Freunde und Kollegen, die auf ihre eigene, charismatische Art zur positiven Atmosphäre am Lehrstuhl beigetragen haben: Zuallererst Herrn Tobias Holzinger für die angenehme Zeit im gemeinsamen

Büro, auf die wir stolz zurückblicken können; sie war eine ausgezeichnete Mischung aus konzentriertem Arbeiten, hoher Produktivität, Spaß und Lockerheit. Die Herren Martin Hauser und Dr.-Ing. Christoph Mayer für ihren wohltuenden Humor und so manchen Schabernack, vor dem man sicher nicht gefeit war. Die Herren Dr.-Ing. Christoph Heinz und Dr.-Ing. Florian Mittermayer, weil man sich als Allgäuer halt einfach versteht. Die Herren Volker Kaufmann, Klaus Vollmer, Dr.-Ing. Fabian Weyermann und Dr.-Ing. Peter Zimmermann für viele gemeinsame Unternehmungen zumeist sportlicher Natur. Schlussendlich Herrn Daniel Morgenweck für den gemeinsamen, wenn auch hoffnungslosen Versuch, als zwei Nicht-Kaffeetrinker die altehrwürdige MPI-Espresso-Runde vor dem Aussterben zu bewahren.

Mein Dank gilt auch allen meinen ehemaligen Studenten, die durch ihre tatkräftige Unterstützung zum Erfolg der hier zusammengefassten Arbeit beigetragen haben. Dies sind in alphabetischer Reihenfolge: Richard Baude, Ralf Boden, Sebastian Bomberg, Yuri Brant, Matthias Bühner, Biyuan Chen, Imen Dandana, Wolfgang Fenninger, Philipp Hack, Andreas Heindl, Matthias Huber, Florian Hugger, Bogdana Ignatko, Christoph Kaser, Andreas Kollmannsberger, Robert Leo, Le Liu, Pedro Magalhães, Andreas Sachsenhauser, Nicola Schwentner, Christian Schinkel, Joachim Schwing, Milen Stanimirov, Lorenz Ungnadner, Klaus Vollmer und Ruize Xu. Meine Anerkennung und mein Dank gebührt ferner meinen Kooperationspartnern aus dem Umfeld von Industrie und Wissenschaft. Neben zahlreichen anderen seien hier vor allem Astrium Space Transportation (Bremen), GE (Garching), JAXA (Tsukuba), Novespace (Bordeaux) und ZARM (Bremen) genannt.

Abschließend danke ich von ganzem Herzen meiner Familie und allen meinen Freunden, die durch ihre stetige Unterstützung und Geduld maßgeblich zum erfolgreichen Abschluss dieser Arbeit beigetragen haben. Allen voran meine Eltern Sieglinde und Georg gaben mir während meiner gesamten Ausbildungszeit uneingeschränkten Rückhalt und die notwendige Freiheit, meinen Weg zu gehen.

München, im September 2012 Klaus Georg Mösl

Kurzfassung

Die vorliegende Arbeit leistet einen Beitrag zum Verständnis der Bildung von Stickoxiden (NO_x) während der Verbrennung von Einzeltropfen und Tropfenreihen. Im Rahmen von Experimenten und numerischen Studien wurde hierzu insbesondere der Einfluss der teilweisen Tropfenvorverdampfung sowie der Umgebungsbedingungen auf die Stickoxidemissionen untersucht. Vor diesem Hintergrund zeigt diese Arbeit die Zusammenhänge der Fachgebiete der Verdampfung, Zündung, Verbrennung und Abgasbildung auf. Mittels einer ganzheitlichen Modellierung wurde vor allem eine realitätsgetreue Stickoxidbildung gewährleistet. Wenngleich die projektrelevanten Arbeiten das Ziel hatten, die grundlegenden Schritte der Tropfenverbrennung an einem idealisierten Aufbau besser verstehen zu lernen, wurden die Prozesse, wie sie in der zugehörigen technischen Sprayverbrennung von Bedeutung sind, ebenso in Betracht gezogen.

Der Schwerpunkt des experimentellen Teils dieser Arbeit liegt auf der Verbrennung von Tropfenreihen, wohingegen sich der numerische Teil auf kugelsymmetrische Einzeltropfenverbrennung konzentriert. Durch Schwerelosigkeitsbedingungen wird eine quasi-symmetrische Tropfenverbrennung gefördert, was letztlich der Vergleichbarkeit der Ergebnisse von Experiment und numerischer Simulation dient. Die Untersuchung der Stickoxidbildung unter technisch relevanten Bedingungen schließt insbesondere eine teilweise Vorverdampfung der Tropfen sowie eine Tropfenverbrennung in heißem Abgas ein.

Die Umgebungstemperaturen und die Sauerstoffkonzentration sind zwei wesentliche Gegenspieler in der Tropfenverbrennung. Sind beide ausreichend hoch, kommt es zu einem Maximum der NO_x-Emissionen. Der Grad der Vorverdampfung hat ferner einen Einfluss auf die Ausbildung der Tropfenflamme sowie auf die Stickoxidproduktion. Mehr als die Hälfte der Tropfenmasse muss vorverdampft werden, bevor sich der entsprechende technische Aufwand in einer Absenkung des NO_x-Wertes niederschlägt. Im Falle der Anwendung einer gezielten Wärmezufuhr zur Modellierung der Tropfenzündung erweisen sich die Stickoxidemissionen als sehr sensibel gegenüber den Zündparametern. Dies erfordert schlussendlich einen erhöhten Modellierungsaufwand, um die Tropfenverbrennung realitätsnah abzubilden.

Abstract

This study contributes to the topic of nitrogen oxide (NO_x) formation at the level of single droplet and droplet array combustion. The influence of the degree of droplet vaporization and the influence of ambient conditions on NO_x emissions are studied in detail by experiments as well as by numerical simulations. Consequently, this study illustrates correlations and dependencies of the most relevant parameters with respect to the formation of NO_x. It merges the fields of droplet pre-vaporization, ignition, combustion, and exhaust gas formation, including a sophisticated approach to NO_x determination. Even though the study was conducted in order to help understand the fundamental process of burning idealized droplets, the processes in spray combustion have also been taken into consideration within its scope. The portability of results obtained from those idealized droplet burning regimes is evaluated for real applications. Thus, this study may also help to derive design recommendations for liquid-fueled combustion devices.

While the experimental part focuses on droplet array combustion, the numerical part highlights spherically symmetric single droplet combustion. By performing experiments in a microgravity environment, quasi-spherical conditions were facilitated for droplet burning, and comparability was provided for the experimental and numerical results. A novelty of the numerical part is the investigation of mechanisms of NO_x formation under technically relevant conditions. This includes partial pre-vaporization of the droplets as well as droplet combustion in a hot exhaust gas environment, such as an aero-engine.

The results show that the trade-off between ambient temperature and available oxygen determines the NO_x formation of droplets burning in hot exhaust gas. If the ambient temperature is high and there is still sufficient oxygen for full oxidation of the fuel provided by the droplet, the maximum of NO_x formation is achieved. The degree of droplet vaporization has an effect on flame stabilization around the droplet and on NO_x formation. More than half of the droplet mass needs to be pre-vaporized, before the required technical effort leads to a significant reduction of the overall NO_x emissions. In the ignition model, the NO_x production rate turns out to be very sensitive against the ignition position. Thus, it is important to adjust the model parameters carefully to obtain realistic emission results.

Contents

List of Figures

List of Tables

Nomenclature

Latin Characters

A	Absorbance	
A	Area	m^2
A	Pre-exponential factor (in Arrhenius equation)	
A/F	Air-fuel ratio (by mass)	$kg\,kg^{-1}$
a	Minor axis of droplet (of ellipsoidal shape)	m
b	Major axis of droplet (of ellipsoidal shape)	m
C_A	Consumption flux of species A	$kg\,m^{-3}\,s^{-1}$
C_{AB}	Consumption flux of species A due to species B	$kg\,m^{-3}\,s^{-1}$
c	Concentration	$mg\,m^{-3}$, ppm
c_p	Specific heat at constant pressure	$J\,kg^{-1}\,K^{-1}$
c_v	Specific heat at constant volume	$J\,kg^{-1}\,K^{-1}$
D	Binary diffusion coefficient	$m^3\,m^{-1}\,s^{-1}$
D	Diameter	m
$\widetilde{D}$	Multi-component diffusion coefficient	$m^3\,m^{-1}\,s^{-1}$
D^T	Coefficient of thermal diffusion	$kg\,m^{-1}\,s^{-1}$
d	Dilution constant	
E_a	Activation energy	$J\,mol^{-1}$
E_{kin}	Kinetic energy	J
E_{pot}	Potential energy	J
$\dot{E}$	Energy flow	$J\,s^{-1}$, W
EI_{NO_x}	Emission index of NO_x	$g\,kg^{-1}$
e	Specific internal energy	$J\,kg^{-1}$
F	Force	N
F/A	Fuel-air ratio (by mass)	$kg\,kg^{-1}$
f	Correction factor	
f	Species distribution function	m^{-3}
G	Group combustion number	

g	Gravitational force	$\mathrm{m\,s^{-2}}$
h	Specific enthalpy	$\mathrm{J\,kg^{-1}}$
h^0	Standard enthalpy of formation (at T_0)	$\mathrm{J\,kg^{-1}}$
Δh_v	Specific enthalpy of vaporization	$\mathrm{J\,kg^{-1}}$
I	Integral of source term (cf. $\dot{\omega}$)	$\mathrm{g\,cm^{-3}\,s^{-1}}$
I	Intensity	J, W
J	Counter for molecules (integer)	
k	Rate coefficient for reaction	
k	Vaporization or burning rate	$\mathrm{m^2\,s^{-1}}$
L	Total number of reaction equations	
L, l	Length	m
M	Molar mass	$\mathrm{kg\,mol^{-1}}$
M	(Third body) Molecule	
m	Mass	kg
m	Slope of function (of first order curve fit)	
$\dot{m}$	Mass flow	$\mathrm{kg\,s^{-1}}$
$\dot{m}''$	Mass flux	$\mathrm{kg\,m^{-2}\,s^{-1}}$
$\dot{m}'''$	Volumetric mass production rate	$\mathrm{kg\,m^{-3}\,s^{-1}}$
N	Molar density	$\mathrm{mol\,m^{-3}}$
N	Number	
n	Counter (integer)	
n	Molecular density (also: species density)	$\mathrm{m^{-3}}$
n	Normal vector	
P_A	Production flux of species A	$\mathrm{kg\,m^{-3}\,s^{-1}}$
P_{AB}	Production flux of species A due to species B	$\mathrm{kg\,m^{-3}\,s^{-1}}$
p	Pressure	Pa, bar
Q	Heat	J
$\dot{Q}$	Heat flow (also: heat transfer rate)	$\mathrm{J\,s^{-1}}$, W
$\dot{q}$	Specific heat flux	$\mathrm{W\,m^{-2}}$
$\dot{q}_v$	Volumetric energy generation rate	$\mathrm{W\,m^{-3}}$
R	Relative quenching efficiency	
R	Response or recovery factor	
r	Interaction coefficient of species prod./con.	
r	Radial distance (in spherical and cylindrical COS)	m
r	Radius	m
S	(Inter-droplet) Distance	m
S	Non-dimensional droplet separation	

S	Species	
S	Surface, interface	
S_L	Flame speed (also: laminar burning velocity)	$\mathrm{m\,s^{-1}}$
s	Mixing parameter (of primary zone)	
T	Temperature	K, °C
t	Time	s
u, v	Velocity	$\mathrm{m\,s^{-1}}$
V	Volume	$\mathrm{m^3}$, l
v	Velocity coordinate	$\mathrm{m\,s^{-1}}$
v_f	Flame spread rate	$\mathrm{m\,s^{-1}}$
X	Mole fraction	$\mathrm{mol\,mol^{-1}}$
$\widetilde{X}$	(Gas) Concentration	%, ppm
Y	Mass fraction	$\mathrm{kg\,kg^{-1}}$
Z	Mixture fraction	

Greek Characters

α	Thermal diffusivity	$\mathrm{mm^2\,s^{-1}}$
Γ	Fraction	
γ	Surface tension	$\mathrm{kg\,s^{-2}}$
δ	Thickness	m
ϵ	Molar absorptivity	$\mathrm{m^2\,mol^{-1}}$
ε	Threshold	
ζ	Flame stand-off ratio	
η	Burning rate correction factor	
η	Dynamic viscosity	Pa s
κ	Ratio of specific heats (also: adiabatic index)	
λ	Thermal conductivity	$\mathrm{W\,m^{-1}\,K^{-1}}$
λ	Wavelength	nm
μ	Mean	
ν	Kinematic viscosity	$\mathrm{m^2\,s^{-1}}$
ν'	Reactant stoichiometric coefficient	
ν''	Product stoichiometric coefficient	
Π	(Cross-sectional) Perimeter	m
ρ	Density	$\mathrm{kg\,m^{-3}}$
σ	Standard deviation	
σ	Wavenumber	$\mathrm{cm^{-1}}$

σ_S	Surface tension	$\mathrm{N\,m^{-1}}$
τ	Shear stress tensor	$\mathrm{N\,m^{-2}}$
τ	Time scale, time interval	s
ϕ	Equivalence ratio	
χ	Fresh air content	
Ψ	Pre-vaporization (rate)	
$\dot{\omega}$	Specific (net) production rate	$\mathrm{kg\,m^{-3}\,s^{-1}}$

Subscripts

0	Initial, standard, or boundary value
ad	Adiabatic
abs	Absolute value (also: nominal value)
atm	Atmosphere
b	Burned (gas)
b	Burnout
boil	Boiling (point)
c	Chemistry
d	Diffusion
diff	Diffusion flame
eq	Equivalent value
ex	Extracted (energy)
exp	Experiment
f	Flame
g	Gas, gaseous phase
i	Index
i	Inner
i, j	Cartesian coordinates
ign	Ignition
in	Introduced (energy)
λ	Wavelength
l	Liquid, liquid phase
l	Reaction equation
M	(Third body) Molecule
m	Mean
m, n	Concentration exponents (in Arrhenius equation)
m, n, o	Species

max	Maximum value
min	Minimum value
N	Number
nom	Nominal value
pre	Premixed flame
R	Reactants
r	Radial direction
r, φ, θ	Spherical coordinate directions
reac	Reaction, reacting
σ	Surface (tension)
S	Surface, interface
s	Specific value
sat	Saturation
sim	(Numerical) Simulation
stoich	Stoichiometry, stoichiometric
tot	Total
u	Unburned (gas)
v	Vapor, vaporization
Ψ	Pre-vaporization, pre-vaporized
x, y, z	Cartesian coordinate directions
∞	Ambient value

Superscripts

$()'$	Fluctuating component
$()^*$	Critical condition
$()^*$	Excited state (due to chemical reaction)
$()^+$	Forward reaction (destruction of reactants)
$()^-$	Backward reaction (production of reactants)
$(\dot{})$	Time derivative
$(\bar{})$	Time-averaged value
$(\tilde{})$	Concentration
$()^0$	Reference value
$()^{\mathrm{con}}$	(Species) Consumption
$()^l$	Reaction equation
$()^n$	Time step
$()^{\mathrm{prod}}$	(Species) Production

$()^T$	Thermal, temperature

Physical Constants

c_0	Speed of light (in vacuum)	$2.997\,92 \times 10^8\,\mathrm{m\,s^{-1}}$
g_0	Standard gravity (at sea level)	$9.806\,65\,\mathrm{m\,s^{-2}}$
k_B	Boltzmann constant	$1.380\,66 \times 10^{-23}\,\mathrm{J\,K^{-1}}$
N_{AV}	Avogadro number	$6.022\,14 \times 10^{23}\,\mathrm{molecules/mol}$
p	Normal atmospheric pressure	$101\,325\,\mathrm{Pa}$
R	Universal gas constant	$8.314\,46\,\mathrm{J\,mol^{-1}\,K^{-1}}$
σ	Stefan-Boltzmann constant	$5.670\,37 \times 10^{-8}\,\mathrm{W\,m^{-2}\,K^{-4}}$

Non-Dimensional Numbers

Da	Damköhler number
Kn	Knudsen number
Le	Lewis number
Ma	Mach number
Nu	Nußelt number
Pe	Péclet number
Pr	Prandtl number
Re	Reynolds number
Sc	Schmidt number
Sh	Sherwood number

Abbreviations

AFR	Air-fuel ratio
BNC	Connector for coaxial cable
CARM	Computer assisted reduction method
CCD	Charge-coupled device
CCS	Capsule control system
CDR	Critical design review
CEL	CFX expression language
CFD	Computational fluid dynamics
COG	Center of gravity
COS	Coordinate system
CPS	Combustion Properties of Partially Premixed Spray Systems

CPU	Central processing unit
CSP	Computational singular perturbation
CV	Coefficient of variation
DC	Direct current
DCU	Droplet array combustion (experiment) unit
DGSE	Domestic ground support equipment
DLR	Deutsches Zentrum für Luft- und Raumfahrt
DRAM	Dynamic Random Access Memory
EADS	European Aeronautic Defence and Space Company
EGS	Exhaust gas sampling (system)
EGSE	Electronic ground support equipment
EM	Engineering module/model
EPROM	Erasable programmable read only memory
ESA	European Space Agency
FAR	Fuel-air ratio
FFT	Fast Fourier transformation
FM	Flight module/model
FT-IR	Fourier transform infrared (spectrometer/spectroscopy)
HFO	Heavy fuel oil (also: heavy crude oil)
HSV	High-speed video
ICD	Interface control document
ICP	Integrated circuit piezoelectric
ILDM	Intrinsic low-dimensional manifold
JAXA	Japan Aerospace Exploration Agency
JCM	Japanese Combustion Module
JEIT	Japan-Europe investigators team
LDI	Lean direct injection
LED	Light-emitting diode
LIF	Laser-induced fluorescence
LP	Lean premixed (combustion)
LPP	Lean premixed pre-vaporized (combustion)
MFO	Medium fuel oil (also: heating oil)
MMS	Memory management system
MPI	Max-Planck-Institut
NTSC	National Television System Committee
ODE	Ordinary differential equations
PAHs	Polycyclic aromatic hydrocarbons

PAL	Phase alternating line
PAN	Peroxyacyl nitrates (also: acyl peroxy nitrates)
PDU	Power distribution unit
PFA	Path flux analysis
PFC	Parabolic flight campaign
PHOENIX	Investigation of Partial Pre-Vaporization Effects in High Temperature on Evolution of Droplet Array Combustion and Nitrogen Oxides Formation
PM	Particulate matter (also: soot or dust)
PSR	Perfectly stirred reactor
RMS	Root mean square
RQL	Rich (quick) quench/mix lean (combustion)
SM	Stepper motor
SNR	Signal-to-noise ratio
TEM	Technical experiment module
TEXNOX	Drop tower campaign with precursor experiments for TEXUS-46 and a scientific focus on NO_x
TEXUS	Technologische Experimente unter Schwerelosigkeit
TIM	Technical interface meeting
TUM	Technische Universität München
TVR	TV relay
UDS	Upwind differencing scheme
UHCs	Unburned hydrocarbons
VOCs	Volatile organic compounds
VSB	Veículo de Sondagem Booster
WLAN	Wireless local area network
WSR	Well-stirred reactor
ZARM	Zentrum für angewandte Raumfahrttechnologie und Mikrogravitation

1 Introduction

Combustion is a fundamental physico-chemical process and the basis of modern human civilization [253]. Its overarching importance to elementary human needs becomes apparent even when looking at mythology, in which Prometheus stole fire from Zeus, chief of the Greek gods, and gave it to the mortals in their dark caves. In today's world, a substantial part of harnessed fire comes from burning petroleum,[1] which was first extracted in Pennsylvania for commercial purposes in 1859 [253, 274, 323].

1.1 Technological Background

Gas turbine, diesel, and rocket engines burn liquid fuels in spray flames, as do oil-fired boilers, furnaces, and process heaters. After the liquid fuel is injected into the combustion chamber using single or twin-fluid atomizers, the fuel is atomized due to instabilities of the liquid and momentum exchange with the gas phase. Droplets are created and partially vaporized before the radical pool can be formed that finally leads to the chemical breakdown of the fuel [241, 244, 418, 443, 457, 461].

Most modern, low emission combustion concepts are based on partial or full premixing of fuel and oxidant, and pre-vaporization in the case of liquid fuels. Premixed combustion takes place if the droplets are completely vaporized and fuel and air molecules are mixed by molecular or turbulent diffusion before ignition. With respect to exhaust gas formation, experimental and numerical studies of this case are more easily carried out than in partially premixed combustion, where complicated interactions of the diffusion of fuel vapor, air, and combustion products prevail in the flame zone.

[1] In the United States of America, 80 to 85 % of primary energy consumption were covered by fossil fuels throughout the last two decades (1990 to 2010) [450]. The Arbeitsgemeinschaft Energiebilanzen and the Statistisches Bundesamt recorded an almost identical value for Germany. Here, petroleum was by far the most relevant energy source with a portion of 33 to 40 % of primary energy consumption [24, 421].

In thermal engines the time between atomization and ignition often is too short to achieve full premixing, or premixed flames are not even desirable because their heat release characteristics are incompatible with the engine requirements. Often, droplet sizes and vaporization rates allow only small amounts of fuel to be vaporized before ignition, and a nonpremixed flame is observed around the droplets or the droplet cloud. In diffusion-dominated single droplet combustion, vaporized fuel from the droplets is transported from one side into the spherical flame zone, whereas oxygen (O_2) diffuses from the opposite direction. It is observed that the reaction zone stabilizes near stoichiometric conditions. Under these conditions the exothermic reaction sequence of the combustion process produces the highest temperature rise. However, this naturally leads to undesired thermal NO (nitric oxide) formation and imposes limitations on the NO_x (principally NO and NO_2) emission levels that can be reached without full pre-vaporization [253, 298, 443, 451, 458, 461].

1.2 Droplet and Spray Combustion

Spray flames are generally characterized by the coexistence of premixed and nonpremixed flames [241, 242, 244, 263]. Figure 1.1 illustrates the processes of liquid fuel injection and spray combustion. Liquid fuel is injected into a combustion chamber, where the fuel jet is atomized. The resulting droplets vaporize partially. The mixture of fuel vapor and air can auto-ignite or be ignited by an ignition source, depending on local temperature, pressure, and equivalence ratio. Provided a sufficient amount of flammable mixture and heat of reaction is given, a flame zone forms around single droplets or droplet groups [72, 73, 305]. In order to maintain reaction, reactants continually need to diffuse into the flame zones from the droplets and gas phase, respectively, or the flame front itself needs to propagate towards unconsumed reactants. Because of its exothermic nature, the combustion reaction causes a rise in temperature. Furthermore, fuel consumption steepens the concentration gradients, and thus drives diffusive transport in the vicinity of the droplet. Consequently, the droplets burn in a mixed atmosphere of fuel vapor, air, and hot exhaust gas, and vaporization of the surrounding droplets is accelerated due to the increase in temperature.

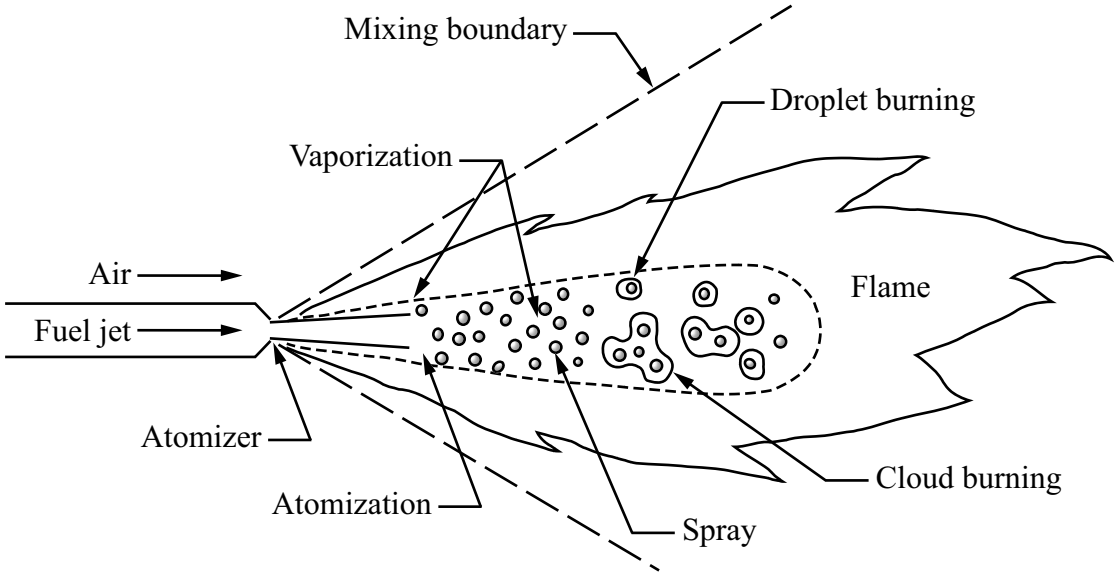

Figure 1.1: Schematic Illustration of Liquid Fuel Injection and Spray Combustion (reprinted from Ref. [253]). The liquid fuel is injected into a gaseous oxidizer.

The vaporization and burning of droplets is a prominent example of non-premixed combustion. Unlike complex sprays, systems of single droplets and well-defined droplet arrays can be analyzed in detail. Analytical and numerical as well as experimental studies of such simplified systems allow identification of how the various combustion phenomena interact. Of particular interest is the influence of droplet size and ambient conditions [443]. For the majority of combustion systems, a reduction of the mean droplet size results in an increased volumetric heat release, easier light-up, wider burning range, and lower overall pollutant emissions within the exhaust [241, 244, 353].

In order to quantify the degree of vaporization, the mass fraction of vaporized fuel Ψ is employed within the present study (Eq. (1.1)). It is defined as the ratio of vaporized (gaseous) fuel $m_{\text{fuel},g}$ and total initial fuel $m_{\text{fuel},0}$:

$$\Psi = \frac{m_{\text{fuel},g}}{m_{\text{fuel},0}} = \frac{\rho_l \frac{\pi}{6} D_0^3 - \rho_l \frac{\pi}{6} D_\Psi^3}{\rho_l \frac{\pi}{6} D_0^3} = 1 - \frac{D_\Psi^3}{D_0^3}. \tag{1.1}$$

The diameters D_0 and D_Ψ refer to the initial droplet at time $t = t_0$ and to the droplet at the end of pre-vaporization ($t = t_\Psi$), i.e. right before ignition, respectively. The density of the liquid phase, resembling the droplet, is expressed by the parameter ρ_l. The terms “degree of vaporization” and “pre-vaporization rate” are used as synonyms throughout this thesis [32, 297, 298].

1.3 Oxides of Nitrogen Formation

The ongoing public discussion of environmental problems caused by the combustion of fossil fuels is mainly focused on the production of carbon dioxide (CO_2). Accordingly, there are a large number of research activities in the field of CO_2 reduction and separation. This includes work on an increase in the efficiency of combustion related processes, as the amount of CO_2 is linearly dependent on the amount of fuel burned. However, a gain in the efficiency of heat engine processes is often also linked to an increase in combustion temperature. This is due to the fact that the achievable efficiency of a thermodynamic process rises with an increase of the temperature differences in the process. Moreover, a higher temperature level may bring with it the added advantage of a lower level of carbon monoxide (CO) production, due to higher fuel burnout. The downside of this increase in combustion temperature is a higher production rate of thermal NO, described by a mechanism postulated by Zeldovich in 1946 [471, 472]. Thermal NO is generated in combustion processes at temperatures above 1800 K, and its generated amount increases exponentially with even higher temperatures. This amount is a function primarily of temperature and of the residence time at the said temperature. Hence, not only the flame zone but its associated post-flame zone is usually of major importance.

Nitric oxide (NO) must not be confused with nitrogen dioxide (NO_2) or nitrous oxide (N_2O). In principle, NO and NO_2 are collectively referred to as "nitrogen oxides" (NO_x) [51, 443, 458]. While the NO portion used to contribute up to 90 % of the NO_x emission in the flue gas of most combustion devices burning fossil fuels, it decreased over the last decades, mostly due to combustion modification techniques or post-combustion methods, both aiming at a general NO_x reduction [51, 69, 201, 380]. Still, NO is considered to be rapidly oxidized in air, forming NO_2. Nitrous oxide is accounted for separately in the majority of combustion literature.

Oxides of nitrogen are, in part, responsible for acidic precipitation, cause photochemical smog in cities, act as a greenhouse gas, participate in the ozone (O_3) chemistry by building harmful ozone in the troposphere and destroying beneficial ozone in the stratosphere, and are directly noxious to humans as they affect the respiratory system [51, 103, 391, 451]. Public debates about

these problems led to political decisions for stricter regulations on NO_x emissions since the 1980s. Thus, two goals have to be considered in the development of new combustion applications: First, the decrease in operating costs represented by an increase in efficiency. Second, the public opinion represented by legislation for a decrease in NO_x emissions. In light of the above described correlation between combustion temperatures and resulting NO_x emissions, a conflict becomes inevitable. Both combustion modification and post-combustion methods need to be considered to meet the most stringent regulations enacted for NO_x reduction [50, 51, 289, 443].

1.4 Motivation and Goals of this Thesis

Global emissions of nitrogen oxides increased at an averaged rate of 3.4 % per year over the past 150 years [103].[2] As a significant amount of the global NO_x emissions is attributed to combustion of biomass and fossil fuels, increasingly stringent regulations have been implemented in a number of industrialized countries. European aeronautics, for instance, has the environmental goal for 2020 to reduce NO_x emissions by 80 % in conjunction with a CO_2 reduction of 50 % per passenger kilometer and a reduction of the perceivable aircraft noise by 50 %, using the year 2000 as a baseline [5, 7].

As a result of the continuing trend towards increased efficiency in liquid fuel combustion and the detrimental effects of NO_x, the development of enhanced NO_x control and reduction concepts becomes necessary. Since most liquid fuels contain virtually no fuel nitrogen, NO formation via the thermal mechanism is dominant in most of the related technical applications and, hence, starting point for NO_x control techniques that rely on combustion modification. The notion of the dependence of the NO formation rate on temperature and oxygen concentration is employed, which involves a reduction of the combustion gas temperature or availability of oxygen, or both. Temperature reduction may be achieved in various ways, including exhaust gas recirculation, water injection, and reduction in fuel-air ratio. Staged combustion is also effective in producing substantial NO_x reduction, as it limits the

[2] While Germany reports an absolute decrease of anthropogenic NO_x emissions by 54 % in the period of 1990 to 2009 [449], an increase by 275 % was projected for Asia for the same period with even higher dynamics for the decades to come [1]. Generally, after World War II, the most rapid increases in emissions have been registered in Asia, South America, and Africa with high dynamics in the power and transport sectors [103, 451].

residence time of the combustion gases in the hot combustion zone and controls the availability of oxygen [51, 201, 240, 241, 251, 353, 367, 368]. Current approaches in technology development adopt staged combustion with a rich and a lean stage (RQL) and lean premixed pre-vaporized (LPP) combustion. The concept of LPP combustion, for instance, requires fine atomization and a careful placement of fuel so that a high degree of mixing can be achieved before the onset of ignition. The potential for NO_x reduction depends on the homogeneity of the fuel-air mixture at the downstream end of the premixing zone [42, 69, 263, 264].

Where lean, fully premixed combustion at moderate temperatures cannot be achieved due to operational, safety, or reliability issues, partially premixed flames will continue to play a major role in future applications. In this context, the NO_x formation of technical sprays was investigated by Cooper [86], Baessler et al. [32], and Beck et al. [39] regarding different degrees of fuel vaporization. However, as illustrated in Figure 1.1, the fundamental processes occur in the proximity of single droplets and droplet clouds. Hence, the present thesis has the goal of improving the understanding of the processes around single droplets and the most simple droplet clouds, namely linear one-dimensional droplet arrays. The study attempts to break down the influence of the degree of droplet vaporization and the influence of ambient conditions on NO_x formation. It aims to highlight correlations and dependencies of the most relevant parameters to the reader. Microgravity environment was selected for the execution of physical as well as numerical experiments, since it is important to provide well-defined and idealized conditions for such basic droplet setups. As depicted in Figure 1.2, microgravity allows for avoidance of the disturbing effects of buoyancy due to density gradients, flame shape deviations from a perfectly spherical shape, convective flow along the flame front, and flame stretching. Furthermore, it allows the simplification of modeling from two or three dimensions to 1D. From a practical point of view, microgravity is also necessary for the formation of equal vapor distribution around each droplet and safe ignition. These requirements are due to the fact that under normal gravity not only the hot combustion products would rise but also the vaporized, gaseous fuel would settle down, resulting in deviations of the drivers of droplet combustion from their nominal value in opposing directions [311].

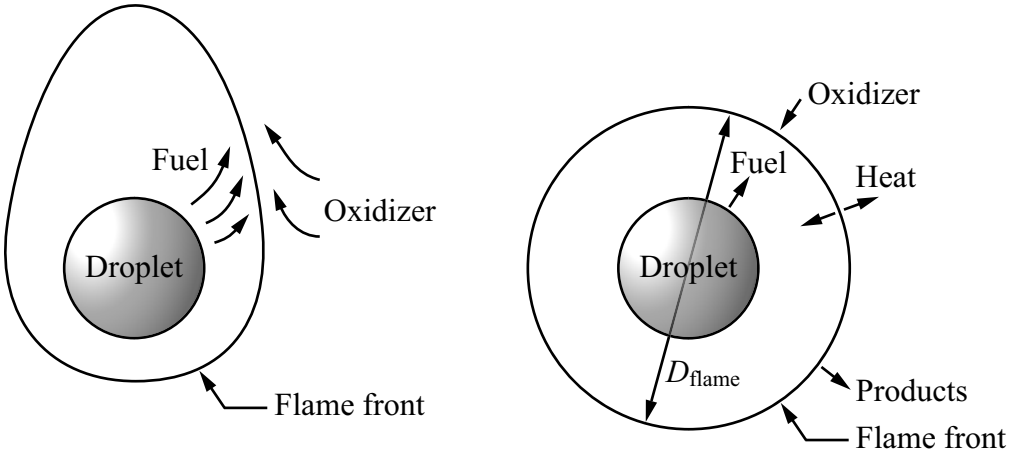

Figure 1.2: Schematic of Droplet Envelope Flames. Left: droplet under normal gravity conditions, right: droplet under microgravity conditions [220, 225, 233, 235, 352].

1.5 Thesis Overview

Chapter 1 is devoted to introducing some technical background of this thesis by outlining current scientific understanding of thermodynamics and fluid mechanics, on the one hand. On the other hand, it positions the scope of the thesis – namely, the issue of NO_x production in droplet and spray flames – within its economical, ecological, and social context. It also provides the reader with the motivation behind this work and the goals of this thesis.

Chapter 2 explains the theory of and provides in-depth information on droplet and spray combustion, including all relevant combustion regimes. It establishes relationships and addresses details starting with general, well-understood combustion phenomena, such as premixed and nonpremixed flames, droplet vaporization, and hydrocarbon kinetics. A straightforward approach extends those formulations to account for the characteristics of droplet combustion. These include amongst others inhomogeneities, the transient nature of the process, and a comparison of reaction mechanisms including the selection of a suitable one for this study. Chapter 2 tries to provide all basics essential to this thesis, keeping the chapter as compact as possible. Additional information on the state of the art of particular details is given throughout all chapters in the course of this work.

Chapter 3 describes the apparatus and methodology of the experiment on droplet array combustion, as conducted within this research. Apart from improving the reader's understanding of NO_x formation, the objective of the experimental part was to provide data of high enough accuracy so that it can also be used for comparison with numerically calculated values. Against this background, specifications of the experimental setup are pointed out, and its integration into the microgravity environments of parabolic flight, drop tower, and sounding rocket is discussed. Furthermore, Chapter 3 covers the utilized measurement and calibration techniques and presents a study of the reacting flow inside of the combustion chamber. This study was conducted primarily for improving the layout of the exhaust gas sampling system within the experiment apparatus.

Based on the framework of thermochemistry put forth in Chapter 2, Chapter 4 recalls fundamentals of molecular transport, fluid mechanics, and chemical kinetics in order to derive a model of spherical single droplet combustion. Particular attention is given to the modeling of the gas-liquid interface, transport mechanisms in the gas phase, ignition by an external energy source, reaction kinetics, and NO_x formation. In addition to these modeling aspects, the validation of the numerical model is of particular interest, since the the most distinct aspect of the numerical part is the appropriate combination of the utilized sub-models, as for instance for physical transport and detailed kinetics.

Chapter 5 comprises the discussion of results. Data from partially pre-vaporized droplets and droplets in a hot exhaust gas atmosphere are reported for the low-volatile fuel n-decane ($C_{10}H_{22}$), which is used as a model fuel for kerosene and diesel here. The chapter contains the assessment of the influence of preheating, droplet size, inter-droplet spacing, pre-vaporization, and reaction kinetics. Chapter 5 also evaluates the results and discusses directions for a continued development in the future.

Chapter 6 summarizes the results in a compact way and concludes this thesis.

2 Combustion Theory

It is generally recognized that the burning of single droplets and well-defined droplet arrays represent idealized conditions for studying the complex interacting phenomena of multi-phase flow, thermodynamics, and chemical kinetics in spray combustion. These simplified setups provide a foundation upon which descriptions and models of complex spray combustion can be developed. The following discourse may help to distinguish the relevant combustion regimes. Information on the state of the art of each subject is provided directly where necessary, both for the experimental and numerical side.

2.1 Classification of Combustion Processes

If a combustible mixture is ignited, the flame propagates either at deflagration or detonation velocity into the unburned mixture. Deflagrations in particular propagate at a velocity that depends on fuel type, pressure p, and initial temperature T_0 of the reactants as well as their mixture ratio AFR (or its reciprocal, FAR) [19, 253, 461]. The deflagration velocity is also denoted as laminar burning velocity or flame speed S_L.

This thesis is concerned exclusively with such deflagrative combustion phenomena. Furthermore, turbulent flames[1] are largely omitted within this work despite the fact that most practical combustion devices operate with turbulent flows. This simplification is due to the special circumstance that emphasis is put on the combustion phenomena in the close proximity of idealized droplet setups in a laminar environment. Here, it is sufficient to treat the relevant combustion processes as laminar flames.

[1] Turbulent flames are in many respects similar to laminar flames, as far as the local conditions are concerned. Their instantaneous flame front can be relatively thin, as observed for laminar premixed flames, but is typically highly convoluted. In turbulent spray flames, the gas phase around the droplets and droplet clouds is turbulent and cannot be captured by a laminar model [443].

2.1.1 Premixed and Nonpremixed Flames

Mallard and Le Chatelier [265] first studied the problem of determining the propagation velocity of a deflagration wave. They considered propagation of heat and heat loss to be of primary importance in flame propagation and the rates of chemical reactions to be secondary. Mikhel'son[2] [284–286] offered the clearest early description of a deflagration structure. In a retrospective view, a large number of experiments were performed to measure the burning velocity of combustible mixtures, since it is essential to predict shape, size, and position of a flame in diverse technical applications. Figure 2.1 depicts a typical profile of a laminar premixed flame, showing the mass fraction of reactants Y_R, volumetric heat release rate $\dot{q}_v$, and temperature T [253, 418, 461]. Laminar premixed flames are often employed in technical applications in combination with nonpremixed flames or so-called diffusion flames. These terms refer to

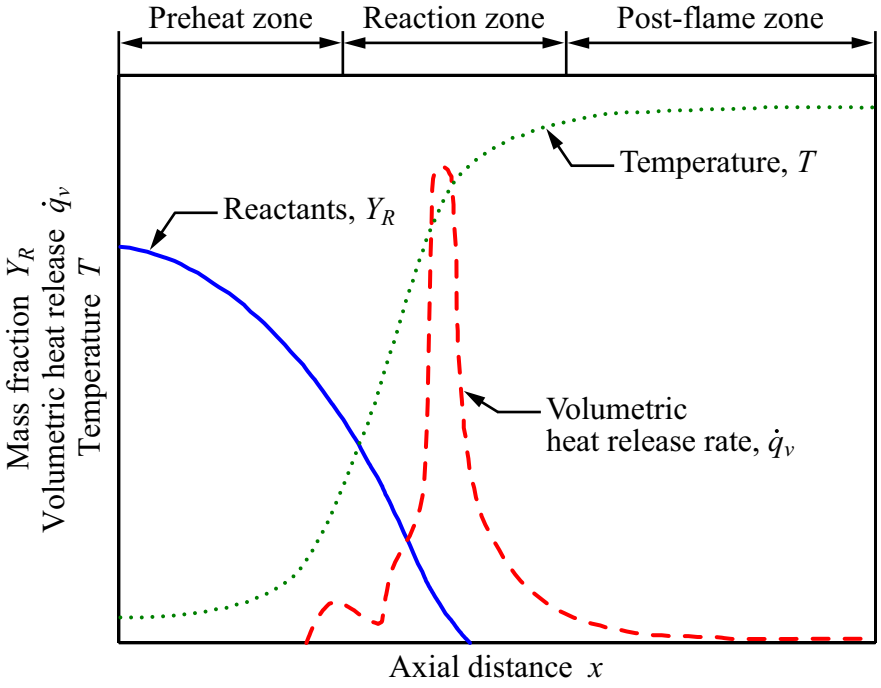

Figure 2.1: Structure of Laminar Premixed Flame (reprinted from Refs. [138, 443]). The flame is stationary to its reference frame, and the premixed reactants enter the flame from the left with a velocity equal to the flame propagation velocity S_L.

[2] In 1887, Mikhel'son went from Russia to Germany for continuing his education (magister) at the Helmholtz laboratory, where he prepared his thesis "On the Normal Ignition Rate of Fulminating Gas Mixtures". When he passed his magister examination, the work was so good that he was at once awarded a Ph.D. Even though he did not work long in combustion science, he managed to ground modern combustion physics [253, 461].

two classes of flames and relate to the state of mixedness of the reactants. A more detailed differentiation is necessary within the class of premixed flames regarding this thesis: A mixture can be partially premixed (see Chap. 2.1.2) or fully premixed. “Fully premixed” insinuates ideal/perfect premixing, which is the goal of numerous technical applications but often hard to achieve or validate. Hence, the term “technically premixed” gains its justification and might be the more appropriate choice for certain applications [146].

Laminar Premixed Flames

In a premixed flame, the reactants – fuel and oxidizer – are mixed at a molecular level prior to the occurrence of any significant chemical reaction. Gas ranges and spark-ignition engines are two prevalent examples of the application of premixed flames. Here, as well as in other technical devices, the flame speed S_L is one of the fundamental design parameters because it dictates the flame shape and is decisive for flame stability, including blowoff and flashback characteristics. As illustrated in Figure 2.1, the flame heats the combustion products, and thus product density ρ_b becomes less than reactant density ρ_u. Since continuity (Eq. (2.1)) requires that the burned gas velocity v_b be greater than the velocity of unburned gas v_u, there is a considerable acceleration of the gas flow across the flame [443].

$$\rho_u S_L A \equiv \rho_u v_u A = \rho_b v_b A \tag{2.1}$$

The flame may be freely propagating or be stabilized, for example on a burner, which implies that the reactants enter the flame front with a velocity equal to the flame propagation velocity S_L. In both cases, the flame is assumed to be one-dimensional with the unburned gas entering the flame in the direction normal to the flame sheet, but the reference frame for the coordinate system might be different [443].

According to Annamalai and Puri [19], Turns [443], and Glassman and Yetter [149], a premixed flame may be divided into two to four zones: preheat, reaction, recombination, and product/post-flame zone. The reaction zone itself may in turn be categorized into a thin region of very fast chemistry (also called primary reaction zone) and a much wider region of slow chemistry (the secondary reaction zone). The sequential breakdown (destruction) of fuel

molecules by early pyrolysis reactions and the creation of many intermediate species occur in the fast-chemistry region. As this zone is thin, gradients in temperature and species concentration are very large.[3] These gradients act as driving forces that cause the flame to be self-sustained. The resulting diffusion of heat and radicals from the high-temperature, fast-chemistry region is opposed to convective flow of the reactants into the preheat zone. Here, diffusion is dominated by hydrogen (H) atoms, and the luminous flame zone can also be located in that region of maximum heat release. On the other hand, three-body recombination reactions of radicals are dominant in the slow-chemistry region, and final burnout of CO proceeds via the reduction of OH [146, 149, 443]. As a consequence of these recombination reactions, equilibrium conditions develop at a relatively slow pace, after the fuel is completely gone and the major portion of the total temperature rise has already occurred. The recombination reactions are very exothermic, but the radicals recombining have such low concentrations that the temperature profile does not evidently reflect this phase. This may be the reason for Glassman and Yetter [149] to relate recombination to the zone of burned gas or the so-called post-flame zone.

The fuel-air ratio, FAR or (F/A), of a premixed flame is one of the key factors governing type and quantity of pollutants formed in the combustion process. Flame speed S_L and temperature T are directly dependent on it. For hydrocarbon-air systems, both parameters peak slightly on the fuel-rich side of the stoichiometric fuel-air ratio $(F/A)_{\text{stoich}}$ [149, 443]. Generally, the fuel-air ratio (F/A) is represented by the equivalence ratio ϕ.[4] Both are linked according to Equation (2.2) with the actual fuel-oxidizer ratio being divided by the stoichiometric fuel-oxidizer ratio [149, 443, 458]:

$$\phi \equiv \frac{(F/A)}{(F/A)_{\text{stoich}}} = \frac{(A/F)_{\text{stoich}}}{(A/F)}. \tag{2.2}$$

The combustion of fuel-rich mixtures ($\phi > 1$) principally leads to an increase in CO formation. In spark-ignition engines and mobile heating devices, for instance, residual fuel can be observed in the exhaust in addition, either partially burned or unburned (UHCs). Lean mixtures ($\phi < 1$) produce considerably less CO and UHCs. Nitrogen oxide (NO_x) emissions are typically lowest,

[3] The fast-chemistry region has a typical thickness of less than 1 mm at atmospheric pressure [149, 443].

[4] The reciprocal value of the equivalence ratio ϕ is used to a large extent in German combustion terminology as "Luftzahl" with $\lambda = 1/\phi$ [458].

too, for lean mixtures on account of excess air that does not participate in the combustion process but acts as thermal ballast. However, if the mixture is too lean, it may not ignite properly, leading to misfiring and large amounts of fuel passing through the combustion zone unburned. As a consequence, lean premixed combustion is employed in many technical applications with a fuel-air ratio sufficiently above the lower flammability limit. Increasing the initial/inlet temperature of a premixed fuel-air mixture increases the burned gas temperature by about the same amount. Dissociation and temperature-dependent effects usually cause a small deviation of the results from this direct dependence. However, there will be a significantly greater increase in flame speed S_L with that increase in initial/inlet temperature. The thermal NO mechanism is also strongly dependent on even moderate temperature changes, which have to be well-controlled by avoiding positive peaks, when aiming for overall low NO_x emissions [149, 391, 443].

The luminescence of the flame is due to visible radiation, and its color changes with the equivalence ratio ϕ. For hydrocarbon flames that are operated with an excess of air ($\phi < 1$), a blue to deeply violet radiation appears. It results from excited CH^* radicals. Green radiation can be found when the mixture is fuel-rich, which is due to excited C_2^* molecules. When the fuel-air mixture is adjusted to be very rich, an intense yellow radiation appears, which can be attributed to soot formation. Furthermore, OH^* radicals contribute to the visible radiation at any fuel-air ratio with the maximum peak in the ultraviolet range at 308 nm. The burned gases at high temperatures typically show a reddish glow, which arises from CO_2^* and water vapor radiation [146, 149, 443].

Laminar Diffusion Flames

In contrast to premixed flames, nonpremixed combustion does not intrinsically propagate but occurs in a flame into which fuel and oxidizer are transported from opposite sides. As molecular diffusion of species is decisive to this type of combustion, nonpremixed flames are often called diffusion flames. Unlike premixed flames, they do not have a burning velocity and tend to be nonexplosive because their heat release rates are limited by diffusion rates. Since the fuel-air mixture ratio varies in space, an additional variable such as the mixture fraction Z is needed to describe and model diffusion flames [253]. Tsuji [442], for instance, categorizes laminar counterflow diffusion flames into

four types. Out of these, “Type I” may be the most common with a diffusion flame established between two opposing jets [326, 343, 417]. “Type III” is very close to droplet combustion with the diffusion flame established in the forward stagnation region of a spherical porous burner [398, 416]. Based on the fact that the characteristic chemical time τ_c is much smaller than the characteristic diffusion time τ_d, Tsuji [442] draws the following conclusions for diffusion flames [146, 249, 461]:

- A chemical reaction occurs in a narrow zone between fuel gas and oxidizer.
- Concentrations of the reactants (fuel and oxidizer) are very low in the reaction zone.
- The combustion rate is controlled by the rate at which fuel and oxidizer flow into the reaction zone.

A well-known example of a diffusion flame is the candle [253]. Turns [443] also cites laminar jet flames as an example. Those are employed in many residential appliances, particularly in the United States of America, where they cause reoccurring concerns about the emission of toxic gases, such as NO_2 and CO. Since the early work of Burke and Schuhmann [61], published in 1928, the design parameters to control flame size, shape, and emission signature have been of particular interest, and thus the subjects of various studies [69, 176, 281, 328, 345, 354, 358–360, 442, 454].

Soot and nitrogen oxide (NO_x) formation are two prominent combustion phenomena of diffusion flames. Particularly in hydrocarbon (diffusion) flames, soot is present and often an issue in terms of air quality regulations, as well. Soot is typically formed on the fuel side of the reaction zone and consumed when it flows into the oxidizing region, in either case provided there is sufficient time. The incandescent soot within the flame gives the diffusion flame its typical orange to yellow appearance and contributes to its increased radiant heat losses in contrast to premixed flames [62, 148, 174, 443, 455]. Temperature, residence time, and composition of the reactants are decisive for NO_x formation, in a similar way to premixed flames. Here, however, the mixture fraction Z varies from point to point within the flow, as does temperature distribution. In a first estimate, thermal NO, representing the major portion of

overall NO_x emissions, is formed in regions with mixture conditions close to stoichiometry ($\phi \approx 1$) and a correspondingly high temperature level [443].

2.1.2 Inhomogeneous and Partially Premixed Combustion

The design of many combustion devices, including liquid-fueled gas turbines, is affected by factors such as combustion efficiency, combustion stability, auto-ignition, flashback, relight-at-altitude capability, and exhaust gas formation [241, 245, 246, 443]. Essential to these factors is the state of mixedness (homogeneity) of the oxidant air with the gaseous and/or liquid fuel at the moment of combustion [125, 194, 305, 422]. In gas turbine combustion, lean premixed (LP) or lean premixed pre-vaporized (LPP) combustion can be seen as opposing conventional diffusion flame combustion (Chap. 2.1.1) [86, 87, 99, 263, 264]. However, premixers for gaseous fuels as well as liquid fuel pre-vaporizing premixers rarely achieve homogeneity to such an extent as to truly satisfy the conditions of a "perfectly premixed" flame. In light of this, Barnes and Mellor [34, 35] present a method of quantifying unmixedness in lean premixed gas turbine combustors and discuss the results, as determined in their experiments. They follow the assumption of Mikus and Heywood [287] and Fletcher and Heywood [137] assuming that the local equivalence ratio has a Gaussian distribution around its true global value if the main fuel-air mixture of the gas turbine is inhomogeneous. The study of Schlegel et al. [388] highlights the influence of fuel-air unmixedness on NO_x emissions in lean premixed combustion for both non-catalytic and catalytically stabilized combustion.[5] Gravity effects on partially premixed methane-air flames are compared on an experimental and numerical basis by Lock et al. [255].

As summarized by Anderson [18], Lefebvre (ed.) [246], and Mularz [301], spray atomization of fuel results in a wide range of the local equivalence ratio with a spectrum from lean to rich values. Since the formation of thermal NO is exponentially dependent on the local temperature level, this distribution of stoichiometry leads to large quantities of NO being produced in some regions and virtually none in others, even for global mixture ratios far from stoichiometry. Consequently, it becomes a major challenge to predict NO and/or NO_x emissions from the average equivalence ratio of the reaction zone in a con-

[5] Apart from yielding lower NO_x emissions, a catalyst is capable of reducing temporal fluctuations in the fuel concentration as well as in combustion temperature.

ventional combustor with a nonuniform mixture. Heywood and coworkers [23, 137, 177, 178, 287, 342] studied the effect of mixture uniformity in the primary zone of gas turbine combustors with a focus on NO production.[6] As mentioned above, their work is based on a statistical evaluation of the equivalence ratio distribution. Figure 2.2 represents a cross-plot of typical analytical results from Fletcher and Heywood [137] and shows the strong effect of mixture uniformity on the NO concentration $\widetilde{X}_{NO}$. It is apparent from Figure 2.2 that a lean, uniformly mixed primary zone allows significant reductions in NO formation compared to a conventional combustor operating near stoichiometric conditions with a nonuniform mixture preparation [18]. While using different definitions for the mixing parameter s, Mikus et al. [288] and Lyons [261] derive two, slightly different theories of NO_x formation in nonuniform fuel-air mixtures. Here, the parameter s is a measure of the nonuniformity of mixing within the primary zone, and $s = 0$ corresponds to perfect premixing

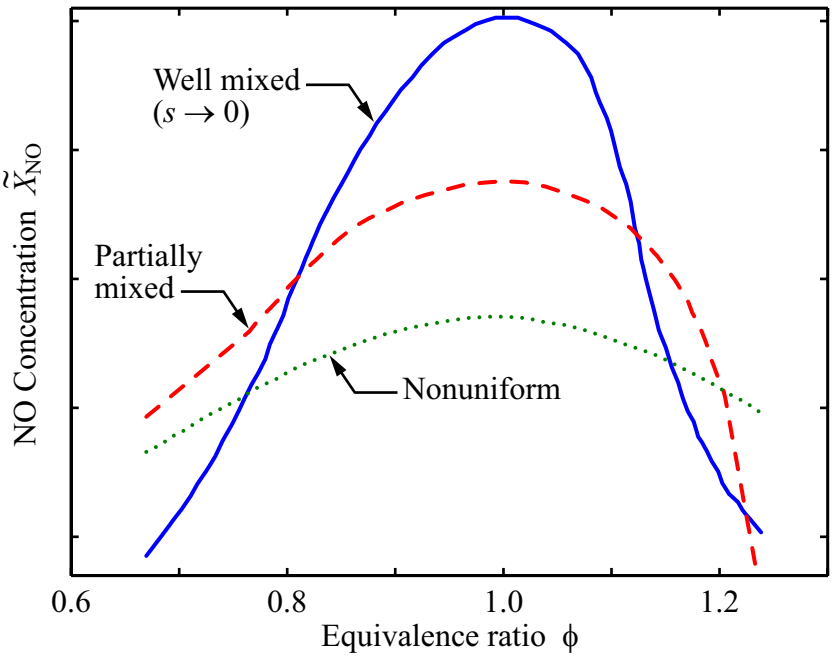

Figure 2.2: Effect of Equivalence Ratio and Unmixedness in the Primary Zone of a Combustor on NO Formation (reprinted from Refs. [18, 137]). The NO concentration is given in arbitrary units in this cross-plot. Further parameters important for determining the exhaust NO concentration are inlet air pressure and temperature, residence time, and air dilution rate upstream of the (primary) combustion zone [178, 287].

[6] The work addresses jet engines as well as automotive gas turbines [287].

(Fig. 2.2). In a later work, published by Rizk and Chin [354] and Rizk et al. [355] in 2002, the authors present a model for predicting NO_x formation during simultaneous droplet burning and partially premixed combustion. An arrangement of reactors, coupled with a detailed chemical reaction scheme, accounts for various combustion zones. The primary zone comprises first a reactor representing the contribution from droplet burning under stoichiometric conditions and second a mixing reactor that provides additional air or fuel to this zone. The additional flow forms a fuel vapor-air mixture distribution that reflects the nonuniformity of the fuel injection process [354, 355].

The thesis at hand also aims at contributing to the understanding of NO_x formation in inhomogeneous and partially premixed combustion systems. Hence, the combustion of partially pre-vaporized droplets and droplet arrays is the primary issue of this study (cf. Eq. (1.1)). In this context, the prior work of Cooper [86, 87], Baessler [31], and Beck [38] is of particular interest (see Fig. 2.3). While earlier research had been limited to fully premixed, pre-vaporized mixtures, Cooper [86, 87] first conducted experiments on the effect

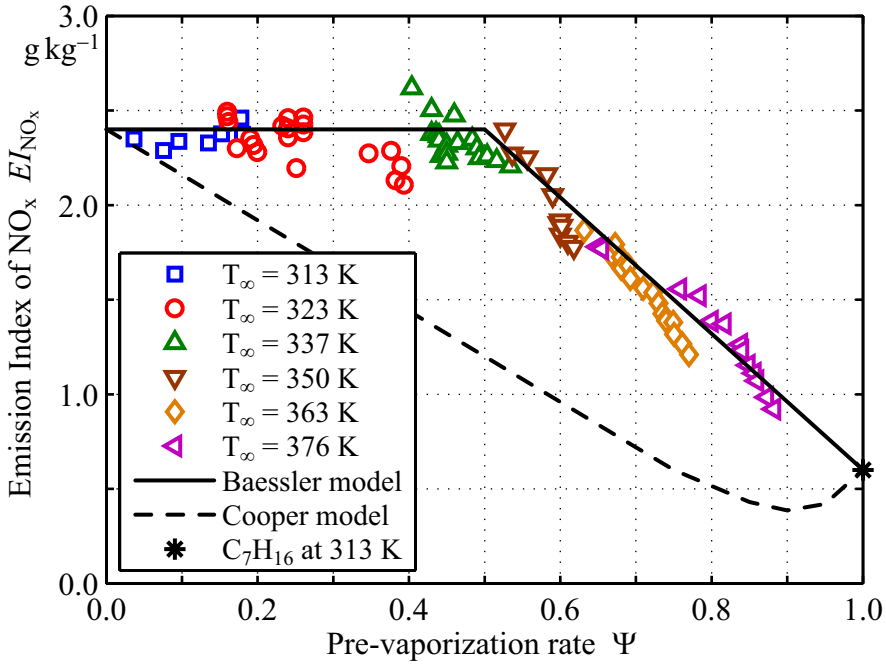

Figure 2.3: Impact of Liquid Fuel Pre-Vaporization on Nitrogen Oxide Emissions (reprinted from Refs. [31, 32]). The data points show results from the study of Baessler [31] for a global equivalence ratio of $\phi = 0.7$. These data are corrected to the reference temperature of 313 K. The experiments were conducted under normal gravity.

of partial pre-vaporization on NO_x emissions in "globally premixed" sprays. Based on his experimental results, Cooper postulates an analytical model stating that NO_x emissions are due to a contribution of vapor-phase combustion and droplet combustion at stoichiometric conditions. However, the influence of a flame holding device installed primarily to sustain recirculation zones and, thus, stabilize the combustion process itself on the attainable mixture quality proved to be substantial. Consequently, Cooper considers the interrelationships between droplet collection efficiency, reatomization efficiency, and blockage of the flame holder as well as the initial droplet size distribution with respect to NO_x formation. The model postulated requires knowledge of the following combustor conditions: temperature, pressure, fuel type, equivalence ratio, and residence time, plus preparation characteristics of the initial fuel-air mixture, including droplet size distribution and degree of vaporization. Cooper himself admits the lack of supporting experimental data that hinders the application of his procedures developed for predicting NO_x emissions [86, 87]. Baessler [31] uses kerosene to assess the influence of the pre-vaporization rate Ψ on NO_x emissions; an approach he has in common with Cooper. However, the setup of Baessler differs from Cooper's in that turbulence level and preheating temperature are lower. On the other hand, the achievable range of Ψ is much more widespread in the work of Baessler, particularly for low values of Ψ with a high liquid fuel mass fraction (see Fig. 2.3). Due to the broad basis of experimental results, Baessler reports a constant progression of NO_x emissions starting from low degrees of vaporization followed by a linearly decreasing dependence for high degrees [31, 32].

Beck [38] utilizes a swirl-stabilized burner in his studies and supposes this stabilization mechanism to have a significant impact on the flame structure. In order to provide an incomplete liquid fuel pre-vaporization, two liquid fuel injectors are installed in the experimental setup. The first injector is located far upstream of the combustor and generates a fully pre-vaporized and premixed fuel-air mixture, whereas the second injector is located at the combustor inlet. The droplet slip observed is fundamentally different compared to the setups of Cooper and Baessler because the gas-phase velocity fluctuates significantly along the droplet trajectories. Therefore, Beck expects his setup to best represent the characteristics of a gas turbine combustor. The results obtained by experimental investigation suggest that a variation of the pre-vaporization rate Ψ may be abstracted as the superposition of a droplet and premixed flame.

Since significant droplet slip velocities are known to cause a transition from the stoichiometric envelope flame to a wake flame, the influence of this flame type transition on NO formation is also investigated on a single droplet flame by a numerical study [38–41].

Even though a lean premixed combustion zone resembles an optimum in terms of low NO_x emissions in all of the studies outlined above, combustion stability will suffer due to homogeneity of the mixture: The associated lean flammability limit lies at an equivalence ratio of $\phi \approx 0.5$ for most hydrocarbon fuels [241, 443]. In nonuniform systems, however, the mean equivalence ratio can be considerably less than this lean limit, as locally rich zones will maintain combustion. Such a system is safeguarded against blowout near the lean flammability limit; a lean premixed system is not [18, 295, 375]. Other issues of lean flames are flashback [19, 119, 120, 226] and combustion instabilities. Fritz [139] and Kröner [218], for instance, first reported on combustion induced vortex breakdown, which is a type of sudden flame flashback that is driven by the interaction of turbulence and chemistry. Sattelmayer and Polifke [377–379], Lieuwen et al. [252], and Nguyen [313], for instance, investigated the role of unmixedness and equivalence ratio fluctuations in LP and LPP combustion with respect to combustion induced instabilities. In this context, heat release oscillations of large amplitude excite pressure oscillations of some of the combustor's acoustic modes that couple with the reactants feed lines, and thus drive the combustion instabilities [26].

2.1.3 Droplet Combustion

Power generation by means of hydrocarbon combustion will keep its predominant role for the decades to come despite the increasing share of renewable energy sources in the global energy mix [24, 421, 450]. In particular, combustion of liquid fuels will remain a major energy source in the transport sector due to its high energy density. As outlined in Chapters 1.4 and 2.1.2, lean, partially premixed spray flames are discussed for novel combustion concepts to allow a further abatement of NO_x emissions. The relevant knowledge is based to a large extent on combustion research of manageable and observable droplet setups. Partially pre-vaporized droplets at moderate temperatures, ignited by an external energy source, are representative here [102, 296–298].

Formation of Fuel Droplets

The disintegration of bulk liquid is a main principle of droplet generation. The generation of sprays but also of single droplets and droplet systems is described in detail in the work of Lefebvre [244] and Frohn and Roth [140]. These authors put emphasis on techniques and technical devices that allow the generation of droplets of a particular size, velocity, temperature, and distance from neighboring droplets. The resulting droplet diameter principally has a lower limit of a few micrometers, with technical sprays typically displaying a spectrum from approximately 10 to 100 µm. The benefit of the transformation of bulk liquid into fine droplets is the enormous increase in surface. Thus, the physico-chemical processes can be enhanced.

According to Lefebvre [244], the atomization process is characterized by the disintegration of a liquid jet or sheet into ligaments and succeeding drops. The kinetic energy of the liquid itself, exposure to high-velocity gas, or external mechanical energy drive the process. In addition, there is a notable effect of the internal geometry of the atomizer, the properties of the gaseous medium into which the liquid stream is discharged, and the physical properties of the liquid itself. In order to understand the physical processes in sprays in general and to model complex spray systems, it is essential to obtain empirical data and to master well-defined, regular droplet configurations [15, 32, 140, 296].

Single droplets can be investigated either as moving or as motionless droplets. In the latter case, different suspension techniques, such as thin fibers, threads, and filaments, have been employed by various groups of researchers [130, 282, 395]. Droplet streams and droplet arrays are feasible as one-, two-, and even three-dimensional arrangements. However, as neighboring droplets have a strong influence on the evaporation and combustion characteristics of each individual droplet, droplet interaction has also been the subject of numerous experimental, analytical, and numerical studies [58, 59, 107, 108, 203, 212, 280, 318, 319, 327, 329, 349, 352, 366, 430, 441, 445, 448, 463, 464]. Labowsky [227], for instance, introduced the correction factor η for the burning rate, which represents the ratio of the actual burning rate and the burning rate of an isolated droplet. One of the results is that droplets in an array burn nearly 40 % more slowly ($\eta = 0.6$) than isolated droplets if the droplet spacing falls below a certain limit. Generally, the burning rate correction factor η decreases with an increase of the droplet number or a decrease of the droplet distance [140, 227].

Droplet Vaporization and Burning

Recalling the schematic of Figure 1.1, Liñán and Williams [253] provide the following summary on the process of liquid fuel injection and spray combustion. The authors state that a quantitative prediction of the histories of all of these processes is difficult, but progress is being made by addressing different aspects separately:

- Atomization
- Vaporization
- Heat transfer
- Droplet-air mixing
- Vapor-air mixing
- Ignition
- Turbulent diffusion flames
- Premixed combustion
- Production of NO_x and other pollutants
- Extinction

The majority of these combustion processes take place in the gas phase, and the combustion products are typically gaseous [253, 443]. Law and Sirignano [233, 236, 402, 403, 405] and Faeth [126, 127] give a detailed review of the fundamentals of droplet vaporization and combustion. Discussing the major elements of an integrated approach, Sirignano [403] points out the necessity of treating unsteady, multi-dimensional, turbulent reacting flows with polydisperse, multi-component sprays. A model has to account for transient droplet heating and vaporization, liquid-phase mass diffusion, and droplet drag and trajectory in a numerically efficient manner. Furthermore, Law and Faeth [235] recall that droplet vaporization and combustion is a classical problem of heterogenous combustion, in particular when assuming quasi-steadiness and spherical symmetry. This simplifies the mathematical aspects of the problem.

Moreover, experiments at microgravity provide an opportunity to merge theories and reality for a better understanding of the fundamental combustion phenomena involved [153, 219, 222, 223].

Godsave [152] and Spalding [415] first developed a basic, spherically symmetric model for an isolated single component droplet in a stagnant environment. The model is well-known as "D^2 law" and predicts a linear relationship between droplet surface area and time. Quasi-steadiness[7] is assumed and temperature inside of the droplet is taken to be uniform and constant at the wet-bulb temperature. In addition, constant values are employed for the thermophysical properties as well as a unity Lewis number ($Le = 1$). In order to include the effect of liquid-phase heating, Law [231] modified the D^2 law. While the gas phase is taken to be spherically symmetric and quasi-steady (as in the D^2 law before), the droplet temperature is assumed to be spatially uniform but temporally varying. Results of this extended model showed that droplet heating is a significant source of unsteadiness and should be incorporated into any realistic model of droplet vaporization and combustion [231, 350]. In this context, Sirignano [401] illustrates that the assumption of a spatially uniform temperature within the droplet requires an infinite thermal conductivity in the associated liquid phase. Hence, this model is denoted as the "infinite-conductivity model". A further advancement of the D^2 law is the "conduction-limit model" due to Law and Sirignano [236]. In this third model, molecular diffusion exclusively controls the nonuniform temperature field in the liquid phase, implying that liquid circulation within the droplet is negligible. The droplet surface temperature is regarded as uniform. As summarized by Renksizbulut et al. [350], this is reasonable for a nonconvective environment and represents the slowest heat transfer limit. In fact, Law and Sirignano [236] showed that transient heating dominates the first 10 to 20 % of the droplet life time. Additionally, Aggarwal et al. [9] conducted a comparative study on the effect of the different liquid-phase models. It shows that the selection of the particular heating model is substantial for the liquid phase temperature. The infinite-conductivity and conduction-limit models are commonly considered as two limiting cases bounding the possible range of real conditions [4, 350]. Still, droplet vaporization occurs in a convective environment in almost all

[7] Despite the fact that a fuel droplet may not attain steady-state evaporation/vaporization during its lifetime, it is often convenient to consider a quasi-steady gas phase. This means that the process can be described as if it were in steady state at any instant of time. This assumption eliminates the need to deal with partial differential equations and still provides a reasonable level of accuracy [244, 341, 443].

technical applications. Convection enhances the vaporization process due to an increase in the rate of heat transfer to the droplet and due to an increase in the rate of liquid phase heat and mass transport in the droplet by generating internal circulation. On the other hand, vaporization also induces Stefan flow, which thickens the momentum, species, and thermal boundary layers, and thus inhibits the associated transport processes [149, 159, 350, 364, 381].

Comparing the thermal diffusivities $\alpha = \frac{\lambda}{\rho c_p}$ of the liquid and gas phase yields a much smaller value for the liquid phase ($\alpha_l \ll \alpha_g$). Transport processes in the gas phase proceed much faster than in the liquid phase [236, 320, 350, 381]. Consequently, the majority of models applied for droplet vaporization and combustion treat the gas phase as quasi-steady [4, 91, 184, 236, 381]. It is supposed to adapt instantaneously to new interface conditions at the droplet surface. However, the validity of these quasi-steady models is questionable towards the end of droplet lifetime, since transient effects are assumed to be important when the surface regression rate becomes comparable to droplet size [236, 238, 381].

The fuel droplets investigated in the present work are at rest in the case of both experiments and numerical simulations. Microgravity conditions are given in either case. n-Decane ($C_{10}H_{22}$) is used, being a single component fuel. Even though convective flow might develop around the droplets, induced by changes in density due to combustion, it is expected to result in only very small Reynolds numbers.

As a consequence, internal circulation inside of the droplets is not taken into account within the numerical part of the work. Droplet deformation and droplet break-up are not part of this analysis either. Thus, the droplets can be treated as spherically symmetric. A uniform droplet surface temperature is assumed. The physical properties of the liquid fuel are set as constant. Radiation and pressure work are neglected (Chap. 4). However, since combustion is a main part of the numerical simulation, it is highly desirable to predict accurate vaporization rates and interface temperatures. Transient heating of the droplets must be included. Hence, the conduction-limit model is employed for the liquid phase, and the energy conservation equation is the only equation to be solved for the droplet itself [9, 74, 75, 149, 236, 381]:

$$r^2 \rho_l c_{p,l} \frac{\partial T}{\partial t} = \lambda_l \frac{\partial}{\partial r} \left(r^2 \frac{\partial T}{\partial r} \right). \tag{2.3}$$

For the gas phase, the whole set of conservation and transport equations is solved. That is the conservation of mass (continuity equation), species, momentum, and energy. The widely used assumption of quasi-steadiness is abandoned here to account for the rapidly changing interface conditions of the liquid and gas phase due to the combustion process. Instead, the transient equations for both liquid and gas phase are solved simultaneously on a moving mesh by a block-coupled solver[8] [325, 341, 362–365]. No semi-empirical Nußelt and Sherwood correlations have to be employed because boundary layers are resolved in detail [268, 384]. The model takes into account many important effects, such as variable physical properties and a non-unitary Lewis number in the gas phase, the influence of Stefan flow (blowing), and, as mentioned above, the effect of transient liquid heating inside the droplet.

Definition of Group Combustion Modes of Liquid Droplets

Chiu and coworkers [71–73, 427] developed a physical model on "group combustion" of droplets. Amongst others, it predicts a single diffusion flame surrounding a cloud of droplets, with the flame separated some distance from the interface of the cloud (Fig. 2.4). Suzuki and Chiu [427] give a quasi-steady analysis of this combustion mode. The analysis reveals that flame size and burning rate depend on a non-dimensional parameter, which is termed as group combustion number G. It represents the degree of interaction between the gas and liquid phase and consequently serves to differentiate strong from weak interactions. The calculation of G includes the correlation of Frössling [141] that accounts for the effects of convection on heat and mass transfer with Reynolds number Re and Schmidt number Sc:

$$G = 3\left(1 + 0.276\, Re_{\text{drop}}^{\frac{1}{2}}\, Sc^{\frac{1}{3}}\right) Le\, N^{\frac{2}{3}}\, \frac{r}{S}. \tag{2.4}$$

The droplet Reynolds number Re_{drop} represents the relative velocity between droplet and surrounding gas. Small droplets rapidly attain the same velocity as the surrounding gas, after which they are susceptible only to the fluctuating component of velocity u' [70]. According to Sirignano [404], the droplet Reynolds number is $Re_{\text{drop}} = 0$ for the case of spherically symmetric vaporiza-

[8] A block-coupled (matrix) solver solves the fully block-coupled Jacobian system at each step of Newton's iteration. A subsequent calculation of the gas and liquid phase is not necessary.

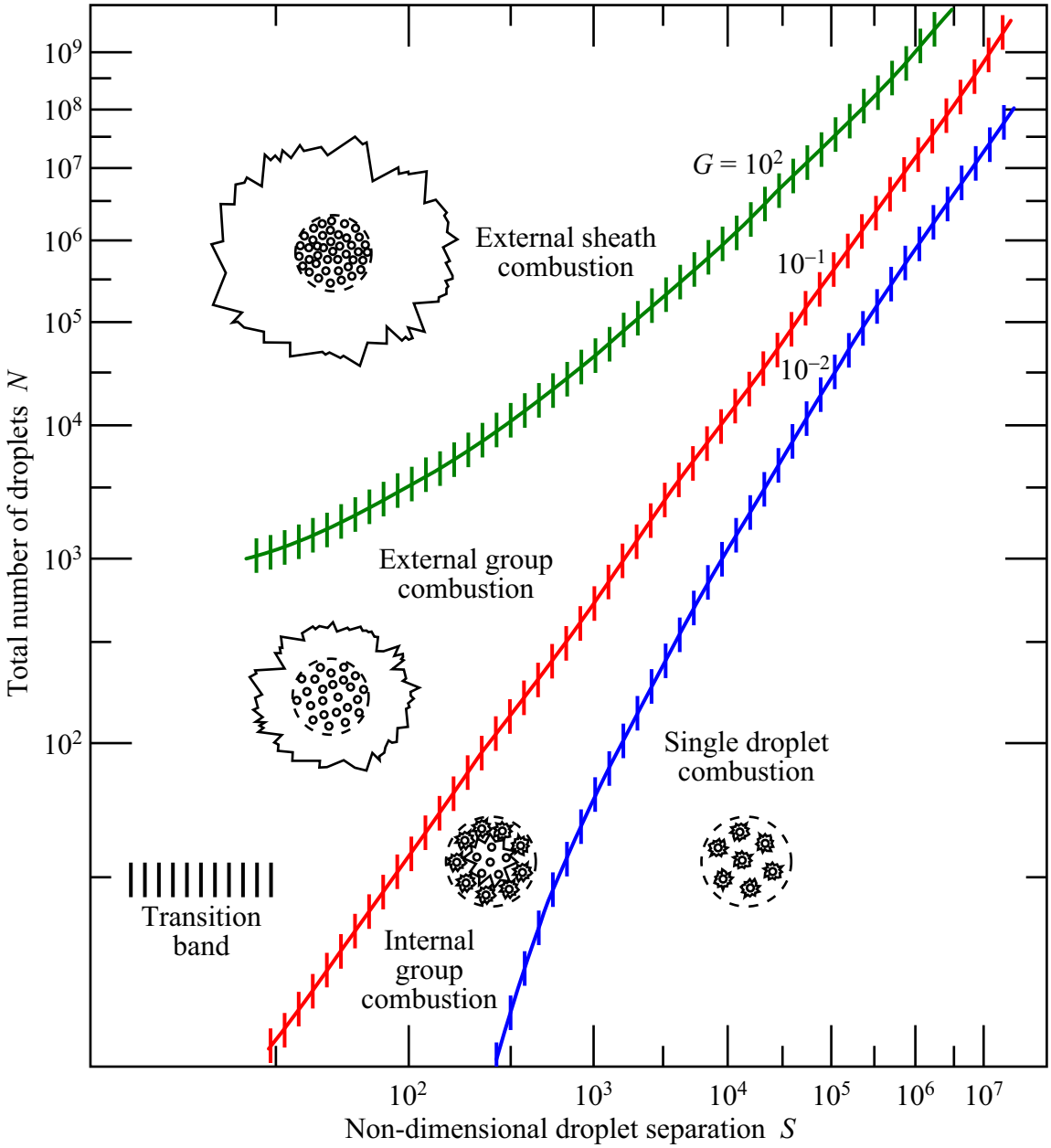

Figure 2.4: Group Combustion Modes of a Droplet Cloud (reprinted and adapted from Refs. [20, 73]). The group combustion number G acts as the index of the excitation of a particular combustion mode [71–73, 427].

tion. Still, if vaporization can yield Stefan flow, as in the present study, Re_{drop} is not small compared with unity.

Group combustion is realized when the parameter G exceeds a critical number. As illustrated in Figure 2.4, group combustion of a droplet cloud can be categorized by the occurrence of four combustion modes: external sheath

combustion, external group combustion, internal group combustion, and single droplet combustion.[9] The abscissa S denotes the non-dimensional separation between the droplets and ordinate N the total number of droplets in the cloud. In addition to the classification given in Figure 2.4, Chiu et al. [72, 73] found that the so-called internal group combustion mode occured in the range of $1\times10^{-2} < G < 1$, depending on fuel properties, stoichiometry, and conditions of the environment. The group behavior of the droplet cloud produces a rich, non-flammable mixture, and thus inhibits ignition in the vicinity of an individual droplet. In general, an increase in G results in an increase of flame size and characteristic burning time. According to Suzuki and Chiu [427], the increase in burning time due to group combustion is also conjectured to be a possible mechanism for incomplete combustion.

As far as droplet setups investigated within the present study are concerned, the group combustion number calculates to $G \approx 0.05$ for single droplets and $0.6 < G < 7.3$ for droplet arrays. This includes an estimate of Gogos et al. [153] on the initial droplet Reynolds number due to the movement of the droplet setup into the preheated combustion chamber. The scope of G covered by the present study can be allocated at the lower left corner of Figure 2.4 but does not fully fit into the area predefined by Chiu et al. [72, 73] as a result of an overall small number of droplets and a quiescent ambient environment.

A different classification was proposed by Umemura and coworkers [446, 447] with respect to droplet behavior during flame spread over a linear droplet array. Five different flame propagation modes were theoretically predicted, as shown in Figure 2.5. The appearance of these modes depends on two characteristic parameters: the non-dimensional gas temperature $R_s T_\infty / \Delta h_v$ and the non-dimensional inter-droplet distance S/D_0. Most essential to flame propagation are Mode I, II, and III. In the case of Mode I, a partially premixed flame propagates through a flammable fuel-air mixture, rapidly enclosing non-burning droplets that start to vaporize abruptly due to the sudden heat transfer. In the case of Mode II, the flame front at the "leading" droplet accelerates vaporization of a close-by droplet until ignition and flame spread. The ignited droplet is immediately enclosed in an envelope flame and burns as a diffusion flame in the group combustion mode. In the case of Mode III, the sequence is identical to Mode II until ignition. However, the droplet ignited

[9] Annamalai et al. [19, 20] use a breakdown into six categories and a slightly different terminology.

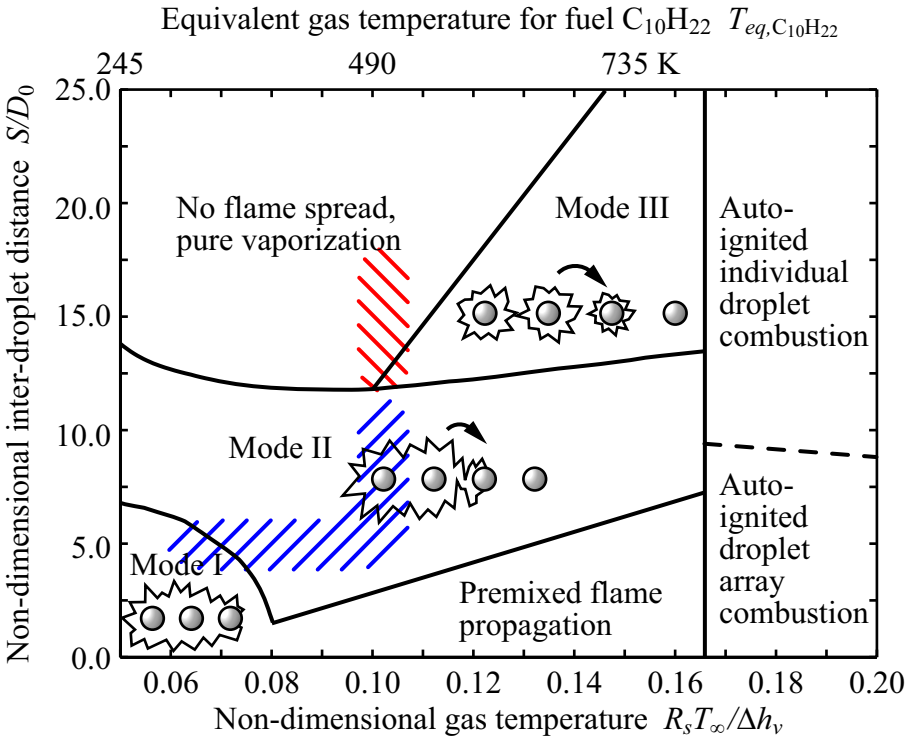

Figure 2.5: Schematic of Flame Propagation Modes for Linear Droplet Arrays (reprinted and adapted from Refs. [318, 456]). Experimental setups of the present study are included in the plot and marked by hatched areas.

continues burning by itself without participating in group combustion. The mode map, as depicted in Figure 2.5, is applicable to any kind of liquid hydrocarbon fuel and combustion under atmospheric pressure [318, 446, 447, 456].

The droplet array setups of the present study are also indicated in Figure 2.5. Setups without fuel pre-vaporization can be located in Mode I and II, whereas setups with pre-vaporization are on the border of "no flame spread" and Mode III. Due to pre-vaporization and the ensuing formation of a combustible gas layer in the proximity of the droplets, this region becomes accessible to flame propagation, offering some potential for NO_x abatement (cf. Fig. 2.2).

2.2 Theory of Exhaust Gas Formation

There are a number of different emission sources of pollutant gases into the atmosphere. Many of them are not of anthropogenic origin and might be

termed “natural sources” [391, 443]. These include among others geological processes, microbial processes, and animal excrements. Microbial processes, for instance, form carbon dioxide (CO_2), carbon monoxide (CO), methane (CH_4), ammonia (NH_3), nitrous oxide (N_2O), nitrogen oxides (NO_x), hydrogen sulfide (H_2S), and organic sulfur compounds. Lightning and forest fires are thermal processes producing NO_x, ozone (O_3), CO, volatile organic compounds (VOCs), sulfur monoxide (SO), and particulate matter (PM). Anthropogenic emission sources are mostly related to the burning of different kinds of fuel, and they may be classified into process-related and user-related emissions. Differentiation is also possible according to chemical composition, physical state, and the manner in which pollutants reach the atmosphere (primary or secondary pollutants) [391, 443].

The term “nitrogen oxides” (NO_x) in the first instance refers to any binary compounds of nitrogen and oxygen. However, in the particular field of atmospheric chemistry and air pollution, it is typically assigned to the sum of nitric oxide (NO) and nitrogen dioxide (NO_2), as is the case in this thesis. Besides, the term “oxides of nitrogen” is a synonym for nitrogen oxides in its general meaning, and thus is sometimes used to prevent ambiguousness. Nitrous oxide (N_2O) is commonly also known as laughing gas. Here, it is not included in the entity of NO_x [214, 391, 443, 451].

2.2.1 Carbon Monoxide

Apart from the major combustion products CO_2 and H_2O, carbon monoxide (CO) is the most copious air pollutant in the lower atmosphere. With respect to anthropogenic sources, emissions of CO exceed in quantity the mass of all other air pollutants combined. According to Annamalai and Puri [19] and Seinfeld [391], carbon monoxide pollution in urban areas correlates closely with motor traffic volume, with 84 % of the overall CO fraction stemming from vehicle exhaust. Increased levels of CO production are typically encountered in rich combustion systems, in nonpremixed combustion systems, in systems with partial oxidation of unburned fuel (e.g. in over-lean regions or during operation with insufficient liquid fuel vaporization), and in areas with quenching by cold surfaces or aerodynamic quenching. Carbon monoxide is a product of the incomplete oxidation of carbon-containing compounds before the final product CO_2 is attained. Thus, the CO content within the exhaust is a mea-

sure of combustion efficiency[10] [241–245]. In a flame, the conversion of CO into CO_2 results in a major heat release of the system. In general, CO oxidation proceeds slowly, unless some hydrogen-containing species are present, such as small quantities of H_2O and H_2 [149, 443]. The key reaction of the overall scheme is given as follows [408]:

$$CO + OH \rightarrow CO_2 + H, \tag{2.5}$$

where the reaction rate in mol cm^{-3} s^{-1} can be expressed as

$$\frac{d[CO]}{dt} = 4.76 \times 10^7 \; T^{1.23} \exp\left(\frac{-35}{T}\right) [CO][OH]. \tag{2.6}$$

Due to its high toxicity, but colorless, odorless, and tasteless nature, CO poisoning makes up more than half of the fatal air poisonings in many industrial countries. Its prevention and detections will remain a vital public health issue in the future [324, 391].

2.2.2 Unburned Hydrocarbons

Lefebvre [241] states that unburned hydrocarbons (UHCs) are the main source of the odors prevalent around airports. On the one hand, UHCs include fuel that emerges from the combustor in the form of droplets or vapor. On the other hand, they include products of thermal degradation of the parent fuel into species of lower molecular weight, such as methane (CH_4), acetylene (C_2H_2), or formaldehyde (CH_2O). In gas turbine combustion, UHCs are associated with poor atomization, deficient burning rates, the chilling effect of film-cooling air, or any combination of these [241]. Annamalai and Puri [19] quote limited residence time and quenching by walls in automobile engines. In a well-designed combustion process, the flame develops and expands within the combustion chamber free of obstacles and interferences. Fuel burnout will be achieved. Thus, UHCs are usually negligible in combustion devices employing premixed reactants. Furthermore, the nature of pollutant formation is such that concentrations of CO and UHCs are highest at low-power conditions and diminish with an increase in power. If a flame is extinguished a short distance from a cold surface, the quenching process leaves a

[10] Combustion efficiency is primarily a function of the equivalence ratio ϕ. It is only secondarily a function of the specific combustion progress.

thin layer of unburned fuel-air mixture adjacent to this wall. If a lean or dilute mixture approaches the flammability limit, flame propagation into the whole bulk of the mixture may be inhibited. In either case, the combustion process remains incomplete, which facilitates the formation of pollutants as well as the release of combustion remnants including CO and UHCs [160, 241, 443].

2.2.3 Oxides of Nitrogen

The U.S. Environmental Protection Agency [451] and the textbook of Annamalai and Puri [19] cite seven oxides of nitrogen that may be present in ambient air: nitric oxide (NO), nitrogen dioxide (NO_2), nitrogen trioxide (NO_3), nitrous oxide (N_2O), dinitrogen trioxide (N_2O_3), dinitrogen tetroxide (N_2O_4), and dinitrogen pentoxide (N_2O_5). Of these oxides, NO and NO_2 are the most important species because they are emitted in large quantities, and thus present in the highest concentrations in the lower atmosphere. Due to their interconvertibility in photochemical smog reactions, they have notably been grouped together under the designation NO_x [25, 98, 214, 451].

Being emitted by both anthropogenic and natural sources, nitric oxide (NO) is an odorless gas. Since its absorption bands lie at wavelengths below $\lambda = 230\,\text{nm}$, which is well below the visible range, it is also a colorless gas. It is only slightly soluble in water. Nitric oxide has an uneven number of valence electrons but does not dimerize in the gas phase, as does NO_2. The burning of fuels is the primary anthropogenic source of NO, and NO is the predominant oxide of nitrogen formed during high temperature combustion. These issues arise from oxidation of atmospheric, molecular nitrogen (N_2) in the combustion air, on the one hand, and from interaction of organically bound nitrogen, present in certain fuels such as coal and heavy fuel oil (HFO), on the other [19, 391, 451]. Bowman [50, 51] and Miller and Bowman [289] classify the following major categories of NO formation with respect to the oxidation of nitrogen in combustion. A breakdown of each category is given further along in the chapter:

- Extended Zeldovich mechanism – also called “thermal mechanism”
- Fenimore pathways via CN and HCN (i.e. prompt NO)
- N_2O-intermediate route

- NNH-intermediate route
- Fuel nitrogen mechanism
- Formation of NO_2

Nitrogen dioxide (NO_2) is a reddish-brown toxic gas with a characteristically pungent odor. It is corrosive and highly oxidizing. Although the boiling point of NO_2 is high at $T = 294\,K$ [453], its low partial pressure in the atmosphere prevents condensation. Nitrogen dioxide also has an uneven number of valence electrons and forms the dimer N_2O_4 at higher concentrations and lower temperatures [391, 451]. For gas turbines of previous generations, characteristic NO_2/NO_x ratios were determined to be in the range of 15 to 50 %, with highest values prevailing under lean conditions or in idle mode. Yellow smoke was frequently encountered and seen as a formidable challenge in combustion engineering. The extensive formation of NO_2 was finally located in the primary zone of the combustor [100, 229, 241, 248]. In typical modern combustion processes, NO_2 is emitted in small quantities of 5 to 10 % by volume of the total NO_x emissions along with NO, and it is formed in the atmosphere by the oxidation of NO [391, 451].

In general, NO_2 is unlikely to be formed in a premixed flame under stoichiometric conditions. However, nonpremixed flames and/or local areas of lower temperature of 600 to 1200 K are conducive to NO_2 formation. Furthermore, the temperature level succeeding the initial combustion stages is essential, as NO_2 destruction is initiated at temperatures above 900 to 950 K due to equilibrium with NO [214] and the presence of the radicals O, H, and OH that play an important role in recombination reactions [229, 380]. Nevertheless, there has been controversy surrounding the question to which extent the NO_2 measured in some experiments is due to the actual combustion process or to sample probe effects [15, 149, 241]. As summarized by Kramlich and Malte [217], combustor-formed NO_2 is believed to be due to the rapid cooling of pockets of combustion gases as they turbulently mix with cooling air. This could also be demonstrated in measurements by a sharp increase in the NO_2/NO_x ratio while varying the equivalence ratio as well as parameters responsible for flame length and aerodynamic quenching [15, 69, 217].

Nitrous oxide (N_2O) is ubiquitous, even in the absence of any anthropogenic sources. It is neither known to be involved in photochemical smog reactions

nor generally considered to be an air pollutant. Still, it is a greenhouse gas and participates in atmospheric chemistry involving the ozone layer by forming NO and destroying the ozone [428, 451]. Currently, N_2O emission is the single most important ozone-depleting emission and expected to remain so throughout the 21st century. In the troposphere, N_2O has a lifetime of 100 to 200 years, compared to NO_x in the range of minutes to days. Thus, the contribution of combustion processes to the overall N_2O formation is meaningful, despite the fact that combustion is only a minor direct source of N_2O formation and NO_x formation is predominant with regard to the sum of all oxides of nitrogen [19, 51, 135, 347].

The remaining representatives of oxides of nitrogen, as introduced above, (NO_3, N_2O_3, N_2O_4, and N_2O_5) are present in the lower atmosphere only in very low concentrations, even in polluted environments. Nonetheless, they play a role in atmospheric chemistry leading to the transformation, transport, and ultimate removal of nitrogen compounds from ambient air [451]. Discussing the mechanisms on photochemical smog formation, Demerjian et al. [98] for instance provide estimates of concentrations of the various oxides and acids of nitrogen that would be present in the equilibrium state, initially assuming only molecules of nitrogen and oxygen at atmospheric pressure, 25 °C, and a relative humidity of 50 %.

Extended Zeldovich Mechanism

The two most important parts of NO_x chemistry are the thermal NO and prompt NO reactions. These two pathways comprise the major initial steps of breaking up air nitrogen molecules. Thermal NO can be described by the chain reactions of Equations (2.7) and (2.8) that were first postulated by Zel'dovich in 1946 [471, 472]. The strong temperature dependence from which this particular type of NO derives its name is due to the fact that the N_2 molecule has an extremely strong triple bond. This bond needs to be broken in order to form NO [19]:

$$O + N_2 \rightleftharpoons NO + N, \tag{2.7}$$

$$N + O_2 \rightleftharpoons NO + O. \tag{2.8}$$

It is common practise to include the step of Equation (2.9) in the thermal mechanism, even though the reacting species are both radicals, and thus the concentration terms are typically very small in the chemical rate expression. This combination of reactions (Eqs. (2.7) through (2.9)) is referred to as the "extended Zeldovich mechanism" [149, 289, 443, 471, 472].

$$\mathrm{N} + \mathrm{OH} \rightleftharpoons \mathrm{NO} + \mathrm{H} \tag{2.9}$$

As stated by Bowman [50], the formation of NO from atmospheric nitrogen compares well for these three reactions and results extracted from detailed kinetics calculations. However, it is essential that radical concentrations and temperature are correctly evaluated during the combustion process. For fuel-rich mixtures, the extended reaction (Eq. (2.9)) is of particular importance. Equation (2.7) represents the rate limiting step with the highest activation energy of $E_a = 3.190 \times 10^5\,\mathrm{J\,mol^{-1}}$, coupled with its essential function of breaking the strong N_2 triple bond [19, 443]. Consequently, the whole thermal mechanism proceeds at a somewhat slower rate than the reactions of the fuel constituents. Moreover, the production of atomic oxygen (O) required in Equation (2.7) is also highly temperature sensitive. The local equivalence ratio has a first-order effect on the available concentration of O, and the high-temperature regime of the flame in combination with the hydrocarbon kinetics of the fuel can boost the O concentration to several times its equilibrium level [50, 391, 451].

Since the overall formation rate of NO due to the thermal mechanism is generally slow compared to the fuel oxidation reactions, and following the suggestion of Zel'dovich et al. [472], it is often assumed that the above reactions on thermal NO can be decoupled from the fuel oxidation process. Equilibrium is assumed for temperature and the concentrations of O_2, N_2, O, and OH.[11] The concentration of atomic nitrogen (N) is calculated from a steady-state approximation applied to the reactions of Equations (2.7) through (2.9) [64, 289]. This approach was also chosen for the theoretical and numerical studies of Bracco [54, 55], Altenkirch et al. [17], and Kesten [204] on NO generation in single droplet flames conducted in the early 1970s. However, fuel oxidation

[11] Even though this approach is more convenient than detailed chemistry modeling, its use has to be carefully assessed. It may provide reasonable results if an extremely high temperature level and long residence times are given, such as in automobile engines. A major shortcoming of the approach is that NO_x formation is underestimated in the reaction zone. Hence, this approach is not employed within the scope of this thesis.

is assumed to occur infinitely fast (by use of a one-step second-order mechanism), and the transient effect of droplet combustion is not captured. Nitric oxide formation is modeled by the simple Zeldovich mechanism (Eqs. (2.7) and (2.8)) using a quasi-steady state assumption to calculate temperature as well as the mass fractions of O and N [297, 298].

Fenimore Pathways

Fenimore [131] discovered through experiments that some NO was rapidly produced in premixed hydrocarbon flames long before enough time had passed for reactions of the extended Zeldovich mechanism to gain any real significance. Since this fast, transient formation of NO was confined to the primary reaction zone, it was termed "prompt NO" by Fenimore [131–135, 149, 289, 443]. In particular under fuel-rich conditions this mechanism can become the dominant mode of breaking the N_2 bond [123].

The initial reactions of the Fenimore pathways are less endothermic and require a lower activation energy than the respective reactions of the thermal mechanism. Thus, they can proceed at a rate comparable to hydrocarbon conversion [193]. The initial steps and rate-limiting are [19, 149, 443]:

$$\mathrm{CH} + \mathrm{N_2} \rightleftharpoons \mathrm{HCN} + \mathrm{N}, \tag{2.10}$$

$$\mathrm{HCN} + \mathrm{O} \rightleftharpoons \mathrm{NCO} + \mathrm{H}. \tag{2.11}$$

The CH radical in Equation (2.10) is an intermediate product of hydrocarbon combustion. Amines and cyano compounds, such as hydrogen cyanide (HCN) and nitrogen carbon monoxide (NCO), are formed as precursors to NO formation, which is omitted here [297, 298].

N_2O-Intermediate Route

According to Bowman [51] and Miller and Bowman [289], the principal gas phase reactions forming N_2O in the combustion of fossil fuel are:

$$\mathrm{NCO} + \mathrm{NO} \rightleftharpoons \mathrm{N_2O} + \mathrm{CO}, \tag{2.12}$$

$$\mathrm{NH} + \mathrm{NO} \rightleftharpoons \mathrm{N_2O} + \mathrm{H}. \tag{2.13}$$

The formation of N_2O as an intermediate species (Eq. (2.14)) and its subsequent conversion to NO (Eq. (2.15)) is important in fuel-lean mixtures ($\phi < 0.8$) at low temperatures and elevated pressures, as experienced in lean premixed gas turbine combustion (see Chap. 2.1.1) [88, 428]. Turns [443] summarizes Equations (2.13) through (2.15) as the "N_2O-intermediate route".

$$O + N_2 + M \rightleftharpoons N_2O + M \tag{2.14}$$

$$O + NO \rightleftharpoons N_2O + CO \tag{2.15}$$

NNH-Intermediate Route

In 1994, Bozzelli et al. [53] proposed that NO can also be formed via the intermediate NNH, that itself is metastable with respect to N_2 and atomic hydrogen (H) by about 2.510×10^4 J mol^{-1} (Eq. (2.16)) [171, 173]. The authors suggest the following main route:

$$N_2 + H \rightleftharpoons NNH, \tag{2.16}$$

$$NNH + O \rightleftharpoons NH + NO. \tag{2.17}$$

Evidence from different experimental setups confirms this pathway and supports its importance for NO_x modeling [171, 173, 215]. The associated investigations included lean, stoichiometric, and fuel-rich mixtures burned at low and high pressures in premixed flames as well as in stirred reactors. Hughes et al. [185] provide a detailed discussion of the reactions of NNH, while Rutar et al. [369] evaluate the NO_x formation pathways in lean premixed, prevaporized combustion of seven different fuels. The authors of the latter study conclude that the Fenimore and NNH pathways dominate the formation of NO_x in the flame, while the Zeldovich and N_2O pathways are primary contributors to the NO_x formation in the post-flame zone [149, 369]. Thus, this mechanism can pose additional limits on the lowest NO_x emissions achievable.

Fuel Nitrogen Mechanism

If fuels, including coal and HFO, contain nitrogen in their molecular structure, this organically bound nitrogen runs through the ordinary combustion pathways. It is rapidly converted into hydrogen cyanide (HCN) or ammonia (NH_3)

before it follows the prompt NO mechanism [443]. The formation of fuel NO is relevant for temperatures above 1100 K. For coal and medium fuel oil (MFO), for instance, 60 to 80 % of the fuel-bound N_2 are converted into NO [19, 451].

Formation of NO_2

Equation (2.18) illustrates the exothermic reaction that is responsible to some extent for NO_2 present in the combustion emissions but only of minor importance in most ambient situations due to its slow progress under the associated ambient conditions [214]:

$$2\,NO + O_2 \rightarrow 2\,NO_2. \tag{2.18}$$

According to Sano [373, 374] and Miller and Bowman [289], the essential step of NO_2 formation in flames is represented by Equation (2.19). Significant amounts of the hydroperoxy radical (HO_2) are produced in flame regions of lower temperatures and transported by diffusion into the high-temperature regime, where NO is formed and available for oxidation. The subsequent HO_2 attack on NO (Eq. (2.19)) is two orders of magnitude faster than the reaction of Equation (2.18) [149]:

$$NO + HO_2 \rightarrow NO_2 + OH. \tag{2.19}$$

As NO_2 is an efficient absorber of light over a broad range of ultraviolet and visible wavelengths, it participates in photochemical smog reactions by photolysis (i.e. photodissociation). Nitrogen dioxide absorbs sunlight and subsequently decomposes to NO and O, thus triggering a complex series of reactions involving organic compounds that lead to photochemical smog:

$$NO_2 + h\nu \rightarrow NO + O, \tag{2.20}$$

$$O + O_2 + M \rightarrow O_3 + M. \tag{2.21}$$

Here, M represents a third body molecule that absorbs the excess vibrational energy and thereby stabilizes the O_3 molecule formed [149, 391, 451].

Review on NO_x Formation with Regard to Technical Applications

In 1975, Ludwig et al. [258] reported on experimental measurements[12] of the major stable species, including NO, within diffusion flames around simulated ethanol (C_2H_5OH) droplets burning in air under atmospheric conditions. Despite the fact that the measured flame temperatures were considerably lower than the estimated ones, the NO concentrations were greater than predicted theoretically. In another investigation and a further step towards technical applications, Nizami et al. [315, 316] discuss experimental results of NO and NO_x emissions from the atmospheric, monodisperse fuel spray combustion of different hydrocarbon fuels. The authors observed a significant effect of droplet size, with NO and NO_x reaching minima around a droplet size of 48 to 55 µm. These minima shift towards a smaller droplet size for single component fuels of lower vapor pressure. Pre-vaporization in the spray and the transition from diffusive to pre-vaporized, premixed combustion are considered important factors in determining the minimum NO_x point.

A comprehensive case study on the contribution of the different NO_x formation mechanisms was conducted by Nishioka et al. [314] for methane-air double flames.[13] The numerical study specifies production of NO via the thermal mechanism, Fenimore pathway, N_2O-intermediate route, and NO_2 formation. In this regard, the authors highlight the importance of the velocity gradient within the flame. Rutar and Malte [367] discuss the contribution of the different pathways of NO_x formation for high pressure jet-stirred reactors, being significant for lean premixed gas turbines. Aggarwal et al., on the one hand, investigated the behavior of single and multi-component fuels by applying different vaporization models [8–10], and on the other hand, studied the impact of various NO formation mechanisms, including thermal and prompt NO, in partially premixed flames in a counterflow configuration [303, 304, 468, 469]. Chen and Driscoll [68, 69] examined the contribution of the different NO_x species in experiments, studying a jet diffusion flame. An increased level of partial premixing, as for instance realized by forcing coaxial air into the flame, could drastically (up to sixfold) decrease NO_x emissions. Here, the authors attribute the large NO_x reduction to the diminishing flame length and the flame

[12] This work is in a series with the theoretical studies of Bracco [54, 55] stated above.

[13] Double flames have a structure that is characterized by an initial rich premixed flame that produces CO and H_2 as the two main intermediate products. A final diffusion flame consumes these intermediate products together with the surrounding air.

position, which shifted towards the nozzle. This coincides with larger flow velocities, lower local residence times, and a smaller reaction zone volume. Utilizing a similar configuration, Lyle et al. [260] investigated the NO_x formation characteristics of partially premixed turbulent jet flames. They found that the global volumetric NO_x production rate cannot be explained by the Zeldovich mechanism alone and different regimes of partial premixing have a significant impact on the absolute NO_x values. Employing spatially resolved, linear laser-induced fluorescence (LIF) measurements, Cooper and Laurendeau [84, 85] quantitatively evaluated NO production in preheated lean direct injection (LDI) spray flames at elevated pressures. A pressure scaling of NO is derived from these profiles, which is in line with the results of NO_x formation previously obtained by Aigner et al. for a partially premixed injector [13, 88]. Most of these research groups specify the NO_x emissions obtained by the emission index EI_{NO_x}, as is done in the study at hand.

In conclusion, NO_x formation is a function of temperature, residence time, excess air, oxygen concentration (N_2/O_2 ratio), and extent of mixing. To achieve the NO_x levels currently set by regulatory agencies, a combination of the following combustion techniques is necessary. Individual solutions may differ significantly for different applications, as for instance in stationary gas turbines or boilers [50, 51, 136, 149, 241, 242, 443]:

- Lean (premixed) operated primary zone – resulting in lower local flame temperatures
- Reduced combustion zone volume – minimizing residence time
- Increased liner pressure drops – increasing turbulence and mixing
- Water or steam injection – lowering flame temperatures
- Combustion zone cooling by flue gas recirculation – lowering local flame temperatures and depleting the available oxygen
- Staged combustion – reducing temperatures and available oxygen

After all, most of these approaches involve a direct or indirect deficit of efficiency of the thermal engine. On the downside of such a reduction of efficiency, the NO_2 component typically increases. Moreover, the NO_2/NO_x ratio is very likely to increase with a decrease in the total NO_x level [68, 69, 149, 241].

2.2.4 Particulate Matter

The term “particulate matter” (PM) refers to any substance, except pure water, that exists as a liquid or solid in the atmosphere and is of microscopic or submicroscopic size but has larger dimensions than molecules. Particulate matter may not only result from the direct emission of particles but also from condensation processes or chemical transformation. In order to provide a full description of PM, it is essential to specify the particle concentration, size, chemical composition, state of phase, and morphology [391].

Combustion-generated particulates mainly consist of carbon and have an empirical formula of approximately C_8H [19]. These carbonaceous particulates are generally formed in gas-phase processes and referred to as soot. Those that are a product of the pyrolysis of liquid hydrocarbon fuels are commonly termed coke or cenospheres. The main constituents of soot are carbon and polycyclic aromatic hydrocarbons (PAHs) [148, 149]. In particular, the fractions containing PAHs were demonstrated to be carcinogenic and even mutagenic [96, 257, 391]. In premixed combustion, emissions of particulate matter mainly result from fuel additives or rich operation, with the latter usually stemming from some type of malfunction [443]. In diffusion flames, the flame luminosity gives an approximate impression of soot distribution. The maximum concentration occurs where the rate of particulate formation equals the rate of its oxidation. Since the presence of carbon particulates increases the radiative power of the flame and, thus, the heat transfer rates, it can be beneficial to operate an industrial system in a particular diffusion flame mode with an enhanced formation of carbon particles [62, 174, 455]. Despite the complex chemistry and physics of soot formation in diffusion flames, Turns [443] summarizes the process by a four-step sequence:

- Formation of precursor species
- Particle inception
- Surface growth and particle agglomeration
- Particle oxidation

2.3 Kinetic Modeling

This chapter reviews the fundamentals of kinetic modeling of hydrocarbon combustion. It is intentionally included in the combustion theory of Chapter 2, as the chemical mechanisms employed are well-established in combustion technology. However, this chapter also provides a link to the following chapters with a very particular approach on kinetic modeling. It aims at providing a reliable, compact hydrocarbon mechanism including NO_x chemistry. The proposed approach was also applied in the numerical modeling of the present thesis (Chap. 4). Moreover, a significant number of studies were previously carried out aiming for simplified chemical kinetic models [89, 94, 167]. For instance, Dagaut [93] investigated different model fuels for kerosene oxidation. Surrogate fuels for diesel engines were examined by Bounaceur et al. [49] and Pitz et al. [340]. In all three publications, n-decane ($C_{10}H_{22}$) yielded the best modeling of kerosene and diesel combustion.[14]

To capture the formation of soot, which is influenced by aromatics, it would be necessary to use more complex model fuels containing polyaromatic compounds. However, multi-component fuels and soot formation are not considered here due to the focus on NO_x formation and a general trade-off between model complexity and computational cost. Hence, pure $C_{10}H_{22}$ is the fuel of choice for the scope of this work [297, 298].

2.3.1 Hydrocarbon Mechanism

As pointed out by Moesl et al. [297, 298], there are only two reaction mechanisms for n-decane that are applicable here, meaning they are sufficiently precise but with a species number not significantly above 100. The mechanisms of Honnet et al. [182] and Zhao et al. [474] include auto-ignition, are valid for wide ranges of temperature and pressure, and are limited to a reasonable number of species. The $C_{10}H_{22}$ mechanism developed by Honnet et al. [182] is based on the work of Bikas and Peters [43, 44]. The mechanism compiled by Zhao et al. [474] is an improvement of the work of Zeppieri et al. [473].

[14] n-Heptane (C_7H_{16}) is a minor component in practical fuels but often used as a model fuel in technical applications, as well [31, 175, 304, 340].

Zhukov [475, 477] compares both mechanisms to experimental data for ignition at high temperature and pressure that are typical for conditions in internal combustion engines. In order to achieve a realistic modeling of two-stage ignition in the low-temperature regime and a good agreement with shock tube experiments [337], Zhukov [476] also extends a mechanism previously proposed for lower alkanes to include the $C_{10}H_{22}$ chemistry of Bikas [43]. Battin-Leclerc [36] reviews and compares detailed kinetic models to simulate low-temperature oxidation and auto-ignition of gasoline and diesel fuel components. In an early step, Battin-Leclerc et al. [37] generated a detailed mechanism for $C_{10}H_{22}$ by using the software package EXGAS. However, the mechanism contains no auto-ignition chemistry, on the one hand, and a large number of species (1216) and reactions (7920), on the other. Buda et al. [60] present a unified model of detailed kinetics for the auto-ignition of alkanes from C_4 to C_{10}, which is based on the same software package. The size of the mechanisms seriously increases with the number of carbon molecules, and thus contains 715 species and 3872 reactions for $C_{10}H_{22}$. Because of their size, none of these latter models is considered a real option here. Another mechanism of Lindstedt and Maurice [254] is limited to the high temperature oxidation of $C_{10}H_{22}$ at atmospheric pressure with 193 species and 1085 reactions.

The $C_{10}H_{22}$ mechanism of Honnet et al. [182] itself contains 122 species and 527 reactions. Aromatic compounds are included in this mechanism. It is validated against experiments with shock tubes, rapid compression machines, jet stirred reactors, burner stabilized premixed flames, and a freely propagating premixed flame for mixtures of n-decane and 1,2,4-trimethylbenzene. In comparison, the mechanism developed by Zhao et al. [474] has only 86 species but 641 reactions. Experimental data of a flow reactor for decane oxidation and pyrolysis at atmospheric pressure, a jet stirred reactor, and a shock tube were used for validating the reaction kinetics. This mechanism is a significant improvement on Zeppieri et al. [473], as low temperatures were considered during the optimization of the mechanism, resulting in a better prediction of laminar flame speeds at room temperature.

Figure 2.6 presents the laminar flame speed S_L calculated using the n-decane chemistry of Zhao et al. [474] and Honnet et al. [182], denoted as “Princeton mechanism” and “Aachen mechanism”, respectively [297, 298]. The numerical results of this figure and the whole chapter were obtained with the software package Cantera [156]. Here, the 0D module was used to calculate perfectly

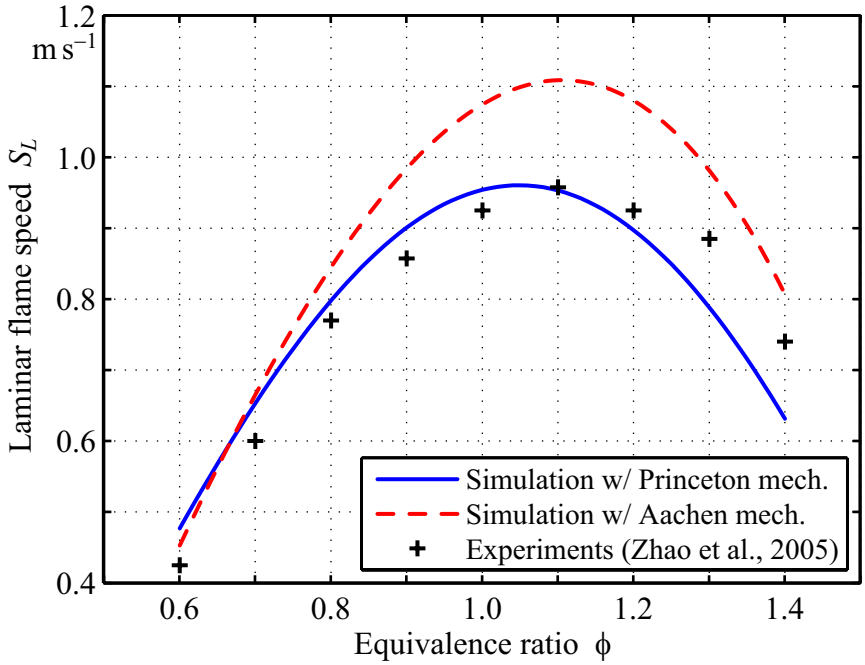

Figure 2.6: Laminar Flame Speed of a Premixed n-Decane Flame. Two $C_{10}H_{22}$ mechanisms are compared with experimental results of Zhao et al. [474]. The software package Cantera is used for calculating the laminar flame speed S_L [298].

stirred reactors, whereas the 1D module was used to investigate counterflow diffusion flames and laminar premixed flames. The results are compared to the experiments published by Zhao et al. [474]. Under stoichiometric conditions ($\phi \approx 1.0$), the Aachen mechanism overestimates laminar flame speed S_L by around 15 %, a discrepancy also pointed out by Zhao et al. [474] with reference to Bikas and Peters [44], which is the basis of the Aachen mechanism. As can be seen in Figure 2.6, the chemistry developed in Princeton is in very good agreement with the experimental results. However, the peak of S_L is shifted to a lower equivalence ratio ϕ compared with the experimental results.

Apart from all these detailed mechanisms, some concepts are presented in Appendix A that allow to obtain user-specific mechanisms involving fewer species and reactions. These may be a viable alternative when increasing the dimensional order and complexity of the computational domain with regard to multi-dimensional sprays [38–41]. In this case, convection and droplet interaction also have a significant impact on the burning behavior [154, 466].

2.3.2 Nitrogen Oxide Chemistry

Since neither the Princeton nor the Aachen mechanism contains nitrogen oxide chemistry, it had to be added to the hydrocarbon mechanism. In terms of applicable NO_x kinetics, literature refers to Li and Williams [250], based on the NO_x chemistry of Hewson and Bollig [176], as well as to Hughes et al. [186], known as the "Leeds mechanism". Thus, the following discourse deals with the approach towards a combined mechanism (Chap. 2.3.3).

Thermal

Since the extended Zeldovich mechanism is a strong function of temperature, the concentration of NO is evaluated for different reference mechanisms and representative combinations of hydrocarbon and NO_x chemistry. Figures 2.7 and 2.8 show results obtained from an adiabatic, perfectly stirred reactor after 1 ms residence time (reactor loading). This is a reasonable time because the present process is only a function of the chemical time scale, which is well below this time. No fuel (hydrocarbon) is applied to the initial conditions on the reactant side within this NO_x chemistry study. Thus, the air is initialized with a composition identical to ISO standard reference conditions, with the following mole fractions [190, 298]:

$$X_{N_2} = 0.782\,028, \tag{2.22}$$

$$X_{O_2} = 0.207\,881, \tag{2.23}$$

$$X_{H_2O} = 0.010\,091. \tag{2.24}$$

The exponential increase of NO formation with temperature is obvious and a result of the extended Zeldovich mechanism. Since there is no carbon in the gas phase, NO formation via the prompt NO path can be neglected. Although the thermal NO chemistry is similar in the mechanisms shown in Figure 2.7, the scatter in the results appears to be large. This is due to the fact that the kinetics compared are lumped mechanisms including only a reduced set of species. Moreover they are optimized to fit certain experimental data and validated against a limited range of problems. The formation of O, H, and OH radicals is critical to the production of NO_x in air at high temperatures but dominated by the respective radicals due to fuel oxidation in the presence of

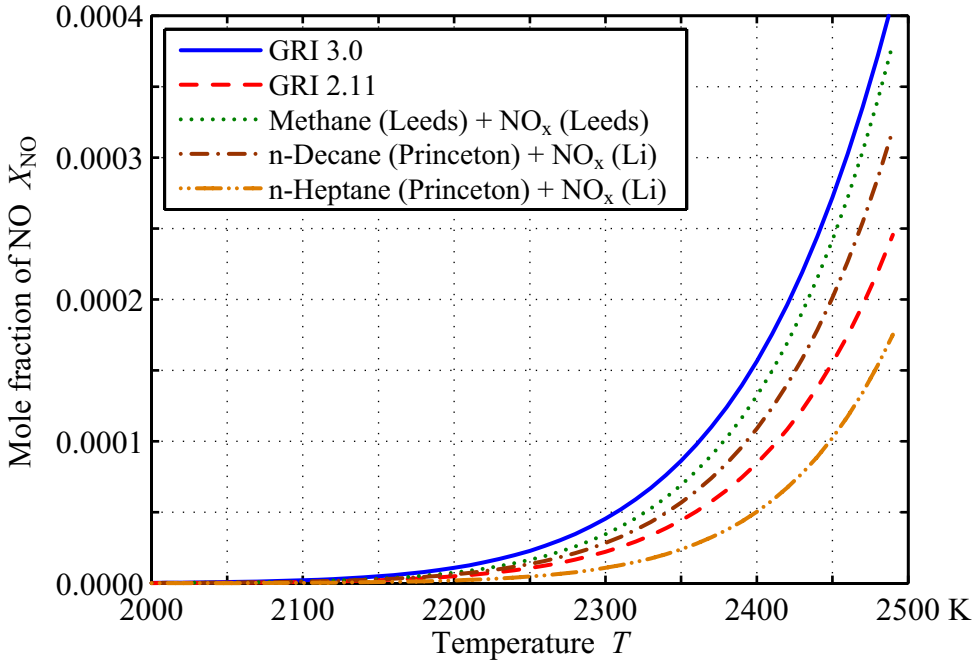

Figure 2.7: Temperature Dependence of the Extended Zeldovich Mechanism (no fuel included in the reactants). The plot shows the variation between three reference mechanisms (GRI 3.0, GRI 2.11, and "Methane (Leeds) + NO_x (Leeds)") and two representative combinations of $C_{10}H_{22}$ mechanism and NO_x kinetics ("n-Decane (Princeton) + NO_x (Li)" and "n-Heptane (Princeton) + NO_x (Li)") [298].

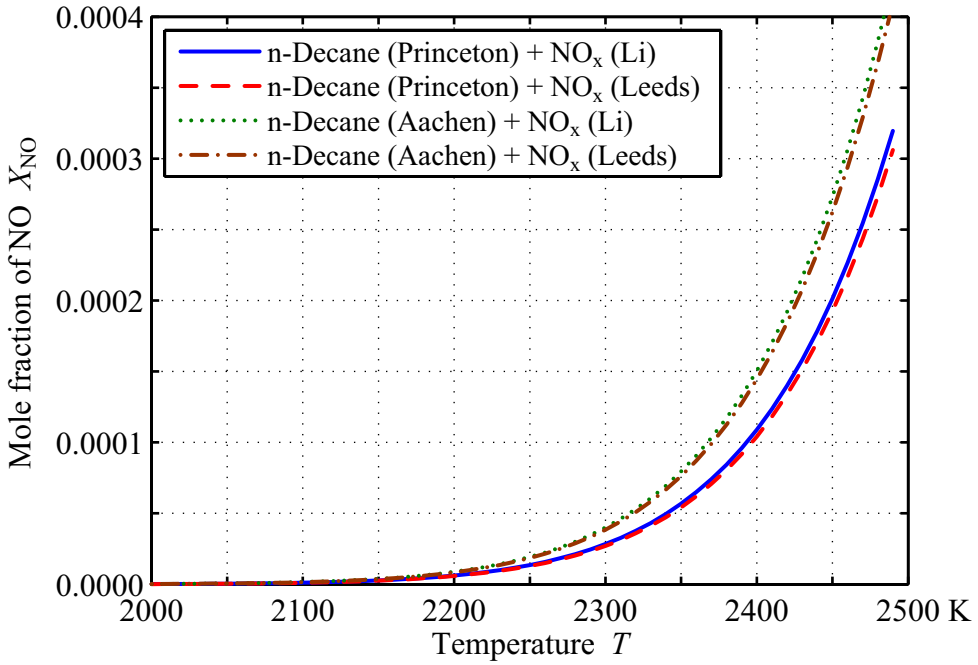

Figure 2.8: Temperature Dependence for Investigated Combinations of $C_{10}H_{22}$ Mechanism and NO_x Kinetics. The simulation parameters are identical to Figure 2.7 [298].

a flame. The GRI 3.0 mechanism (Fig. 2.7) was published by Smith et al. [408], GRI 2.11 by Bowman et al. [52], and the Leeds methane mechanism by Hughes et al. [187]. As illustrated in Figure 2.8, the influence of the fuel mechanism is much stronger than the difference between the NO_x kinetics of Li and Williams [250] and the Leeds NO_x mechanism. The results are similar for combinations with either the Princeton or the Aachen n-decane mechanism [298].

Prompt

Apart from the reaction of N_2 and CH (Eq. (2.10)), the Leeds mechanism [187] additionally includes reactions of N_2 with C and CH_2 radicals as the initial reactions of prompt NO formation. Figure 2.9 compares the reactivity of the three radicals. The activation energy of the nitrogen reaction with CH is by far the lowest with $E_a = 7.508 \times 10^4\,\mathrm{J\,mol^{-1}}$, thus making it the most reactive. The activation energy of the reaction with C and CH_2 is $E_a = 1.879 \times 10^5$ and $3.096 \times 10^5\,\mathrm{J\,mol^{-1}}$, respectively [298]. Consequently, the reaction of N_2 and CH is the most important of the prompt NO mechanism.

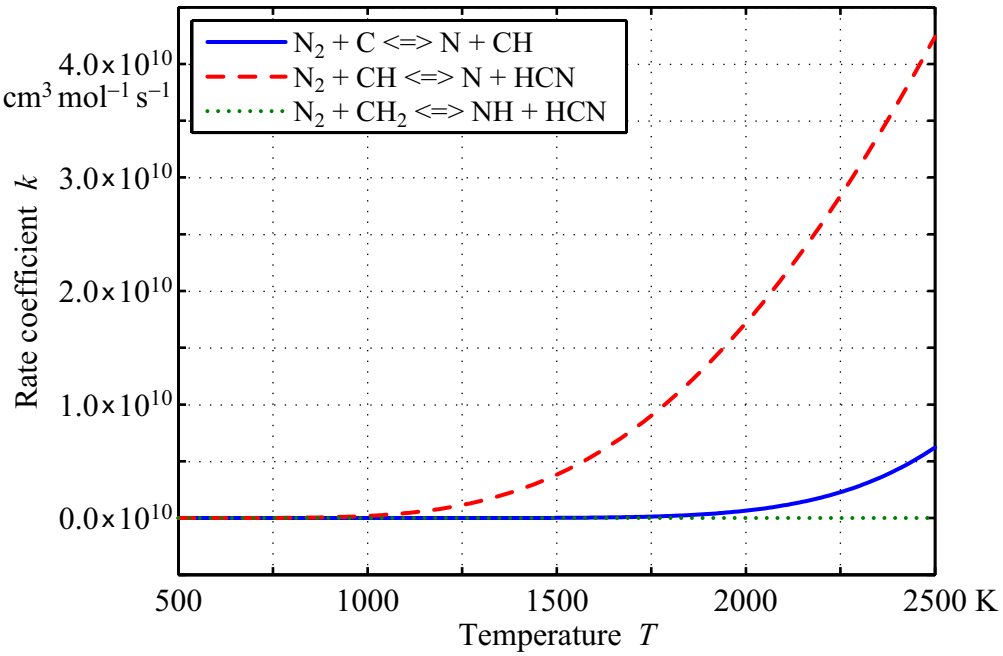

Figure 2.9: Reactivity of the Initial Reactions of the Prompt NO Mechanism.

Reburn

Miller and coworkers [289–291] and Dagaut et al. [95] worked out the main paths and radicals responsible for the reburn of NO. Concerning the reduction of NO by CH, CH_2, and CH_3, the mechanisms are in agreement [298]. Miller et al. [289, 291] also demonstrated the importance of HCCO for the temperature range of 1200 to 1500 K. The Leeds NO_x mechanism [188] accounts for this path but not the one of Li and Williams [250].

Normalization

As indicated in Chapter 2.2.3, the amount of NO_x can be summarized as a volumetric concentration in parts-per-million (ppm, ppmv, ppm(v), or ppm(v/v)) or as the emission index EI_{NO_x} in g_{NO_x}/kg_{fuel}. Regarding single droplets and numerical investigations, the emission index is the more convenient measure, as the overall molar fraction of NO_x depends very much on the size of the computational domain. The emission index is calculated from the production rates of the respective species and given in NO_2 equivalents (see also Chap. 4) [214, 370]:

$$EI_{NO_x} = \frac{m_{NO}\frac{M_{NO_2}}{M_{NO}} + m_{NO_2}}{m_{fuel}}. \tag{2.25}$$

The mass of nitrogen monoxide m_{NO} is multiplied by the factor M_{NO_2}/M_{NO}, where M_{NO_2} is the molar mass of NO_2 and M_{NO} is the molar mass of NO.

2.3.3 Validation of the Combined Mechanism

In order to validate the approach of combining the hydrocarbon mechanism and NO_x kinetics, four reasonable combinations were investigated [298]. A number of different combustion regimes were used for these studies: perfectly stirred reactors, laminar premixed flames, diffusion flames, and last but not least the droplet combustion model of Chapter 4.5 including partial droplet pre-vaporization. Extensive parameter variations were conducted with each of these setups to cover all combustion related aspects and to avoid a stiff system of equations or numerical singularities. Accurate mass fractions of the

NO_x species generally imply an accurate modeling of temperature and major products due to strong correlations between the species mass fractions, reaction rates, and temperature. Therefore, NO_x production sensitivity was evaluated as well as the influence of the attached NO_x kinetics on the main $C_{10}H_{22}$ mechanism. This included a comparison of the mass fractions of OH, CH_x, and the relevant radical pool between original $C_{10}H_{22}$ mechanisms and the respective combinations of $C_{10}H_{22}$ and NO_x mechanisms [297].

Validation of NO_x Production Sensitivity Against Reference Mechanisms

The Princeton and Aachen mechanisms (Chap. 2.3.1) were each combined with the NO_x kinetics of Li and Williams [250] and the Leeds NO_x mechanism [186] (Chap. 2.3.2 and Fig. 2.8). Thus, four combinations were investigated whose integral parts as such were of subordinate importance since only a unit of main hydrocarbon mechanism and NO_x kinetics could be employed in the final combustion model of Chapter 4. Here, results of these combinations are compared to simulations with the GRI 3.0 and GRI 2.11 mechanisms [52, 408] and the Leeds methane mechanism [188]. Since each of these three reference mechanisms features particular advantages in heterogeneous droplet combustion, the validation process was conducted on a broad basis. Barlow et al. [33], for instance, compare measured profiles of temperature and species mass fractions with the two GRI mechanisms. The agreement is within the estimated experimental uncertainty, and the two GRI versions roughly bracket the error bars of the measurements for calculations under lean and near-stoichiometric conditions [298].

The main validation focus of this section is set on diffusion flames due to their similarity with droplets, which allows for analogous analysis. Nevertheless, 1D laminar premixed flames were also included in the plausibility analysis of the combined mechanism. Methane (CH_4), ethane (C_2H_6), carbon monoxide (CO), and hydrogen (H_2) were used as fuel here because they are part of each of the four combinations and the three reference mechanisms. All numerical simulations were carried out at atmospheric pressure, and the initial temperature of fuel and air was set to 500 K. The composition of the combustion air was set according to reference conditions (Eqs. (2.22) through (2.24)).

The results of the validation were analyzed utilizing statistical means. Normal relative difference $\epsilon_{m,\mathrm{abs}}$ (Eq. (2.26)) and total relative difference $\epsilon_{m,\mathrm{tot}}$ (Eq. (2.27)) were evaluated for each case consulting spatial profiles of the mass fraction Y_m of critical species m. The normal relative difference is a measure for the degree of agreement of two curves, whereas the total relative difference gives an idea of whether a mechanism overestimates or underestimates the production of species m [298]:

$$\epsilon_{m,\mathrm{abs}} = \frac{\int \left| Y_m - Y_{m,\mathrm{ref}} \right| \, dx}{\int Y_{m,\mathrm{ref}} \, dx}, \tag{2.26}$$

$$\epsilon_{m,\mathrm{tot}} = \frac{\int \left(Y_m - Y_{m,\mathrm{ref}} \right) \, dx}{\int Y_{m,\mathrm{ref}} \, dx}. \tag{2.27}$$

A quantitative summary of the results is given in Tables 2.1 and 2.2 taking into consideration laminar premixed flames of CH_4, C_2H_6, CO, and H_2. The equivalence ratio ϕ was successively set to 0.8, 1.0, and 1.2 for each of these flames. The Aachen $C_{10}H_{22}$ mechanism together with the Leeds NO_x kinetics ("n-Decane (Aachen) + NO_x (Leeds)") exhibited poor convergence and stiff

Table 2.1: Mean Values of Normal Relative Difference of Mass Fraction of NO for Laminar Premixed Flames. All values of the normal relative difference $\epsilon_{m,\mathrm{abs}}$ are given in %.

	GRI 3.0	GRI 2.11	Leeds	Princeton + Li	Princeton + Leeds	Aachen + Li
GRI 3.0	0.0	24.4	20.4	16.1	17.5	24.4
GRI 2.11	16.6	0.0	15.9	17.7	16.3	39.0
Leeds	21.2	20.9	0.0	24.3	23.4	40.3

Table 2.2: Mean Values of Total Relative Difference of Mass Fraction of NO for Laminar Premixed Flames. All values of the total relative difference $\epsilon_{m,\mathrm{tot}}$ are given in %.

	GRI 3.0	GRI 2.11	Leeds	Princeton + Li	Princeton + Leeds	Aachen + Li
GRI 3.0	0.0	8.9	3.1	4.1	13.5	2.5
GRI 2.11	−5.3	0.0	−3.7	−1.8	6.4	1.7
Leeds	1.4	10.3	0.0	7.4	17.4	10.1

characteristics. Only three out of twelve calculations produced suitable results. Consequently, this combination is not considered further. The best agreement between combined kinetics and reference chemistry is achieved with the Princeton $C_{10}H_{22}$ mechanism. The normal relative difference $\epsilon_{m,\mathrm{abs}}$ is between 15 and 20 % compared to both GRI mechanisms. At the same time, the reference mechanisms themselves show a similar scatter. The total relative difference $\epsilon_{m,\mathrm{tot}}$ of the combination "n-Decane (Princeton) + NO_x (Li)" is close to zero, meaning that the results spread quite evenly around the reference values. On average, the calculated curves lie slightly above GRI 3.0 but below GRI 2.11. The combination "n-Decane (Princeton) + NO_x (Leeds)" tends to overestimate NO formation compared to all three reference mechanisms. The standard deviation of all four types of fuel is in the range of 10 to 15 % for both combinations of the Princeton $C_{10}H_{22}$ mechanism compared to GRI chemistry. Figures 2.10 and 2.11 show the temperature profiles and mass fractions Y_m of the oxides of nitrogen in a laminar premixed flame at an equivalence ratio of $\phi = 0.8$ for CH_4 and $C_{10}H_{22}$. Reactants are injected at the left side, exhaust leaves to the right. Nitric oxide (NO) is formed in the flame front as well as in the post-flame zone (see Fig. 2.1). Nitrogen dioxide (NO_2) production starts in the exhaust gas but is considerably lower than the formation of NO. The peak of NO_2 in the flame front indicates a narrow zone of NO_2 production followed by an immediate decrease downstream. Nitrous oxide (N_2O) develops a state of equilibrium downstream but close to the flame front.

One-dimensional counterflow diffusion flames have a strong semblance to droplet combustion and allow studying the effect of diffusion. The setup investigated within this study consists of two opposing jets [298]: one fuel jet and a jet of air. The distance between both jets is set to 0.020 m, mass flux of air to $0.5\,\mathrm{kg\,m^{-2}\,s^{-1}}$, and global strain rate to values in the range of 70.6 to $170.7\,\mathrm{s^{-1}}$ for the different fuels. Fuel flow is chosen in such a way that the conservation of momentum is fulfilled. Figure 2.12 illustrates the progression of temperature, axial velocity, and the mass fractions of fuel, oxygen, carbon dioxide, and water as a function of the axial coordinate x. Fuel and oxygen react in the flame zone, which can be determined to be around $x = 0.011$ m. Both reactants vanish, while the mass fractions of CO_2 and H_2O peak where temperature T reaches its maximum. A positive axial velocity u to the left of this maximum indicates a fuel flow from left to right. The negative axial velocity at $x = 0.020$ m accounts for air flow in the opposite direction. The stagna-

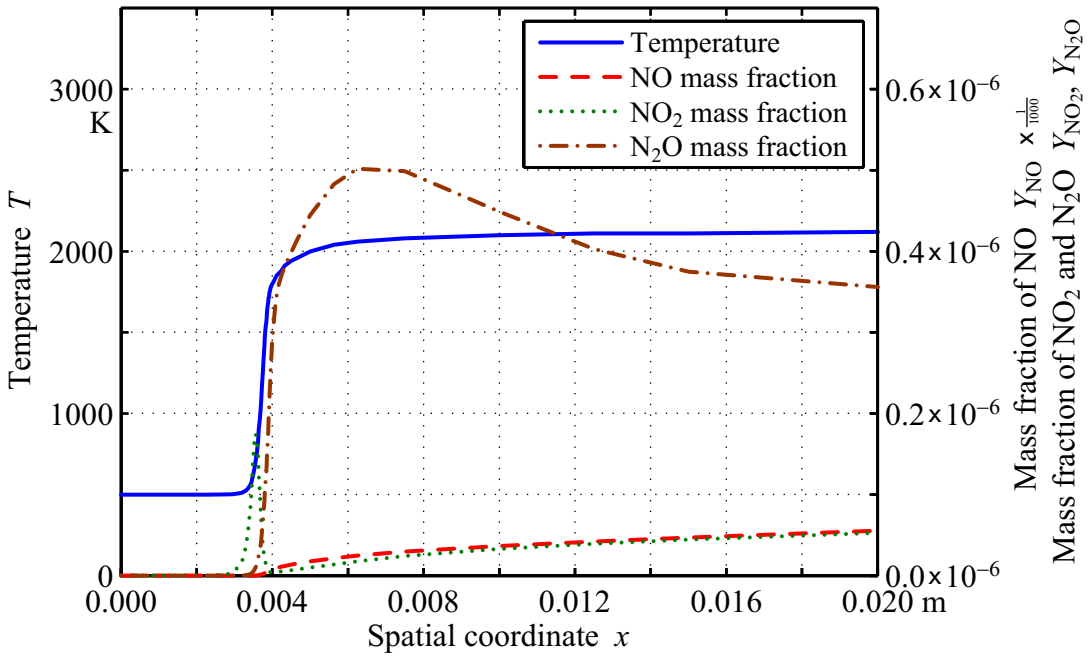

Figure 2.10: Temperature Profile and Mass Fractions of the Oxides of Nitrogen over a Laminar Premixed Flame of Methane. Results are shown for the GRI 3.0 mechanism and an equivalence ratio of $\phi = 0.8$ (note the scaling factors for Y_{NO}).

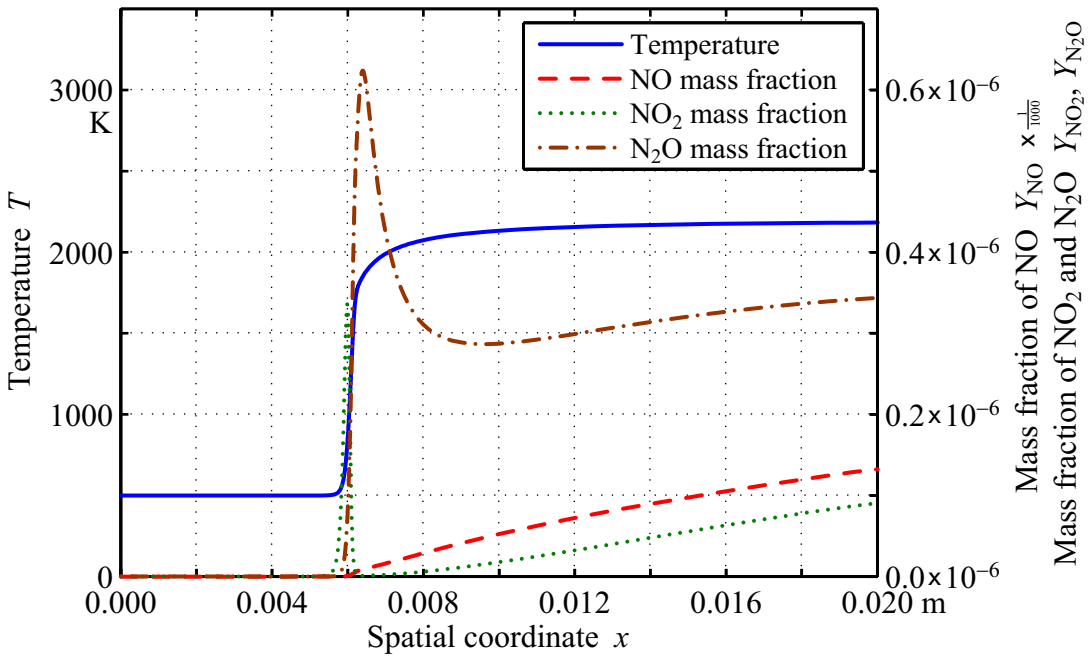

Figure 2.11: Temperature Profile and Mass Fractions of the Oxides of Nitrogen over a Laminar Premixed Flame of n-Decane. Here, results of the combination "n-Decane (Princeton) + NO_x (Li)" are shown for an equivalence ratio of $\phi = 0.8$.

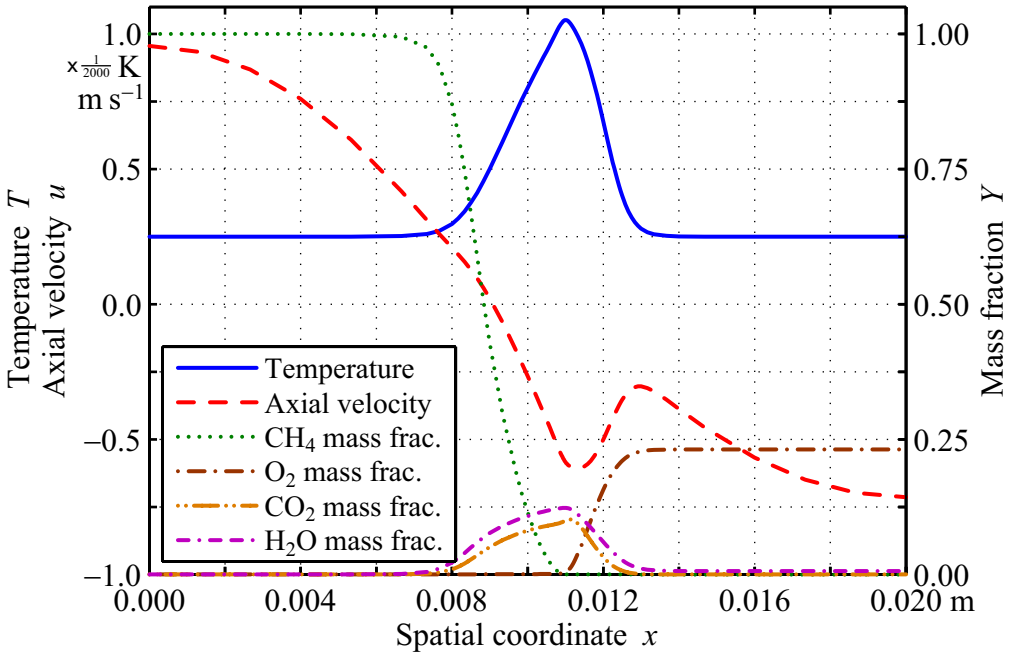

Figure 2.12: Profiles of Temperature, Axial Velocity, and Mass Fractions over a Counterflow Diffusion Flame of Methane. Apart from the fuel CH_4 displayed, similar studies were conducted on C_2H_6, CO, and H_2 [298].

tion point can be located where the axial velocity is $u = 0$. In the flame zone, the bulk velocity is $u < 0$, a characteristic of diffusion flames also described, for instance, in Nishioka et al. [314]. As a consequence, molecules of the fuel CH_4 need to overcome this convective flow by diffusion [298].

Depicting a counterflow diffusion flame of CH_4, Figure 2.13 is representative of the NO production of CH_4 and C_2H_6 flames. Both GRI mechanisms converge for this flame type. However, the spatial profile of GRI 2.11 is only half of that of GRI 3.0. Nonetheless, the low values of the GRI 2.11 mechanism are consistent with the work of Ravikrishna and Laurendeau [345, 346], in which a modified rate coefficient is proposed for the initiating reaction of prompt NO based on a comparison of experimental data and numerical calculations. The Leeds methane mechanism cannot be used as a reference here, as simulations converged only in one out of four cases. Figure 2.13 unveils the best agreement between GRI 3.0 and the combination "n-Decane (Princeton) + NO_x (Li)". The normal relative difference $\epsilon_{NO,abs}$ is around 10 % for hydrocarbon fuels (CH_4, C_2H_6), and the total relative difference $\epsilon_{NO,tot}$ is 2 % for CH_4 and 8 % for C_2H_6.

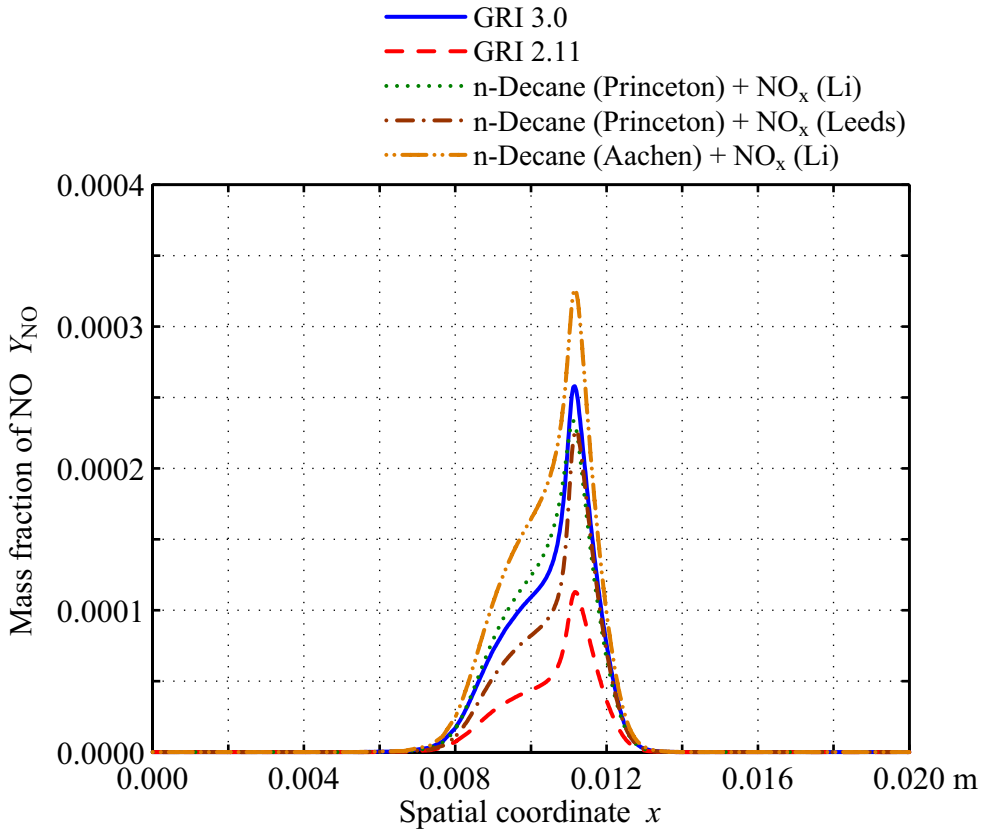

Figure 2.13: Mass Fraction of Nitric Oxide over Counterflow Diffusion Flame of Methane (chosen as an example). The results were obtained from different kinetics [298].

The combination "n-Decane (Aachen) + NO_x (Li)" overestimates NO formation.

Since the reference mechanisms differ widely, no straightforward recommendation is possible for the optimum combination of mechanisms, based on simulations conducted for counterflow diffusion flames. However, the combination "n-Decane (Princeton) + NO_x (Li)" converges best. Its results are comparable to those of the GRI 3.0 mechanism for hydrocarbon fuels. The combination "n-Decane (Princeton) + NO_x (Leeds)" gives slightly lower results.

Compatibility of Attached NO_x Kinetics with the Main Hydrocarbon Mechanism

In addition to NO_x production sensitivity, the influence of the NO_x kinetics attached to the main hydrocarbon mechanism was investigated simulating laminar premixed and counterflow diffusion flames. This was done by com-

paring the combined mechanisms with the original $C_{10}H_{22}$ mechanisms, with the latter acting as reference in terms of Equations (2.26) and (2.27). The difference (i.e. the relative error) was studied for temperature, velocity, fuel mass fraction, and product species [298].

Laminar premixed flames were calculated at an equivalence ratio of $\phi = 0.6$ to 1.4 in steps of 0.1. Laminar flame speed S_L obtained with the Princeton $C_{10}H_{22}$ mechanism decreases by up to 0.4 % under near-stoichiometric conditions and up to 1 % at both $\phi = 0.6$ and 1.4 as a consequence of adding the NO_x chemistry of Li and Williams [250] or the Leeds NO_x kinetics [186]. Flame speeds estimated with the combination "n-Decane (Aachen) + NO_x (Li)" lie 0.3 % below the original Aachen mechanism. By comparison, laminar flame speed is similar for the Princeton and Aachen mechanism at $\phi = 0.7$, but the difference goes up to almost 30 % at an equivalence ratio of $\phi = 1.4$ (cf. Fig. 2.6).

Relative differences ϵ_m (Eqs. (2.26) and (2.27)) were evaluated to analyze the deviation in mass fraction Y between the combined and the original $C_{10}H_{22}$ mechanisms. The mass fractions Y of $C_{10}H_{22}$, H_2O, CO_2, and CO were studied in detail. Various calculations showed that neither fuel nor the NO_x mechanism has a significant influence on the absolute values of ϵ_m. The values were generally very small for $\epsilon_{m,\text{abs}}$ and $\epsilon_{m,\text{tot}}$: The profile of the fuel $C_{10}H_{22}$ was modified by less than 0.4 %. The H_2O fraction decreased by around 0.15 %, while the CO_2 profile increased by 0.3 %. The formation of CO was reduced by up to 4 % under lean conditions, but the difference remained negligible for stoichiometric and rich conditions. Furthermore, the mass fractions Y of OH and CH_x and the relevant radical pool for NO_x formation were compared for both the original and combined mechanisms. The relative differences ϵ_m of these NO_x precursor species were consistently below 1 %.

Counterflow diffusion flames performed in a similar manner to laminar premixed flames, employing the mechanisms investigated. There was a comparable agreement between the unmodified/original mechanism and combined $C_{10}H_{22}/NO_x$ chemistry. The maximum relative difference ϵ_m was 0.5 % for the Princeton $C_{10}H_{22}$ kinetics considering temperature, axial velocity, spreading rate, and mass fractions of $C_{10}H_{22}$, O_2, H_2O, CO_2, and CO. The respective value for the Aachen $C_{10}H_{22}$ mechanism was 0.8 %.

In conclusion, the best performance could be obtained with the combination "n-Decane (Princeton) + NO_x (Li)". The results were reliable and convergence was very good. The combination "n-Decane (Princeton) + NO_x (Leeds)" showed a number of problems concerning numerical stability. On the other hand, the combination "n-Decane (Aachen) + NO_x (Li)" had similar problems and slightly inconsistent results in regard to laminar flame speed. The combination "n-Decane (Aachen) + NO_x (Leeds)" exhibited insufficient convergence for CH_4, C_2H_6, and $C_{10}H_{22}$ flames. Here, it is very likely that fuel and NO_x chemistry interfere negatively, producing a stiff system of equations [298].

Validation of NO_x Values Against Experimental Measurements

As illustrated in Figure 2.14, the NO_x formation characteristics of the combination "n-Decane (Princeton) + NO_x (Li)" were finally tested against the experimental measurements of Egolfopoulos [118]. A counterflow configuration was employed with a jet of nitrogen (N_2) counter-flowing against premixed n-decane/air, thus quenching the flame. Lean, stoichiometric, and fuel-rich

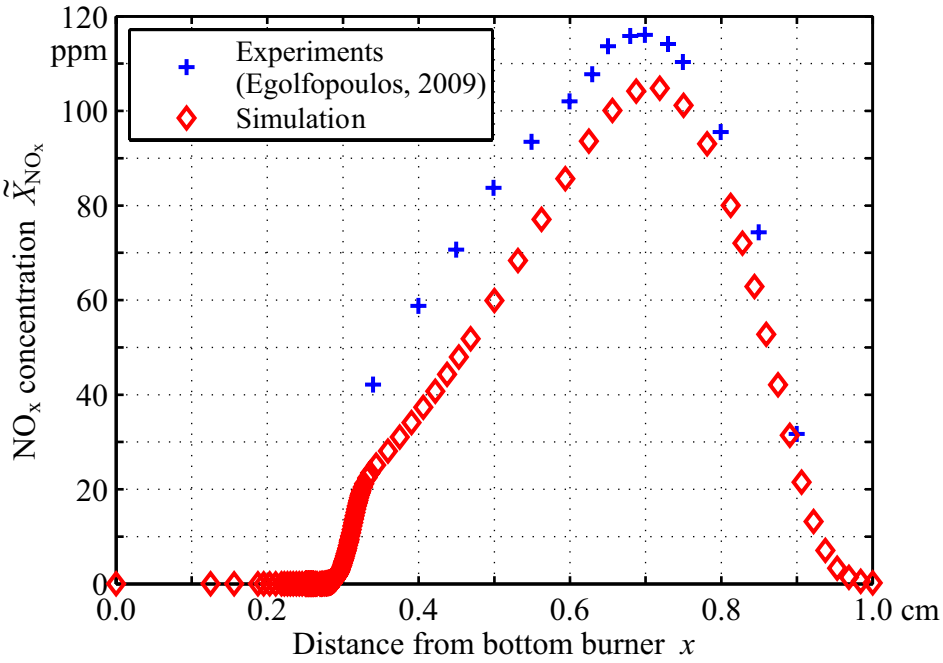

Figure 2.14: Experimental and Numerical Data on Nitrogen Oxide Formation for Counterflow Configuration. The comparison shows data for an equivalence ratio of $\phi = 1.0$. The experimental results are taken from Egolfopoulos [118].

conditions were tested. For an equivalence ratio of $\phi = 1.0$, the absolute values agree very well between experiments and simulations with a deviation below 10 %. The qualitative agreement is excellent with identical slopes on both sides of the NO_x peak value. In the lean regime, the concentrations of NO_x decrease with a decrease of ϕ. Results are consistent for experimental measurements and numerical simulations in a qualitative and quantitative manner. The gradients of the NO_x value (Fig. 2.14) decrease for both rich and lean mixture fractions. The NO_x peak itself is shifted upstream the fuel/air direction for nonstoichiometric conditions [298].

3 Experiments on Droplet Array Combustion

Emissions of nitrogen oxides (NO_x) in sprays are a complex and crucial topic. Current scientific knowledge about NO_x formation in sprays is based on research of droplet combustion, since a droplet can be regarded as the primary element of a spray. Single droplets, droplet arrays, and droplet matrices have therefore been investigated experimentally by various researchers and research groups to acquire a basic understanding of the fundamental processes involved in spray combustion [6, 27, 29, 47, 48, 59, 75–77, 101, 102, 105, 121, 141, 151, 152, 161–164, 170, 192, 202, 203, 207, 212, 221–223, 228, 237, 239, 267–270, 278–280, 282, 283, 292, 307–309, 312, 317–319, 327, 329, 352, 353, 357, 392, 394, 412–415, 425, 431–433, 444, 465, 467, 470]. Law [234] and Kono et al. [216] review state of the art and recent advances in this research field. As far as the present thesis is concerned, Chapters 2.1.3 and 2.2.3 provide the theoretical framework on droplet combustion and NO_x formation, respectively.

This chapter presents the experimental setup for the combustion of an n-decane droplet array under microgravity conditions as utilized within the studies contributing to this thesis. The setup accounts for undisturbed burning characteristics and a representative NO_x formation. Different droplet regimes were investigated in order to enhance the understanding of the physical and chemical processes of combustion, such as vaporization, transport, chemical kinetics, and their interaction. The pre-vaporization rate Ψ of the liquid droplets, mainly realized by the adjustable pre-vaporization time, was the main experiment parameter. The microgravity environment was needed for uniform and idealized experiment conditions during the entire process of droplet vaporization and combustion, particularly the extended pre-vaporization periods (cf. Figs. 1.1 and 1.2). It allowed an experiment conduction without the effect of natural convection, which causes difficulties apart from the complexity inherent to combustion itself.

Scientific experiments were performed in the drop tower of ZARM (Zentrum für angewandte Raumfahrttechnologie und Mikrogravitation) and in the sounding rocket environment of TEXUS (Technologische Experimente unter Schwerelosigkeit). A parabolic flight campaign (PFC) using the engineering module (EM) of the experimental setup was conducted for technical demonstration, testing, and parameter optimization.

3.1 Droplet Combustion Facility

The experiment parameters investigated in particular are: preheating temperature T_Ψ, pre-vaporization time t_Ψ, and dimensionless droplet spacing S/D_0, with S and D_0 being the inter-droplet distance and the initial droplet diameter. The degree of fuel vaporization Ψ and the local equivalence ratio ϕ along the droplet array are a function of these primary experiment parameters.

Figure 3.1 shows a schematic of the approach pursued for droplet pre-vaporization, utilizing a linear array of five droplets as an example. The experimental concept relies on a variable pre-vaporization time matched to the vaporization characteristics of the low-volatile fuel n-decane ($C_{10}H_{22}$). Droplet generation is performed at an ambient temperature of 300 to 315 K in the first instance, whereas pre-vaporization is enforced in the combustion chamber at an elevated temperature level of T_Ψ. As a general reference, T_Ψ is set to 500 K, and thus the majority of the experiments as well as the bulk of the numerical simulations (see Chap. 4) were conducted at this preheating temperature. As soon as the predefined pre-vaporization time t_Ψ is reached during an experiment run, ignition is initiated by an electrically heated ignition wire at one end of the droplet array. After flame spread, droplet burning, and flame extinction, an exhaust gas sample is extracted from the combustion chamber

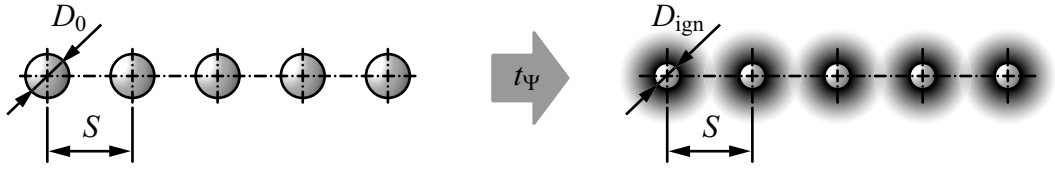

Figure 3.1: Schematic on Pre-Vaporization of a Linear Droplet Array. Left: before pre-vaporization, right: after pre-vaporization [294].

and stored for subsequent gas analysis. All combustion runs are conducted under isobaric conditions at an ambient pressure of 1 bar [208, 293, 294, 296].

An overview of the combustion facility is given by Figure 3.2, exhibiting the experiment platforms of the “Droplet Array Combustion Unit” (DCU), as they

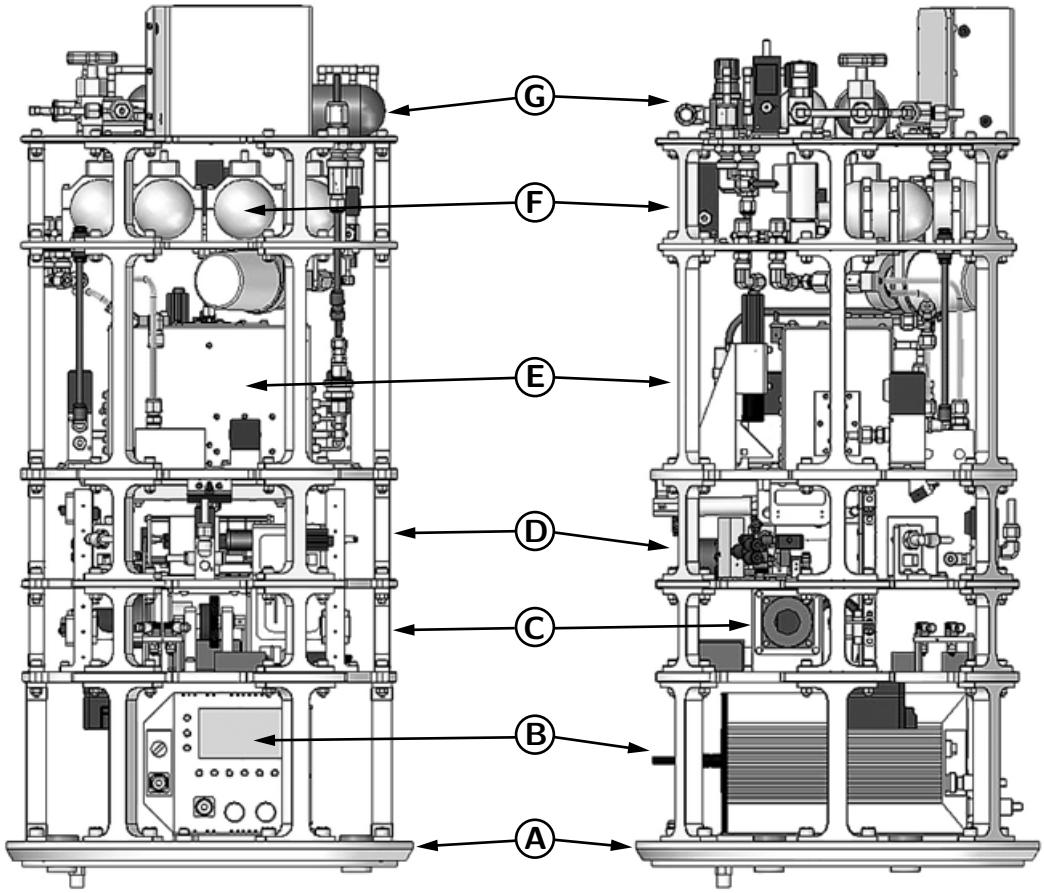

Figure 3.2: Droplet Array Combustion Unit (DCU). The DCU represents the hardware core section of the experiment [196, 208, 296].

A Experiment deck (common baseplate of JCM and DCU)

B High-speed video camera system (recorder)

C Droplet lifting system (motor and gears)

D Droplet array generation system

E Combustion chamber and observation system

F Exhaust gas sampling system (sample cylinders)

G Air supply and exhaust system (air tank)

are arranged bottom-up [195–197]. Within the framework of a cooperation, the Japan Aerospace Exploration Agency (JAXA) had the main responsibility in developing and integrating the "Japanese Combustion Module" (JCM), with the DCU being the experiment core section. The remaining devices of the JCM, including mechanical interfaces, electronic components, and outer structure are not shown here for the sake of clarity. Height and weight of the JCM are 1290 mm and 103 kg, respectively. The DCU itself is built of six platforms (Fig. 3.2, **B** - **G**), supported by six props each, with a total height of 813 mm and a platforms diameter of 372 mm (see also Tab. C.1). A vacuum dome covers the DCU in order to keep it pressurized. Electronic control devices and batteries are mounted outside of this pressurized dome, below the experiment deck. The modular design of the DCU facilitates adjustment and modification work, as is necessary, for instance, with the droplet generation setup and the exhaust gas sampling system (EGS). The DCU consists of droplet array generation and lifting devices, combustion chamber, air supply and exhaust system, observation system, exhaust gas sampling system, and main structure [208, 296]. Figure 3.3 gives a close-up view of the droplet array lifting devices that are installed on the second and third platform of the DCU and are used to move a newly generated droplet array into the combustion chamber (cf. Fig. 3.2, **C** and **D**).

The outlined combustion facility was used for cooperative experiments by the "Droplets Combustion Dynamics Research Working Group" of JAXA and the research team on "Combustion Properties of Partially Premixed Spray Systems", which was financially supported by the European Space Agency (ESA). The collaborative study addressed the effects of partial pre-vaporization of fuel droplets on subsequent flame propagation and exhaust gas formation, being the research foci of the two respective partners. Thereupon, the scientific experiment was entitled "PHOENIX" (Investigation of Partial Pre-Vaporization Effects in High Temperature on Evolution of Droplet Array Combustion and Nitrogen Oxides Formation). Its scientific requirements were formulated by the two research groups, within which the European part was executed by the author of this thesis. Since the concept of the combustion facility is based on a Japanese apparatus for drop shaft experiments, the setup needed to be retrofit for exhaust gas sampling and customized to its operation during sounding rocket flight on the TEXUS system [208, 293, 294, 296].

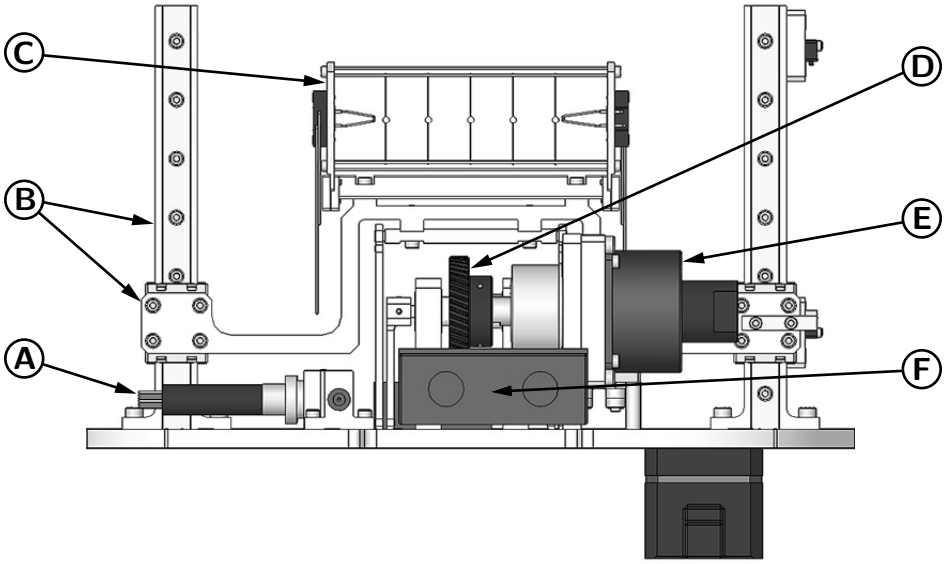

Figure 3.3: Droplet Array Lifting Devices. The droplet array holder is shown in its lower position, as used during droplet generation with the combustion chamber closed [196]. **A**: fuel-dosing pump with servo motor SM3, **B**: linear bearing with guidance carriage, **C**: droplet array holder, **D**: gears, **E**: stepper motor SM2 for lifting, **F**: fuel storage case.

3.1.1 Droplet Array Generation Device

In the 1980's, Haggard Jr. and Kropp developed a distinct droplet generation concept that was extensively used in drop tower and space flight experiments throughout the following years [12, 76, 77, 79, 101, 161–163, 312, 394]. Its design allows the generation of free droplets by two opposing fuel supply tubes. These are slowly separated from one another, while forming a droplet of desired diameter. The droplet is deployed via a final, rapid retraction. Even though the droplet has a spherical shape and no negative effects on droplet vaporization/burning have to be expected due to the absence of a droplet suspender, this approach has some shortcomings: The probability of generating a stationary droplet is low, and the droplet may not maintain its initial position for the full burning period. As a result, the droplet could drift out of the field of view of the observation system or even touch the combustion chamber walls. Furthermore, it is impossible to generate a well-defined droplet array, as for instance depicted by Figure 3.1 [234, 282, 393]. Avedisian et al. [29] used a piezoelectric droplet generator propelling a continuous stream of droplets on a parabolic trajectory. When the last droplet emerging from the

generator reaches the apex of its upward trajectory, a state of single droplet levitation can be achieved by releasing the whole experimental setup into free fall. Subsequently, Jackson and Avedisian [192] and Avedisian and Callahan [28] employed the same piezoelectric droplet generator in combination with single as well as crossed pairs of silicon carbide (SiC) fibers. As a droplet hits the single fiber or the fiber intersection, it sticks to it. The droplet diameter of interest is built up by impingement and coalescence of successive droplets. Nevertheless, a technical limit is also reached for this latter droplet generation technique, when investigating droplet arrays. Compact droplet generators operating at a high success rate and with excellent reproducibility characteristics become indispensable in this case. The most common technique, after all, is droplet generation on a single quartz fiber by fuel supply through a hypodermic needle. It allows a defined droplet positioning in space. Still, the fiber can affect droplet vaporization and combustion in a negative way, as it is typically only one order of magnitude smaller than the droplet diameter itself. Additionally, the droplet shape is spheroidal, which is a result of droplet elongation in the direction of the suspending fiber axis [129, 222, 278–280, 282, 317, 376, 429, 431–433].

Here, a new droplet array is generated by the droplet array generation device for every combustion run (Fig. 3.4). For this purpose, the droplet array generation device needs to interoperate with the droplet array holder. The utilized technique attempts to overcome as many disadvantages of the pervi-

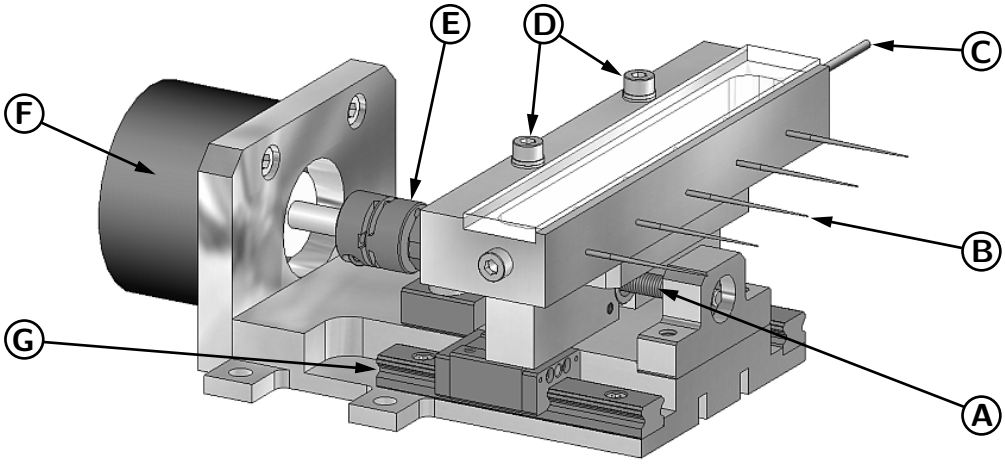

Figure 3.4: Droplet Array Generation Device. **A**: ball screw, **B**: fine glass tube, **C**: fuel supply, **D**: fixation of fuel supply block, **E**: shaft coupling, **F**: stepper motor SM1, **G**: linear bearing [196, 208].

ously mentioned techniques as possible. Figure 3.5 illustrates the procedure: Fuel is dripped through fine glass tubes in order to accumulate as full-size droplets at the intersections of crossed SiC fibers. The droplet diameter is controlled by the amount of fuel supplied. After verification of a successful droplet array generation, the droplet array holder is lifted up into the combustion chamber (see Fig. 3.3). Mikami et al. [282] extensively report on this droplet generation technique, also evaluating other existing techniques. The present technique stands out due to its high reliability and reproducibility characteristics. It is applicable to difficult experiment conditions, as for instance droplet pre-vaporization experiments with highly volatile fuels. The characteristics of the utilized technique may be summarized as follows [282]:

- High droplet sphericity with minimal deformation in fiber contact areas
- Wide range of droplet diameters achievable
- High success rate of droplet deployment on suspension fibers
- No droplet vibrations due to the droplet generation process
- No droplet drift during ignition and burning (self-stabilizing suspension)
- Rapid droplet generation process
- Capability of simultaneous multi-droplet generation for droplet arrays
- Compact droplet generation device

Due to the interaction of the droplet array generation device and the droplet array holder, it is essential to verify the alignment of the glass tubes with their corresponding suspension fibers (cf. Fig. 3.5). Preliminary tests under normal gravity as well as microgravity conditions helped with this verification. Furthermore, experience taught that a slight offset of the glass tube orifices from the fiber intersections in the vertical and in the forward direction is favorable for reliable droplet generation under both gravity conditions. A positive offset within the range of 1 to 2 mm is the optimum for these two directions, as it is pictured in Figure 3.5. However, direct contact has to be secured in the lateral direction in order to anchor the droplets successfully. In very rare cases, a glass tube hits a SiC fiber without slipping off this unstable position, while

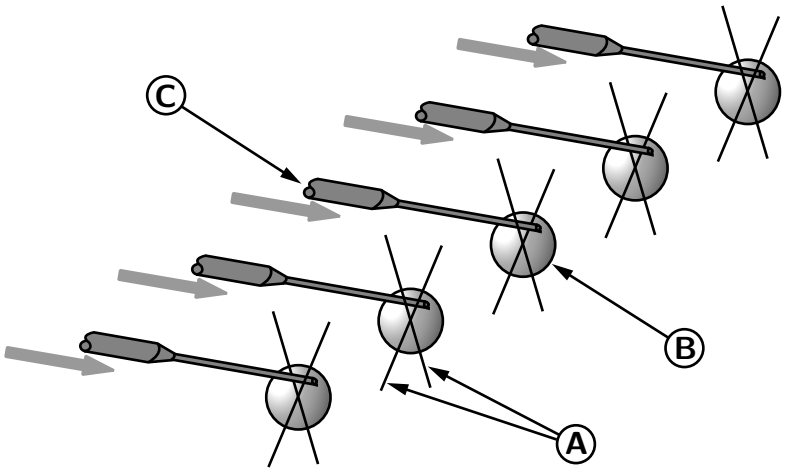

Figure 3.5: Schematic of Droplet Generation Process. All droplets of the array are simultaneously generated [282]. **A**: crossed pair of SiC fibers, **B**: tethered fuel droplet, **C**: fuel supply through fine glass tube.

the fuel supply block moves forward. The fine glass tube will then bend elastically due to the forward movement (Fig. 3.4, **B** - **D**). However, either unit being damaged by the droplet generation process is improbable.

The fuel supply block consists of the main cuboid of aluminum with fixture bores for the glass tubes and the glass tubes themselves. Additional drill holes assure the internal fuel distribution within the block. Two threads, one on each side of the block, are used to seal these fuel supply channels after manufacturing and to bleed trapped air. In order to ensure an assembly process without any damage to the fine glass tubes as well as a smooth operation without blocking single glass tubes, the aluminum block had to be cleaned from chips and manufacturing residues in an ultrasonic cleaner. By anodizing the aluminum block and the other metallic parts within the field of view of the droplet generation process, reflections obscuring the observation of this process could be minimized. The high precision manufacturing process of the fine glass tubes is outlined in Chapter C.2.

Generally, the single-part fabrication of fuel supply block and droplet array holder implies high precision and a considerable degree of hands-on experience for the manual labor steps. After completion of all single component manufacturing steps, a fuel supply block is finalized by inserting the fine glass tubes into their support and applying glue to the fitting locations. Before curing, a correct alignment of the glass tube orifices needs to be secured. Setups

for 5, 9, 13, and 17 droplets were manufactured and used in the experiments. The deviation of the orifice area within the glass tube sets composed was below $\pm 5\,\mu m^2$. For the TEXUS-46 sounding rocket campaign, this resulted in a maximum error of the generated droplet diameter D_0 from its nominal value $D_{0,nom} = 1.5\,mm$ of less than 5 %. The diameter reproducibility within the experiment campaign was high, with a deviation below 1 %.

3.1.2 Droplet Suspension Technique

In order to generate a droplet array, the droplet array generation device interoperates with the droplet array holder (Fig. 3.6). The latter features the droplet suspension technique, as reported in Avedisian and Callahan [28] and Mikami et al. [282, 283]. Silicon carbide (SiC) fibers are aligned as X-shaped fiber pairs, corresponding to the fine glass tubes of the droplet array generation device (cf. Fig. 3.5). A single suspension fiber has a diameter of 14 µm (manufacturer: Nippon Carbon; type: Hi-Nicalon). It has a low oxygen content, is heat resistant up to 1700 °C in an inert gas atmosphere, and is primarily designed for application in the hot parts of gas turbines. The SiC fiber setup imposes smaller disturbing effects on shape and heat transfer of a tethered droplet than the most commonly used quartz fibers of 100 to 150 µm diame-

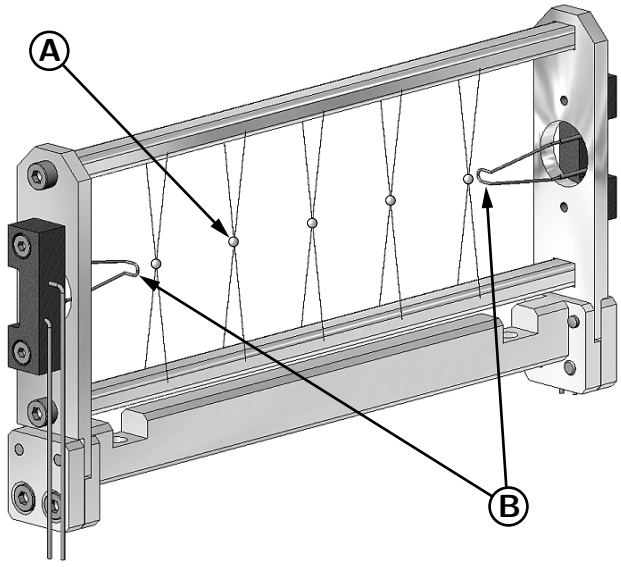

Figure 3.6: Droplet Array Holder. The assembly is shown for a setup of five droplets, as used on the TEXUS-46 campaign [196, 208]. **A**: tethered fuel droplet, **B**: ignition wire.

ter [129, 222, 280, 317, 376, 429]. These effects become increasingly important at a late stage of droplet burning, when the droplet diameter approaches the diameter of the quartz fiber. A broad discussion on the general use of suspension fibers can be found in the work of Mikami et al. [282], Shih and Megaridis [395], and Farouk and Dryer [130]. These studies include a comparison of the relevant geometric and thermal properties as well as an evaluation of the particular vaporization and burning rates, the flame stand-off ratio, and the effect of thermal radiation. According to the experimental work of Avedisian and Callahan [28], the evolution of the droplet diameter during droplet burning shows an excellent conformity for free and fiber supported droplets. Farouk and Dryer [130], on the other hand, predict a significant influence of the suspension fiber based on their numerical simulations, using a transient one-dimensional, spherically symmetric droplet combustion model that implicitly accounts for the effects of a supporting fiber. The main argument in favor of using a droplet suspension technique at all within the present experimental setup is the realization of a well-defined linear droplet array. Multiple droplets can be generated simultaneously, and droplet drift during the burning period can be avoided, including the most critical ignition phase. The X-shaped fiber pairs stabilize the droplets. Droplets up to 1.5 mm can be tethered this way under normal gravity conditions, while much larger droplets are realizable in microgravity. Furthermore, the retraction of the fine glass tubes from the fiber intersections, after completion of the fueling process, generally has no negative effect on the droplet suspension.

Recalling the scientific requirements for the present experiment, the droplet array holder has to fulfill the following technical specification:

- Equal horizontal distances between the different fiber pairs
- Equal vertical level of all fiber intersections
- Droplet stabilization at fiber intersections, especially during the critical acceleration phase of the droplet array lifting devices
- Support of the droplet ignition system

The droplet array holder is a stainless steel frame made of four parts that are bolted together. It is highly important to have accurately manufactured single

parts to guarantee that the fiber intersections are located at their exact positions. In each case, two SiC fibers are stretched across the two horizontal beams and glued onto them in a crossing pattern normal to the direction of flame spread and at an angle of about 17° (see Fig. 3.6). An initial load must be similarly applied to all fibers during this process until curing is complete. In previous work, four instead of two beams were used for this setup, allowing a wider opening angle of the fiber pairs, and thus an even better balanced restoring moment [206, 207, 282, 283]. However, the current design was restricted by the combustion chamber design (Chap. 3.1.3) and the investigation of high pre-vaporization rates Ψ, and thus kept as slim as possible. Table 3.1 lists the key data of the utilized droplet array holders. The inter-droplet distance S is chosen as a multiple of 1.5 mm, which was the nominal droplet diameter $D_{0,\mathrm{nom}}$ of the TEXUS-46 sounding rocket campaign (Fig. 3.1).

Table 3.1: Geometric Data of Investigated Droplet Arrays.

Number of droplets N	Inter-droplet distance S in mm	Total length of droplet array L in mm
5	18.0	72
9	9.0	72
13	6.0	72
17	4.5	72

Apart from the SiC fibers, a hot-wire igniter made of iron-chrome alloy is integrated on either side of the droplet array holder (Fig. 3.6). However, only one igniter is nominally used for initiating combustion on the closest droplet. The second igniter is for redundancy purposes as well as for varying degrees of droplet vaporization.

3.1.3 Combustion Chamber

After the generation of a droplet array at room temperature, it is inserted into the preheated combustion chamber by lifting the droplet array holder (Fig. 3.3). Figure 3.7 provides two views of the thermally insulated combustion chamber. The transparent view shows the vertical middle along the axis

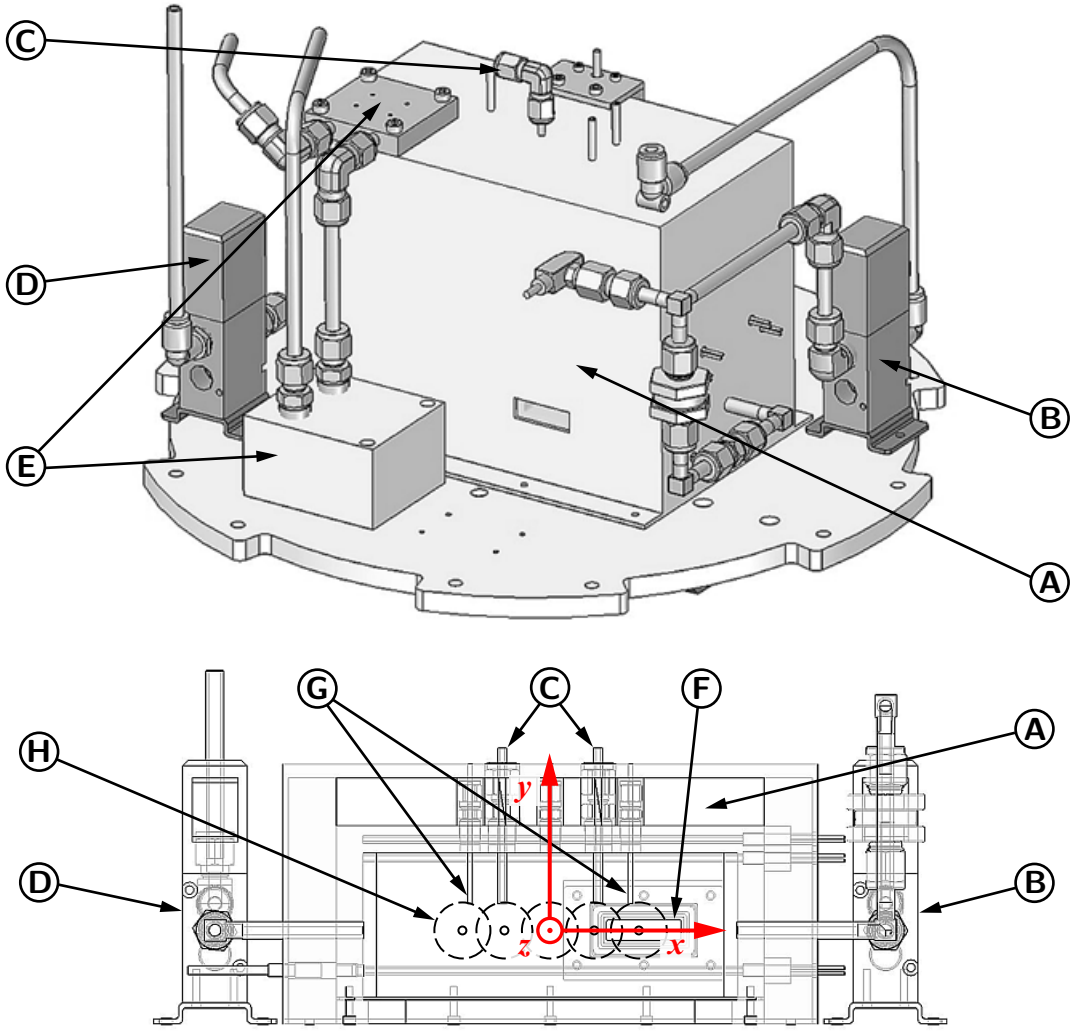

Figure 3.7: Isometric and Transparent View of the Combustion Chamber. **A**: thermally insulated combustion chamber, **B**: solenoid valve connecting vent line to outer vacuum, **C**: connection of sample probes with sample cylinders, **D**: solenoid valve for air supply, **E**: cooling units, **F**: window for backlit images, **G**: thermocouple setup, **H**: anticipated region of vaporizing droplet array [196, 197, 208, 293, 294, 296].

of the droplet array with $z = 0\,\text{mm}$. The combustion chamber serves as an experimental environment for droplet vaporization and combustion, allowing the formation of a gaseous vapor layer around the fuel droplets by exposing them to a "high temperature" situation. However, the preheating temperature is kept below the auto-ignition point of the fuel for all combustion runs. It is set to $T_\Psi = 500\,\text{K}$ (= 226.85 °C) by default. Ignition needs to be initiated by either one of the two hot-wire igniters (see Chap. 3.1.2).

The combustion chamber is installed on the fourth platform of the DCU (Fig. 3.2, **E**) and has inner dimensions of (140×50×54) mm^3 (W×D×H). Its temperature is precisely controlled by a K-type thermocouple that is attached to the inner combustion chamber wall and by heating cartridges that are integrated into the combustion chamber housing. Two further thermocouples (S-type) measure the gas temperature inside the combustion chamber. Apart from these thermal aspects, the combustion chamber also houses four symmetrically aligned sample probes for exhaust gas sampling [208, 293, 294, 296].

The combustion chamber is designed in line with the following operational specification:

- Facilitate fast heat-up periods starting from an ambient temperature level (within 45 to 60 min)
- Maintain preheating temperature at set-point of e.g. 500±1 K
- Exchange air/exhaust from inside the combustion chamber within 15 s
- Restore set-point temperature within 40 s after an air exchange
- Facilitate execution of nominal experiment sequence including the insertion of the droplet array holder and the exhaust gas collection through the exhaust gas sampling system (see also Chap. 3.2.6)
- Operate combustion chamber shutter (open/close position) in accordance with the experiment sequence
- Minimize heat loss of combustion chamber induced by the insertion of the cold droplet array holder (steel frame)

In particular the shutter design (Fig. 3.8) must not counteract the thermal insulation and airtightness of the combustion chamber. The latter requirement is essential for the flushing sequence at the end of a combustion run, which is subdivided into a complete evacuation and a succeeding refilling with fresh air. A leak at the shutter sealing might cause a major interference with the global pressure regulation of the DCU.

By lifting the droplet array into the combustion chamber, a little air gap of 1 mm on average remains between the combustion chamber opening (Fig. 3.8, **D**) and the steel frame of the droplet array holder inserted. This gap must

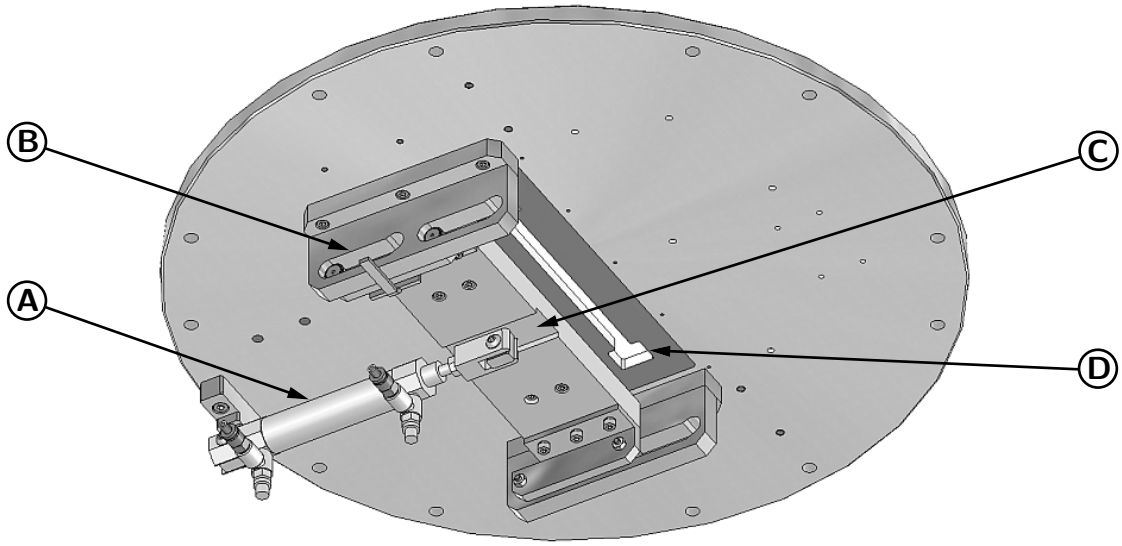

Figure 3.8: Combustion Chamber Shutter. **A**: pneumatic cylinder, **B**: shutter rail, **C**: shutter, **D**: combustion chamber opening [196, 197, 293, 294, 296].

stay open for two reasons: First, the experiment is conducted under isobaric conditions, and a gap sealing would result in an unwanted pressure increase due to combustion. Second, a gap sealing is impractical from the technical point of view due to an unavoidable impact of the deployment mechanism on the combustion chamber baseplate in such a case [293].

However, due to the expansion of the air/exhaust mixture inside the combustion chamber during the combustion process, on the one hand, and the gas extraction during the exhaust gas sampling process, on the other hand, gas will pass in and out of the combustion chamber. To get a deeper insight into this discharge process, the entrainment of "fresh" ambient air into the central combustion zone, and the mixing of burned and unburned gases inside the combustion chamber, a numerical study was conducted using computational fluid dynamics (CFD). Its findings are summarized in Chapter 3.3.

3.1.4 Exhaust Gas Sampling System

Tiné [440] gives an extensive overview of ideal and practical gas sampling, discusses relevant design aspects, and describes analysis methods. He points out the importance of the reliability of sample composition since sampling procedures can include errors. The work of Halstead et al. [165, 166] constitutes

a conclusive study on the chemical transformations of nitrogen oxides when sampling combustion products, comparing stainless steel and silica tubing as probe material. Samuelsen and Harman III [371] review sampling environments and the occurring transformations of NO_x within probes and sample lines while sampling combustion products. The authors distinguish between homogeneous and heterogeneous transformation reactions and examine a temperature range of 25 to 400 °C. Stainless steel tubing is found to promote chemical transformation when sampling fuel-rich combustion products [122, 371]. Furthermore, stainless steel is observed to promote the reduction of NO_2 to NO in temperature ranges in which silica tubing is passive to chemical transformation, in the absence as well as in the presence of CO and/or H_2. Apart from the problems associated with the catalytic reduction of NO_x in metallic probes, Allen [15] reports on the NO to NO_2 conversion as well as possible reformation reactions of NO in non-metallic probes. Aerodynamic quenching, enforced by a sonic flow orifice causing rapid adiabatic expansion and cooling, and wall quenching during the sampling process are considered to be of major importance for the destruction of radicals and free atoms in the probe. The research report of Fitz and Welch [136] summarizes a series of tests to quantify error sources in NO_x measurement methods. Its focus is set on biases resulting from sampling materials, temperature effects, moisture removal systems, NO_2 converter strategies, and the presence of ammonia in sample streams. Fitz and Welch [136] evaluated three different types of sample lines: teflon PFA, stainless steel (316 L, respectively 1.4435), and 316 L Silcosteel®. Three different temperatures (25, 107, and 175 °C) were applied to the sample lines for evaluation. The authors demonstrated accurate NO_x measurements for all sample conditioning systems and all sample lines for NO_x sample concentrations at or above 2 ppm. For concentrations below 2 ppm, there were considerable differences with the vast majority of the NO_x losses occurring in the sample conditioning system [136]. Nitric oxide (NO) and nitrogen dioxide (NO_2) are especially susceptible to chemical transformation. Three general types of chemical transformation of these nitrogen oxides prevail in probes and sample lines [136, 217, 266, 371]:

- Oxidation of NO to NO_2, with total NO_x conserved
- Reduction of NO_2 to NO, with total NO_x conserved
- Overall reduction of NO_x to N_2, with total NO_x not conserved

The different causes of NO_x transformation are often hard to distinguish from one another. As a minimum requirement, the quality of scientific results is not compromised as long as the total oxides of nitrogen are conserved. However, the assessment of the exact NO_2/NO_x ratio is often essential, too. For instance, local concentrations of NO and NO_2 are required to assess the chemical mechanisms responsible for the formation of NO_x [56, 183, 371, 374]. Summing up the findings on sampling materials against the background of NO_x analysis, the widely observed catalytic activity of sampling components made of stainless steel (probes, sample lines, valves, or sample cylinders) is due to the presence of catalytic agents in this alloy. Chromium, nickel, and copper, for instance, are well-known to be active catalysts, and it can be concluded that untreated stainless steel is not an adequate material for gas sampling equipment [122, 136, 145, 179, 247, 371, 387].

Considering the present experimental setup, an intrusive concept is the only feasible solution to quantify the combustion products. Sample probes are installed in the combustion chamber to extract the exhaust for its subsequent analysis (see Fig. 3.7, **C**). Thus, gas sampling is the first crucial event after the combustion process, and the hardware involved accounts for the reception of a sample at the analytical instrumentation that is chemically identical to the composition existing at the point of extraction. Potential sampling artifacts were minimized by a careful selection of materials for the entire sampling equipment [293, 371].

The primary problem, which had to be solved using this concept, is to obtain a representative gas sample from every single combustion run. Based on this general goal, and on the constraints of the sounding rocket and drop tower environment, the specification of the exhaust gas sampling (EGS) system can be outlined as follows [15, 293, 294, 386]:

- High level of automation – by control routines
- Compact design – for weight and space reasons
- Shock resistance – for launch and touch-down/deceleration
- Simple operability – for a short evacuation time of the sample cylinders
- Small dead volume – by using small cross sections

- High surface quality – by applying surface coating
- High temperature resistance – by using special sealing
- High vacuum level and low leakage rate

As illustrated in Figure 3.2, the EGS system is installed on the fifth experiment platform, in close proximity to the combustion chamber. It is shown in greater detail in Figure 3.9. The installation directly above the combustion chamber is chosen to keep the dead volume of the piping low, which results in low contamination of the samples and an optimized performance of the EGS system. The design meets the strict relation of $V_{\text{piping}}/V_{\text{sample}} \leq 1\,\%$, and the piping itself has a surface to volume ratio of 1.85 with an inner diameter of $D_i = 2.16\,\text{mm}$. Since four combustion runs were scheduled on the TEXUS-46 sounding rocket campaign, the layout is based on four sample cylinders. Each of them has a volume of 200 ml, which is optimized towards the minimum volume required for gas analysis. All metal surfaces of the EGS system being directly exposed to the combustion products are coated with amorphous silicon[1] to prevent negative surface effects on the gas composition and a distorting gas adsorption.

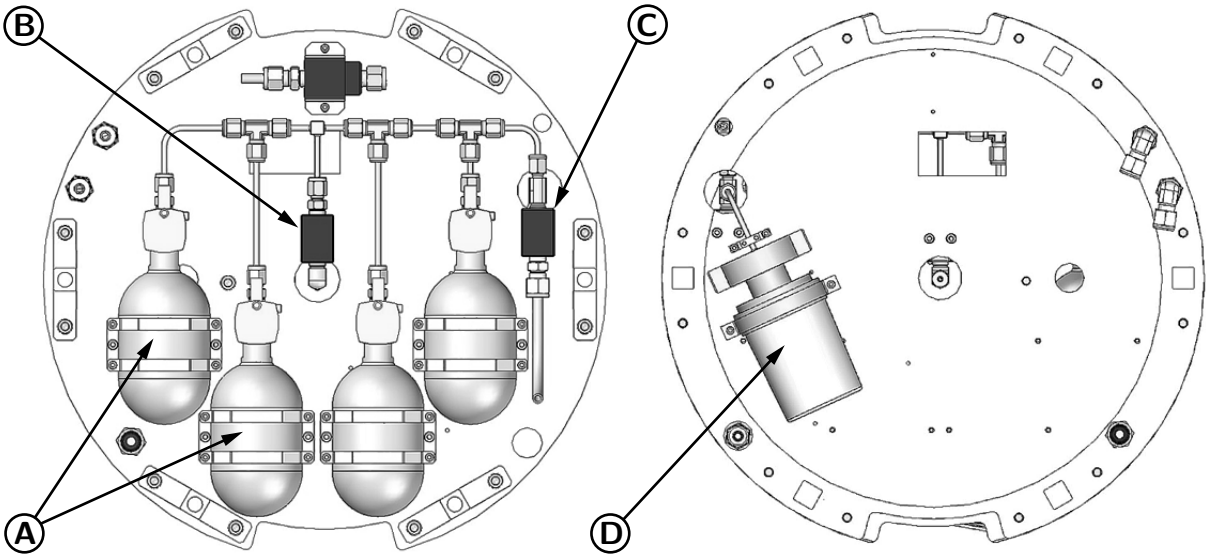

Figure 3.9: Exhaust Gas Sampling Platform. Left: top view, right: bottom view [196, 197, 293, 294, 296]. **A**: sample cylinders, **B**: solenoid vacuum valve for connection to combustion chamber, **C**: solenoid vacuum valve for connection to evacuation line, **D**: vacuum gauge.

[1] Sulfinert® coating was used instead of the Silcosteel® coating mentioned above. Both are very similar from the chemical point of view but have different product names.

Chapter C.2 also provides results on the application of the coating by opposing coated to untreated sample cylinders. This surface treatment particularly increases the resistance to corrosion, reduces interactions between the steel surface and active compounds, and inhibits coking. Furthermore, extensive tests confirmed faster pump-down times due to a significantly reduced outgassing and an improved moisture uptake (wet-up) and release (dry-down) by at least one order of magnitude. The coating is applied on the surface to a depth of 0.1 µm, and thus incorporated into the lattice of the host substrate by forming a flexible, non-adsorptive layer. That depth does not interfere with the mechanical performance of the coated components; still, it imparts rainbow colors on the treated surfaces [294, 296, 351, 406].

Regarding the sounding rocket campaign, access for the evacuation of the gas sample cylinders by a turbomolecular pump was realized through a late access port in the TEXUS module. In order to fulfill the scientific requirements, a minimum leakage rate of $<1\times10^{-5}$ mbar l s^{-1} with a remaining vacuum level $<1\times10^{-1}$ mbar inside of each sample cylinder was specified for the moment of the exhaust gas sampling. The achievable vacuum level before the rocket launch (at −90 min) was 2×10^{-5} to 3×10^{-5} mbar with an associated leakage rate of $<2\times10^{-6}$ mbar l s^{-1}. Thus, all requirements on the EGS system could be met [296]. The gas analysis hardware itself is ground-based and consists of a FT-IR (Fourier Transform Infrared) spectrometer as well as a NO/NO_x chemiluminescence analyzer (see also Chap. 3.2.4).

3.1.5 Experiment Integration into Microgravity Facilities

Table 3.2 lists the three setups as they were utilized under microgravity conditions. During the JAXA PFC (parabolic flight campaign), hardware testing and the validation of the experiment operation were the main tasks. Apart from that, four representative gas samples were collected. During the TEXNOX drop tower campaign, operational experience was gained on the operator side, operational parameters were fine-tuned for optimized control routines, and a significant number of combustion experiments were conducted to generate scientific reference data. During the TEXUS-46 sounding rocket campaign, three selected combustion runs were finally performed with the PHOENIX experiment at high microgravity quality and with high degrees of droplet pre-vaporization.

Table 3.2: Integration of DCU into Different Microgravity Facilities.

Experiment name	Utilized module	Integration into microgravity facility	Campaign date	Number of experiments
JAXA PFC	EM	Common rack with DGSE	05./06.10.2007	20
TEXNOX	EM	Drop capsule stringer structure	08.07.-01.08.2008	30
PHOENIX	FM	TEXUS structure	22.11.2009	3

The DCU was manufactured as both engineering module (EM) and flight module (FM). In either case, it is mounted on the experiment deck (cf. Figs. 3.2, **A** and 3.10, **A**), which in turn is fastened to the outer structure

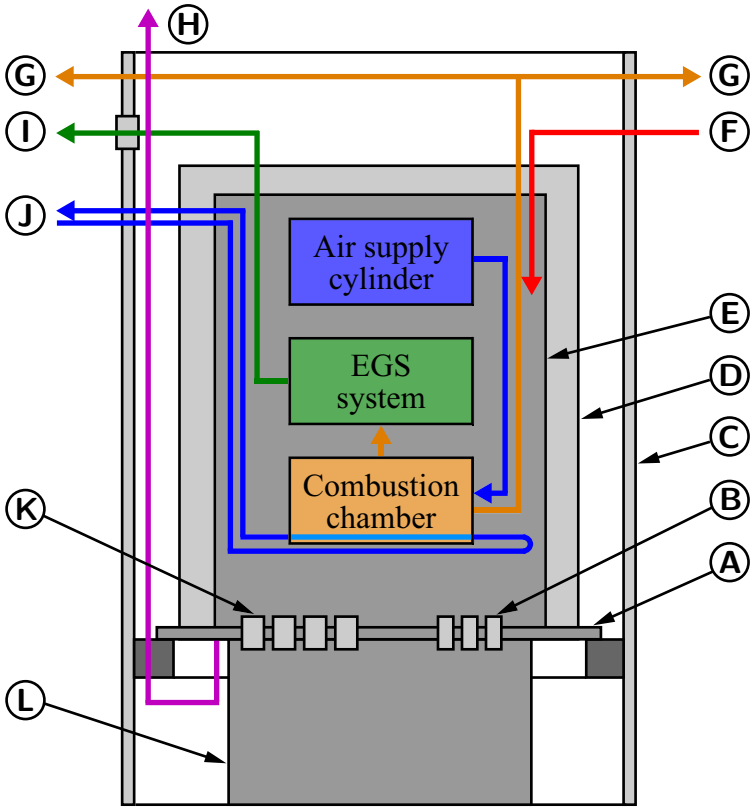

Figure 3.10: Schematic Overview of JCM Interfaces. The JCM/DCU is shown, as it is installed for the TEXUS-46 sounding rocket campaign [196]. **A**: experiment deck, **B**: electrical connectors (BNC), **C**: outer structure, **D**: vacuum dome, **E**: DCU, **F**: pressurized air supply, **G**: symmetrical ventline for combustion chamber, **H**: image data for downlink, **I**: late access port for EGS evacuation, **J**: water cooling system, **K**: electrical connectors (Amphenol®), **L**: service system.

(Fig. 3.10, **C**). Since the DCU including the combustion chamber is an open structure, an enveloping vacuum protection is naturally needed to keep the module pressurized. While the aircraft cabin and drop capsule performed this task automatically on parabolic flight and in the drop tower, respectively, an additional vacuum dome (Fig. 3.10, **D**) was required during all stages of the sounding rocket flight. The electrical interface is realized by three BNC and four Amphenol® connectors (Fig. 3.10, **B** and **K**). The water cooling system (Fig. 3.10, **J**) is used to keep the temperature inside the vacuum protection at an acceptable level. The external system is capable of removing a thermal output of 1 kW, and the cooling water can be controlled in the range of 10 to 30 °C. It is mainly employed for heat removal during extended phases of combustion chamber preheating.

Before, during, and after the integration of the experiment, a large number of tests were conducted in order to verify the operability of the equipment in general and under microgravity conditions in particular:

- Mechanical and electrical interface verification
- Functional tests of all subsystems and full functional tests including combustion sequence and exhaust gas sampling
- Temperature tests and monitoring during all experiment stages
- Leak test of vacuum dome, air supply system, and exhaust gas sampling system, including vacuum level and leakage rate
- Data recording and data transmission including telecommand
- Interference and electromagnetic compatibility
- Spin, acceleration, and vibration simulation on shaker
- Flight sequence testing and training
- Official acceptance tests through EADS Astrium
- Quality assurance arrangements
- Safety evaluation of equipment under all relevant aspects, including sharp edges, discharge of material, high pressure blowout, and fire hazard

Figure 3.11 illustrates as an example the experiment integration into the drop capsule stringer structure of TEXNOX. The DCU itself is enclosed in the upper half of the setup. Auxiliary and supporting systems of the DCU and drop tower are mainly arranged below the experiment deck. Hidden is the turbomolec-

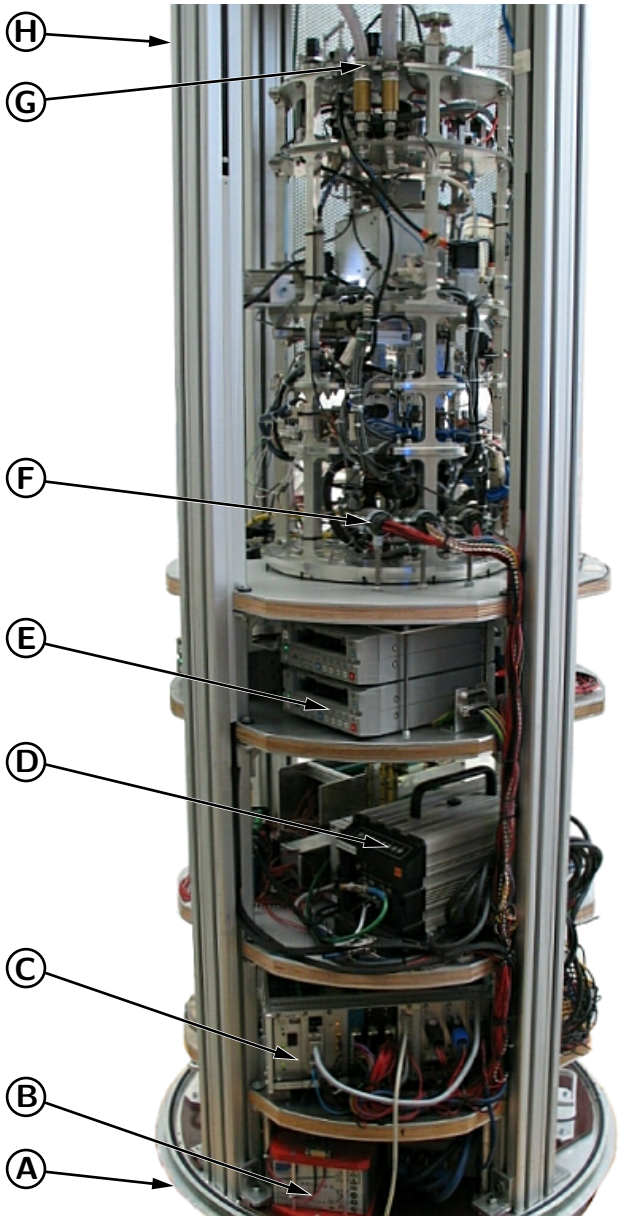

Figure 3.11: Drop Capsule Stringer Structure with Integrated DCU. During the final experiment preparation, the outer drop capsule structure is lowered over the stringer structure and sealing is established. **A**: drop capsule bottom plate, **B**: internal power supply, **C**: control module, **D**: high-speed video camera recorder, **E**: DV recorders for CCD cameras, **F**: electrical interface with DCU (Amphenol®), **G**: interface for water cooling system, **H**: drop capsule stringer structure.

ular pump that was used for evacuation of the exhaust gas sample cylinder during the final preparatory steps. Also, the whole drop tower being under evacuation could be employed as a backing pump here.

3.2 Measurement Techniques and Data Acquisition

The experimental measurements conducted within the study at hand can be subdivided into direct, in-situ measurements and subsequent measurements. However, regardless whether parabolic flight, drop tower, or sounding rocket campaign, almost all physical parameters were recorded in-situ. Only the quantification of the exhaust gas concentrations of interest needed to be split into two steps: exhaust gas sampling and exhaust gas analysis.

3.2.1 Influence of Microgravity Environment

Since the effects of gravitational forces hamper most of the combustion related processes, a vast number of fundamental studies have been conducted under microgravity conditions since the early work of Kumagai et al. [219, 222]. Particularly, laboratory scale experiments are compromised by buoyant motion due to experimental setups of reduced size and the lack of turbulence in comparison with full-scale industrial applications. Furthermore, good temporal and spatial resolution are needed for the very specific investigations.

As pointed out in Chapter 1.4, combustion naturally involves the production of high-temperature gases and a decrease of density. Under “normal” gravity, those local areas of low density trigger buoyant motion, and thus complicate the execution and interpretation of experiments. However, under microgravity conditions, interfering effects due to buoyancy are canceled out. Consequently, the microgravity environment can contribute to a better understanding of combustion phenomena, including the interaction of fluid dynamics, scalar transport, thermodynamics, and chemical kinetics. From the technical point of view, it is possible to control low-speed flows, purely diffusive transport regimes, and large droplet diameters. For instance, the fuel used in the study at hand ($C_{10}H_{22}$) has a vapor density of $3.564\,\mathrm{kg\,m^{-3}}$

at 500 K, which is approximately 5 times higher than the respective density of air [311]. Under normal gravity, the hot combustion products would rise and the vaporized fuel would settle down, resulting in rapid flame extinction. Hence, microgravity is of particular benefit in studies on vaporization, ignition, combustion, and extinction of flames around droplets. Settling effects of the droplet and buoyancy-induced flows around it are eliminated, leading to a one-dimensional, spherically symmetric geometry [128, 153, 209, 235, 356].

The basic droplet combustion model, as discussed, for instance, in Law [233] and Law and Faeth [235], was introduced with Figure 1.2. Evaporation of the liquid fuel occurs on the droplet surface, accompanied by diffusive transport of the gaseous fuel in the outward direction. The oxidizer, on the other hand, diffuses in the inward direction. Both reactants meet and are consumed in a thin, shell-like flame region. Assuming spherical symmetry, quasi-steadiness, and flame-sheet combustion, the classical D^2 law is derived (cf. Chap. 2.1.3). A large number of attempts have been made under normal gravity and microgravity to verify the respective linear decrease of the droplet diameter squared. Experiments under normal gravity already confirmed this trend very well with deviations from linearity being due to second-order effects [48, 141, 142, 151, 152, 155, 164, 202, 221, 228, 239, 308, 352, 372, 412, 462]. However, microgravity conditions alone provide for the quantification of the flame size behavior as a result of the above mentioned dependencies, including absence of buoyant flow, absence of flame shape elongation, and the transient character of the whole process [233, 235, 244].

Idealized droplet vaporization and burning is dominated by Stefan flow, which is a diffusion-controlled process [19, 443]. Since the density-weighted mass diffusivities are pressure insensitive, experiments under reduced pressure but normal gravity are an alternative to minimize buoyant effects. This approach is suitable for studying particular small-scale phenomena at a pressure down to 0.1 bar. The reduced chemical reactivity can, in turn, be partially compensated by an oxygen-enriched environment [102, 235, 238].

Microgravity experiments, to a greater extent than normal gravity experiments, are subjected to the formation of a soot layer between droplet and flame. The Soret effect – also called thermodiffusion or thermophoresis – forces an inward diffusion of soot particles formed near the flame zone. As this inward diffusion is opposed to the Stefan flow of fuel vapor, the soot par-

ticles eventually stagnate and accumulate in soot shells [76, 78, 235, 394]. Xu et al. [465, 467] report in detail on the effects and interaction of soot formation, aggregation, and oxidation under microgravity conditions.

As far as this study is concerned, the representativeness of the collected exhaust gas samples was a major issue for the interpretation of the experimental results. Thus, a great effort was put into a sophisticated design as well as into the operational procedures. Concerning the technical implementation of the measurement techniques and operational procedures, full access by remote control needed to be ensured apart from the standard "hard line" access. For the drop tower environment, remote access to the drop capsule was secured by the Capsule Control System (CCS), the switchable power supply PDU, and the radio telemetry/telecommand system with a WLAN transmitter unit [104]. During the sounding rocket flight, a more elaborate telemetry/telecommand system was used to communicate with the experiment module. It was operated by DLR MORABA and is outlined in detail in Table C.2. EADS Astrium was in charge of the telemetry/telecommand interface, and a single timer (manufacturer: Kayser-Threde; type: KM1038) was utilized allowing 24 commands. Timer events and sequencing commands finally controlled the experiment at the physical level. Nevertheless, the two respective control rooms with the experiment operators have to be considered as an extension of the experimental setup.

From the mechanical point of view, the experimental setup is exposed to microgravity conditions, on the one hand, but to vibration and high loads during launch, landing, and touchdown, on the other hand (Figs. C.2 through C.4). In the case of drop tower experiments, the residual acceleration (microgravity quality) during the "capsule flight" is in the range of 1×10^{-6} to 1×10^{-5} of g_0, which are the best achievable values amongst all microgravity facilities. In the case of sounding rocket experiments, a microgravity quality of 1×10^{-4} of g_0 can be achieved for a duration of approximately 6 min. Comprehensive information on the different loads acting on the setup is given in Chapter C.1. Parabolic flight experiments are an exception to this comparison, as they are directly operated by the experimentalist. The microgravity quality as well as external loads remain at a moderate level (see also Chap. B.1) [66, 104].

3.2.2 Standard Measurement Techniques

The standard measurement techniques were almost identical for the three utilized microgravity environments of parabolic flight, drop tower, and sounding rocket flight. As the sounding rocket environment generally imposes the most complex technical framework, the respective setup is presented in the following discourse. If significant, modifications within the parabolic flight or drop tower setup are emphasized separately.

Measurement of Position

Three motors are installed within the DCU, as summarized in Table 3.3. In order to control the operation of motors SM1 and SM2, microswitches are used for sensing the initial and the end position of the moving units. Here, the actual subsequences are programmed in such a way that the motors either run a specific number of steps or stop when a microswitch is actuated, as in the case of a malfunction. The status of the microswitches is logged in the measurement recordings and is used as a supplementary interlock in the sequence of the drop tower experiments. Furthermore, a micro annular gear pump (SM3/mzr®-2521[2]) with a flow rate of 0.15 to 9 ml min^{-1} and a smallest dosage volume of 0.25 µl is employed for fuel dosing. It has a precision of 1 %, is driven by a DC motor, and controlled by a discrete program saved on the motor controller memory.

Table 3.3: Overview of Motor Utilization.

No.	Manufacturer	Type	Utilization	Reference
SM1	Danaher Motion	P430	Droplet array generation device	Fig. 3.4, **F**
SM2	Danaher Motion	P530	Droplet array lifting device	Fig. 3.3, **E**
SM3	HNP Mikrosysteme	mzr®-2521	Fuel dosing system	Fig. 3.3, **A**

[2] This number identifies a combination of pump (type: 118639) and its controller (type: 110778).

Measurement of Pressure

The pressure inside the DCU vacuum protection is controlled in the range of 0 to 2 bar at 5 Hz. The responsible pressure control unit is activated just after lift-off of the sounding rocket module. The most critical event is a pressure drop in the whole DCU during exhaust gas sampling and air displacement in the combustion chamber, caused by a leak of the combustion chamber shutter (cf. Chap. 3.1.3). Therefore, pressure control is disabled during this crucial event to avoid an excess consumption of air. Apart from that, compensation is regularly started when the pressure is out of its nominal range of $(1.000 \pm 0.025) \times 10^5$ Pa. Besides this direct control, three further sensors are employed for monitoring purposes in the pressurized air supply system.

A dynamic pressure sensor (manufacturer: PCB Piezotronics; type: M112A05) is installed in the combustion chamber in order to capture pressure fluctuations for scientific purposes at a sampling rate of 500 Hz. It has a sensitivity of 0.160 pC kPa^{-1} and its signal is amplified by an in-line charge converter and an ICP® amplifier. Two different models of the in-line charge converter (both also manufactured by PCB Piezotronics) were used: the 422E36 and the 422E12 model in the drop tower and the sounding rocket setup, respectively. Both of them have a charge conversion sensitivity of 10 mV pC^{-1} [330–333].

The exhaust gas sampling (EGS) system including its four sample cylinders is repeatedly evacuated during experiment preparation and countdown to keep contamination low and re-evacuation times short. The vacuum level is monitored directly at the central EGS backbone (cf. Fig. 3.9, **D**) by a compact Full-Range™ gauge (manufacturer: Pfeiffer Vacuum; type: PKR 251). It combines a cold cathode and Pirani gauge to cover a vacuum/pressure range from 5×10^{-9} to 1000 mbar. Thus, the associated leakage rates of the whole EGS system or single sample cylinders became calculable from the given volumes and the pressure readings at fixed time intervals. The pressure readings themselves were included in the data logging of the drop tower campaign but not in the one of the sounding rocket campaign. In the case of the latter, monitoring by an external program was performed until −90 min before launch, using a separate control unit (manufacturer: Pfeiffer Vacuum; type: TPG 261) and access through the late access panel of the sounding rocket module. Afterwards, the remaining vacuum level of the sample cylinders was extrapolated for the

point of time of exhaust gas sampling on the basis of the known leakage rate [338, 339].

Measurement of Temperature

Three thermocouples are installed in the combustion chamber in total, of which one K-type (Ni-Cr/Ni-Al) thermocouple is attached to the inner combustion chamber wall to control the preheating temperature at 500 ± 1 K within a two-step (on/off) control approach. In doing so, the thermocouple monitors a temperature range of 0 to 250 °C with a sampling rate of 5 Hz. Two S-type (Pt10Rh/Pt) thermocouples directly measure the gas temperature inside the combustion chamber in the range of 0 to 1250 °C at 500 Hz [196]. The platinum hot junction was selected here because of its stable temperature-voltage relationship and the exposition of the two measurement locations to hot combustion gases. The downside is its lower sensitivity of approximately $10\,\mu V\,K^{-1}$ and its higher cost compared to other types. Apart from the recording for scientific purposes, the output of the two S-type thermocouples is used to trigger the exhaust gas sampling (Chap. 3.2.6) [390]. In addition, resistance thermometers (Pt100) are used to monitor the ambient temperature inside the DCU vacuum protection vessel. They are installed on the experiment deck, close to the droplet array generation system, and in the proximity of the combustion chamber. This information is also used for cold-junction compensation of the three thermocouple inputs.

3.2.3 Optical Observation

The optical observation method is threefold:

- Observation of the droplet array generation by a color CCD camera
- Observation of the combustion sequence by a color CCD and a high-speed camera
- Backlit observation of the droplet size by a monochrome CCD camera

Consequently, the camera system consists of four cameras, which are summarized in Table 3.4. The cameras CCD1 and CCD2 are identical color cameras

Table 3.4: Overview of Utilized Camera Systems.

No.	Camera system	Observation	Encoding	Frame rate
CCD1	Sony XC-555P	Droplet generation	PAL	25 Hz
CCD2	Sony XC-555P	Combustion (“normal”)	PAL	25 Hz
CCD3	Sony XC-ES50	Droplet size	NTSC	30 Hz
HSV	KODAK Motion SR-Series NAC Memrecam Ci/RX-2	Combustion (high-speed)	PAL NTSC	500 Hz

that are used to generally observe and evaluate the droplet generation and combustion process [410]. CCD3 is a monochrome camera and is used to obtain backlit images of the first droplet of the droplet array. These images in turn are consulted to calculate the initial droplet size D_0 and the vaporization rate k [411]. Chapter C.1 gives more detailed information on the data acquisition and handling. Here, Figure 3.12 provides a representative outline of droplet size and pre-vaporization, as seen through the backlit illumination.

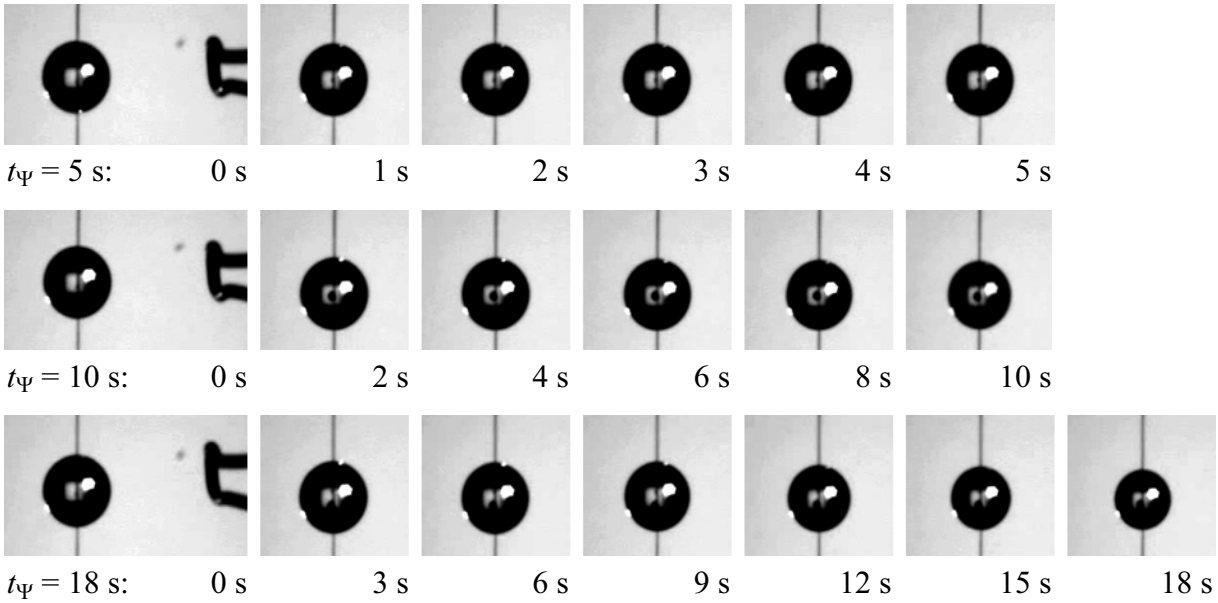

Figure 3.12: Time Evolution of Droplet Diameter During Pre-Vaporization. The backlit images of the monochrome camera CCD3 are consulted for monitoring the droplet size. Illumination is provided by an LED [208, 411]. The droplets have a nominal initial diameter of $D_{0,\mathrm{nom}} = 1.5\,\mathrm{mm}$ at $t = 0\,\mathrm{s}$. The three initial images also show the tip of the hot-wire igniter on their righthand side.

The acronym HSV stands for "High-Speed Video". In the drop tower campaign, a Kodak camera was employed for this purpose (Fig. 3.11, **D**) [110], whereas a camera of NAC Image Technology was utilized in the sounding rocket experiments [302]. Both high-speed cameras have a resolution of 510 × 484 pixel at a frame rate of 500 Hz. High-speed recording with each of these cameras was started with the activation of the hot-wire igniter. In order to allow the necessary optical access to the interior of the combustion chamber, it is equipped with one window on each longitudinal side (Fig. 3.7, **F**). The window sizes are optimized towards a minimum heat loss and a maximum field of view [196].

3.2.4 Exhaust Gas Analysis

A considerable number of measurement techniques are practical for the analysis of combustion products. They include infrared and ultraviolet absorption of electromagnetic radiation, mass spectroscopy, emission spectroscopy, various chemical methods, and electrochemical methods. Sampling and analysis systems can be classified in "cold/dry" and "hot/wet". While a cold/dry system consists of the sample probe, particulate matter filter, heated sample line, moisture removal unit, and the analyzer itself, a hot/wet system forgoes the moisture removal and directly measures the emission concentrations on a wet basis. Besides, those techniques may also be grouped into "methods by separation" and "methods without separation" [97, 136, 181, 275, 321, 390, 420, 440, 460].

Since the spatial distribution of the combustion products within the combustion chamber was three-dimensional at any given time, it is evident that some limitations are imposed on the interpretation of the exhaust gas samples obtained. A concept combining gas sampling during the experimental phase with a successive gas analysis on the ground was pursued here. In the case of parabolic and sounding rocket flight, the sampling process took place during the microgravity period, while it was enforced under normal gravity conditions (i.e. after drop capsule deceleration) in the case of the drop tower experiments. To perform the gas analysis in the particular laboratory environment, the filled gas sample cylinders were physically removed from the DCU. The surface coating discussed above helped in keeping the emission signature stable until the analysis was performed (see Chap. 3.1.4). A combination of a FT-IR (Fourier Transform Infrared) spectrometer and a chemiluminescent NO_x

analyzer was the system of choice for determining the exhaust gas concentrations. In the former case a NEXUS® 470 unit of Thermo Electron was used, in the latter a CLD 700 EL ht as well as a CLD 700 LEV ht unit of ECO PHYSICS [111–115, 434–438].[3] As the constituents of the exhaust were not separated for identification and measurement, and no moisture removal was utilized, the approach chosen for this research can be classified as "hot/wet method without separation".

NO/NO_x Chemiluminescence Analysis

In an early work, Allen [14] reviews numerous methods of analysis for oxides of nitrogen, namely nitric oxide (NO) and nitrogen dioxide (NO_2). The suitability of the chemiluminescence method, which is widely seen as state of the art in NO_x measurement, is evaluated in the work of Allen et al. [16], Black and Sigsby Jr. [46], and Sigsby Jr. et al. [397]. A chemiluminescent analyzer measures the light emitted from an excited NO_2 molecule (NO_2^*, see Eq. (3.3)). This technique provides exceptional sensitivity with a feasible lower detection limit of less than 0.1 ppb. However, only NO can be measured directly, as indicated by the initial reactions of Equations (3.1) and (3.2). For this purpose, ozone (O_3) is generated in the analyzer and added to the gas under investigation. The NO_2 formed is promoted to an excited state in 20 % of the reactions (Eq. (3.2)), and it returns to its ground state according to Equation (3.3) by emitting a photon. The resulting electromagnetic emission spectrum is in the range of 600 to 3000 nm with the intensity maximum at 1200 nm. In order to detect this chemiluminescence, the photoelectric effect is employed, and as long as O_3 is in excess, proportionality to the actual NO concentration is given. As a linear correlation prevails between absolute pressure and the probability of Equation (3.4), the analyzer is generally operated at a low pressure of 40 ± 10 mbar to achieve a high degree of light efficiency. Furthermore, a reducing converter is used in the analyzer forcing the reaction of Equation (3.5), in which NO_2 is reduced to NO prior to its detection. Consequently, the total NO_x is determined as one quantity from the original NO plus the NO resulting from the NO_2 to NO conversion; and the NO_2 concentration is calculated by the difference of the NO and NO_x values measured. The reaction of Equation (3.5) is outlined for carbon here, but the CLD 700 EL ht and the CLD 700 LEV ht unit

[3] The CLD 700 LEV ht is a modified CLD 700 AL unit, that features a heated gas inlet.

use a metal converter at 400 °C and a molybdenum converter at 350 to 370 °C, respectively [16, 111, 113–115, 150].

$$\mathrm{NO} + \mathrm{O_3} \rightarrow \mathrm{NO_2} + \mathrm{O_2} \qquad (80\,\%) \tag{3.1}$$

$$\mathrm{NO} + \mathrm{O_3} \rightarrow \mathrm{NO_2^*} + \mathrm{O_2} \qquad (20\,\%) \tag{3.2}$$

$$\mathrm{NO_2^*} \rightarrow \mathrm{NO_2} + h\nu \tag{3.3}$$

$$\mathrm{NO_2^*} + M \rightarrow \mathrm{NO_2} + M \tag{3.4}$$

$$\mathrm{NO_2} + \mathrm{C} \rightarrow \mathrm{NO} + \mathrm{CO} \tag{3.5}$$

When quantifying NO_x concentrations, measuring NO_2 is generally the primary problem. As this species is highly soluble in water, water condensation in the sample line as well as in the supply line of the analyzer has to be prevented. Furthermore, the significance of the emission data rests on reliable converter components, in particular for low concentrations, because the NO_2/NO_x ratio tends to increase with overall decreasing NO_x levels [371].

FT-IR Spectroscopy

Since the spectroscopic FT-IR method is ideally suited for capturing the concentrations of a larger number of species, it was used to determine the major combustion products including CO_2, CO, and H_2O. Oxides of nitrogen (NO, NO_2, and N_2O) were measured by FT-IR as a back-up solution to the chemiluminescence method. The FT-IR method also solely utilizes physical exhaust properties, ignoring chemical properties. It is based on Beer's law, which relates the absorption of light to the concentration and path length of the material through which the light is traveling [97, 158, 420, 434–438]. Equation (3.6) shows the correlation for a given wavelength λ:

$$A_\lambda = -\log\left(\frac{I}{I_0}\right) = c\,\epsilon_\lambda\,l. \tag{3.6}$$

The absorbance A_λ is the ratio of the intensity of light I that has passed through the sample and the intensity of light I_0 before it enters the sample, expressed as a logarithm with base 10. A linear correlation is valid for the concentration c of the absorbing species, molar absorptivity (molar extinction co-

efficient) ϵ_λ, and distance l the light travels through. Hence, an infrared spectrum represents a fingerprint of a sample with numerous absorption peaks. These absorption peaks correspond to the vibrational frequencies between the bonds of the atoms making up the sample material. Generally, a molecule interacts with infrared light only when it is capable of absorbing specific spectral components by changing its dipole moment due to vibration. Symmetric stretch, asymmetric stretch, and deformation vibrations are most relevant here [97, 158, 420, 435].

The NEXUS® 470 FT-IR spectrometer uses a Michelson interferometer to generate an interferogram in the first instance (cf. Fig. 3.13). Light from the infrared source is split into two beams by a beam splitter, one of them being reflected off a fixed mirror and the other one reflected off a moving mirror. Essentially, an electromagnetic wave is combined with a copy of itself that is delayed by time. This leads to interference between the two beams. By measuring the temporal coherence of the light beams at each time delay setting, the time domain is effectively converted into a spatial coordinate. Thus, the interferogram of Figure 3.13 shows the signal intensity in volts versus the displacement of the moving mirror measured in data points. Then, the raw data of the interferogram is Fourier transformed (FFT) into a single-beam spectrum, which is frequency dependent. It shows the energy distribution of the light source, and it includes the characteristics of the detector, beam splitter, and atmospheric conditions along with those of the sample that is contained in the optical measurement cell. Since a relative scale is required to determine the uncorrupted absorption intensity of the sample, a background spectrum must additionally be measured. It is typically obtained from either a cell with a constant flow of zero reference gas or a completely evacuated cell. To remove the information of the instrumental characteristics, the single-beam sample spectrum is divided by the single-beam background spectrum (Fig. 3.13). The resulting spectrum is depicted in percent transmittance or percent absorbance.

Finally, by collecting more than one scan within a measurement cycle, the system averages all of the data to improve the signal-to-noise ratio (SNR). Consequently, an increasing number of scans significantly improves the detection of individual gas components. Thus, 32, 40, or 64 scans were averaged for obtaining one spectrum within the present experiments, and a $0.5\,\mathrm{cm}^{-1}$ resolution was chosen with one scan per second [97, 158, 420, 423, 434–436].

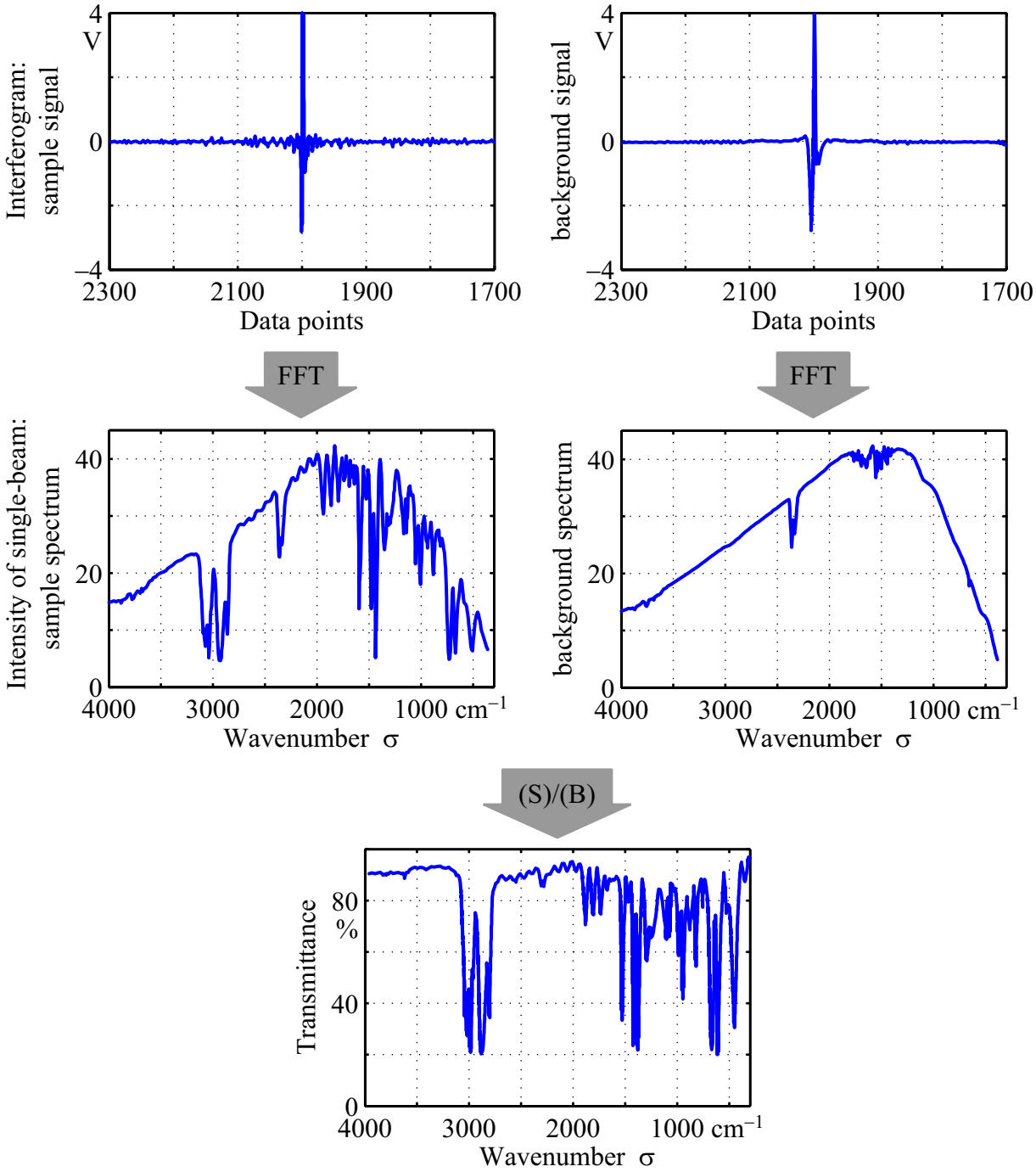

Figure 3.13: Process of Obtaining a Transmission Spectrum. For optical spectroscopy in the infrared spectrum, it is customary to work with wavelength λ and wavenumber σ ($= 1/\lambda$). The expression (S)/(B) indicates the ratio of sample and background.

Combined Measurement Setup

Both analysis devices were coupled according to Figure 3.14 to become one unit with the chemiluminescent NO_x analyzer downstream of the FT-IR spec-

trometer. The apparatus requires 200 ml of gas (at ambient conditions), which were provided by each of the sample cylinders. After conditioning the gas sample to the FT-IR operational parameters of $T = 458\,\mathrm{K}$ and $p = 866\,\mathrm{mbar}$, a quasi-stationary analysis was performed keeping the sample in the 2 m optical path length cell. Subsequently, the chemiluminescence analysis was carried out with the sample drawn from the optical cell, thus, evacuating the cell at the same time. While doing so, the sample was lost as a consequence of the analysis process. As this fact necessitated an error free procedure, extensive calibration and test runs were conducted in preparation of the exhaust gas analysis (see Chap. 3.2.5) [296, 434].

3.2.5 Calibration of Measurement Setup

The calibration of the standard measurement technique was straightforward and no particular measures were required to provide an operational system. On the other hand, the calibration of the exhaust gas analysis system necessitated an elaborate step-by-step procedure, which is outlined in the following paragraphs.

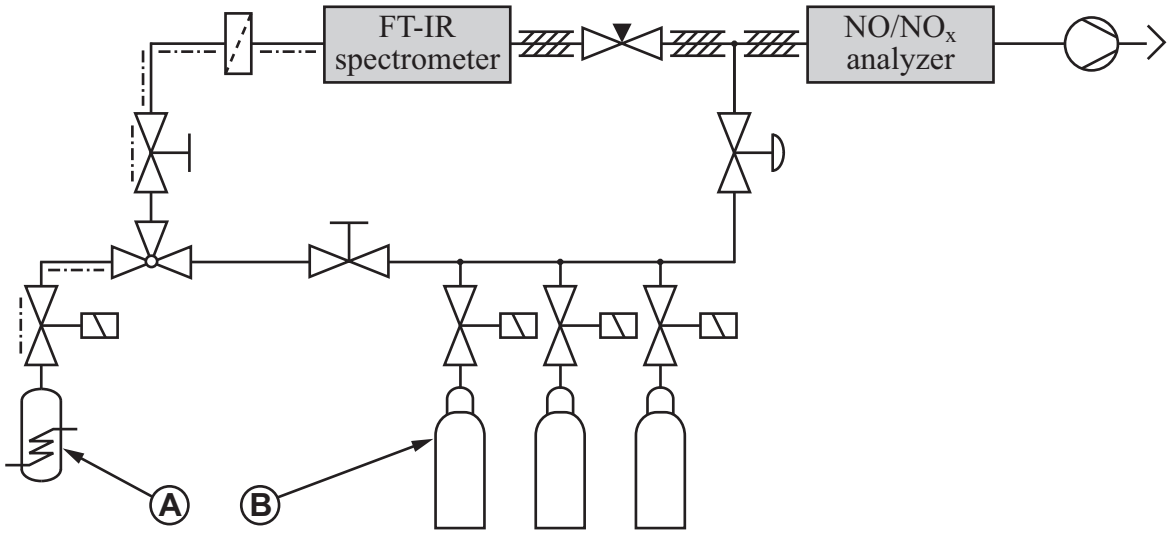

Figure 3.14: Combined Gas Analysis Setup. First, the FT-IR analysis is performed, second, the chemiluminescence analysis. **A**: Sample cylinder, **B**: Calibration gases (zero and span gases).

Calibration of Chemiluminescent NO_x Analyzer

The chemiluminescent NO_x analyzer was calibrated with NO at concentrations of 2.00, 8.66, and 9.80 ppm in an N_2 balance [111]. However, when sampling from combustion systems, additional species apart from N_2 are introduced, including H_2O, CO_2, CO, H_2, UHCs, and soot. Under certain circumstances, the composition of the exhaust can affect the measurement value indicated for NO due to differences in third body quenching reactions between the span gas used and the final sample gas (Eq. (3.4)). Fitz and Welch [136], for instance, report on an NO concentration that is 30 % lower than the actual concentration, using synthetic exhaust simulated for a gas-fired power plant with water vapor at 17 % by volume. For such an exhaust analysis, the water must either be removed prior to NO_x detection, the detector be calibrated with saturated span gas, or the NO_x reading be corrected on the basis of third body quenching. The third body quenching effect is most crucial in samples that have large concentrations of non-diatomic constituents. Gärtner [144], Matthews et al. [273], and Tidona et al. [439] investigated interferences in the chemiluminescent measurement of NO and NO_2 emissions from combustion systems. Generally, the NO_x measurement error increases with an increasing H/C ratio of the fuel and an increasing equivalence ratio ϕ. Measurements taken in very fuel-rich systems or in the fuel-rich regions of diffusion flames may be subject to error well above 20 % due to the potential presence of polyatomic fuel molecules with high quenching characteristics.

As third body quenching may be such a significant source of error in NO measurement with the effect of excessively low NO_x indication, the relative quenching efficiencies of various third bodies were included in the post-processing. The calculation follows the procedure of Matthews et al. [273], which was also employed in the work of Gärtner [144], Baessler [31], and Brückner-Kalb [57]. If the concentrations of the important third bodies are known, the actual NO concentration can be calculated from the concentration indicated using the following relations:

$$\frac{[\mathrm{NO}]_{\mathrm{actual}}}{[\mathrm{NO}]_{\mathrm{indicated}}} = \frac{X_{\mathrm{NO,actual}}}{X_{\mathrm{NO,indicated}}} = 1 + \sum_{M=1}^{J} (R_M - 1), \tag{3.7}$$

where

$$R_M \equiv \frac{I_{\mathrm{N_2}}}{I_M}. \tag{3.8}$$

The respective intensities of photoemission measured in the presence of nitrogen and in the presence of a third body species are indicated by I_{N_2} and I_M. The relative quenching efficiency R_M may be calculated from the relation

$$R_M = 1 + m\, d\, \widetilde{X}_M. \tag{3.9}$$

Equation (3.9) is a line equation where m is the slope of the first-order curve fit of measured reference data (Tab. 3.5), d is the dilution constant (a function of the analyzer used), and $\widetilde{X}_M$ is the third body concentration in mole percent (volume percent) in the sample stream. Generally, the quenching effect is a strong function of the particular analyzer type. The chemiluminescent NO_x analyzer used by Matthews et al. [273] and Tidona et al. [439] had a 8 mil (= 0.203 mm) sample capillary; the CLD units used here have a 7 mil (= 0.178 mm) sample capillary. Thus, the dilution constant presented in these two publications was also adopted here with $d = 0.4545$. Table 3.5 lists values for the slope m of Equation (3.9), as reported by Matthews et al. [273] and Tidona et al. [439]. They are similar except for Ar and H_2O. In order to expound the quenching effect by means of an example, equilibrium concentrations at equivalence ratios of 0.5, 1.0, and 2.0 are taken as a basis for obtaining the ratio of actual and indicated NO concentration in Table 3.6. The equilibrium species concentrations are calculated for atmospheric pressure and n-decane/air flames. The bottom line results in Table 3.6 clearly indicate that the chemiluminescence method is sensitive to third body quenching. The difference between the correction factors at a constant equivalence ratio ϕ is primarily due to the difference in the H_2O correction. Finally, the m-values provided by Tidona et al. [439] are adopted in the work at hand because they showed higher consistency in the raw data relevant for the relative quenching efficiency of water R_{H_2O}.

The utilized CLD units feature a linearity of ±1 % of the full scale reading within each measurement range, which can for instance be set to 0 – 0.1, 0 – 1, or 0 – 10 ppm. However, the CLD 700 LEV ht outperforms the CLD 700 EL ht unit by one to two orders of magnitude regarding minimum detectable concentration and noise at zero point. This presumes a nominal operation with a constant analysis pressure of 40±10 mbar [111–114]. Nominal operation of the NO/NO_x analyzer is not feasible, though, as the gas sample is limited to 200 ml and the source “FT-IR measurement cell” is subsequently evacuated during CLD analysis (see Fig. 3.14).

Table 3.5: Slopes of First Order Curve Fits Based on Relative Quenching Efficiencies.

	Slope of first-order curve fit m	
Third body species	Matthews et al. [273]	Tidona et al. [439]
Ar	−0.00480	−0.00118
CO	−0.00118	−0.00141
O_2	0.00115	0.00132
H_2	0.00337	0.00288
CO_2	0.01047	0.00896
H_2O	0.03430	0.04756

Figure 3.15 shows a typical measurement reading of genuine exhaust gas from the CLD 700 LEV ht unit. The concentrations measured by both parallel reaction chambers are indicated here, providing for a simultaneous determination of NO and NO_x. The NO_2 value is the arithmetic difference of these two values. The analysis pressure of the CLD highlights the temporal state of the analyzer's

Table 3.6: Ratio of Actual and Indicated NO Concentrations due to Third Body Quenching. The calculation of the equilibrium species concentrations is performed with the software package Gaseq [300]. Since minor species are not included, the sum of the mole percentages do not total 100 %.

		Equilibrium species concentration $\widetilde{X}_M$ in %		
Species		$\phi = 0.5$	$\phi = 1.0$	$\phi = 2.0$
CO		0.001	1.948	17.191
CO_2		6.529	10.484	2.746
H_2		0.000	0.419	13.705
H_2O		7.172	12.968	8.219
O_2		10.021	0.866	0.000
N_2		76.062	72.305	58.126
Total		99.786	99.990	99.987
$\frac{X_{NO,actual}}{X_{NO,indicated}}$	Matthews et al. [273]	1.326	1.555	1.337
	Tidona et al. [439]	1.413	1.710	1.431

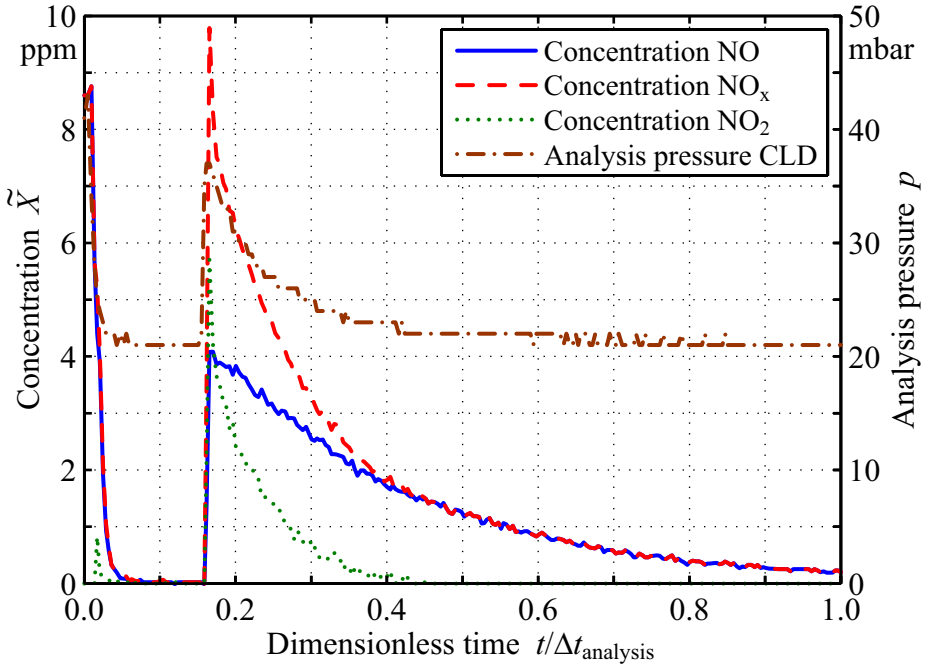

Figure 3.15: Measurement Reading of Exhaust Gas from Chemiluminescent NO_x Analyzer. Exhaust gas supply starts at $t/\Delta t_{analysis} = 0.16$. The pressure reading indicates the analysis pressure in the reaction chamber. This pressure does not drop below $p = 21$ mbar, while the pressure level approaches zero in sample cylinder.

reaction chambers. Here, the lowest achievable pressure is $p = 21$ mbar, which is limited by the hardware of the analyzer and, in particular, the vacuum pump employed. Initially, span gas of 8.66 ppm NO is supplied and the analysis pressure is within its nominal range at $p = 43$ mbar. This approach verifies operability and calibration of the analyzer. To assure a discrete start of the transient NO_x measurement, the supply of the sample is delayed in relation to the shut-off of the span gas ($t/\Delta t_{analysis} = 0.02$ to 0.16). Since no constant and/or an excessively low measurement profile might be obtained with this method, the time integral of the measurement readings is employed here. It basically represents the total number of photoelectric counts of the given analysis volume "FT-IR measurement cell" and is based on Equations (3.2) and (3.3). Consequently, it can be correlated to the nominal NO_x concentrations that would be obtained at a fixed volumetric flow rate and a given analysis duration.

Figures 3.16 and 3.17 outline the concept pursued: For statistical evidence, a large number of reference measurements were recorded for calibration gases with concentrations of $\widetilde{X}_{NO} = 2.00$, 8.66, and 9.80 ppm (cf. Fig. 3.16). They

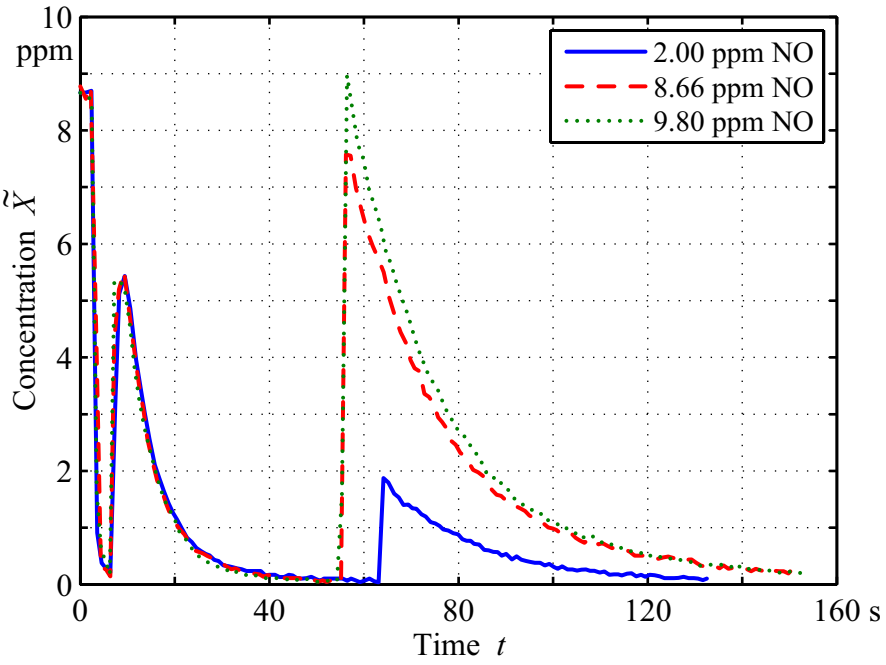

Figure 3.16: Measurement Reading for Different Calibration Gases.

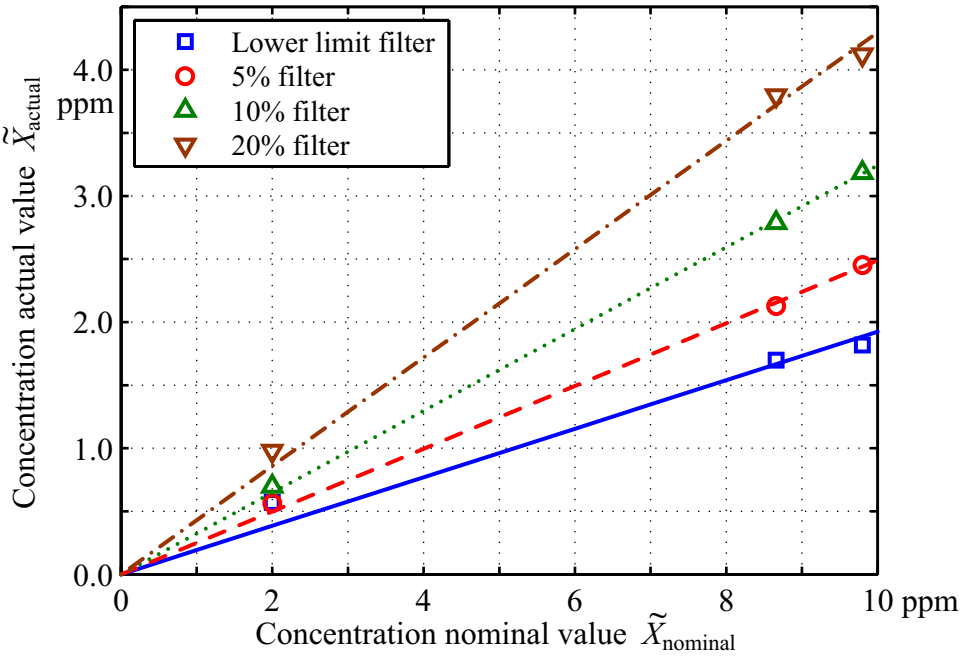

Figure 3.17: Correlation Between Actual and Nominal Value of NO_x Concentration. The actual concentration $\tilde{X}_{\text{actual}}$ represents the time integral of the total number of photoelectric counts of the given analysis volume "FT-IR measurement cell". Accurately put, it is a time-averaged value.

form the basis of the calibration method. As the lower limit of the time integral can easily be linked with the obvious increase of the measurement signal (Fig. 3.16), a reasonable value has to be identified for its upper limit only. Therefore, different filters define contrasting upper limits. Figure 3.17 displays resulting calibration curves based on the recorded data basis and linear curve fits for four exemplary filters (i.e. time integrals). Data are consistent and deviations from the ideal trend are marginal for all four examples. Nevertheless, the 10 % filter shows the best performance and was selected for the present study. It stops integration as soon as the measurement signal drops below 10 % of its maximum value. The related raw data have a standard deviation σ of the range of 0.032 to 0.090, typical error ($\sigma / N^{\frac{1}{2}}$) of the range of 0.011 to 0.027, and coefficient of variation (CV = 1/SNR = σ / μ) of the range of 0.91 to 3.64 % [409]. The line equation of the linear curve fit is: $y = 0.3242\,x$ (Fig. 3.17, 10 % filter). The respective coefficient of determination is $R^2 = 0.9995$.

Furthermore, the converter efficiency according to Equation (3.5) was determined by gas phase titration and totaled 94.5 % during the final measurement campaign [115]. It is typically in the range of 83 to 97 % but depends on the absolute NO_2 concentration, the age and use history of the converter, and the gas matrix used for its determination [136].

Calibration of FT-IR Spectrometer

The calibration of a FT-IR spectrometer requires a high temperature and pressure stability of the calibration gas supplied, as does the final analysis process. Misinterpretation would be a consequence of varying density in the optical measurement cell. Ideally, both the reference and final analysis spectra are recorded with identical hardware setups as well as identical operational parameters.

In order to quantify the gaseous compounds in the exhaust gas, two existing multi-component gas analysis methods were refined and employed with the NEXUS® 470 spectrometer of Thermo Electron [334, 423]. They include corrections for interferences and are outlined in Tables 3.7 and 3.8. For Standard No. 1 (Tab. 3.7), the FT-IR measurement cell was controlled at a constant temperature of $T = 458\,\mathrm{K}$ and an absolute pressure of $p = 866\,\mathrm{mbar}$. Potassium bromide (KBr) windows were used for optical access to the cell due to their

Table 3.7: Calibration of FT-IR Spectrometer (Standard No. 1). This calibration data is based on the setup used by Steinbach [423]. The calibration method was developed at an absolute pressure of $p = 866\,\text{mbar}$.

		Calibration spectra	
Component	Spectral region in cm^{-1}	range in ppm	number
NO	1850.8 – 1930.9	1 – 7000	19
NO_2	1580.8 – 1631.2	10 – 1000	10
N_2O	2187.6 – 2205.2	5 – 50	5
CO_2	2372.2 – 2388.1	50 – 200 000	16
CO	2002.0 – 2184.5	1 – 100 000	25
H_2O	3978.0 – 3986.9	23 000 – 61 000	7
CH_2O	2600.0 – 2784.0	93 – 905	6

wide spectral range of 10 000 to $400\,\text{cm}^{-1}$. The flow rate of the calibration gas was kept within the range of 2.0 to $2.5\,\text{l}\,\text{min}^{-1}$. For Standard No. 2 (Tab. 3.8), the cell temperature was set to $T = 453\,\text{K}$, and recording was performed under atmospheric pressure, allowing however, for the corrections necessitated by daily pressure variations. Here, the measurement cell was equipped with zinc selenite (ZnSe) windows, as ZnSe rather than KBr is resistant to water

Table 3.8: Calibration of FT-IR Spectrometer (Standard No. 2). This calibration data is based on the work of Peitz et al. [334]. The calibration method was developed under atmospheric pressure, incorporating corrections for daily variations.

		Calibration spectra	
Component	Spectral region in cm^{-1}	range in ppm	number
NO	1849.7 – 1939.8	25 – 1000	13
NO_2	1578.2 – 1634.1	16 – 1000	13
N_2O	2133.6 – 2215.0	10 – 200	2
CO_2	2380.0 – 2410.0	150 – 12 000	21
CO	2080.0 – 2130.5	150 – 15 000	18
H_2O	2985.3 – 3072.6	10 000 – 200 000	17
CH_2O	2700.0 – 2940.0	0 – 120	1

vapor and acidic gases such as NO_2. A constant flow rate of 3.0 l min^{-1} was ensured. Development of the analytical methods was done in the software package QuantPad (version: 6.1), followed by implementation into the software package OMNIC® (version: 6.1a), both supplied by Thermo Nicolet [435, 436].

One spectral region was regularly selected for the determination of a particular component (species). This region had to include portions without significant absorption, as they built the baseline to determine the absorbance A_λ (cf. Eq. (3.6)). Furthermore, each spectral region needed to be subdivided into different subregions to allocate the component-specific bands employed for spectral analysis. Interference occurring on account of cross-sensitivity additionally increased the fragmentation within a spectral region. Cross-sensitivity due to H_2O and CO_2 renders measurement extremely difficult in the infrared spectrum. It is high for NO, in particular under ambient pressure. Even though tilted, shifted, and curved baselines are feasible and baseline correction may be applied by the user, it is a disadvantage to have wide-spread spectral regions and high absorbance A_λ of, for instance, 0.8 to 1.0. The latter may occur due to strongly varying levels of concentration. If absorption and hence signal-to-noise ratio (SNR) get too large with an increase of concentration, switching to a different spectral region might deliver better results. Consequently, more than one spectral region might be required for a single component under certain circumstances [435–438].

Since light gases, such as NO and CO, absorb rotational energy in addition to vibrational energy, a polynomial instead of a linear curve fit became necessary for the calibration of these components. This involved a larger number of span gases because the number of available data points must outnumber the polynomial order.

To cover all these effects, both calibration standards (Tabs. 3.7 and 3.8) were employed in the present study on a “competitive” basis, as they represent differing approaches. Nevertheless, they showed consistent results that were in good agreement with theory (see Chap. 5). In the end, the reliability of the results depends on the maintenance and calibration of the FT-IR spectrometer, which is time-consuming in comparison with other analytical methods, but the analysis time itself is short.

3.2.6 Experiment Sequence and Operational Parameters

In order to perform an experiment run, a droplet array is generated by the droplet array generation system at an ambient temperature T_∞ of 300 to 315 K (Fig. 3.18). The droplets are suspended onto the droplet array holder by a fuel pump through fine glass tubes. Each droplet is suspended at the intersection of a pair of X-shaped 14 µm SiC fibers, which imparts lowest residual motion and highest sphericity (Chap. 3.1.2) [282]. The shutter at the bottom of the combustion chamber is opened and the droplet array holder with the droplet array is lifted into the preheated combustion chamber by the droplet lifting system. Pre-vaporization of the droplets is performed at an elevated temperature level of T_Ψ. Depending on the predefined degree of vaporization Ψ, an ignition wire ignites one end of the droplet array to initiate com-

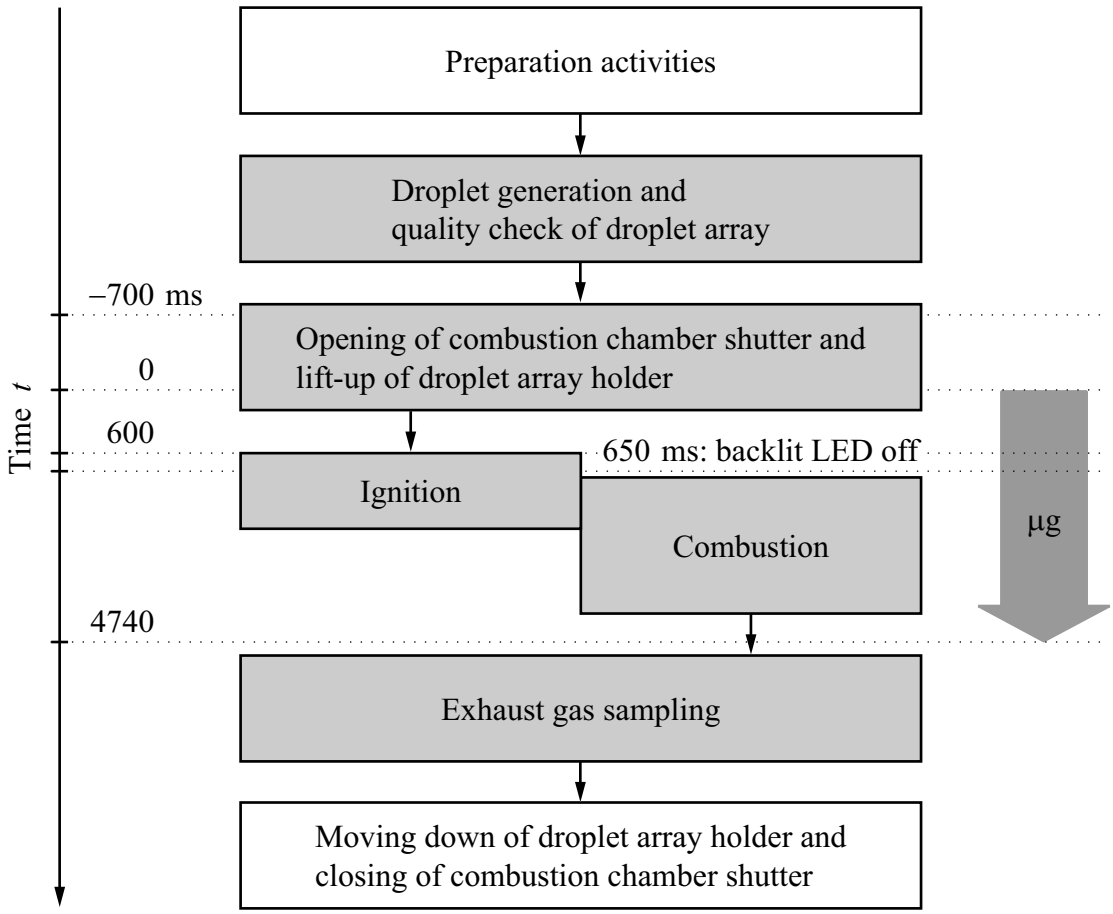

Figure 3.18: Experiment Sequence of TEXNOX Drop Tower Campaign. Microgravity time starts at $t = 0$ s and lasts for 4.74 s (not to scale here) [104].

bustion (cf. Fig. 3.12). Flame spread occurs along the droplet array. Subject to the vaporization rate Ψ, the combustion process is initially characterized by a partially premixed flame but followed by a diffusion flame around the droplets until flame extinction. After flame extinction, exhaust gas sampling is performed by the exhaust gas sampling (EGS) system using one evacuated gas sample cylinder per combustion run. Finally, the droplet array holder is moved down to its initial position, and the shutter of the combustion chamber is closed for venting and subsequent refilling with fresh air. All gas samples are stored in those gas sample cylinders until their analysis in the particular laboratory environment (Chap. 3.2.4). Visual observation of the combustion process as well as temperature and pressure logging support the scientific interpretation of the gas analysis results [195–197, 208, 293, 294, 296].

In comparison to the other microgravity facilities, the experiment sequence in the drop tower is most crucial in time. This is because of the limitation to 4.74 s microgravity time, which is outlined in Figure 3.18. Apart from various tests (Chap. 3.1.5), the experiment preparation activities include compressed air charging, fuel charging, battery charging, evacuation of gas sample cylinders, and initialization of control and data acquisition systems. The subsequence that opens the combustion chamber shutter and lifts the droplet array holder (cf. Fig. 3.18) comprises the drop capsule release, and thus initiates microgravity at $t = 0$ ms.

Key Operational Parameters

A wide range of different combustion regimes was investigated in parabolic flight, drop tower, and sounding rocket flight with the experiment apparatuses described (see also Tab. B.1). While keeping the pressure at $(1.000 \pm 0.025) \times 10^5$ Pa, the combustion chamber temperature at 500 ± 1 K, and the total amount of fuel constant, the pre-vaporization time t_Ψ was varied in the range of 5 to 18 s on the TEXUS-46 sounding rocket campaign (cf. Tab. 3.9). According to the degree of vaporization Ψ and using the analytical D^2 law, the burnout time t_b can be calculated to 8.8 and 4.0 s for one droplet for $t_{\Psi,\min} = 5$ s and $t_{\Psi,\max} = 18$ s, respectively. Table 3.9 summarizes the parameter space of the experiments originally scheduled on TEXUS-46. In total, four experiment runs were envisioned of which three could be performed successfully. Experiment No. 4 was rendered fruitless due to a timing/sequencing error, resulting

Table 3.9: Nominal Experiment Parameters for Droplet Arrays on TEXUS-46. The droplet number is $N = 5$, and the non-dimensionless droplet spacing $S = 18\,\text{mm}$ [195].

No.	Pre-vaporization time t_Ψ in s	Droplet diameter		Dimensionless spacing ratio S/D_{ign}
		initial D_0 in mm	ignition D_{ign} in mm	
1	18	1.5	1.01	17.8
2	10	1.5	1.34	13.4
3	5	1.5	1.47	12.2
4	15	1.5	1.15	15.7

from repeated countdown holds during the final steps of the TEXUS launch sequence. Apart from testing and validation, the experiments of the TEXNOX drop tower campaign were destined to diversify the scientific output. Here, the initial droplet diameter D_0 was varied in the range of 0.8 to 1.0 mm, a dimensionless spacing ratio S/D_0 of 4.5, 6.0, and 9.0 with 17, 13, and 9 droplets was applied (Tab. 3.1), and preheating temperature T_Ψ was set at 300, 400, 450, and 500 K. The different amounts of pre-vaporization time t_Ψ and preheating temperature T_Ψ were essential for the development of a flammable gas layer around the droplets and for diversification [195–197, 208, 293, 294, 296].

Control of Droplet Lifting System

The droplet lifting system moves the droplet array holder 105 mm vertically from its initial position to the end position inside the combustion chamber. Stepper motor, gear system, and crank arms are adjusted for a quick but smooth operation. The working time for covering the distance of 105 mm was set to 2.0 s for the TEXUS-46 sounding rocket flight but to 1350 ms for the TEXNOX drop tower campaign due to the limited microgravity time. Furthermore, the lift-up process was started 700 ms before the drop capsule release to extend the available time for droplet burnout within the drop tower experiments (cf. Fig. 3.18). This approach split the process into two phases: a first phase under normal gravity with the droplet array in ambient temperature T_∞ and a second phase under microgravity with the droplet array exposed to the preheated combustion chamber. Bringing forward the lift-up process further is limited by the abrupt drop of surface tension during the temperature

transition $T_\infty < T < T_\Psi$. The remaining surface tension at $T \rightarrow T_\Psi$ would not be sufficient to counteract the droplet's weight any longer, and the droplet would fall off its suspension fibers. Microgravity conditions are essential for this sensitive phase. Figure 3.19 shows the dependency of surface tension γ on temperature T for hydrocarbon fuels. Here, the parametric relative density is calculated from the density ratio of n-decane at the minimum temperature of droplet generation $T_\infty = 300\,\mathrm{K}$ and water at $T = 277\,\mathrm{K}$ [244, 453].

Control of Exhaust Gas Collection

In a first estimate, droplet combustion can generally be assumed to be a physically controlled phenomenon. Thus, the relevant processes proceed at rates that can be calculated without precise knowledge of the chemical-kinetic constants involved [418, 443]. It is sufficient to presume that the reaction continues until completion. Therefore, empirical tests in parabolic flight and drop tower were used to derive a correlation between flame extinction and the gas

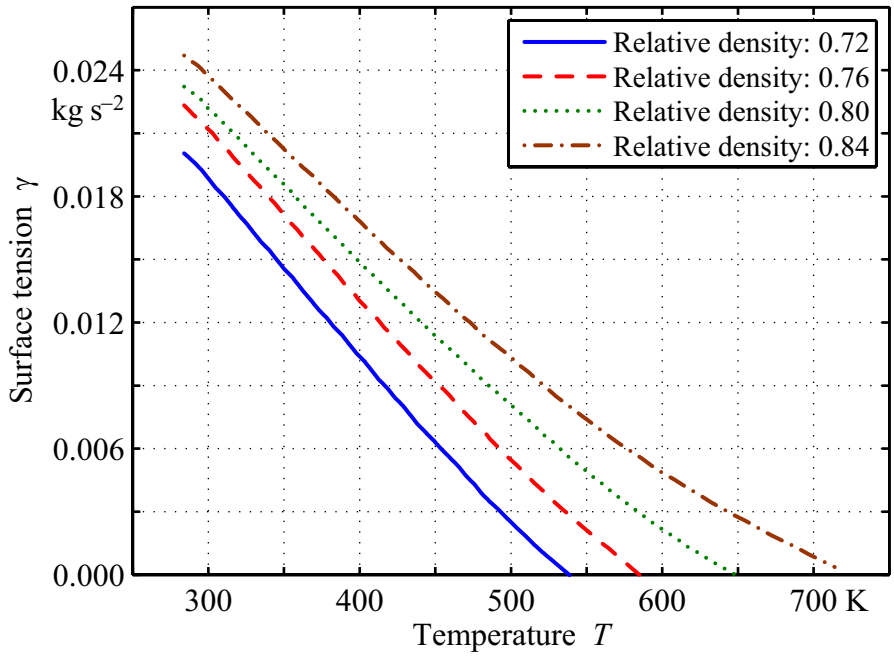

Figure 3.19: Surface Tension-Temperature Relationship for Hydrocarbon Fuels (reprinted from Ref. [244]). Relative density – formerly called specific gravity – is the ratio of mass of a given volume of liquid to the mass of an equal volume of water. For the present setup (fuel and operating conditions) a relative density of 0.72 at 300/277 K can be assumed [244, 453].

temperature readings of the combustion chamber. This correlation was used within the trigger algorithm to initiate exhaust gas sampling. Figure 3.20 depicts a schematic of the temperature readings underlying the trigger algorithm. The trigger signal is sent from the control logics when the following criteria are satisfied:

- Both thermocouple readings exceed T_1: flag "condition 1".
- Both thermocouple readings drop below T_2: flag "condition 2".
- Trigger logic is enabled after t_{min}.
- If conditions 1 & 2 are both satisfied and $t_{\text{min}} < t < t_{\text{max}}$, the trigger signal is to be sent immediately.
- If the elapsed time exceeds t_{max} (without fulfilling conditions 1 & 2), the trigger signal is to be sent immediately, acting as a timeout limit.

The time limits t_{min} and t_{max} are independent of the temperature conditions T_1 and T_2, and they can be specified individually for each combustion

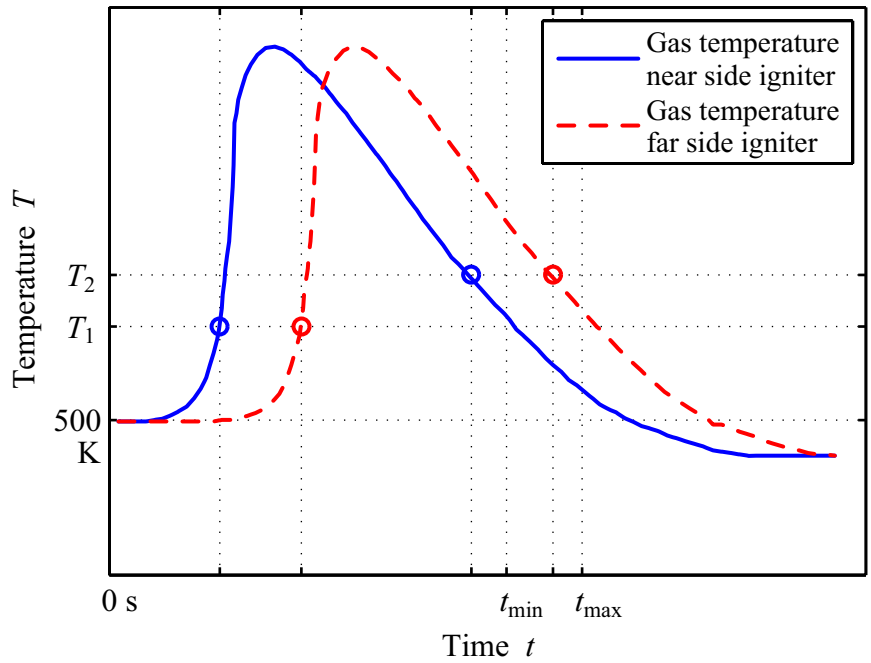

Figure 3.20: Trigger Logic for Exhaust Gas Sampling. The minimum and maximum time limits for exhaust gas sampling, t_{min} and t_{max}, are specified according to the expected burnout times for each particular droplet setup [196, 197, 293, 294, 296].

run. Furthermore, t_{min} does not necessarily need to be as early as shown in Figure 3.20. It can also be specified in such a way that it might chronologically lie behind the achievement of the two temperature conditions. For the sounding rocket campaign, the temperature conditions were uniformly set to $T_1 = T_2 = 508.15\,\mathrm{K}$ (= 235 °C) [196, 197]. Figures D.1 through D.3 show the actual experiment readings including the values specified for t_{min} and t_{max}.

3.3 Numerical Study of the Fluid Dynamics Within the Combustion Chamber

The density decrease of the gas inside the combustion chamber, accompanied by the temperature increase of the combustion process, is one of the most crucial issues of the experiment.[4] It causes an estimated volume expansion of 1.2 to 1.8. This expansion results in a discharge of some exhaust gas from the open combustion chamber. Furthermore, "fresh" air is entrained into the combustion chamber by exhaust gas sampling. As a volume of 200 ml exhaust is to be collected for the gas analysis and the combustion chamber itself has a volume of 378 ml, the losses are significant and need to be considered within the analysis process and scientific interpretation of the results. Consequently, a numerical study of the two gas exchange processes was conducted within the design process of the experiment setup, reflecting the open combustion chamber [293]. The coordinate system employed for studying both processes is identical to the one introduced in Figure 3.7.

Computational fluid dynamics (CFD) was used to solve the fluid flow in a three-dimensional full-scale model of the combustion chamber. The experimental parameters of the TEXUS-46 sounding rocket flight, with five n-decane droplets, were the basis for this study. The software package ANSYS® CFX® 11.0 was used for the numerical studies and ICEM™ CFD for mesh generation. The discretization in CFX® 11.0 is realized by the finite volume method [21, 22]. Heat transfer by radiation is neglected due to the simplicity of the droplet model of this CFD study, which results in noticeable deviations from the physical experiment. However, this CFD study was conducted with the

[4] Assuming, hypothetically, a perfectly premixed fuel-air mixture inside the combustion chamber and a preheating temperature of 500 K, the global equivalence ratio calculates to $\phi = 0.36$, which is well below the lean flammability limit. The equilibrium temperature for these conditions would be 1387 K [300, 443].

primary goal of supporting the experiment design process (Chap. 3.1) and not of delivering scientific results [418, 443].

3.3.1 Fluid Dynamics During Ignition and Combustion

Modeling of the fluid dynamics during ignition and combustion aims at reproducing the experimental conditions as well as possible and keeping the numerical complexity low to a reasonable extent. The simulation is transient, the domain is stationary, thermal energy is selected for the heat transfer model, and finite rate chemistry is employed for the combustion model. However, neither a buoyancy model is needed as a result of microgravity nor a turbulence model due to laminar conditions. Since the selection of an upwind differencing scheme (UDS) did not result in a significant improvement of stability when increasing time discretization, the CFX®-specific high resolution scheme was finally adopted for advection. The transient terms were computed with a second-order backward Euler scheme and an implicit time discretization. The residual target was defined at 1×10^{4} (RMS) in the basic solver control settings, and an optimized time step size of 3×10^{-5} s was used with a maximum of 15 coefficient loops (inner iterations). The Lewis number (*Le*) is chosen as unity for this CFD study, assuming simple molecular transport with identical values of thermal and mass diffusivity (Eq. (3.10)) [21, 22, 443]:

$$Le \equiv \frac{\alpha}{D} = \frac{k}{\rho\, c_p D} = 1. \tag{3.10}$$

The droplets are modeled as spherical volumetric sources of vaporized (gaseous) fuel. Thus, the liquid phase is modeled only indirectly, and one could speak of a substitution by “imaginary” droplets, occupying the volume of the corresponding real droplets in the ordinary gas phase domain. Figure 3.21 illustrates the modeling approach. The fuel source diameter decreases due to vaporization, as indicated by the time-dependent diameter $D(t)$. At simulation start, it coincides with the sphere of radius r_1: $D(t_0) = 2r_1$. In order to model the gradual shrinkage, three user FORTRAN routines were included in the CFX® solution process. They are called by the CFX® solver through a source code interface and individually calculate the remaining droplet masses after each time step according to Equation (3.11), subtracting the fuel amount Δm_v^n that vaporized during the current time step n from the

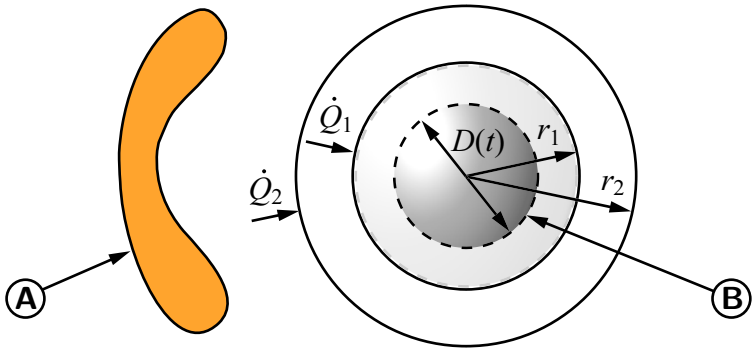

Figure 3.21: Model of Heat Transfer to Droplet Surface. The diameter $D(t)$ of the fuel source is a function of time and part of the numerical solution. The two spheres of the constant radii r_1 and r_2 are employed for the calculation of the heat transfer to the imaginary droplet. **A**: area of heat release, **B**: spherical volumetric source of vaporized fuel (i.e. extension of "imaginary" droplet).

fuel mass m^{n-1} of the previous time step $(n-1)$. In contrast to user CEL (CFX® expression language) functions, user junction box routines allow a defined execution of user-specified routines and are chosen here on this account. The mass m of each droplet is stored as a single, integral value in an additional variable managed by the CFX® memory management system (MMS).

$$m^n = m^{n-1} - \Delta m_v^n \tag{3.11}$$

The fuel amount Δm_v^n is determined from the averaged mass flow $\dot{m}_v$ due to vaporization, which is based on Fourier's law and the given heat of vaporization Δh_v. Equation (3.12) is valid, implying the absence of any heat sources as well as a negligible variation of heat capacity c_p between the two end points of the temperature gradient $\frac{\Delta T}{\Delta r}$, r_1 and r_2 (Fig. 3.21) [443]:

$$\lambda A \frac{\Delta T}{\Delta r} \equiv \dot{m}_v \Delta h_v = \dot{Q}_v. \tag{3.12}$$

A single-step reaction scheme of Westbrook and Dryer [459] for $C_{10}H_{22}$ is employed to model combustion (Eq. (3.13)), where the reaction rate is expressed in $\mathrm{mol\,cm^{-3}\,s^{-1}}$. It is comprised of an activation energy of $E_a = 1.255\times10^5\,\mathrm{J\,mol^{-1}}$, a pre-exponential factor of $A = 3.8\times10^{11}\,(\mathrm{mol/cm^3})^{(1\text{-}m\text{-}n)}/\mathrm{s}$, and the concentration exponents $m = 0.25$ and $n = 1.5$:

$$\frac{d[C_{10}H_{22}]}{dt} = A\,\exp\left(-\frac{E_a}{R\,T}\right)[X_{C_{10}H_{22}}]^m[X_{O_2}]^n. \tag{3.13}$$

As exhaust gas sampling is not yet relevant in this first part of the CFD study (cf. Chap. 3.3.2), the sample probes are implemented as a wall with an isothermal, no-slip boundary condition, similar to the regular combustion chamber walls. The open area at the bottom of the combustion chamber is modeled by an opening in order to allow a bidirectional gas exchange with the environment. Special subdomains are created for the fuel sources (droplets) and the area of heat release (ignition wire). The area of the fuel sources and their surroundings is meshed by spheres, using multiple nested O-grids for each fuel source. The O-grids provide a refined mesh, and thus improved heat and mass transfer. The innermost O-grid in each case matches the inner sphere of Figure 3.21, has the radius of $r_1 = 0.75\,\mathrm{mm}$, and is discretized by 17 cells. Accordingly, r_2 allocates the second O-grid. It is separated only one cell and 0.05 mm from the inner sphere. The zone of heat release (ignition) is schematically included in Figure 3.21 and colored orange (**A**). Both fuel sources and zone of heat release are realized by step functions within their particular subdomain using CEL, which allows temporal, spatial, and conditional control. Each fuel source is patched with a spatially uniform temperature that is the wet-bulb temperature of $C_{10}H_{22}$ associated with the actual temperature $T_{r_1}(t)$ at the respective inner sphere. The relevant correlation was assessed beforehand by the heat and mass transfer model of Spalding [418] for ambient temperatures in the range of 300 to 1000 K and is provided as a polynomial fit function within a separate CEL expression for each fuel source [418, 453]. Thus, the model is also capable of reproducing the transient heating process of each fuel source, i.e. fuel droplet. In summary, the final computational domain of this combustion simulation consists of a structured hexahedral mesh of 1 353 992 elements. Parallel computing with up to 8 CPUs was performed to reduce the overall simulation time. Time-stepping was optimized, obtaining a final time step size of $3\times10^{-5}\,\mathrm{s}$ and convergence within the seventh coefficient loop in approximately 90 % of the time steps.

Since the software package CFX® 11.0 does not include the thermophysical properties of $C_{10}H_{22}$ by default, a new data set for gas-phase combustion was integrated in the software libraries. Data sources were the NIST Chemistry WebBook [311] and the VDI Wärmeatlas [453]. Particularly the VDI Wärmeatlas provides instructions for the calculation of the dynamic viscosity η in Pa s, specific heat capacity c_p in $\mathrm{J\,kg^{-1}\,K^{-1}}$, and thermal conductivity λ in

$\mathrm{W\,m^{-1}\,K^{-1}}$. All these property values refer to the gaseous state, as liquid fuel is not part of this CFD simulation.

Figure 3.22 illustrates the temporal evolution of the combustion process during the initial second, starting from ignition. Left and right side of the figure depict the vertical middle plane of the combustion chamber with $z = 0\,\mathrm{mm}$ (cf. Fig. 3.7). The left side shows the temperature profile in the gaseous phase with the five fuel sources being the locations of the lowest temperatures, whereas the right side shows the velocity field indicated by the absolute velocity $|v| = (v_x^2 + v_y^2 + v_z^2)^{\frac{1}{2}}$. The velocity vector of the flow is visualized by white streamlines. Being the main subject of this first part of the CFD study, the discharge of hot exhaust gas from the open bottom of the combustion chamber by convection is clearly indicated by the evolution of the temperature and velocity fields. This process is particularly responsible for the temperature field becoming more and more asymmetric along the axis of the droplet array. Here, the initial time ($t = 0\,\mathrm{s}$) is defined as the time when ignition is enforced by the implemented heat release mechanism. Ignition of the first droplet occurs at $t = 29\,\mathrm{ms}$ with a local temperature rise to 2118 K. Starting from this local kernel, the flame front propagates along the flammable gas layer, forming a spherical flame around the fuel source. At $t = 0.2\,\mathrm{s}$, the flame ball around the first fuel source is fully developed and a temperature of $T = T_{\max} = 2515\,\mathrm{K}$ is indicated. Subsequently, the flame spreads from fuel source to fuel source (Fig. 3.22, from left to right). At $t = 0.4\,\mathrm{s}$, the fourth droplet is ignited but not yet enclosed by the flame. The ensuing flame propagation and volume expansion due to combustion are clearly observable in combination with the contour plot of absolute velocity $|v|$. At $t = 0.6\,\mathrm{s}$, all fuel sources are ignited and the flame stabilizes at a high burning rate k. Still, a small eddy of unburned air prevails in the upper right corner of the droplet array holder before it dissipates around $t = 0.8\,\mathrm{s}$. It is a consequence of flame propagation towards the "cold, metallic containment" of the droplet array holder. Finally, the highest velocities within the combustion chamber are observed at the opening in the vicinity of the vertical props with $|v|_{\max} = 0.595\,\mathrm{m\,s^{-1}}$ at $t = 0.6\,\mathrm{s}$. After ignition of the fourth and fifth fuel source, the flow field becomes uniform, as underlined by the white streamlines.

The utilized single-step mechanism of Westbrook and Dryer [459] can inherently only be an approximation, as it is trimmed mainly to predict correct flame speeds S_L. Thus, it is subject to some restrictions: At flame temperatures

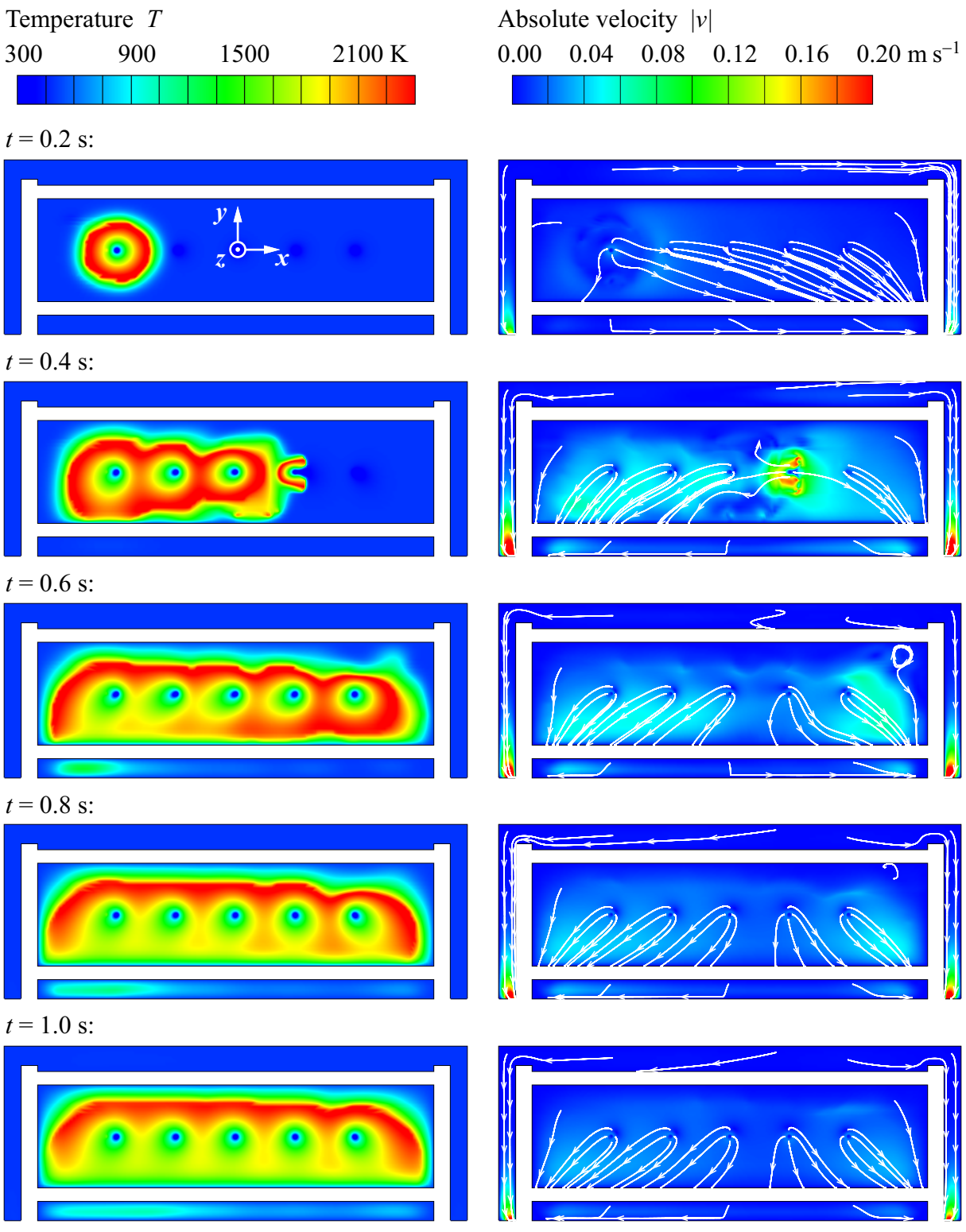

Figure 3.22: Transient Combustion Process in a Geometric Model of the Combustion Chamber Computed with CFD. The middle plane is shown with $z = 0$ mm. Time $t = 0$ s corresponds to the start of heat release (i.e. enforced ignition). Left: temperature distribution ($T_{max} = T(t{=}0.2\,\text{s}) = 2515\,\text{K}$); right: velocity profile of absolute velocity with selected streamlines ($|v|_{max} = |v|(t{=}0.6\,\text{s}) = 0.595\,\text{m s}^{-1}$).

of typical hydrocarbon fuels of approximately 2000 K, substantial amounts of CO and H_2 exist in equilibrium with CO_2 and H_2O. However, by assuming that CO_2 and H_2O are the only combustion products, the total heat of production is overpredicted. This effect was pointed out by the authors of the mechanism [459], and it is illustrated in Figure A.1 for $C_{10}H_{22}$. Here, the temperature difference in the flame and post-flame zone adds up to 170 K, comparing the single-step mechanism used with the detailed kinetics of Zhao et al. [474]. Consequently, the results of this first numerical simulation may only be consulted for a first estimate of flame spread and are not suitable for any quantitative NO_x studies, such as those involving NO_x post-processing. In addition, there are significant heat losses in the physical experiment due to radiation that are not accounted for within this basic CFD study. In this respect, a rough estimate of the real temperature rise due to combustion can be derived from the measurement readings plotted in Figures D.1 through D.3. Despite the thermocouple positions some distance away from the flame zone and the inertia of the system, the temperature increase observed remains low. Consequently, as expected, there is a noticeable difference between physical experiment and the CFD study. Furthermore, Figure 3.22 clearly illustrates the fluid flow through the combustion chamber opening. In contrast to the present design, an idealized combustion chamber setup would foresee symmetry so that an even exhaust gas distribution could be maintained throughout the combustion process. However, this obvious design recommendation was beyond the scope of this design study.

3.3.2 Fluid Dynamics During Exhaust Gas Sampling

The second relevant gas exchange process of the combustion chamber is the exhaust gas sampling itself, where evacuated sample cylinders collect the combustion products. Position and orientation of the related sample probes inside the combustion chamber are important here, in particular in combination with the individual sampling approach for every single combustion run. Therefore, four symmetrically aligned probes were defined in the experiment specifications to allow a spatially uniform gas collection from the combustion chamber. The probe orifices were positioned as close as possible to the combustion zone, which facilitated a direct collection of the combustion products. Nevertheless, the ensuing gas exchange is even more complex than the one

due to combustion discussed above. On the one hand, gas is extracted from the combustion chamber through the sample probes, and on the other hand, "fresh" air is entrained from outside through the opening in the bottom of the combustion chamber [293].

In order to clarify and quantify the fluid dynamics of the sampling process in the combustion chamber, a second CFD study was conducted. Due to the preceding combustion process and the implemented trigger logic (Fig. 3.20), flame extinction and homogenization of the combustion products within the volume of the combustion chamber is presumed for the start of exhaust gas sampling in a first estimate. In reality, however, some pockets of fresh, unconsumed air remain, for instance, in the corners of the combustion chamber. Still, this CFD study was conducted independently of the solution of the previous study on combustion. As the sampling process itself also aims at avoiding contamination effects due to fresh air entrainment, the numerical results were used in an iterative optimization of the probe locations by minimizing the amount of fresh air collected. Negative effects are possible for the succeeding exhaust gas analysis if high amounts of fresh air are collected as a consequence of direct jets between the open bottom of the combustion chamber and the sample probes. Other negative effects are possible if the probes are arranged either too close to or too far from the combustion zone. Furthermore, the fresh air content calculated was used as a verification value in the correction procedure for the dilution of the physical gas samples, which is a crucial step in post-processing of the gas analysis. The additional variable χ is introduced for this purpose into the CFD model, monitoring the local volume fraction of fresh air. At the start of exhaust gas sampling ($t = 0\,\mathrm{s}$), it takes the value zero for the whole combustion chamber, whereas it tends to one for pure fresh air from outside the combustion chamber.

The numerical model of this second process is similar to the above CFD model used on the combustion process. However, as no modeling of vaporization and combustion is needed here, it is simplified in several aspects, which reduces the requirements for computational power. Additionally, symmetry is implemented as a boundary condition in the longitudinal middle plane ($z = 0\,\mathrm{mm}$) of the combustion chamber, the plane as shown in Figure 3.22. Consequently, only two sample probes are part of this second numerical domain. The boundary condition for the gas extraction through the sample probes is realized in CEL by the temporal specification of mass flow (down-

stream of the probe orifices in the plane that is flush with the combustion chamber ceiling). It is driven by the pressure gradient between the evacuated sample cylinder and the isobaric combustion chamber. To provide the necessary input for this boundary condition, the total time of the gas sampling process $\Delta t_{\text{sampling}}$ was empirically determined by hardware tests, but the remaining parameters could be derived from gas dynamics. Choked flow is assumed downstream of the physical probe orifices, where the four probes are fitted to one piping joint. The fluid properties in the combustion chamber are expected to be homogeneous everywhere and are equal to the stagnation properties, denoted by the subscript zero [224, 396]. Thus, sonic (critical) conditions are reached at the "throat" of the piping. They are denoted by an asterisk. Employing the ratio of specific heats of a gas,

$$\kappa \equiv \frac{c_p}{c_v}, \tag{3.14}$$

where

$$c_p = \frac{\kappa}{\kappa - 1} R, \quad c_v = \frac{1}{\kappa - 1} R, \quad \text{and} \quad R = c_p - c_v, \tag{3.15}$$

critical temperature T^* and critical pressure p^* can be calculated via the isentropic relations of Equations (3.16) and (3.17), respectively. As a first estimate, $\kappa = 1.4$ is applied here, as generally valid for diatomic gases.

$$\frac{T^*}{T_0} = \frac{2}{\kappa + 1} \tag{3.16}$$

$$\frac{p^*}{p_0} = \left(\frac{2}{\kappa + 1} \right)^{\frac{\kappa}{\kappa - 1}} \tag{3.17}$$

Introducing the definition of the speed of sound for a perfect gas, the one-dimensional continuity equation for steady flows gives:

$$\dot{m}^* = p^* A^* \left(\frac{\kappa}{R\, T^*} \right)^{\frac{1}{2}}. \tag{3.18}$$

Everything but the throat area A^* is given, which is derivable from the total sampling time $\Delta t_{\text{sampling}}$ and the sampling time under critical conditions Δt^* using a goal seek function. The time Δt^*, in turn, can be obtained from the total mass collected during critical flow (Eq. (3.19)) and the sample temperature

T_{sample} after its isentropic expansion into the sample cylinder. The latter correlation is derived from the first law of thermodynamics by using Equation (3.20) and assuming an adiabatic sample cylinder, which is justified due to the short duration of the sampling process [224, 322, 396, 419].

$$m_{\Delta t^*} = \frac{p^* V_{\text{sample}}}{R\, T_{\text{sample}}} \tag{3.19}$$

$$\kappa = \frac{T_{\text{sample}}}{T_{\text{piping}}} \tag{3.20}$$

Finally, the throat area A^* can be attained including its respective diameter $D_{A^*} = 0.73\,\text{mm}$. This value is well below the physical pipe diameter of $D_i = 2.16\,\text{mm}$ but confirms the expectations towards boundary layer thickening and local flow separation [389].

Figure 3.23 illustrates the gas sampling process modeled with the total mass flow $\dot{m}$ implemented as an outlet boundary condition. The mass flow of fresh air through the same outlet is shown, too. It is a function of the fluid dynamics

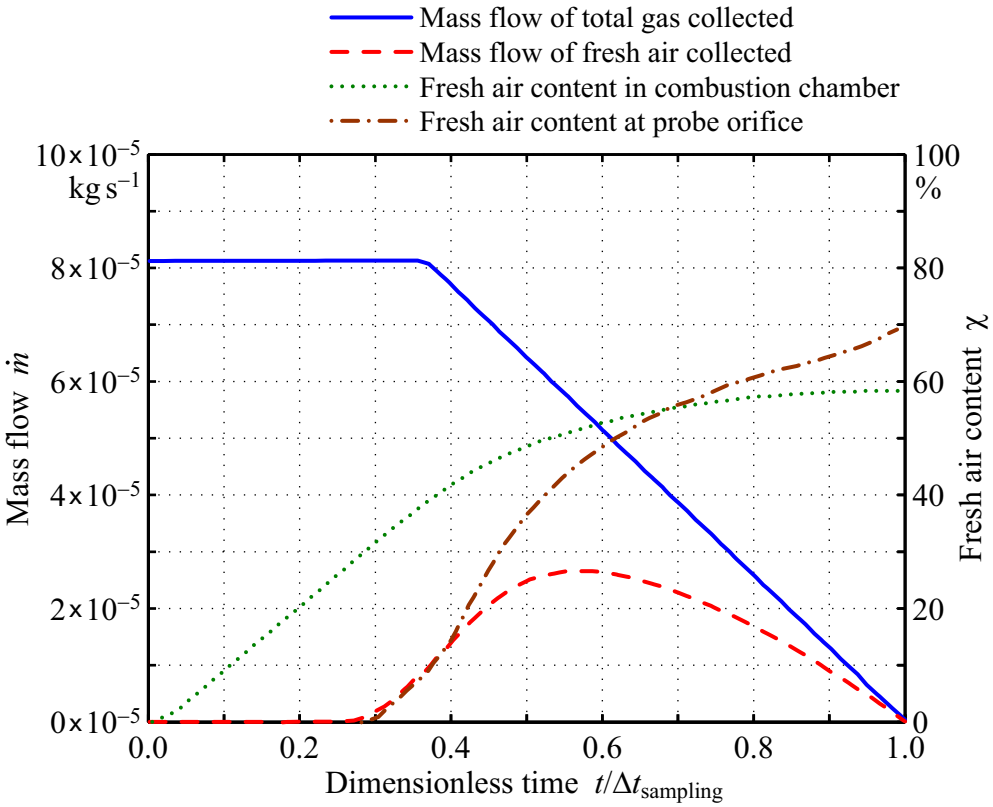

Figure 3.23: Evolution of Fresh Air Content During Gas Sampling.

of the combustion chamber and the total mass flow given as an outlet boundary condition. Moreover, it approaches the total mass flow at a late stage of the sampling process, which is a positive indication of having found a favorable combination of combustion chamber volume, sample volume, and probe layout. Furthermore, the fresh air content χ is also shown in Figure 3.23. It is a measure of air entrainment into the combustion chamber due to exhaust gas sampling and does not include "unconsumed" air that was already present in the combustion chamber before the start of exhaust gas sampling. After 68 % of the sampling time and having collected 88 % of the total mass of the gas sample, the local fresh air content at the probe orifice rises above the fresh air content averaged for the whole combustion chamber. Nevertheless, the final gas sample comprises 81 % of gas as present in the combustion chamber after termination of the combustion process, and only 19 % of fresh air.

Figure 3.24 shows contours of the sampling process by highlighting the fresh air content χ. The coordinate system is identical to Figures 3.7 and 3.22. Four parallel planes are depicted (z = 0, 4, 8, and 12 mm). The color blue (χ = 0.0) indicates "combustion gases" that were present in the combustion chamber before the initiation of the sampling process, whereas the color red (χ = 1.0) stands for fresh air. Time t = 0 s corresponds to the start of exhaust gas sampling. For the first time steps ($t/\Delta t_{\text{sampling}} < 0.3$), the gas collection is indirectly observable by the rise of fresh air through the open bottom of the combustion chamber. It consecutively replaces the sampled exhaust. After $t/\Delta t_{\text{sampling}} = 0.3$ and having collected 44 % of the total mass, the first fresh air is indicated inside the sample probes (cf. Figs. 3.23 and 3.24). White streamlines additionally visualize the flow field in the plane of the sample probes (z = 12 mm).

The flow regime within the combustion chamber, and in particular in the critical regions of opening (i.e. the remaining gap at the bottom of the combustion chamber) and outlet (i.e. the gas sample probes), may be characterized by the Reynolds number according to Equation (3.21). On the one hand, the opening is critical due to its geometry and the main flow of fresh air that is oriented in inwards. Here, the Reynolds number can be calculated using the kinematic viscosity of air at ambient conditions of $\nu = 15 \times 10^{-6}\,\mathrm{m^2\,s^{-1}}$ and the hydraulic diameter D_h, as stated in Equation (3.22) with the cross-sectional area A and its wetted perimeter Π. On the other hand, the outlet is critical in respect of a

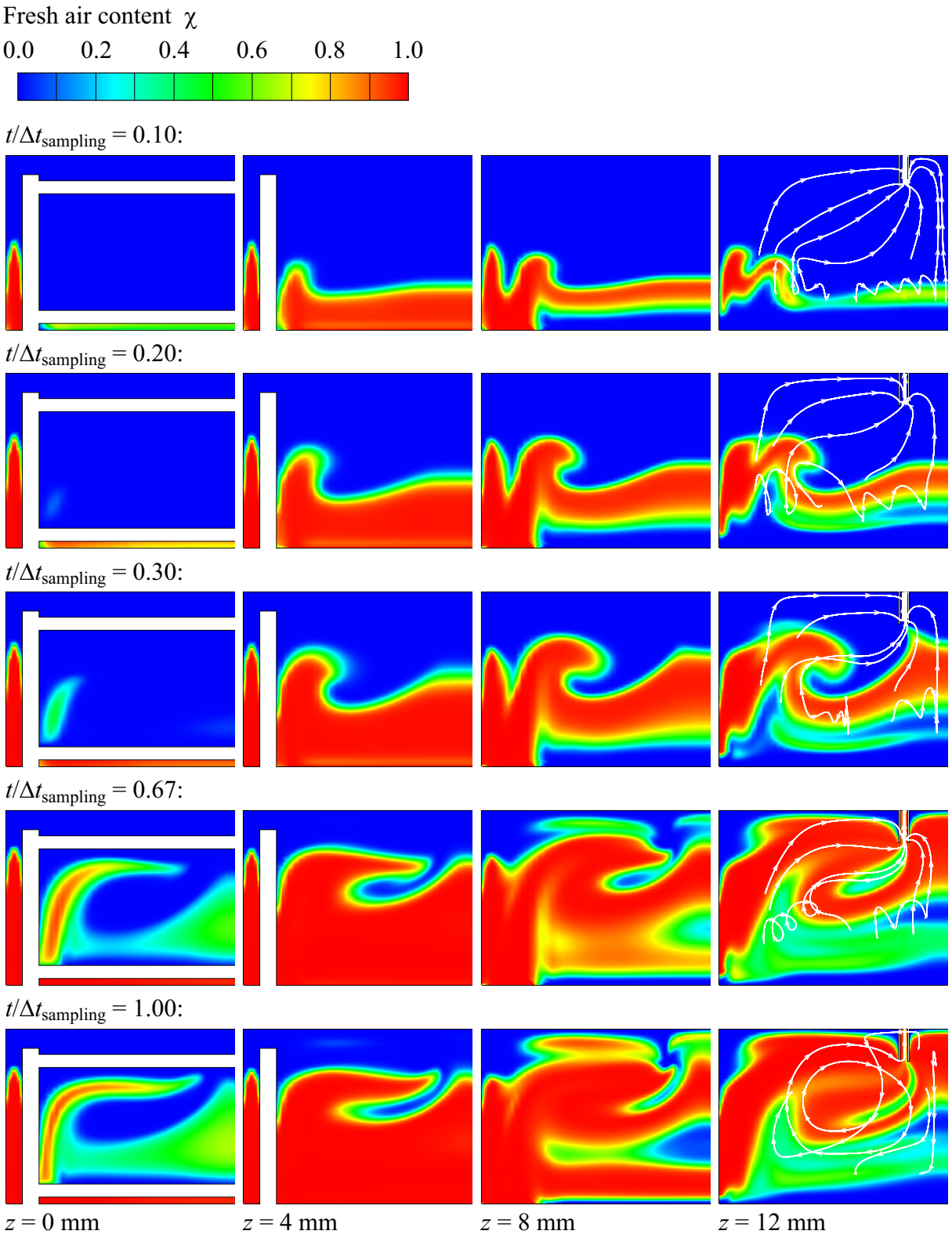

Figure 3.24: Transient Gas Sampling Process in a Geometric Model of the Combustion Chamber Computed with CFD. Here, a set of half views is shown for different time steps (from top to bottom). The views are parallel to the middle plane of the combustion chamber (from left to right).

high flow velocity v (with $|v|_{\max} = 14.75\,\mathrm{m\,s^{-1}}$). For the round tube of the sample probes used, the hydraulic diameter simplifies as $D_h = D_i$ [189, 396, 453]:

$$Re = \frac{v\,D_h}{\nu}, \tag{3.21}$$

$$D_h = 4\,\frac{A}{\Pi}. \tag{3.22}$$

The Reynolds number calculates to $Re = 67$ for the opening and to $Re = 670$ to 830 for the outlet, depending on the varying gas composition and temperature caused by the fresh air entrainment. In either case, it is well below the critical Reynolds number for the respective type of geometry of $Re_{\mathrm{opening,crit}} = 1100$ and $Re_{\mathrm{outlet,crit}} = 2300$, as stated by Sigloch [396]. Consequently, laminar flow can be assumed for the whole combustion chamber, and, in summary, Figures 3.24 and 3.23 reveal that the probe arrangement was specified to allow a spatially and temporally smooth exhaust gas sampling.

4 Numerical Modeling and Simulation

Numerical simulations of single droplets were conducted in order to complement the experimental findings of this study (cf. Figs. 1.1 and 1.2). Particularly, the physical and chemical mechanisms promoting NO_x emissions were systematically investigated including a configuration to elucidate the effect of partial droplet pre-vaporization. Therefore, an approach for modeling and simulation of NO_x generation in the gas phase surrounding single burning droplets is presented.

Presuming spherical symmetry, with no gravity and no forced convection, the governing equations are derived first. Then, the essentials of forced droplet ignition by an external energy source are introduced. Special attention is given to the modeling of NO_x formation, as the numerical work focuses on the adequate combination of detailed chemistry and the pre-vaporization process as well as droplet combustion in hot exhaust gas. Both are technically relevant in liquid fuel combustion. Simplifications are introduced and shown to be appropriate. The model is validated, and finally the portability of the results from the one-dimensional, spherically symmetric model to more complex droplet arrays and cluster regimes is evaluated (Fig. 1.1).

4.1 Description of Involved Processes

The main phenomena characterizing droplet combustion are transport of heat and mass as well as chemical reaction [443, 461]. A description of the combustion in flows is, therefore, based upon fluid mechanics coupled with the conservation laws of thermodynamics, including particular transport phenomena of heat and mass transfer. Typical ways to describe droplets in a continuous phase are the Euler-Lagrange and Euler-Euler methods. However, as the droplets given are presumed to be at rest, both approaches are identical, and it is not necessary to differentiate here. Still, the liquid phase of the droplet

and the gaseous phase surrounding the droplet must be treated separately but coupled at the phase interface of the droplet [65, 297, 298].

This numerical study brings together subjects such as droplet vaporization, ignition, combustion, and exhaust gas formation. The first issue is to employ an adequate physical model for the transport processes. The second issue is to model the NO_x formation correctly and in sufficient detail. Combinations of $C_{10}H_{22}$ mechanisms and well-established NO_x kinetics were evaluated for their applicability in the previous Chapter 2.3 for this purpose. Each sub-model employed had already been tested and validated for itself by the research group that introduced it in the first place. Nonetheless, all sub-models were retested and revalidated. The combination of the sub-models is new and a unique feature of this work. Moreover, refinements and adjustments are implemented, but basically no new sub-model is proposed within the numerical scope of this thesis.

In line with the experiments conducted, $C_{10}H_{22}$ is used as a model fuel in the calculations here because its properties of combustion are similar to those of kerosene and diesel fuel. The number of species involved is reduced to 86 species with 641 reactions for the hydrocarbon main mechanism in addition to 14 species and 52 reactions for the NO_x chemistry. Generally, the total number of species and reactions are decisive criteria when choosing a mechanism, apart from accuracy and range of validity. Therefore, it is shown that those moderately extensive reaction kinetics can be handled in combination with the single droplet model without requiring excessive computational effort [297, 298].

4.2 Basics for Numerical Modeling

Starting with fundamental mathematics and thermodynamics, a set of conservation equations for multi-component reacting flows is developed. This set of equations is closed applying kinetic gas theory and chemical reaction kinetics. Finally, boundary and interface conditions are stated. The major objective is to show and quantify the influence of the different physical/chemical variables and to derive the structure of the equations [31, 45, 180, 277, 297, 298, 362–365].

4.2.1 Governing Equations for Reacting Flows

In the following discussion, the indices i and j specify Cartesian coordinates, and Einstein notation is used with them by summing over all their possible values. The radial direction has the index r, which is used together with the spherical coordinates φ and θ after coordinate transformation of the conservation equations. The indices m and n are used to indicate (different) species or phase components. There is no summation convention automatically used with them.

The continuum assumption is considered to be valid with a Knudsen number $Kn \ll 1$. Thus, the fluid can be regarded as a continuous composition of fluid elements of the mass dm and the volume dV. Furthermore, each species behaves like a continuum with the partial density ρ_m and velocity $u_{m,i}$.

The phenomenon of species diffusion in multi-component mixtures can be described by splitting up the species velocity vector $u_{m,i}$ into two parts:

$$u_{m,i} = u_i + \Delta u_{m,i}, \tag{4.1}$$

where u_i is the bulk velocity, which corresponds to the velocity in a single component flow, and $\Delta u_{m,i}$ is the diffusion velocity, from which additional terms for multi-component flows originate [45, 180, 277]. The bulk velocity is the sum of the mass-weighted species velocities according to Equation (4.2):

$$u_i \equiv \sum_{m=1}^{N} \frac{\rho_m}{\rho} u_{m,i} = \sum_{m=1}^{N} \left(\frac{\rho_m}{\rho} u_i + \frac{\rho_m}{\rho} \Delta u_{m,i} \right) = u_i + \underbrace{\sum_{m=1}^{N} \frac{\rho_m}{\rho} \Delta u_{m,i}}_{=0}. \tag{4.2}$$

As a consequence of Equation (4.2), the sum over the weighted diffusion velocities has to be zero. In contrast to vector components, no summation over the index m is automatically implied here as it represents different species. Consequently, the governing equations for multi-component flow can be calculated as a sum of the conservation equations for the individual species [147, 277]. Molecular gas kinetics accounts for the interaction of species.

A set of differential equations in spherical coordinates – to be exact in the radial coordinate r – is obtained. Due to the assumption of spherical symmetry, only derivatives in time t and radius r are left over. External forces like gravity

are neglected. Here, the species in multi-component mixtures are quantified as mole fractions X_m or as mass fractions Y_m. Specific heat at constant pressure in J kg^{-1} K^{-1} is referenced by c_p, standard enthalpy of formation in J kg^{-1} by h_m^0 (at reference temperature T_0), and dynamic viscosity in Pa s by η. $\dot{\omega}_m$ denotes the net production rate of species m and serves as a source term in the species conservation equation, whereas $\dot{q}$ is the specific heat flux in W m^{-2}. Hence, mass conservation can be written as

$$\frac{\partial \rho}{\partial t} + \frac{\partial \rho u_r}{\partial r} + 2\frac{\rho u_r}{r} = 0, \tag{4.3}$$

conservation of species is given by

$$\rho \frac{\partial Y_m}{\partial t} + \rho u_r \frac{\partial Y_m}{\partial r} + \frac{\partial \rho Y_m \Delta u_{m,r}}{\partial r} + 2\frac{\rho Y_m \Delta u_{m,r}}{r} = \dot{\omega}_m, \tag{4.4}$$

the momentum equation yields

$$\begin{aligned} &\rho \frac{\partial u_r}{\partial t} + \rho u_r \frac{\partial u_r}{\partial r} \\ &= -\frac{\partial p}{\partial r} + \frac{\partial \eta}{\partial r}\left(\frac{4}{3}\frac{\partial u_r}{\partial r} - \frac{4}{3}\frac{u_r}{r}\right) + \eta\left(\frac{4}{3}\frac{\partial^2 u_r}{\partial r^2} + \frac{8}{3}\frac{1}{r}\frac{\partial u_r}{\partial r} - \frac{8}{3}\frac{u_r}{r^2}\right), \end{aligned} \tag{4.5}$$

and the energy equation is

$$\begin{aligned} &\rho \frac{\partial \sum_m Y_m \int_{T_0}^{T} c_{p,m} dT}{\partial t} + \rho u_r \frac{\partial \sum_m Y_m \int_{T_0}^{T} c_{p,m} dT}{\partial r} \\ &= -\frac{\partial \sum_m \rho Y_m \int_{T_0}^{T} c_{p,m} dT \Delta u_{m,r}}{\partial r} - 2\frac{\sum_m \rho Y_m \int_{T_0}^{T} c_{p,m} dT \Delta u_{m,r}}{r} \\ &\quad - \sum_m \dot{\omega}_m h_m^0 + \frac{\partial p}{\partial t} + u_r \frac{\partial p}{\partial r} + \eta\left[\frac{4}{3}\left(\frac{\partial u_r}{\partial r}\right)^2 - \frac{8}{3}\frac{u_r}{r}\frac{\partial u_r}{\partial r} + \frac{4}{3}\left(\frac{u_r}{r}\right)^2\right] \\ &\quad - \frac{\partial \dot{q}_r}{\partial r} - \frac{2}{r}\dot{q}_r. \end{aligned} \tag{4.6}$$

This set of equations is not closed. The species velocity difference $\Delta u_{m,r}$, net production rate $\dot{\omega}_m$, and heat flux $\dot{q}_r$ are unknown. Pressure p is related to temperature T and density ρ in the ideal gas law.

4.2.2 Transport Mechanisms in the Gas Phase

The species velocity difference $\Delta u_{m,r}$ (i.e. the diffusion velocity) and the radial heat flux $\dot{q}_r$ can be derived from molecular gas kinetics [169, 180, 213], which is based on population dynamics. The distribution function

$$f_m(\mathbf{x}, \mathbf{v}_m, t) \tag{4.7}$$

is the number of molecules of species m per volume at position $\mathbf{x}$ with the velocity vector $\mathbf{v}$ at time t. The bulk velocity

$$\mathbf{u}(\mathbf{x}, t) = \frac{\sum_n m_n \int f_n(\mathbf{x}, \mathbf{v}_n, t)\, \mathbf{v}_n \, d\mathbf{v}_n}{\sum_n m_n \int f_n(\mathbf{x}, \mathbf{v}_n, t) \; d\mathbf{v}_n} \tag{4.8}$$

is calculated from the distribution function f_n, with m_n denoting the mass of one molecule of species n. f_m and f_n are used similarly; the only difference is the name of the species – namely m or n. Thus, the species velocity is given by

$$\mathbf{u}_m(\mathbf{x}, t) = \frac{\int f_m(\mathbf{x}, \mathbf{v}_m, t)\, \mathbf{v}_m \, d\mathbf{v}_m}{\int f_m(\mathbf{x}, \mathbf{v}_m, t) \; d\mathbf{v}_m}. \tag{4.9}$$

Note that $\mathbf{v}_m$ is the coordinate in the space-velocity frame, not the mean velocity of species m.

After some rearranging [180], the diffusion velocity $\Delta u_{m,i}$ can be calculated from Equation (4.9), with the bulk velocity u_i in m s^{-1}, the velocity coordinate $v_{m,i}$ in m s^{-1}, the species density n_m in m^{-3}, and the relation $\rho = \sum_m n_m m_m$. Employing $\Delta u_{m,i}$ of Equation (4.10) to the energy (or heat flux) conservation equation and to the species conservation equation, it accounts for the Dufour and Soret effect, respectively. Both second-order effects are included in the general derivations of this section but will be neglected in the final model, as outlined in Chapter 4.5.

$$\begin{aligned} \Delta u_{m,i} &= \frac{1}{n_m} \int \left(v_{m,i} - u_i\right) f_m \, dv_{m,i} = \frac{1}{n_m} \int \Delta v_{m,i} \; f_m \, d\Delta v_{m,i} \\ &= \left(\frac{n^2}{n_m \rho}\right) \sum_n m_n \, \widetilde{D}_{mn} \, d_{m,i} - \frac{D_m^T}{n_m m_m} \frac{\partial \ln T}{\partial x_i} \end{aligned} \tag{4.10}$$

The gradients in molar fraction $X_m = n_m / n$ and in pressure p are summarized as vector $d_{m,i}$ according to Hirschfelder et al. [180] (see Eq. (4.11)). If the sys-

tem is maintained at constant temperature and pressure, there are no external forces acting on the molecules, and diffusion takes place in one direction only.

$$d_{m,i} = \frac{\partial n_m / n}{\partial x_i} + \left(\frac{n_m}{n} - \frac{n_m m_m}{\rho} \right) \frac{\partial \ln(p)}{\partial x_i} \tag{4.11}$$

The thermal diffusion coefficient is denoted as D_m^T and the multi-component diffusion coefficients as $\widetilde{D}_{mn}$. By summing Equation (4.10) for all species n with $n \neq m$, a linear system of $(n-1)$ equations is obtained:

$$\begin{aligned} &\sum_{n;n\neq m} \frac{n_n n_m}{n^2 D_{mn}} \left(\Delta u_{n,i} - \Delta u_{m,i} \right) \\ &= d_{m,i} - \frac{\partial \ln T}{\partial x_i} \sum_{n;n\neq m} \frac{n_m n_n}{n^2 D_{mn}} \left(\frac{D_n^T}{n_n m_n} - \frac{D_m^T}{n_m m_m} \right), \end{aligned} \tag{4.12}$$

which can be solved for the diffusion velocity $\Delta u_{m,i}$, with D_{mn} being the binary diffusion coefficient.

The heat flux

$$\dot{q}_i = -\lambda \frac{\partial T}{\partial x_i} + \frac{k_B T}{n} \sum_m \sum_{n;n\neq m} \frac{n_n D_m^T}{m_m D_{mn}} \left(\Delta u_{m,i} - \Delta u_{n,i} \right) \tag{4.13}$$

is obtained by a similar derivation, studying the transfer of kinetic energy by collisions [180]. The enthalpy flux due to $\Delta u_{m,i} \neq 0$ is part of the energy equation and not of the heat flux here (see Eq. (4.6), in which the sum of enthalpies is considered but not the mean enthalpy). However, some publications treat this convention in a different way [325, 461].

4.2.3 Basics on Reaction Kinetics

Due to the chemical reactions associated with the combustion process, source terms appear on the right hand side of the equations for species transport and energy (Eqs. (4.4) and (4.6)). An expression for the net production rate $\dot{\omega}_m$ of species S_m is found in reaction kinetics [19, 149, 443]. The chemical equation

$$\nu'_{11} S_1 + \nu'_{21} S_2 + \ldots \rightleftharpoons \nu''_{31} S_3 + \nu''_{41} S_4 + \ldots \tag{4.14}$$

expresses the reaction of species S_1 and S_2 to S_3 and S_4 and vice versa. Equation (4.14) typically is part of a whole set of reaction equations of the

number L with S_m and ν_{ml} representing the species name and the stoichiometric coefficient, respectively, of the m-th species in the l-th reaction equation. The stoichiometric coefficients indicate the number of moles reacting, and they are marked with one stroke ($'$) for reactants and two strokes ($''$) for products.

The net production rate $\dot{\omega}_m$ of a species is the sum of its forward and backward reaction rate, which in turn depend on the species molar densities $N_m = NX_m$ and the rate coefficients k_l^+ and k_l^-:

$$\dot{\omega}_m = \dot{\omega}_m^+ + \dot{\omega}_m^-. \tag{4.15}$$

The forward and backward reaction rates are given for species S_1 in Equation (4.14), expressed on a mass basis in $\mathrm{kg\,m^{-3}\,s^{-1}}$ owing to the molar mass M_{S_1}:

$$\dot{\omega}_{S_1}^+ = -M_{S_1} k_1^+ \left(\nu''_{11} - \nu'_{11}\right) \left(NX_{S_1}\right)^{\nu'_{11}} \left(NX_{S_2}\right)^{\nu'_{21}} \ldots \tag{4.16}$$

$$\dot{\omega}_{S_1}^- = +M_{S_1} k_1^- \left(\nu''_{11} - \nu'_{11}\right) \left(NX_{S_3}\right)^{\nu''_{31}} \left(NX_{S_4}\right)^{\nu''_{41}} \ldots \tag{4.17}$$

For elementary reactions, the exponents ν'_{ml} and ν''_{ml} in Equations (4.16) and (4.17) can be related to the elementary molecule collisions, and thus correspond to the coefficients in Equation (4.14). For global reactions, however, reaction rates are often determined empirically, and the exponents may differ significantly from the stoichiometric coefficients. This is the case, for instance, with the global kinetics of Duterque et al. [106], Hautman et al. [172], Jones and Lindstedt [199], and Westbrook and Dryer [459].

The rate coefficient

$$k_1^+ = A\, T^b \exp\left(-\frac{E_a}{R\,T}\right) \tag{4.18}$$

for the forward reaction of Equation (4.14) is given as a modified Arrhenius equation. The empirical law is a measure for the likeliness of collision and reaction. The pre-exponential factor A describes the likelihood of a collision of gas molecules, and the pre-exponential contribution to collision frequency due to temperature is represented by the power of T. The backward rate coefficient k_1^- could be determined similarly to Equation (4.18) but is deduced more easily and precisely from the constant of thermodynamic equilibrium as a minimum of the Gibbs function [149, 297, 298, 443, 461].

4.2.4 Boundary Conditions

Boundary conditions have to be applied in order to solve the coupled governing equations. In the case of a spherical setup with the droplet center in $r = 0$, boundary conditions are necessary in the center and at the radial coordinate $r \to \infty$ or a finite radius $r = R_\infty$ in the gas phase (Fig. 4.1).

For $r = 0$, in the liquid phase, boundary conditions follow from the requirements that the functions of the conservation equations should be spherically symmetric and twice continuously differentiable:

$$\left.\frac{\partial T}{\partial r}\right|_{r=0} = 0, \quad \left.\frac{\partial p}{\partial r}\right|_{r=0} = 0, \quad \left.\frac{\partial Y_m}{\partial r}\right|_{r=0} = 0, \quad \text{and} \quad u_r|_{r=0} = 0.$$

The zero gradient of the temperature T is necessary to avoid a heat sink or source in $r = 0$. The gradient of the species mass fraction Y_m is zero to conserve species, and the radial velocity u_r vanishes because of the conservation of mass [297, 298].

At the outer boundary of the gas phase ($r \to \infty$), boundary conditions must be given for temperature, pressure, and the mass fractions of all species. However, no condition is allowed for the radial velocity u_r here because the convective flow is directed outwards according to the calculation. Thus, the velocity $u_r|_{r\to\infty}$ is a result of the conservation of mass. Furthermore, if an adiabatic, closed system is studied, Neumann formulations must be used for temperature T and mass fraction Y_m at the outer boundary with:

$$\left.\frac{\partial T}{\partial r}\right|_{r\to\infty} = 0 \qquad \text{and} \qquad \left.\frac{\partial Y_m}{\partial r}\right|_{r\to\infty} = 0.$$

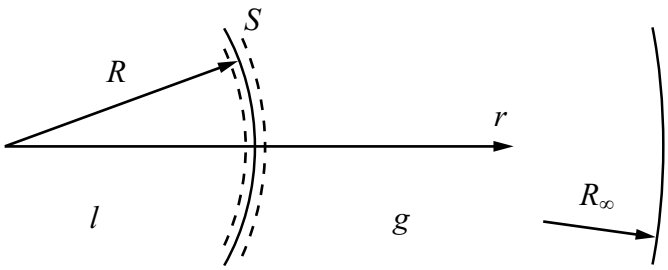

Figure 4.1: Schematic of One-Dimensional Droplet Model with Interface. The interface S links liquid droplet l and gaseous atmosphere g [297, 298].

Presuming the boundary is far enough away from the droplet and the main reaction zone, the boundary conditions may also be set to constant ambient conditions (Dirichlet formulations) according to Equations (4.19) through (4.21):

$$T|_{r\to\infty} = T_\infty, \tag{4.19}$$

$$p\big|_{r\to\infty} = p_\infty, \quad \text{and} \tag{4.20}$$

$$Y_m|_{r\to\infty} = Y_{m,\infty}. \tag{4.21}$$

4.2.5 Modeling of Gas-Liquid Interface

Conservation of mass, species, momentum, and energy is not only valid in the gas and liquid phase but also at the interface S of the two phases, as shown in Figure 4.1 [65]. The interface is presumed to be an infinitely thin layer. Its time-dependent position is denoted by $R(t)$ and its velocity by $u_{S,r}$ (Eq. (4.22)). The summation convention for the indices i and j, as introduced in Chapter 4.2.1, is also pursued in the following paragraphs.

$$u_{S,r} = \frac{\partial R}{\partial t} \tag{4.22}$$

The change in mass of the liquid droplet l is

$$\begin{aligned}\dot{m}_l &= \frac{d}{dt}\int_{V_l(t)} \rho_l \, dV_l = -\int_{S_l(t)} \rho_l \left(u_{l,i} - u_{S,i}\right) n_i \, dS_l \\ &= -4\pi R^2 \rho_l \left(u_{l,r} - u_{S,r}\right)\big|_{R=R(t)} = -4\pi R^2 \rho_l \left(u_{l,r} - \frac{\partial R}{\partial t}\right)\Big|_{R=R(t)}\end{aligned} \tag{4.23}$$

and the change in mass of the gas phase g

$$\begin{aligned}\dot{m}_g &= \frac{d}{dt}\int_{V_g(t)} \rho_g \, dV_g = -\int_{S_g(t)} \rho_g \left(u_{g,i} - u_{S,i}\right) n_i \, dS_g \\ &= 4\pi R^2 \rho_g \left(u_{g,r} - u_{S,r}\right)\big|_{R=R(t)} = 4\pi R^2 \rho_g \left(u_{g,r} - \frac{\partial R}{\partial t}\right)\Big|_{R=R(t)}.\end{aligned} \tag{4.24}$$

The term $u_{g,r}$ denotes the radial velocity in the gas phase g, and $u_{l,r}$ the velocity in the liquid phase l. As mass conservation is valid despite vaporization of the liquid droplet, the change of mass in the volume $V(t)$ has to be balanced

by a flow over the surface $S(t)$. The product $\rho u_{S,i}$ denotes the mass flux over the surface $S(t)$ due to variation of the surface $S(t)$ in time. Since no mass is stored in the interface, the total change of mass in the liquid and gas vanishes. Moreover, the ansatz for the conservation of species follows the one for the conservation of mass.

The governing equations for the conservation of momentum and energy make use of the shear stress tensor τ_{ij} [341]. The shear stress tensor in a Newtonian fluid in Cartesian coordinates in conjunction with the normal vector n_j on a spherical shell is:

$$\begin{aligned}
\tau_{xj} n_j &= \eta \cos\varphi \cos\theta \left(\frac{4}{3}\frac{\partial u_r}{\partial r} - \frac{4}{3}\frac{u_r}{r}\right), \\
\tau_{yj} n_j &= \eta \sin\varphi \cos\theta \left(\frac{4}{3}\frac{\partial u_r}{\partial r} - \frac{4}{3}\frac{u_r}{r}\right), \quad \text{and} \\
\tau_{zj} n_j &= \eta \sin\theta \left(\frac{4}{3}\frac{\partial u_r}{\partial r} - \frac{4}{3}\frac{u_r}{r}\right).
\end{aligned}$$

The momentum balance in x-direction at an infinitesimally thin interface element, at $r = R$, $\varphi = 0$, and $\theta = 0$, with thickness $\delta \to 0$ and volume $V \to 0$, gives

$$\begin{aligned}
&\frac{d}{dt}\int_{V(t)} \rho u_i \, dV \\
&= -\int_{S(t)} \rho u_i \left(u_j - u_{S,j}\right) n_j \, dS - \int_{S(t)} p n_i \, dS + \int_{S(t)} \tau_{ij} n_j \, dS + F_\sigma,
\end{aligned} \tag{4.25}$$

and thus

$$\begin{aligned}
&\rho_l u_{l,r}\left(u_{l,r} - u_{S,r}\right) + p_l - \eta_l \left(\frac{4}{3}\frac{u_{l,r}}{\partial r} - \frac{4}{3}\frac{\partial u_{l,r}}{r}\right) \\
&= \rho_g u_{g,r}\left(u_{g,r} - u_{S,r}\right) + p_g - \eta_g \left(\frac{4}{3}\frac{\partial u_{g,r}}{\partial r} - \frac{4}{3}\frac{u_{g,r}}{r}\right) + \frac{2\sigma_S}{R}.
\end{aligned} \tag{4.26}$$

F_σ are forces due to surface tension, and σ_S is the surface tension itself.

The energy balance at the interface element is calculated according to Equation (4.27), using the energy flow $\dot{E}_l$ in the liquid and $\dot{E}_g$ in the gas phase [200]. The respective changes of specific internal and kinetic energy are derived in line with the conservation of mass and momentum, and following

Equations (4.28) and (4.29). The interface area is denoted by A, and the energy stored in the interface due to surface tension σ_S is proportional to this area. Second order terms in the diffusion velocity $\Delta u_{m,r}$ are neglected.

$$\dot{E}_l + \dot{E}_g + \sigma_S \frac{dA}{dt} = 0 \tag{4.27}$$

The change in internal and kinetic energy in the liquid l is

$$\begin{aligned}
\dot{E}_l &= \sum_m \frac{d}{dt} \int_{V_l(t)} \rho_{l,m} \left(e_{l,m} + \frac{u_{l,m,i}^2}{2} \right) dV_l \\
&\approx -4\pi R^2 \rho_l e_l \left(u_{l,r} - u_{S,r} \right) - 4\pi R^2 \sum_m \rho_{l,m} e_{l,m} \Delta u_{l,m,r} \\
&\quad - 4\pi R^2 \rho_l \frac{u_{l,r}^2}{2} \left(u_{l,r} - u_{S,r} \right) - 4\pi R^2 p_l u_{l,r} \\
&\quad - 4\pi R^2 \sum_m p_{l,m} \Delta u_{l,m,r} + 4\pi R^2 u_{l,r} \eta_l \left(\frac{4}{3} \frac{\partial u_{l,r}}{\partial r} - \frac{4}{3} \frac{u_{l,r}}{r} \right) - 4\pi R^2 \dot{q}_{l,r},
\end{aligned} \tag{4.28}$$

and the energy balance in the gas phase yields

$$\begin{aligned}
\dot{E}_g &= \sum_m \frac{d}{dt} \int_{V_g(t)} \rho_{g,m} \left(e_{g,m} + \frac{u_{g,m,i}^2}{2} \right) dV_g \\
&\approx +4\pi R^2 \rho_g e_g \left(u_{g,r} - u_{S,r} \right) + 4\pi R^2 \sum_m \rho_{g,m} e_{g,m} \Delta u_{g,m,r} \\
&\quad + 4\pi R^2 \rho_g \frac{u_{g,r}^2}{2} \left(u_{g,r} - u_{S,r} \right) + 4\pi R^2 p_g u_{g,r} \\
&\quad + 4\pi R^2 \sum_m p_{g,m} \Delta u_{g,m,r} - 4\pi R^2 u_{g,r} \eta_g \left(\frac{4}{3} \frac{\partial u_{g,r}}{\partial r} - \frac{4}{3} \frac{u_{g,r}}{r} \right) + 4\pi R^2 \dot{q}_{g,r}.
\end{aligned} \tag{4.29}$$

Equations (4.28) and (4.29) applied to Equation (4.27) results in:

$$\begin{aligned}
&\rho_l h_l \left(u_{l,r} - u_{S,r} \right) + \sum_m \rho_{l,m} h_{l,m} \Delta u_{l,m,r} + \rho_l \frac{u_{l,r}^2}{2} \left(u_{l,r} - u_{S,r} \right) \\
&\quad + p_l u_{S,r} - u_{l,r} \eta_l \left(\frac{4}{3} \frac{\partial u_{l,r}}{\partial r} - \frac{4}{3} \frac{u_{l,r}}{r} \right) + \dot{q}_{l,r} \\
&= \rho_g h_g \left(u_{g,r} - u_{S,r} \right) + \sum_m \rho_{g,m} h_{g,m} \Delta u_{g,m,r} + \rho_g \frac{u_{g,r}^2}{2} \left(u_{g,r} - u_{S,r} \right) \\
&\quad + p_g u_{S,r} - u_{g,r} \eta_g \left(\frac{4}{3} \frac{\partial u_{g,r}}{\partial r} - \frac{4}{3} \frac{u_{g,r}}{r} \right) + \dot{q}_{g,r} + \frac{2\sigma_S}{R} u_{S,r}.
\end{aligned} \tag{4.30}$$

Finally, the interface S is located at the radial coordinate $r = R$ (cf. Fig. 4.1). Equilibrium is assumed between the liquid and the vapor phases of species m. As stated by Raoult's law (Eq. (4.31), left), the partial vapor pressure at the interface, $p_m(R)$, equals the vapor pressure of the pure component m at that temperature, $p_m^0(R)$, multiplied by its mole fraction in the liquid phase. With the equilibrium assumption, and furthermore assuming ideal gases (Dalton's law; Eq. (4.31), right), the partial pressure of species m on the gas side of the interface must equal the saturation pressure $p_{\mathrm{sat},m}$ that is associated with the temperature of the liquid [443]:

$$p_m(R) = p_m^0(R)\ X_{l,m}(R) = p_g\ X_{g,m}(R), \tag{4.31}$$

$$p_m(R) = p_{\mathrm{sat},m}. \tag{4.32}$$

More precisely, $p_{\mathrm{sat},m}$ is the pressure of saturated vapor at temperature T with $T = T_l(R) = T_g(R) < T_{\mathrm{boil},m}$. The saturation pressure $p_{\mathrm{sat},m}$ is determined by the Clausius-Clapeyron relation

$$p_{\mathrm{sat},m} = p_g \exp\left[-\frac{h_{v,m} M_m}{R}\left(\frac{1}{T} - \frac{1}{T_{\mathrm{boil},m}}\right)\right]. \tag{4.33}$$

$T_{\mathrm{boil},m}$ is the boiling temperature, $h_{v,m}$ the latent heat or heat of vaporization, and M_m the molar mass of species m. p_g is the thermodynamic pressure in the gas phase [65]. Boiling temperature $T_{\mathrm{boil},m}$ and thermodynamic pressure p_g are related to each other, but can generally be replaced in Equation (4.33) by any known reference state with $T_{\mathrm{sat},m,0}$ and $p_{\mathrm{sat},m,0}$.

4.3 Modeling of Ignition

There are different regimes of single droplet combustion, as for instance droplets burning in a hot atmosphere of exhaust gas or partially pre-vaporized droplets ignited by an external energy source. Apart from these two particular, technically highly relevant cases, there are a few more mainly academic cases of single droplet combustion. In the case of spherically symmetric droplet modeling, special attention needs to be paid to heat and mass transfer during ignition. If detailed chemistry is used additionally, the energy balance of the droplet has to be conserved stringently in order to secure reasonable results.

In the end, the study of nitrogen oxide emissions is only one representative example of how results can be sensitive against the ignition position [297].

Generally, the pre-vaporization of fuel droplets is carried out at temperatures far below the auto-ignition temperature of the respective fuel. In such a low temperature atmosphere, it is necessary to initiate combustion by some kind of forced ignition. A plausible modeling of this ignition process is essential in the case of spherically symmetric single droplet combustion. It has to be correlated to the ignition and burning of fuel sprays. In the experiments of Baessler [31], pre-vaporized fuel sprays were ignited while passing by a hot wire. Here, the hot wire raises the local temperature and acts as an energy source to the atmosphere of fuel droplets passing by. A different mechanism of droplet ignition results from droplet interaction in fuel sprays. There, the droplets are ignited by flame spread from close-by burning droplets.[1] The heat release due to the combustion of a neighboring droplet can be considered as an energy source for a particular single droplet. Roth et al. [366] experimentally studied this type of flame spread in monosized droplet streams, forming planar droplet arrays and igniting them by a hot wire. Experimental and numerical studies of flame spread in one-dimensional droplet arrays under microgravity conditions can also be found in Kikuchi et al. [205, 206] and Mikami et al. [282, 283].

A method to model the ignition of single droplets with spherical symmetry was presented by Moesl et al. [297, 298]. The model allows for heat introduction and heat extraction by prescribing the distribution of a specific heat source in the gas phase of the computational domain. Both experimental cases of droplet ignition and flame spread can be approximated by this model. When only introducing heat (no heat extraction), this model is related to the experimental case of a droplet passing by an ignition source. If heat introduction and extraction are applied, the modeling is rather correlated to the flame spread in droplet arrays. In the latter case, the heat introduction corresponds to the heat release of a burning neighboring droplet, whereas the heat extraction models the heat flow to another close-by but non-burning droplet.

Similar to the work of Dietrich et al. [102], the heat source is modeled by a source term in the energy equation. However, the energy profile is chosen

[1] In general, diffusive transport maintains the flame propagation. It is responsible for the mixing of vaporized fuel, air, and hot exhaust gas until the onset of ignition.

differently in this work. Here, its location is specified by a mean radius r_m and a volume V. The introduced heat is given as an integral quantity Q in J (cf. Eqs. (4.34) and (4.35)). Subsequent to ignition, the same amount of heat can be taken out of the computational domain by a heat sink. This process conserves the energy of the system and allows a reasonable interpretation of, for instance, NO_x generation. Furthermore, NO_x formation is enhanced at temperatures above 1800 K, and thus it is permissible to promote droplet vaporization and combustion within a moderate temperature range by using a well-balanced heat source.[2] Dietrich et al. [102], on the other hand, provide only a heat source, and the droplet's energy balance is not kept. This approach might be sufficient to model droplet ignition and burning rate k, but the results of a detailed chemistry would possibly become questionable.

$$Q = \int_{t_{\min}}^{t_{\max}} \int_{r_{\min}}^{r_{\max}} \dot{q}_v \, 4\pi r^2 \, dr \, dt \tag{4.34}$$

$$\dot{q}_v = \dot{q}_{v,\max} \sin\left(\frac{t - t_{\min}}{t_{\max} - t_{\min}}\pi\right) \sin\left(\frac{r - r_{\min}}{r_{\max} - r_{\min}}\pi\right) \tag{4.35}$$

The model uses half-sine profiles in space and time for the distribution of the volumetric heat source $\dot{q}_v$. The corresponding profiles of heat source and heat sink are illustrated in Figures 4.2 and 4.3.

The volumetric heat source $\dot{q}_v$ is defined within the spatial limits $r_{\min}$ and $r_{\max}$ and the temporal limits $t_{\min}$ and $t_{\max}$ (Eq. (4.35)). In the first instance, the time interval $t_{\min}$ to $t_{\max}$ is arbitrary, with time $t = 0$ s referring to the end of droplet pre-vaporization. Besides, instead of directly specifying the remaining model constants $r_{\min}$, $r_{\max}$, and $\dot{q}_{v,\max}$, more applicable constants are used: $r_{\min}$ and $r_{\max}$ are determined from the total volume

$$V = \frac{4}{3}\pi \left(r_{\max}^3 - r_{\min}^3\right) \tag{4.36}$$

in conjunction with the mean radius r_m, where

$$r_{\min} = r_m - \Delta r, \tag{4.37}$$

$$r_{\max} = r_m + \Delta r. \tag{4.38}$$

[2] This study also includes the auto-ignition of droplets at an elevated temperature level due to the heat transfer from hot exhaust gas (Chaps. 5.1 and 5.3). This particular droplet burning regime resembles a single droplet entering the flame front within spray combustion.

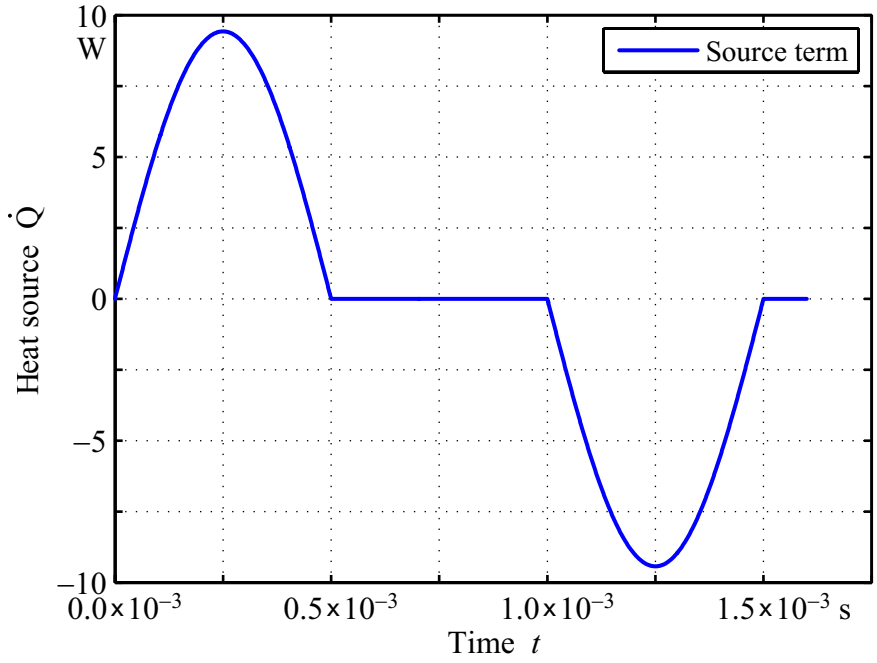

Figure 4.2: Heat Source for Forced Droplet Ignition as a Function of Time [298].

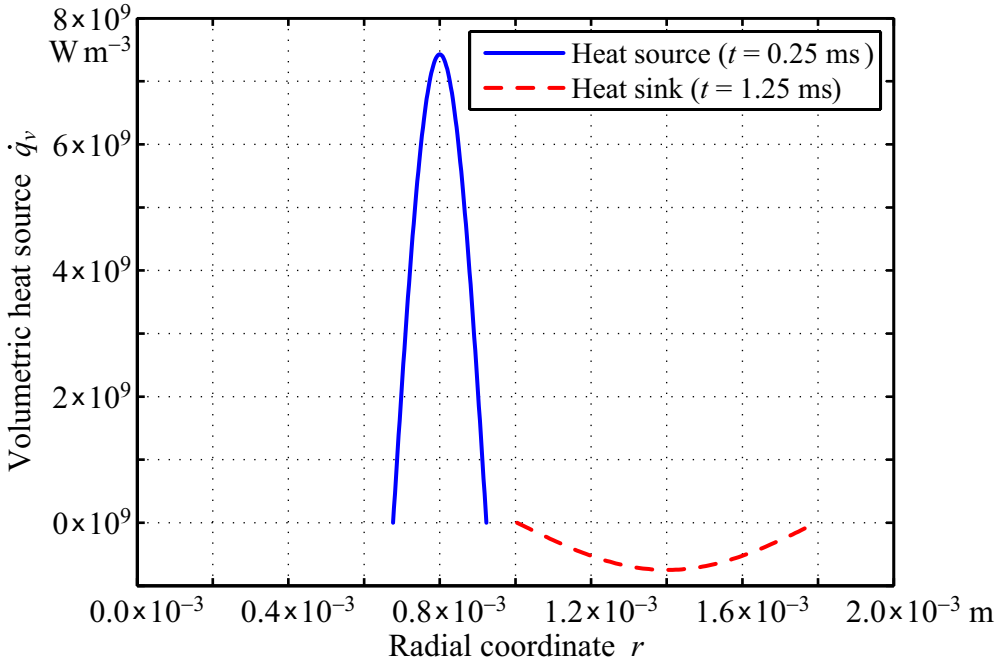

Figure 4.3: Spatial Distribution of Heat Source and Sink. The high positive peak refers to ignition, whereas the wider spread, negative dint indicates heat extraction [297, 298].

Equations (4.36) through (4.38) yield a transcendental equation for the determination of the offset radius Δr. Finally, the total amount of heat Q introduced in or extracted from the system needs to be defined by the user. It delivers the maximum volumetric heat source $\dot{q}_{v,\max}$.

Two different parameter sets realize the heat introduction and extraction process within the numerical model, indicated by "in" and "ex", respectively. Finding appropriate values for the ignition parameters is crucial regarding NO_x emissions. The parameters must be set to ensure a safe ignition, but NO_x emissions are expected to depend on the amount of introduced heat Q_{in}, position of the heat source $r_{m,\text{in}}$, and ignition volume V_{in} [297, 298].

The amount of heat introduced by the heat source is $Q_{\text{in}} = 3\times10^{-3}\,\text{J}$, which is about 20 % of the lower heating value times the mass of the investigated fuel droplet[3] (see Chap. 5.2). The same amount of heat is nominally extracted from the computational domain with $Q_{\text{ex}} = -3.0\times10^{-3}\,\text{J}$ during droplet burning (cf. Fig. 4.2). To avoid negative effects, the absolute amount of heat $|Q|$ is optimized to be as low as possible but still high enough to ensure ignition. The associated times are $t_{\text{in,min}} = 0.0\,\text{ms}$ and $t_{\text{in,max}} = 0.5\,\text{ms}$ as well as $t_{\text{ex,min}} = 1.0\,\text{ms}$ and $t_{\text{ex,max}} = 1.5\,\text{ms}$, with a calculative time shift between heat introduction and extraction of $\Delta t = 1.0\,\text{ms}$. These time scales are chosen according to correlations given in Mikami et al. [282, 283] and Oyagi et al. [327] for the flame spread rate along droplet arrays. The experiments of Mikami et al. [283] show that the flame spread rate is

$$v_f D_0 = 50\,\text{mm}^2\,\text{s}^{-1} \tag{4.39}$$

for an inter-droplet distance of $S \approx 10D_0$ and a preheating temperature of $T = 600\,\text{K}$. v_f denotes the mean velocity of the flame front and can be expressed as

$$v_f = \frac{S}{\tau_{\text{ign}}}, \tag{4.40}$$

where τ_{ign} is the time between the ignition of two neighboring droplets. Solving for time yields

$$\tau_{\text{ign}} = S D_0 \cdot \frac{1}{50}\frac{\text{s}}{\text{mm}^2} \approx D_0^2 \cdot \frac{1}{5}\frac{\text{s}}{\text{mm}^2} = 2.0\times10^{-3}\,\text{s}. \tag{4.41}$$

[3] The droplet itself has an initial diameter of $D_0 = 100\,\mu\text{m}$ before the start of pre-vaporization.

Hence, the characteristic time scale of $\Delta t = 1.0\,\mathrm{ms}$ utilized for the time between heat introduction and extraction is reasonable[4] for an investigated droplet diameter of $D_0 = 100\,\mu\mathrm{m}$.

As for the geometrical parameters, the total volume for heat introduction is optimized for a safe ignition and set to $V_{\mathrm{in}} = 2.0\,\mathrm{mm}^3$. For heat extraction, $V_{\mathrm{ex}} = 20.0\,\mathrm{mm}^3$ is chosen in order to remove heat from a well-spread region of exhaust gas outside of the burning droplet (cf. Fig. 4.3). The particular profiles depicted in Figure 4.3 use values of $r_{m,\mathrm{in}} = 0.8\,\mathrm{mm}$ and $r_{m,\mathrm{ex}} = 1.4\,\mathrm{mm}$ for the mean radius. The solid line shows the introduced heat when $\dot{q}_v\big|_{r_m} = \dot{q}_{v,\max}(t)$, the dashed line the heat sink when $\dot{q}_v\big|_{r_m} = \dot{q}_{v,\min}(t)$. Despite the exemplary r_m-values of Figure 4.3, there are two practical approaches to define a reasonable position for $r_{m,\mathrm{in}}$ (and also for $r_{m,\mathrm{ex}}$). The outcome of both is discussed in Chapter 5.2 regarding NO_x emissions. The first approach uses spatially fixed values for heat introduction and extraction [298], whereas the second uses variable positions [297]. In the latter case, the positions are coupled with the local equivalence ratio ϕ_r. The definition of ϕ_r is derived from the total equivalence ratio ϕ. Since fuel and air diffuse into each other in the area around the droplet, the ratio of nitrogen and oxygen is not constant over the radial coordinate r. Using mass fractions and considering a differential volume enclosing a differential mass dm, the local equivalence ratio ϕ_r can be written as:

$$\phi_r = \frac{\frac{dm_{\mathrm{fuel}}}{dm_{\mathrm{O_2}}}}{\left(\frac{m_{\mathrm{fuel}}}{m_{\mathrm{O_2}}}\right)_{\mathrm{stoich}}} = \frac{\frac{dm\,Y_{\mathrm{fuel}}}{dm\,Y_{\mathrm{O_2}}}}{\left(\frac{m_{\mathrm{fuel}}}{m_{\mathrm{O_2}}}\right)_{\mathrm{stoich}}} = \frac{\frac{Y_{\mathrm{fuel}}}{Y_{\mathrm{O_2}}}}{\left(\frac{m_{\mathrm{fuel}}}{m_{\mathrm{O_2}}}\right)_{\mathrm{stoich}}}. \tag{4.42}$$

Figure 4.4 shows the local equivalence ratio ϕ_r in the gas phase of a single droplet for different pre-vaporization rates Ψ. During vaporization, fuel ($C_{10}H_{22}$) diffuses away from the droplet, whereas oxidizer (O_2) diffuses in the opposite direction. The local equivalence ratio ϕ_r varies between values $\gg 1$ at the droplet surface and zero at the outer gas phase boundary. Consequently, the spatial position for a constant equivalence ratio also changes for different pre-vaporization rates Ψ. For low pre-vaporization, this position is close to the droplet surface but shifts farther away from the droplet for increasing pre-vaporization (given that $\phi_r < 1.5$).

[4] The absolute time between the ignition of neighboring droplets τ_{ign} is much longer in the work of Mikami et al. [282, 283] and Oyagi et al. [327], as most of the experiments are conducted with an initial droplet diameter of $D_0 = 1\,\mathrm{mm}$.

When investigating different degrees of droplet vaporization Ψ, assigning the mean radius r_m to either a fixed absolute position r or a fixed local equivalence ratio ϕ_r may both be effective and may not show any deteriorating impact on the ignition and burning behavior. This is true as long as $r_{m,\mathrm{in}}$ remains within reasonable limits, implying a position within the flammability limits plus their outer proximities. For both approaches, the flame bounces to a stable radial position, immediately after ignition. However, NO_x generation can be very sensitive to a variation of r_m (Chap. 5.2.2) [297].

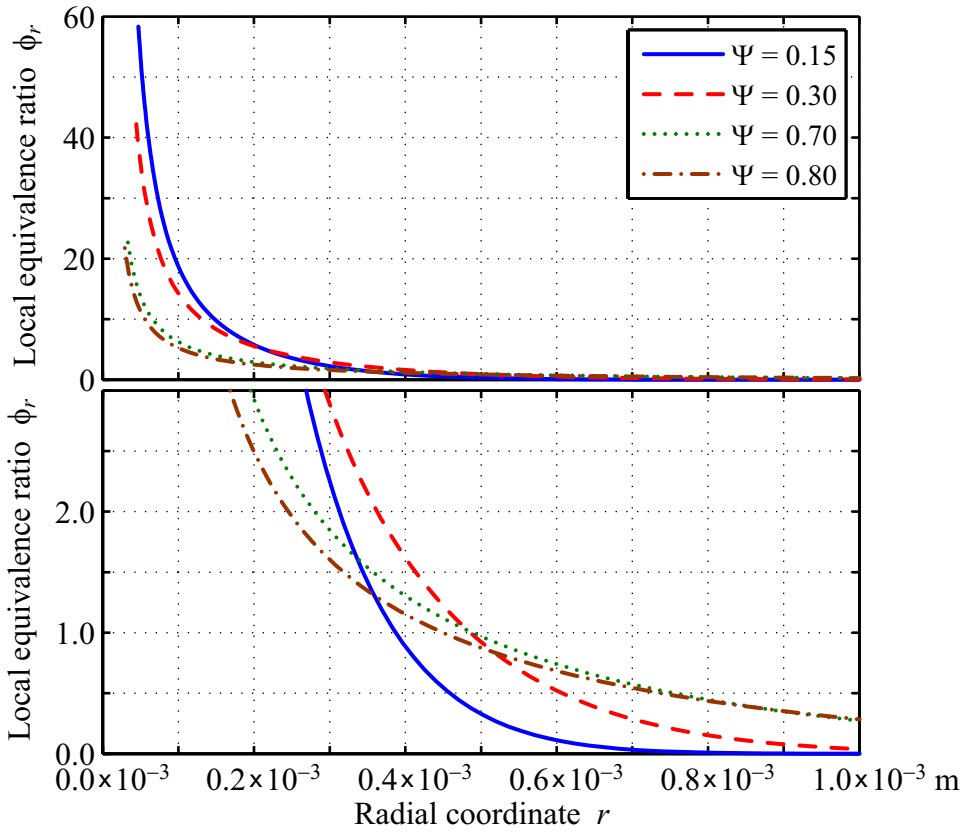

Figure 4.4: Progression of Local Equivalence Ratio for Different Pre-Vaporization Rates. The local equivalence ratio ϕ_r is only shown for the gas phase. The meaningless values for the liquid phase are omitted.

4.4 Modeling of Nitrogen Oxide Formation

The fuel of choice for the present study is n-decane ($C_{10}H_{22}$). This is due to the fact that it resembles the combustion characteristics of kerosene and diesel fuel best (see also Chap. 2.3) [49, 93, 297, 298, 340]. Soot formation is not considered because of the exclusion of polyaromatic compounds. The employed n-decane mechanism was developed by Zhao et al. [474] for oxidation and pyrolysis. It is combined with the nitrogen oxide (NO_x) kinetics of Li and Williams [250]. As shown in Chapter 2.3.3, this combined reaction mechanism produces reliable results, and it shows a good convergence behavior at the crucial evaluation of the species production rates. It includes a total number of 99 species and 693 reaction equations. Humid air at ISO standard reference conditions is taken as an oxidizer [190]. At a temperature of $T = 288.15\,\mathrm{K}$ and pressure of $p = 101\,325\,\mathrm{Pa}$, the relative humidity is $\varphi = 0.6$.

Studying NO_x emissions, the species mass fractions of NO and NO_2 are generally considered. In order to quantify the NO_x emissions, the emission index EI_{NO_x} is used here (Eqs. (4.43) and (4.44)). It is the ratio between the weighted NO_x masses and the fuel mass m_{fuel}, and it comes with the units g_{NO_x}/kg_{fuel} [370]. It is given in NO_2 equivalents in its standard form as

$$EI_{NO_x} = \frac{m_{NO}\frac{M_{NO_2}}{M_{NO}} + m_{NO_2}}{m_{fuel}}, \tag{4.43}$$

and in its extended from as [297, 298]

$$EI_{NO_x,N_2O} = \frac{m_{NO}\frac{M_{NO_2}}{M_{NO}} + m_{NO_2} + m_{N_2O}\frac{M_{NO_2}}{M_{N_2O}}}{m_{fuel}}. \tag{4.44}$$

The total mass produced of any particular NO_x species m is obtained by integration of the respective species production rate $\dot{\omega}_m$. For nitric oxide (NO) for instance, this is

$$m_{NO,tot} = \int_{t_0}^{t_{end}} \int_{R}^{R_\infty} \dot{\omega}_{NO,tot}\, 4\pi r^2\, dr\, dt. \tag{4.45}$$

Furthermore, two different approaches may be used for the calculation of the fuel mass m_{fuel} within the emission index, particularly in the case of par-

tially pre-vaporized droplets. Either the initial droplet mass $m_{\text{fuel},0}$ (before pre-vaporization) or the reacting fuel mass $m_{\text{fuel,reac}}$ (in gas phase) are reasonable for this purpose. The latter is obtained analogously to Equation (4.45):

$$m_{\text{fuel,reac}} = \left| \int_{t_0}^{t_{\text{end}}} \int_{R}^{R_\infty} \dot{\omega}_{\text{fuel}} \, 4\pi r^2 \, dr \, dt \right|. \tag{4.46}$$

Differences between droplet fuel mass and reacting fuel mass arise for a few reasons. On the one hand, regions with low equivalence ratios are generated during pre-vaporization, which remain non-flammable throughout the whole droplet lifetime. On the other hand, as combustion is only considered during droplet lifetime, unburned fuel remains in the gas phase at the end of the simulation, even though within the flammable range [297, 298].

4.5 Simulation of Single Droplets

The governing equations introduced above with Equations (4.3) through (4.6) are simplified for the present numerical studies. Those simplifications are also implemented in the utilized software package Cosilab® [362–365].

4.5.1 Single Droplet Model

The final form of the governing equations as well as the motivation behind those simplifications is presented in the following sections. Still, spherical symmetry is postulated and detailed chemistry is considered for all computations [31, 298].

Gas Phase

For the gas phase, a quasi-steady state approach helps in estimating the magnitude of the radial velocity u_r and its derivatives. Since the Soret and Dufour effects are both hereinafter neglected, the diffusion velocity $\Delta u_{m,r}$ changes in comparison to $\Delta u_{m,i}$ in Equation (4.10). According to Williams [461], diffusion is dominated by concentration gradients. Thus, the thermal diffusion ratio can be neglected, which would account for the Soret effect. Regarding

the Dufour effect, Annamalai and Puri [19] state that heat flux is dominated by ordinary heat conduction. Consequently, the diffusion velocity in the gas phase g simplifies to

$$\Delta u_{m,r} = -\frac{D_m}{X_{g,m}} \frac{\partial X_{g,m}}{\partial r}. \tag{4.47}$$

This is the best first-order approximation to the exact formulation[5] [147, 180, 341] and avoids evaluating a linear system of equations [325]. According to Poinsot and Veynante [341] and Annamalai and Puri [19] the diffusion coefficient of a single species m in a multi-component gas can be approximated by Equation (4.48). In this case, the coefficient D_m is not a binary diffusion coefficient but an equivalent diffusion coefficient of species m into the rest of the mixture.

$$D_m = \frac{1 - Y_m}{\sum_{n;n\neq m} \frac{X_n}{D_{mn}}} \tag{4.48}$$

Besides, as the mass flow of the vaporized liquid $\dot{m}(t)$ is equal to the mass flow through a spherical shell with radius r, the radial velocity u_r is proportional to $1/r^2$ [297, 298].

The mass balance (Eq. (4.3)) and species conservation equation (Eq. (4.4)) remain unaffected by those simplifications for the gas phase, apart from the outlined changes in the diffusion velocity $\Delta u_{m,r}$. The viscous terms in the radial momentum equation (Eq. (4.5)) cancel each other out [363, 364]. This is a meaningful fact, as Euler flow (neglecting viscous effects), in the strict sense, is only valid here for constant vaporization mass flow $\dot{m}$, constant density ρ, and constant viscosity η_g. Furthermore, a low Mach-Number is presumed. This finally reduces the momentum equation (Eq. (4.5)) to a single term, still accounting for Stefan flow [19, 443]. In the energy equation (Eq. (4.6)), viscous terms are also neglected and Euler flow is presumed at a constant pressure p_g in space. The heat flux $\dot{q}_{g,r}$ is evaluated neglecting the so-called Dufour term, the second term on the right hand side of Equation (4.13). Altogether, the governing equations for the gas phase as applied in the model are given below.

[5] In-depth analyses of both second-order effects (Soret and Dufour) can be found in literature [328, 335, 361].

Conservation of mass:

$$\frac{\partial \rho_g}{\partial t} + \frac{\partial \rho_g u_{g,r}}{\partial r} + 2\frac{\rho_g u_{g,r}}{r} = 0 \tag{4.49}$$

Conservation of species:

$$\rho_g \frac{\partial Y_m}{\partial t} + \rho_g u_{g,r} \frac{\partial Y_m}{\partial r} + \frac{\partial \rho_g Y_m \Delta u_{g,m,r}}{\partial r} + 2\frac{\rho_g Y_m \Delta u_{g,m,r}}{r} = \dot{\omega}_m \tag{4.50}$$

Conservation of momentum:

$$\frac{\partial p_g}{\partial r} = 0 \tag{4.51}$$

Conservation of energy:

$$\begin{aligned} &\rho_g \frac{\partial \sum_m Y_m \int_{T_0}^{T} c_{p,m}\, dT}{\partial t} + \rho_g u_{g,r} \frac{\partial \sum_m Y_m \int_{T_0}^{T} c_{p,m}\, dT}{\partial r} \\ &= -\frac{\partial \sum_m \rho_g Y_m \int_{T_0}^{T} c_{p,m}\, dT\, \Delta u_{g,m,r}}{\partial r} - 2\frac{\sum_m \rho_g Y_m \int_{T_0}^{T} c_{p,m}\, dT\, \Delta u_{g,m,r}}{r} \\ &\quad - \sum_m \dot{\omega}_m h^0_{g,m} + \frac{\partial p_g}{\partial t} - \frac{\partial \dot{q}_{g,r}}{\partial r} - \frac{2}{r}\dot{q}_{g,r} \end{aligned} \tag{4.52}$$

Heat flux:

$$\dot{q}_{g,r} = -\lambda_g \frac{\partial T}{\partial r} \tag{4.53}$$

Liquid Phase

In the liquid phase, the physical properties are assumed to be constant [364]. Density ρ_l, specific heat $c_{p,l}$, and thermal conductivity λ_l are independent of space and time as well as heat of vaporization h_v and boiling temperature T_{boil}. There is only one single species in the liquid, the composition is homogeneous, and no chemical reactions occur ($\dot{\omega} = 0$). Diffusion of species is neglected, and no species can be absorbed in the liquid droplet. All gaseous components are insoluble in the liquid by definition.

The final liquid phase model corresponds to the so-called “conduction limit model”, as presented for instance in Aggarwal et al. [9] and Sazhin [381]. The

energy equation (Eq. (4.56)) is the only equation that has to be solved here. The governing equations as applied can be summarized for the liquid phase as follows:

Conservation of mass:

$$u_{l,r} = 0, \quad \text{with} \quad \frac{\partial u_{l,r}}{\partial r} = 0 \quad \text{and} \quad u_{l,r}\big|_{r=0} = 0 \tag{4.54}$$

Conservation of momentum:

$$\frac{\partial p_l}{\partial r} = 0 \tag{4.55}$$

Conservation of energy:

$$\rho_l c_{p,l} \frac{\partial T}{\partial t} - \frac{\partial p_l}{\partial t} = -\frac{\partial \dot{q}_{l,r}}{\partial r} - 2\frac{\dot{q}_{l,r}}{r}, \quad \text{with} \quad u_{l,r} = 0 \tag{4.56}$$

Heat flux:

$$\dot{q}_{l,r} = -\lambda_l \frac{\partial T}{\partial r} \tag{4.57}$$

Coupling at Gas-Liquid Interface

Gas and liquid phase are modeled with one set of governing equations each, as stated directly above. The governing equations are one-dimensional and account for spherically symmetric droplets under microgravity conditions. The coupling of the two phases is achieved by an additional set of equations, as introduced in Chapter 4.2.5. This set of equations takes into account the conservation laws at the interface, and they finally read as follows:

Conservation of mass:

$$\left(\rho_g - \rho_l\right) \left.\frac{\partial R}{\partial t}\right|_{R=R(t)} = \rho_g u_{g,r}\big|_{R=R(t)} \tag{4.58}$$

Conservation of vaporizing species m (liquid-phase):

$$Y_{g,m} \left(1 + \frac{\Delta u_{g,m,r}}{u_{g,r} - \frac{\partial R}{\partial t}} \right) \Bigg|_{R=R(t)} = 1 \tag{4.59}$$

Conservation of non-vaporizing species n ($n \neq m$):

$$\left(u_{g,n,r} - \frac{\partial R}{\partial t}\right)\Bigg|_{R=R(t)} = 0 \tag{4.60}$$

Conservation of momentum:

$$p_l = p_g \tag{4.61}$$

Conservation of energy:

$$\rho_l h_{v,m} \frac{\partial R}{\partial t} + \rho_l \frac{u_{g,r}^2}{2} \frac{\partial R}{\partial t} = \dot{q}_{g,r} - \dot{q}_{l,r} \tag{4.62}$$

In Equation (4.62), $h_{v,m}$ is the heat of vaporization, which represents the energy required to transform the species m from the liquid into the vaporous state. It is derived from the difference of enthalpies with $h_{v,m} = h_{g,m} - h_l$.

4.5.2 Meshing and Solver Settings

In order to find a good compromise between simulation time and numerical accuracy, the model configuration was determined by varying the spatial grid resolution and studying different Cosilab® solvers. This also included assessing different discretization schemes for the convective terms. The results were compared to simulations of the NO_x emissions of n-heptane (C_7H_{16}) droplets performed by Baessler [31, 175]. A reliable quality criterion can be derived in this context from the conservation of mass. The converted fuel mass plus the remaining fuel in the gas phase at the end of simulation has to be equal to the initial fuel mass of the droplet [298].

Convergence studies were conducted on a simple and easily reproducible problem. An n-heptane droplet at $T = 360\,\mathrm{K}$ is placed in an atmosphere of air at 1500 K and 1 bar. The initial droplet diameter is set to $D_0 = 100\,\mu\mathrm{m}$, and the associated liquid phase is resolved with 10 grid points. The outer diameter of the whole numerical domain is $D_\infty = 100 D_0$. Thus, the grid points in the gas phase are initially discretized by

$$D_i = D_0 + (D_\infty - D_0)\left(\frac{i}{N}\right)^3, \tag{4.63}$$

with index $i \in [0,1,\ldots,N]$ and N being the total number of grid points in the gas phase. Consequently, $i = 0$ marks the gas-liquid interface. The choice of $D_\infty = 100 D_0$ is not arbitrary but based on considerations presented in detail in Chapter 5 with the numerical results. The simulation stops if the droplet diameter is $D \leq 1/1000 D_0$.

A Newton and an Euler solver were evaluated, both in combination with an upwind and a central difference scheme. The absolute and relative tolerance were initially chosen to 1×10^{-8}. In doing so, the relative error in the conservation of mass decreases with an increasing number of grid points. Finally, the first choice for the setup investigated was the use of $N = 100$ grid points in the gas phase at a tolerance of 1×10^{-4} together with the Euler solver and the central difference scheme. The typical simulation duration was in the order of one hour on an Intel® Core™2 Duo at 2.4 GHz using one CPU. Generally, the conservation of mass proved to be a simple and reliable means to check the accuracy of the numerical experiments without any additional effort. The conservation of mass could be evaluated after each run and – if necessary – the spatial resolution was adapted [298].

4.6 Model Validation

The detailed chemistry modeling of this thesis necessitates certain model assumptions and an elaborate accuracy of the gas-liquid model. Even though NO_x formation is the scientific focus of the present work, the following validation approach is universal and may also be adopted to other pollutant emissions. The employed single droplet model consists of different submodels and an adequate number of simplifications (see Chap. 4.5.1). All submodels as such have been well-discussed and well-validated in literature [2–4, 9, 63, 151, 152, 230–233, 236–238, 244, 350, 381–384, 402, 403, 405, 412–415, 418].

As outlined in Chapter 4.5, the governing equations for gas and liquid phase need to be coupled at their interface S, which coincides with the droplet surface (cf. Fig. 4.1). During vaporization and combustion, the droplet size decreases as a function of time t with the droplet temperature T_l being a function of both the radial coordinate r and time t (cf. Figs. 4.5 and 4.6). Since the

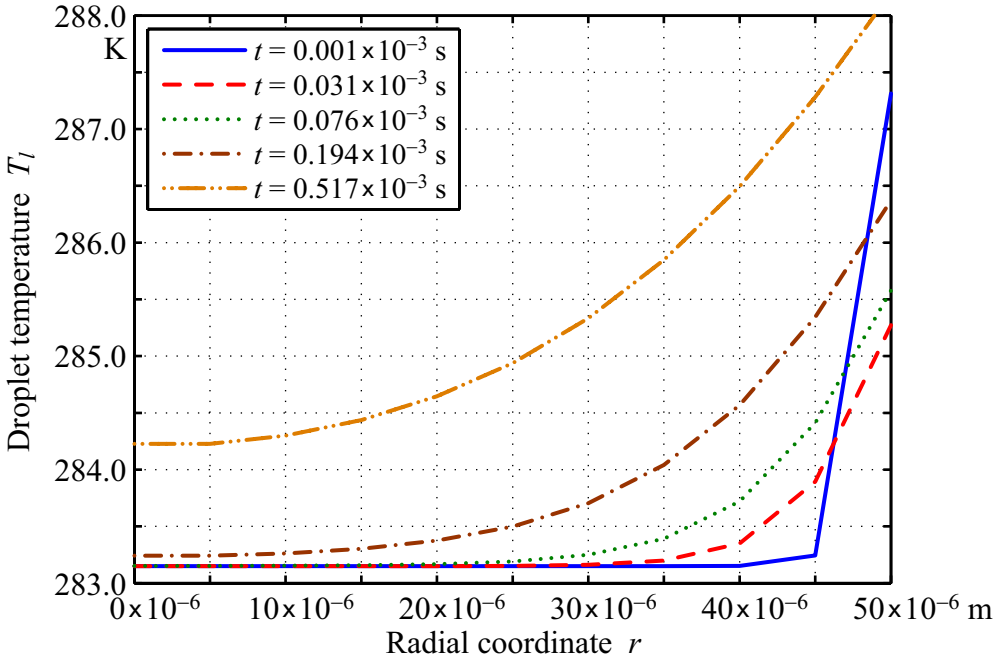

Figure 4.5: Transient Temperature Increase Inside of a Droplet During Initial Droplet Heating Phase. The initial droplet temperature is $T_{l,0} = 283.15\,\mathrm{K}$, and the gas phase temperature is $T_\infty = 473.15\,\mathrm{K}$.

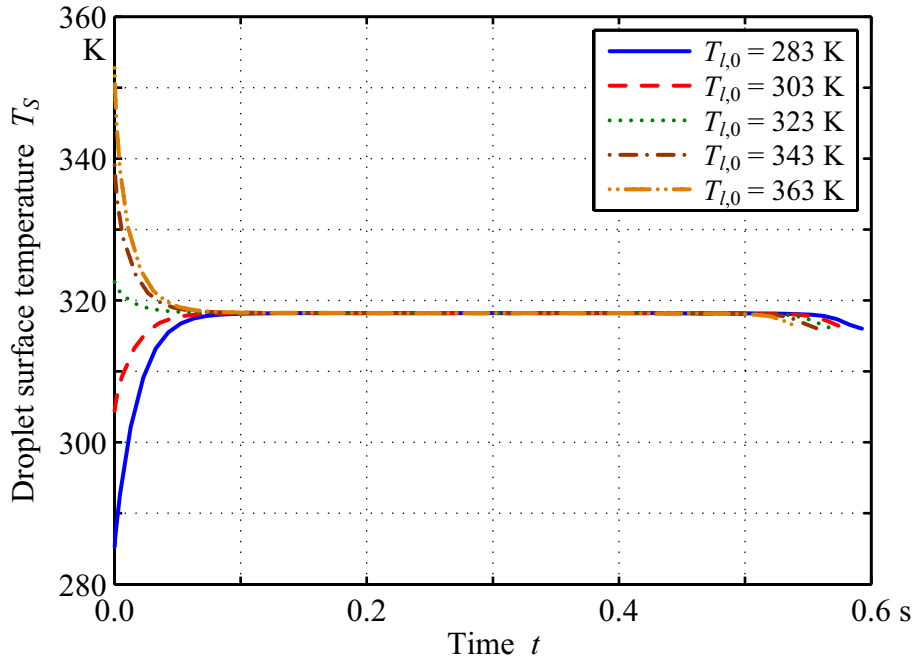

Figure 4.6: Evolution of Droplet Surface Temperature for Different Initial Droplet Temperatures. The initial droplet temperature $T_{l,0}$ is varied, but the temperature of the gas phase is kept constant at $T_\infty = 473.15\,\mathrm{K}$.

utilized model accounts for gradients in the r-direction, transient effects of droplet heating can be resolved correctly on an appropriate scale. The liquid phase model resembles the so-called "conduction limit" or "diffusion limit" model due to Law and Sirignano [236], which is recommended if the droplet Reynolds number is negligible compared to unity [9, 236, 381, 402, 403]. Comparing the thermal diffusivities α of the liquid and gas phase yields $\alpha_l \ll \alpha_g$. Thus, the transport processes in the gas phase happen much faster than in the liquid phase, and the gas phase may be treated as quasi-steady.

Figures 4.5 and 4.6 clarify the temperature sensitivity of the utilized single droplet model. In particular, Figure 4.5 shows the temperature distribution inside a water droplet during the initial, transient heating with $T_{l,0} = 283.15\,\mathrm{K}$ and $T_\infty = 473.15\,\mathrm{K}$. At $t = 1\times10^{-3}\,\mathrm{s}$, the droplet surface temperature T_S is highest due to the initialization of the computational domain. However, it decreases immediately, before it starts to increase continuously, while accounting for the heat flux from the gas phase into the droplet. In Figure 4.6, water droplets are vaporized in an ambient gas environment at $T_\infty = 473\,\mathrm{K}$ with different initial temperatures of the liquid phase (283, 303, 323, 343, and 363 K). The respective wet-bulb temperatures are reached after 3 to 10 % of the droplet lifetime, depending on the temperature difference between $T_{l,0}$ and T_∞. All wet-bulb temperatures match with a relative humidity on the droplet surface in the range of $\varphi = 10\,\%$. Hence, the heat transfer inside the droplet as well as heat and mass transfer over the gas-liquid interface show a correct and consistent behavior. As far as the experiments on droplet array combustion (Chap. 3) are concerned, the heating phase of the droplets is significant and cannot be neglected. It must be included in the calculation of the pre-vaporization rate Ψ (see also Tabs. D.1 through D.3).

4.6.1 Validation of Vaporization Mechanism Without Combustion

Since the calculated vaporization rate k is a further indicator of the accuracy of the simulation results, it is evaluated for water and n-decane droplets against the classical D^2 law as well as experimental measurements. Ansatz, assumptions, and resulting equations are discussed here. In order to facilitate the comparison of the simulation results with the simplified validation model, the vaporization process is studied as an example for droplets in an atmosphere of air.

In addition to the assumptions made for the single droplet model, the following simplifications are introduced to achieve an analytical solution with the D² law: The temperature in the droplet is homogeneous and equal to the temperature at the droplet surface T_S. The problem is quasi-steady, i.e. partial derivatives in time $\partial/\partial t$ vanish. Profiles of temperature and mass fraction are assumed to be in steady state at each time t and droplet radius $R(t)$. This implies that the droplet radius changes slowly compared to the transport of heat and mass [298, 443].

The transport of mass can be written for a water droplet as

$$\frac{\dot{m}_{\mathrm{H_2O}}}{A} = \rho_g D_{\mathrm{H_2O,air}} \frac{dY_{\mathrm{H_2O}}}{dr} + \frac{\dot{m}}{A} Y_{\mathrm{H_2O}}, \tag{4.64}$$

where $\dot{m}_{\mathrm{H_2O}}/A$ is the mass flux of water in kg m^{-2} s^{-1}, $\dot{m}/A$ the total mass flux, $D_{\mathrm{H_2O,air}}$ the diffusion coefficient of water in air, ρ_g the density of the humid air, and $Y_{\mathrm{H_2O}}$ the mass fraction of water. The area A reflects the droplet surface with $A = 4\pi R^2$. The mass flow of vaporizing water $\dot{m}_{\mathrm{H_2O}}$ is equal to the total mass flow $\dot{m}$, as air is insoluble in water in a first estimate. The mass flow $\dot{m}$ is constant in space, as a quasi-steady state assumption was postulated. The mass flow value is generally defined as positive, if water vaporizes and the droplet shrinks.

Heat transfer is described by:

$$\frac{d}{dr}\left(r^2 \frac{\dot{m}}{A} c_p T\right) - \frac{d}{dr}\left(r^2 \lambda \frac{dT}{dr}\right) = 0. \tag{4.65}$$

As the vaporization mass flow $\dot{m}_{\mathrm{H_2O}}$ in Equation (4.65) is linear in $R(t)$ and accordingly in D, the mass fraction $Y_{\mathrm{H_2O},S}$ and droplet temperature T_S at the droplet surface (on the gas side) are independent of time t for this simplified validation model. Thus, the droplet diameter is

$$D^2 = D_0^2 - k\,t, \tag{4.66}$$

where D_0 is the initial droplet diameter at $t = 0$ and k the vaporization rate [244, 443, 461]. Equation (4.66) is known as the D² law. It is used only within this section (Chap. 4.6) for validation purposes but not for any further scientific studies. Equation (4.67) further clarifies the definition of k:

$$k = -\frac{d(D^2)}{dt} = -2\dot{D}D = \frac{2\,\dot{m}_{\mathrm{H_2O}}}{\rho_l\,\pi\,R(t)} = \text{const.} \tag{4.67}$$

Figure 4.7 depicts the vaporization rate k as a function of the ambient temperature T_∞. Crosses show the analytical solutions, and diamonds mark the values calculated with the single droplet model that is implemented in the software package Cosilab®. The initial droplet diameter D_0 is set to 100 µm for all cases here. Furthermore, the initial droplet temperature $T_{l,0}$ is set close to the expected value for the numerical calculations to reduce effects of heat transfer into and in the droplet. Analytical and numerical solutions correspond very well. Both data sets show a similar tendency. The difference is small, especially at a low ambient temperature T_∞. With increasing temperature, the discrepancy in the results increases as well.

The characteristic time of vaporization

$$\tau_v = \frac{D_0^2}{k} \tag{4.68}$$

is the time until all liquid is vaporized. It is presented in Figure 4.8 as a function of the initial droplet diameter D_0 for the range of 25 to 150 µm. The ambient temperature is set to $T_\infty = 473.15\,\mathrm{K}$ here. The numerical calculations are

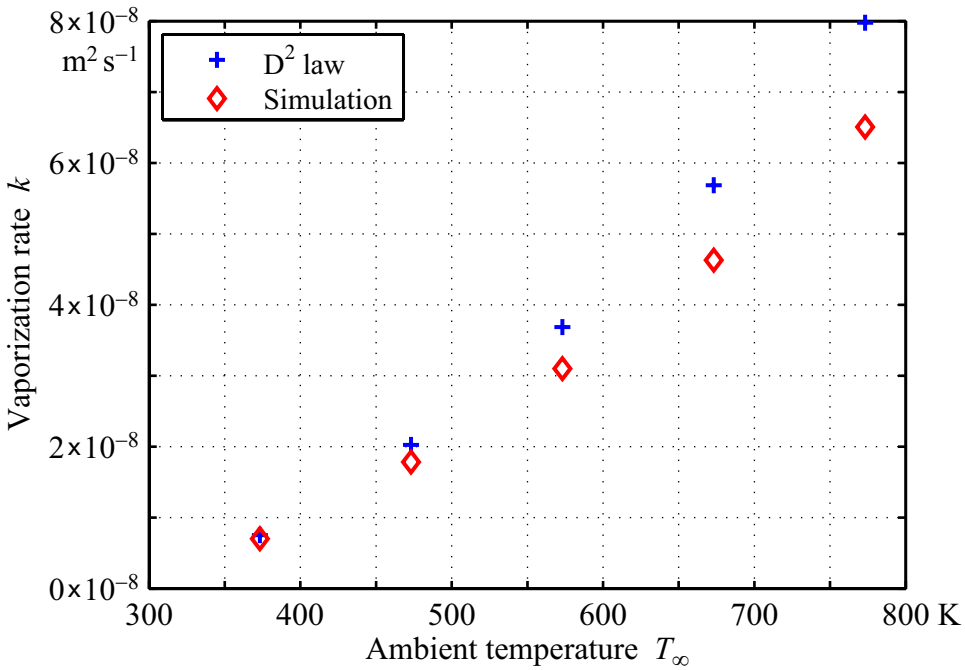

Figure 4.7: Validation of Vaporization Rate for Different Ambient Temperature Levels. The vaporization rate k is evaluated for water droplets at a varying ambient temperature T_∞ [298].

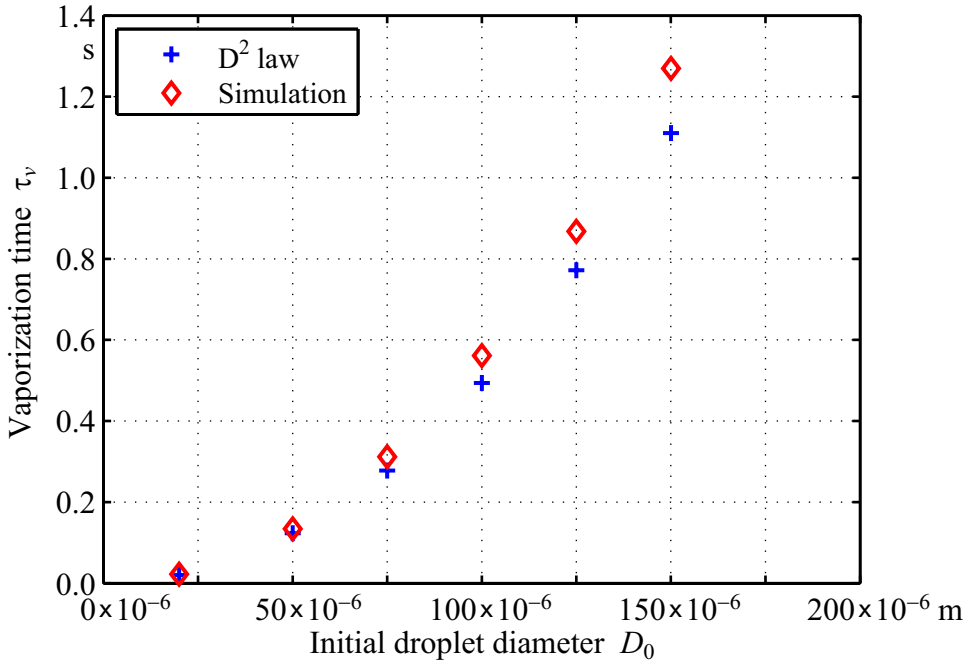

Figure 4.8: Validation of Vaporization Time for Different Initial Droplet Diameters. The vaporization time τ_v is evaluated for water droplets as a function of the initial droplet diameter D_0.

stopped when the droplet diameter D drops below 0.1 % of D_0. The D² law and single droplet model show the same dependency on D_0: The characteristic time of vaporization τ_v is proportional to D_0^2, and the vaporization rate k is approximately constant at a constant ambient temperature T_∞. Generally, the results are in good agreement. However, at large diameters, small differences in k result in an increased absolute difference in τ_v.

The droplet or, more precisely, the droplet surface temperature T_S as a function of the ambient temperature T_∞ is illustrated in Figure 4.9. The initial droplet diameter D_0 is again kept constant at 100 µm. As shown in Figure 4.9, there is a roughly linear increase of T_S with an increase of T_∞, and both models reproduce this behavior. The data points fit very well. The analytical D² law predicts slightly higher droplet (surface) temperatures T_S at high ambient temperature T_∞ [298].

Generally, the analytical D² law is in good agreement with the numerical calculations of the single droplet model. However, there are some discrepancies, especially at high ambient temperature T_∞: The vaporization time τ_v is lower

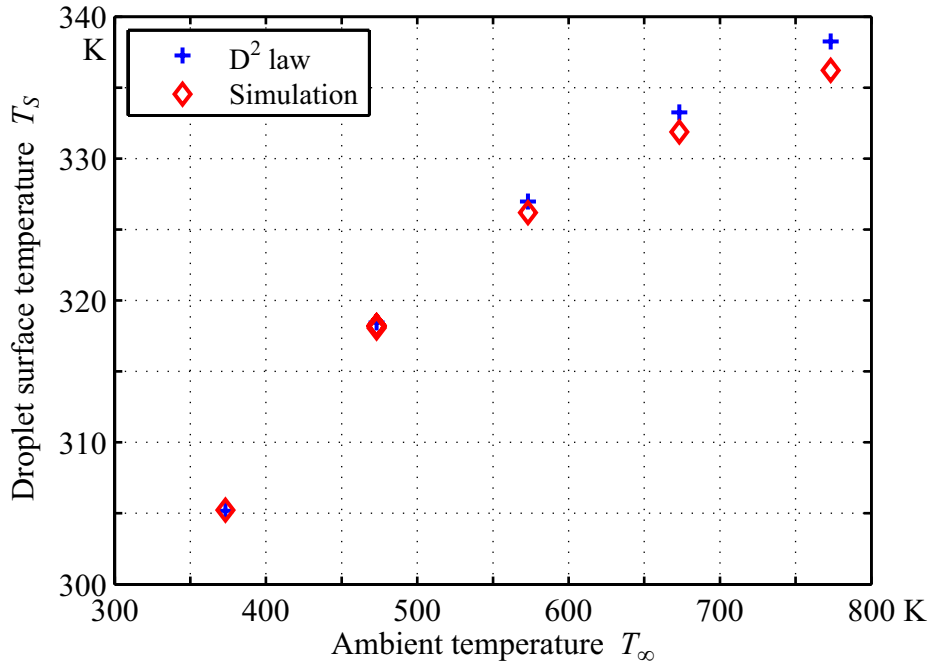

Figure 4.9: Validation of Droplet Surface Temperature for Different Ambient Temperature Levels. The droplet (surface) temperature T_S is evaluated for water droplets as a function of the ambient temperature T_∞ [298].

in the analytical solution than in the numerical results, and the respective vaporization rate k is higher. This can be explained by assuming constant values for density ρ_g, heat conductivity λ, specific heat c_p, and diffusion coefficient $D_{H_2O,air}$ in the D² law. The corresponding values are chosen for ambient conditions, precisely at the ambient temperature T_∞. As heat conductivity λ and diffusion coefficient $D_{H_2O,air}$ increase with temperature, and the temperature in the proximity of the droplet is closer to the droplet temperature T_S than to the ambient temperature T_∞, transport of mass and heat are overestimated there. This leads to a faster shrinking droplet, and thus to a higher vaporization rate k and a lower vaporization time τ_v [298].

4.6.2 Validation of Combustion Process and Combustion Products

A further indicator of the accuracy of numerical results is the deviation of the calculated vaporization or burning rate k from measurements under identical conditions. In this case, the hydrocarbon $C_{10}H_{22}$ is used for the liquid phase,

since not only vaporization but also burning rates are relevant. Besides, the impact of chemistry can also be included in this step of the validation process.

In an early, still ground-based work, Hall and Diederichsen [164] experimentally investigated the burning characteristics of free and suspended droplets of alkanes and alcohols for a pressure range of 1 to 20 bar. Law and Williams [237] derive a burning rate of $k = 0.93\,\mathrm{mm^2\,s^{-1}}$ from those experiments for a n-decane droplet of $D_0 = 1.10\,\mathrm{mm}$ (with $T_\infty = 293\,\mathrm{K}$ and $p_g = 1\,\mathrm{bar}$). Their own model predicts values of 0.79 and $0.66\,\mathrm{mm^2\,s^{-1}}$ for the respective cases with and without natural convection. The work of Shaw et al. [394] represents one of the first investigations conducted under microgravity conditions that is relevant to the present study. Shaw et al. measured the quasi-steady burning rate k of n-decane droplets in air at room temperature and atmospheric pressure, ignited by a spark-ignition system. The reported k-values spread over a wide range, and results are shown as subdivided into minimum, maximum, and orthogonal least-square values – probably due to scattering. In later work, Shaw and Dee [392] measured $k = 0.78\,\mathrm{mm^2\,s^{-1}}$ for a burning $C_{10}H_{22}$ droplet with $D_0 = 1.12\,\mathrm{mm}$ at $T_\infty = 298\,\mathrm{K}$. They also report unsteady flame stand-off ratios for an ambient oxygen mole fraction of 0.21 combined with different diluents. In the experimental work of Nakaya et al. [307, 309], an averaged k-value of $k = 0.72\,\mathrm{mm^2\,s^{-1}}$ is obtained for similar conditions. The corresponding instantaneous burning rate fluctuates between values of 0.5 and $1.0\,\mathrm{mm^2\,s^{-1}}$. Dietrich et al. [102] also performed microgravity experiments plus numerical modeling. However, most experimental results are retrieved from atmospheres with reduced pressure. Jackson and Avedisian [192] report a decreasing tendency of the k-value with an increase in the initial droplet diameter for n-heptane and 1-chloro-octane, both for suspended as well as free-floating droplets. Xu et al. [465] extend this observation for n-decane towards an inverse influence of the initial droplet diameter on the vaporization and burning rates in cold and hot ambiences. The effects of flame radiation and soot formation as well as soot oxidation are discussed in detail, including their impact on the burning rates of droplets of different diameter. On the one hand, the work of Xu et al. [465] naturally covers a wide range of ambient temperatures and is therefore considered for validating the single droplet model of the present study (cf. Tab. 4.1). On the other hand, the mentioned effects of radiation and soot formation are not captured with the present model. Consequently, a certain deviation from the measurements has to be expected. Fur-

Table 4.1: Validation Test Cases for Vaporization and Burning Rate. All experimental results, acting as references, are for the fuel n-decane ($C_{10}H_{22}$) [465]. The initial droplet diameter is set to $D_{0,\mathrm{sim}} = 1.0\,\mathrm{mm}$ for all simulation runs, here [298].

	Ambient	Experiment		Simulation
	temperature	diameter range	vap./burn. rate	vap./burn. rate
Test case	T_∞ in K	$D_{0,\mathrm{exp}}$ in mm	k_{exp} in $\mathrm{mm^2\,s^{-1}}$	k_{sim} in $\mathrm{mm^2\,s^{-1}}$
Vaporization	773	0.72 – 1.39	0.42 – 0.55	0.43
Burning	943	0.91 – 1.51	0.85 – 1.03	1.10
Burning	973	0.88 – 1.25	0.94 – 1.06	1.10
Burning	1093	0.97 – 1.54	1.05 – 1.44	1.13
Burning	1123	1.29	1.38	1.15

thermore, taking into account all experimental data available, data scattering is large and seems, in part, to be subject to the experiment setup [298].

For validation, the combustion related parameters are set almost identical to the ones used in the numerical simulations contributing to the results of Chapter 5. Only the initial droplet diameter D_0 is adjusted to the target value of the experimental data, which is $D_{0,\mathrm{exp}} \equiv D_{0,\mathrm{sim}} = 1.0\,\mathrm{mm}$. Table 4.1 compares the experimental and numerical results of the vaporization and burning rates k. The results agree very well in a qualitative and quantitative manner, with the numerical results lying in the upper range of the experimental data. The experimental results tend to be lower due to radiant heat losses from the flame and due to soot formation. Generally, both effects cause a decrease of flame temperature and k-value. As reported by Nakanishi et al. [306] and Xu et al. [465, 467], an increase of the ambient temperature enhances Stefan flow, soot formation, and soot oxidation, resulting in three different burning regimes. The second of these regimes is characterized by the most significant increase of the soot formation rate. The third of them reveals a dominance of soot oxidation. Here, transition from the second to the third of these regimes can be observed at temperatures around $T_\infty = 1093\,\mathrm{K}$ by comparing the experimental burning rate k_{exp} with the numerical burning rate k_{sim} (Tab. 4.1) [298].

Figure 4.10 confirms that a variation of D_0 according to the validation test cases of Table 4.1 does not result in a significant gain of insight. This is due

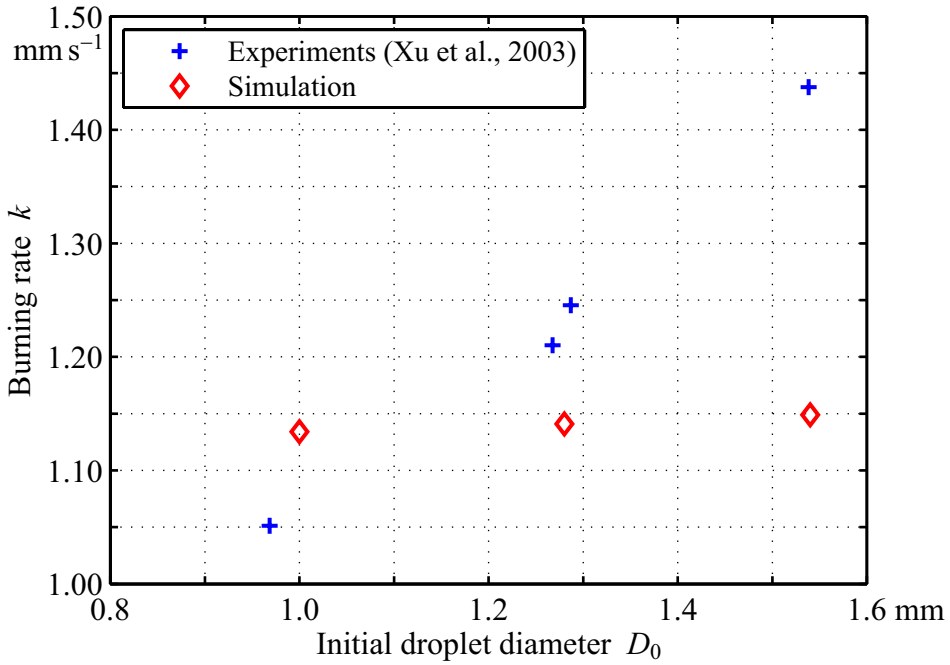

Figure 4.10: Evaluation of Burning Rate for Different Initial Droplet Diameters. Experiments and numerical simulations were conducted at $T_\infty = 1093\,\mathrm{K}$ [465].

to the fact that the effects of radiation and soot formation, as for instance reported in Nakaya et al. [307, 309] and Xu et al. [465, 467], are not taken into account in the present single droplet model. Besides, this particular validation test case at $T_\infty = 1093\,\mathrm{K}$ yields the same k-value for droplets burning due to auto-ignition as well as due to forced ignition by an external heat source (cf. Chap. 4.3). However, auto-ignition requires more ignition delay time than forced ignition.

4.7 Scope and Limitations of Single Droplet Combustion

Utilizing the one-dimensional single droplet model, as outlined above (see Chap. 4.5), it is not possible to investigate two or more droplets including their interactions. Effects of convective flow cannot be studied either. On the other hand, detailed chemistry modeling, as required within this study, necessitates massive computational resources. The computation of a full geometry comparable to the one of Chapter 3.3 with detailed chemistry is infeasible at present and will remain to be so for the foreseeable future. However, it may

be practicable to employ a higher degree of abstraction within the modeling process, for instance for the processes in the boundary layer near the droplet surface or in the chemistry modeling itself. In the latter case, the utilization of single-step mechanisms is most common, which is supplemented by NO post-processing if NO_x emissions are of interest. Furthermore, tabulation of chemistry or intermediate results is also a very common option for reducing the computational costs.

Apart from the numerical study presented in Chapter 3.3, which is precise regarding geometry but simplified regarding the physico-chemical processes, Kikuchi et al. [205, 206] have also conducted numerical studies on droplet array combustion. These studies focus on the flame spread mechanisms in different temperature environments and for different dimensionless droplet spacing ratios S/D. Baessler [31] conducted numerical studies on single droplets with the alkane n-heptane (C_7H_{16}) against the background of NO_x formation, with which he laid the foundation for the numerical work at hand. His single droplet studies also supported the interpretation of his experimental results on spray combustion [32]. Beck [38] and Beck et al. [39, 40, 41] report on an advanced axisymmetric droplet-gas phase model that is capable of predicting NO production as a function of the slip velocity between droplet and gas phase, ambient temperature and pressure, and droplet size. This two-dimensional single droplet model can be embedded into a primary CFD context to reproduce the environment of gas turbine combustion chambers. Parametrization and tabulation of a reduced set of model variables account for the detailed processes of NO formation around single droplets in this overall complex technical configuration. Beck [38] further advances the hypothesis that single droplet combustion can be used as the basis of modeling partially pre-vaporized droplets in lean spray flames.

For the case of droplets being ignited and burning in a hot atmosphere of exhaust gas, the following analytical derivation helps in assessing the impact of droplet interaction [298]: A first attempt to model sprays from single droplets might be to superpose emissions due to droplets and due to ambient conditions.[6] The interaction between droplets would be neglected within this first

[6] Ambient NO_x emissions are basically a function of residence time of the ambient gas atmosphere at a particular temperature level (cf. Fig. 2.7). On the other hand, droplet-caused NO_x emissions are a somewhat theoretical value and due to the presence of the droplet only. This value needs to be calculated by the difference of a droplet atmosphere with and without droplet, thus canceling the impact of the atmosphere itself.

estimate. Consequently, the model would be limited to configurations where diffusive transport between two neighboring droplets τ_d takes more time than the vaporization and combustion τ_v of one single droplet:

$$\tau_v \ll \tau_d. \tag{4.69}$$

The diffusive transport of mass is characterized by the time scale

$$\tau_{d,m} = \frac{L^2}{D_{O_2}}. \tag{4.70}$$

The respective transport of heat is

$$\tau_{d,h} = \frac{L^2}{\alpha}, \tag{4.71}$$

where the thermal diffusivity α in $m^2\,s^{-1}$ is

$$\alpha = \frac{\lambda}{\rho\, c_p}.$$

The half distance between two droplets is denoted L, and D_{O_2} is the diffusion coefficient of oxygen (Eq. (4.70)). As a consequence of Equation (4.69), the half distance L has to fulfill the conditions

$$L \gg \sqrt{D_{O_2}\,\tau_v} \quad \text{and} \tag{4.72}$$

$$L \gg \sqrt{a\,\tau_v}. \tag{4.73}$$

Using the thermophysical properties of exhaust gas at an equivalence ratio of $\phi = 0.8$ as an example, the thermal diffusivity and the diffusion coefficient of oxygen can be retrieved as $\alpha = 0.58\times10^{-3}\,m^2\,s^{-1}$ and $D_{O_2} = 0.56\times10^{-3}\,m^2\,s^{-1}$, respectively. Estimating the vaporization time τ_v from numerical results and the D² law,

$$\tau_v = \frac{D_0^2}{k} = D_0^2 \cdot 0.94\times10^6\,s\,m^{-2} \tag{4.74}$$

yields the condition

$$L \gg 25 D_0. \tag{4.75}$$

In order to compare the amount of fuel spread homogeneously in the gas atmosphere to the fuel given in the liquid droplets, each droplet is packed into a cubical imaginary atmosphere of the side length $2L$. Thus, the amount of fuel in the droplet is calculated from

$$m_{l,\mathrm{fuel}} = \rho_l \, \pi \, \frac{D_0^3}{6} = D_0^3 \cdot 319.7 \, \mathrm{kg \, m^{-3}},$$

and the mass of gaseous fuel in the surrounding atmosphere ($\phi = 0.8$) is

$$m_{g,\mathrm{fuel}} = \rho_g \, Y_{\mathrm{fuel}} \, (2L)^3 = D_0^3 \cdot 1038.3 \, \mathrm{kg \, m^{-3}}.$$

The mass fraction Y_{fuel} is an input value here and corresponds to the selected equivalence ratio of $\phi = 0.8$ for the gas phase. Finally, the fraction of the above amounts of fuel is calculated for the present case to

$$\frac{m_{g,\mathrm{fuel}}}{m_{l,\mathrm{fuel}} + m_{g,\mathrm{fuel}}} = 0.7646.$$

Almost 80 % of the fuel[7] have to be spread homogeneously in the gaseous state in the imaginary atmosphere discussed to fulfill the condition presented in Equation (4.69). Hence, one cannot speak of a “classical” spray anymore. For droplets burning in a hot exhaust gas atmosphere, a superposition of ambient NO_x and droplet-caused NO_x emissions is not directly justified. Heat transfer from one droplet to another and competition for oxygen have to be considered, as well [298]. Generally, the validity of the approach of superposing NO_x emissions depends on the prevailing group combustion and flame propagation modes, as illustrated in Figures 2.4 and 2.5, respectively.

[7] This value does not automatically correspond to droplet pre-vaporization with $\Psi = 0.7646$, as commonly understood, because a homogeneous gas phase is presumed here. Furthermore, this estimation is derived for droplets burning in an atmosphere of hot exhaust gas.

5 Results

In general, an increase of the preheating temperature of the gas atmosphere is followed by an increase of the nitrogen oxide (NO_x) emissions. This is due to higher effective flame temperatures. However, in the lean burning regime, an increase of droplet pre-vaporization results in a decrease of NO_x emissions due to the reduction in droplet size and in the total number of burning droplets acting as hot spots. For conditions close to stoichiometry, the effect of pre-vaporization remains moderate, and the NO_x emissions are almost independent of the pre-vaporization rate Ψ. Previous studies of Baessler et al. [31, 32], for instance, showed that a high degree of vaporization is required to achieve a substantial NO_x abatement.

In order to achieve a better understanding of the processes involved, the NO_x emissions of n-decane ($C_{10}H_{22}$) droplets are discussed and evaluated in detail on the basis of experimental and numerical results. The impact of the ambient atmosphere, droplet pre-vaporization, preheating, initial droplet size, and reaction kinetics is investigated. The respective droplet setups and the general conditions were introduced in the above Chapters 3 and 4.

For the numerical studies presented in the following sections, the thermophysical properties of the liquid fuel are taken from the NIST database [311] and verified with Abramzon and Sazhin [3] and Cuoci et al. [92]. The single droplet model, as described in Chapters 4.2 and 4.5, is employed with the conduction limit model being used for the liquid phase [9, 236, 381–383, 402, 403, 405]. The initial temperature of the droplet is set to $T_0 = 440\,\mathrm{K}$ for all simulation runs to avoid large heat losses due to heating of the liquid fuel and, thus, the need to cope with secondary effects. This temperature is 7 K below the boiling temperature of $C_{10}H_{22}$. Moreover, the properties of the gas phase are calculated from the input data of the chemical reaction mechanism. The mechanism itself is a combination of the n-decane kinetics of Zhao et al. [474] and the nitrogen oxides chemistry of Li and Williams [250]. It was tested for different flame types in a wide range of equivalence ratios (see Chap. 2.3).

In total, it includes 99 species and 693 reactions, and nitrogen (N_2) is treated as the species in excess. The emission index of NO_x (Eqs. (4.43) and (4.44)) is calculated from the production rates $\dot{\omega}_m$ of the respective species m (Eq. (4.50)).

5.1 Droplets in Exhaust Gas Atmosphere

Droplet combustion in a hot exhaust gas atmosphere is investigated in this first configuration by a mere numerical study. Generally, an atmosphere of hot exhaust gas can be assumed for the frequent case of fuel droplets being injected into a combustion chamber where combustion has already been taking place. The composition of the atmosphere depends on the combustion-related parameters and the progress of the whole combustion process under consideration. On the other hand, atmospheres of pure (i.e. unburned), hot oxidizer around a droplet are interesting when studying the influence of atmosphere composition. Thus, presuming an elevated temperature level, an exhaust gas atmosphere features a higher conformity with engine-like conditions than regular air. The latter case was studied in the pioneering work of Bracco [54, 55], Altenkirch et al. [17], and Kesten [204]. They performed numerical studies on the nitric oxide (NO) generation in single droplet flames in the early 1970s. However, strongly simplifying assumptions limit the significance of those references regarding realistic NO_x emissions (see also Chap. 2.2.3).

Some supplementary work is required before proceeding to the actual single droplet study here. Its purpose is to determine the exhaust gas composition used as input data in the main simulations. A one-dimensional laminar premixed flame with an inlet temperature of 300 K is employed for this purpose by utilizing the software package Cantera. The pressure is kept constant at 1 bar. The fuel is $C_{10}H_{22}$ again, and the composition of air is set according to reference conditions (Eqs. (2.22) through (2.24)). The equivalence ratio ϕ is varied in the range of 0.5875 to 0.9375. The resulting exhaust gas composition is taken from a constant axial position within the calculation domain at $x = 0.02\,\mathrm{m}$.[1] This position is chosen only slightly downstream of the flame front as the exhaust gas approaches equilibrium state farther downstream.

[1] Typical profiles of temperature T and the NO_x mass fractions were presented beforehand in Figure 2.11 for a laminar premixed flame and an equivalence ratio of $\phi = 0.8$.

The main droplet simulations are conducted in the second step using the single droplet model of Chapter 4.5. For all investigated equivalence ratios, the initial conditions of the droplet atmosphere are preset with temperature T_0 and species mass fraction $Y_{m,0}$ according to the exhaust gas of the respective premixed flame. As the temperature of the exhaust gas atmosphere is well above the auto-ignition temperature of $C_{10}H_{22}$ [276], no particular ignition modeling by an external heat source is required here (cf. Chap. 4.3).

Figure 5.1 depicts spatial profiles of temperature T and NO mole fraction X_{NO} for droplet combustion in such a hot exhaust gas atmosphere. The particular

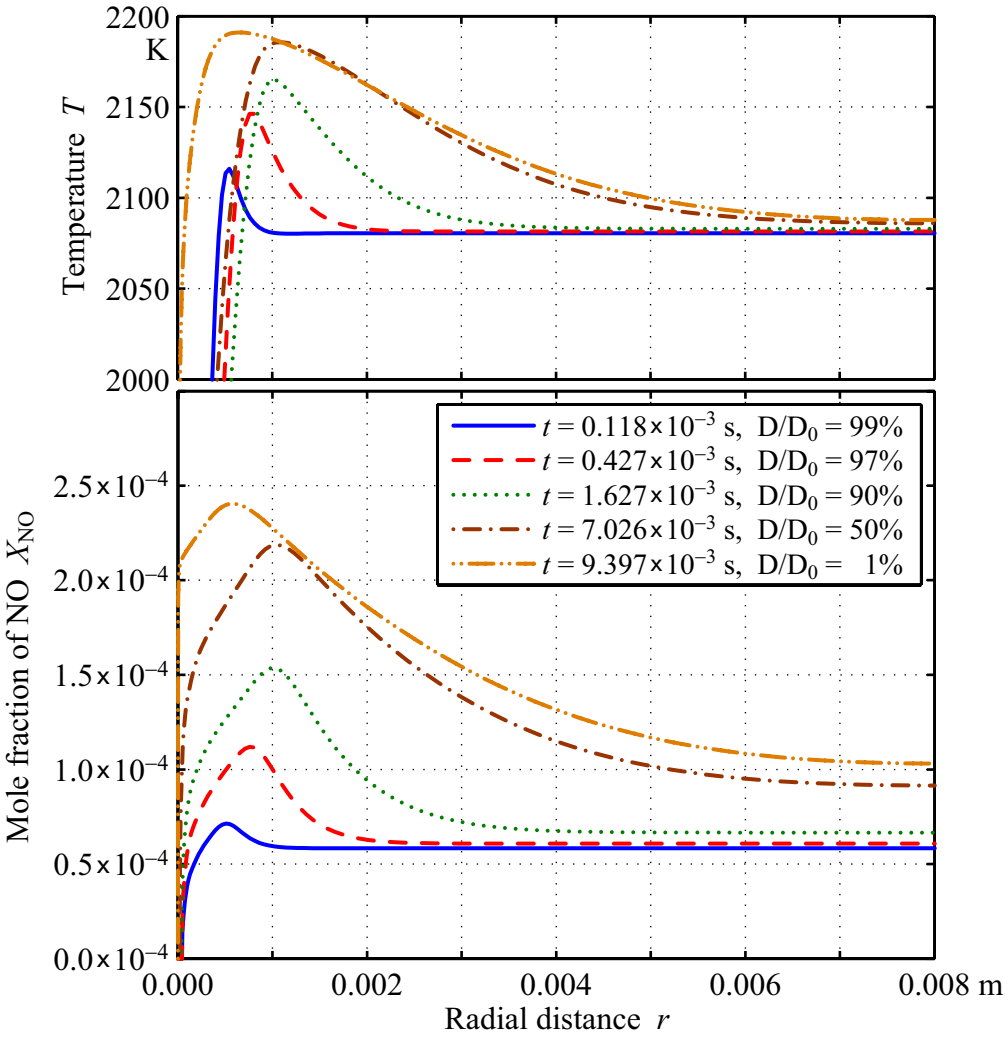

Figure 5.1: Spatial Profiles of Temperature and NO Mole Fraction at Selected Times. A droplet of the initial diameter $D_0 = 100\,\mu m$ vaporizes and ignites in the hot exhaust gas of a premixed flame, which itself has an equivalence ratio of $\phi = 0.8$ [298].

atmosphere of Figure 5.1 is based on an equivalence ratio of $\phi = 0.8$, providing well-burned intermediate combustion products with sufficient oxygen remaining for the ensuing droplet combustion. In the present case, the boundary conditions at $r = R_\infty$ are set to zero gradients (see Chap. 4.2.4). Otherwise it would be difficult to account for any exhaust gas formation due to possible concentration gradients at the outer boundary. The initial conditions of T_0 and $Y_{m,0}$ are set uniformly in the gas phase, and thus yield block profiles. After droplet ignition and flame stabilization, the flame diameter slowly increases in size, before it drastically decreases in response to the approaching droplet burnout. Nitric oxide (NO) peaks in a narrow region in the proximity of the flame front and diffuses into the regions on either side of the flame front. Moreover, the high ambient temperature of $T_\infty = 2080\,\mathrm{K}$ is responsible for the non-zero NO mole fraction throughout the computational domain at $t = 0\,\mathrm{s}$ as well as for a significant positive offset during the succeeding time steps [298].

The exhaust gas atmosphere for itself has a high temperature and noticeable concentrations of N_2, O_2, and atomic oxygen (O), which already leads to a considerable formation of thermal NO. For studying the contribution of the burning droplet to the total NO_x formation, the effects resulting exclusively from droplet combustion need to be isolated. Hence, the difference in production of NO_x is evaluated between exhaust gas atmospheres with and without a droplet (cf. Fig. 5.1 and Eq. (5.1)). The latter setup acts as the reference for this purpose. By subtracting the spatially integrated NO_x production rates of this reference from the results of the regular simulation, the actual NO_x emissions can be disclosed as they are generated by the presence of the droplet in the hot exhaust gas atmosphere,

$$m_{\mathrm{NO_x,droplet}} = m_{\mathrm{NO_x,tot}} - m_{\mathrm{NO_x,atm}}. \tag{5.1}$$

The total mass produced, $m_{\mathrm{NO_x,tot}}$, is obtained by integration in line with Equation (4.45):

$$m_{\mathrm{NO_x,tot}} = \int_{t_0}^{t_\mathrm{end}} \int_{R}^{R_\infty} \dot{\omega}_{\mathrm{NO_x,tot}}\, 4\pi r^2\, dr\, dt. \tag{5.2}$$

Assuming homogeneous conditions within the reference domain, the NO_x production of the mere exhaust gas atmosphere calculates to

$$m_{NO_x,atm} = \int_{t_0}^{t_{end}} \dot{\omega}_{NO_x,atm} \frac{4}{3}\pi R_\infty^3 \, dt. \tag{5.3}$$

There are no partial derivatives in space in Equation (5.3), and the NO_x production rate $\dot{\omega}_{NO_x,atm}$ can be taken directly from the outer gas phase boundary if it remains unimpaired by droplet combustion. Besides, the droplet volume does not need to be subtracted from the volume of the atmosphere in Equation (5.3) because, by definition, the impact of the presence of the droplet is investigated. This convention even includes small savings in NO_x production for the volume occupied by the liquid phase of the droplet and its boundary layer (see also Fig. 5.1).

This whole approach and the associated data processing are indicated by the term "Droplet NO_x" in the legend of Figure 5.2 below. The term "ref. droplet mass" implies that the initial mass of the fuel droplet is taken as a reference when calculating the emission index of NO_x, EI_{NO_x}, but not the reacting fuel mass (cf. Fig. 5.3).

The temperature and, in particular, the amount of the remaining oxygen in a laminar premixed flame are a function of the equivalence ratio ϕ. While the temperature of the exhaust gas increases with an increase in ϕ (see Fig. 5.2), a continuously decreasing amount of oxygen remains available in the exhaust gas atmosphere. Consequently, only lean combustion can be considered here, which is $\phi \in [0,1]$. Still, both parameters have a significant influence on droplet combustion. On the one hand, a high ambient temperature leads to an even higher flame temperature, and thus promotes NO production (see also Fig. 2.7). On the other hand, there is a decreasing amount of oxygen and an increasing fraction of thermal ballast stemming from the initial premixed flame with an increase in ϕ. These reduce the adiabatic flame temperature, thereby retarding the NO_x formation process. These two effects are conflicting here, and the result becomes apparent in Figure 5.2 with the maximum temperature during droplet combustion approaching the initial temperature before droplet combustion: For exhaust gas under stoichiometric conditions ($\phi = 1.0$), no droplet combustion could even occur in the second, main step because there is no oxidizer left. In a first estimate, all NO_x is formed in the exhaust gas atmosphere and none due to the presence of the droplet. In the

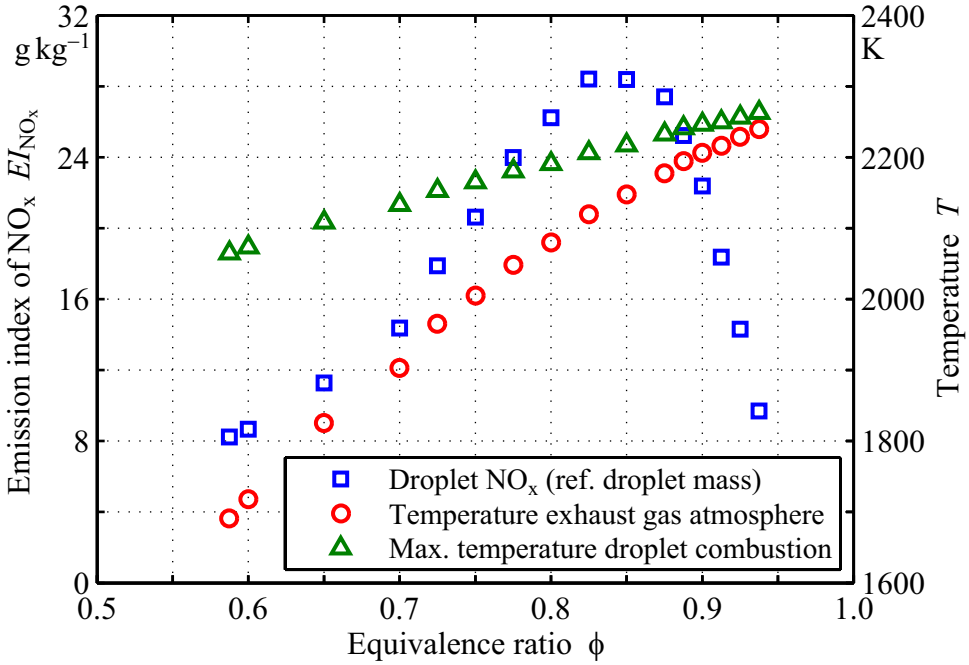

Figure 5.2: Emission Index of NO_x for an n-Decane Droplet in Hot Exhaust Gas as a Function of the Equivalence Ratio and Temperature. The emission index EI_{NO_x} is shown for a droplet diameter of $D_0 = 100\mu m$. Furthermore, the correlation between equivalence ratio ϕ and exhaust gas temperature T_0 of the preceding premixed flame is illustrated.

opposite case ($\phi \rightarrow 0.5$), the equivalence ratio is below the lower flammability limit of the primary premixed flame, and there is no combustion possible either. Besides, the ambient temperature becomes too low for auto-ignition. Consequently, the maximum of the droplet-caused NO_x emissions appears in between those two limiting cases. In the interval of $\phi = 0.810$ to 0.875, the NO_x emissions are very high but vary only little in ϕ. Still, the maximum of the emission index EI_{NO_x} can be located at an equivalence ratio around $\phi = 0.825$.

Thus, a trade-off for low NO_x emissions may also be found within the design of technical applications. For instance, in staged combustion and by employing fuel scheduling, airblast atomization, partial premixing, and lean combustion, it is feasible to optimize the pilot stage towards a minimum of CO and UHC emissions, while the main stage is optimized for lean combustion at full power to achieve low emissions of NO_x and soot [241].

5.2 Combustion of Partially Pre-Vaporized Droplets

In this second configuration, droplets are partially pre-vaporized in an atmosphere of air at moderate ambient temperatures before initiation of the actual combustion process. A temperature level of $T_\infty = 500\,\mathrm{K}$, below the auto-ignition point, is chosen as the reference here. The pressure is atmospheric ($p = 1\,\mathrm{bar}$). The following results are based on experimental as well as numerical work. The experimental results are obtained with the setup as introduced in Chapter 3 for linear droplet arrays. The numerical results are generated by use of the single droplet model of Chapter 4.5, including ignition modeling by an external heat source, which in turn is outlined in Chapter 4.3. For both, experiments and numerical simulations, spherically symmetric droplets can be presumed as well as absence of gravity and forced convection.

The pre-vaporization rate Ψ is the main parameter characterizing this droplet combustion regime. It was introduced by Equation (1.1) and can be resumed in compact notation by

$$\Psi = 1 - \frac{\rho_{l,\Psi}\,\frac{\pi}{6}D_\Psi^3}{\rho_{l,0}\,\frac{\pi}{6}D_0^3}. \tag{5.4}$$

Here, a variation of density is introduced for the respective droplet masses.

5.2.1 Numerical Results on Single Droplet Combustion

The emission index $EI_{\mathrm{NO_x}}$ is shown in Figure 5.3 as a function of the pre-vaporization rate Ψ. The results of this figure are obtained exclusively from numerical simulations with droplets of an initial diameter of $D_0 = 100\,\mu\mathrm{m}$. Here, the numerical domain is modeled large enough so that Dirichlet boundary conditions can be applied for temperature, pressure, and mass fractions at $r = R_\infty$. The initial values of temperature T_0 and species mass fractions $Y_{m,0}$ are uniform block profiles. Thus, boundary and initial conditions of temperature are set to the reference value of 500 K. The respective species mass fractions are initialized according to the composition of air at reference conditions [190]. Heat introduction and extraction is enforced at fixed positions according to Figure 4.3. As heat introduction during the ignition phase is limited to a narrow region, steep temperature gradients are expected. For this reason, the

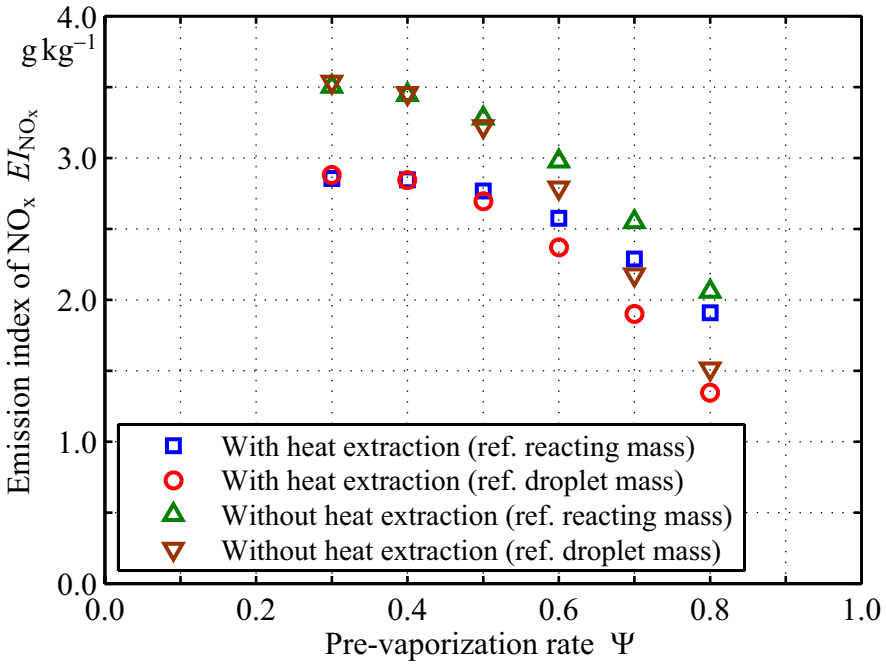

Figure 5.3: Emission Index of NO_x as a Function of Pre-Vaporization Rate. The initial droplet diameter of the illustrated simulation runs is set to $D_0 = 100\,\mu m$. The positions of heat introduction and extraction are set to the constant values of $r_{m,in} = 0.8\times10^{-3}\,m$ and $r_{m,ex} = 1.4\times10^{-3}\,m$, respectively [298].

gas phase is discretized with $N = 200$ grid points, twice as many as used for the configuration discussed in Chapter 5.1. Apart from that, the production of NO_x remains negligible in the outer radius of the gas phase because of moderate ambient temperatures of the burning regime investigated. The emissions caused by mere droplet combustion are equivalent to the total emissions here (cf. Eqs. (5.1) and (5.2), i.e. $m_{NO_x,atm} \approx 0$) [297, 298].

Baessler et al. [31, 32] reported that pre-vaporization of fuel spray becomes beneficial with respect to NO_x formation only if the degree of vaporization is above a minimum limit and combustion is run in the lean regime. If insufficient fuel is vaporized before ignition, the NO_x emissions stay almost unaffected. This correlation is clearly observable in the results reprinted in Figure 2.3. The numerical simulations discussed here reproduce this trend for single droplets, and its characteristics are reflected in detail in Figure 5.3. Squares and circles indicate setups in which heat is introduced into the computational domain to enforce ignition and where it is also extracted after a characteristic time to keep the energy balance (cf. Figs. 4.2 and 4.3). For comparison, the triangles mark emissions if heat is introduced only but not ex-

tracted. The amount of fuel referred to is either the reacting fuel mass, that is consumed until simulation end (Eq. (4.46)), or the initial mass of the droplet.

In general, NO_x emissions are almost constant for $\Psi < 0.5$. This tendency suggests that combustion behavior is similar in this range. As the radial profile of the fuel mass fraction $Y_{C_{10}H_{22}}(r)$ is steep in the gas phase, the amount of flammable, premixed gas is low. Most of the pre-vaporized fuel is oxidized in a diffusion flame. However, at large degrees of pre-vaporization ($\Psi > 0.5$), the amount of fuel under flammable, partially premixed conditions increases. Immediately after ignition, the flame type tends more and more towards a premixed flame. The NO_x emissions decrease. Besides those effects due to fuel premixing and pre-vaporization, the temporal and spatial scales are important in terms of NO_x formation, as well. Their impact is discussed in detail in the context of the verification of the ignition position (Chap. 5.2.2).

As can be seen in Figure 5.3, it is not relevant to distinguish between the two fuel masses referred to within one and the same ignition method, as long as the pre-vaporization rate is low ($\Psi < 0.5$). However, this becomes important for larger values of Ψ. Comparing the two referencing methods, the emission index EI_{NO_x} generally decreases with an increase in Ψ, which is due to an overall decreasing NO_x production. Still, it decreases at a slower rate, when referring to the reacting fuel mass instead of to the initial droplet mass. This trend is not an indicator of insufficient convergence. Vaporized fuel simply diffuses outwards in the radial direction. Thus, with an increase of Ψ, more gaseous fuel is shifted towards regions with an equivalence ratio remaining below the lower flammability limit. This fuel is lost as far as the spherical droplet flame is concerned. However, given an appropriate design of the combustion zones within a technical application, it can be consumed in the subsequent combustion zone at a lower partial pressure of oxygen, resulting in a significant overall NO_x reduction.

5.2.2 Impact of Ignition Position

Generally, heat introduction to initiate ignition is conducted within a region spanned by the flammability limits and their outer proximities, taking a wide variation of droplet pre-vaporization Ψ as a basis. Two feasible approaches are outlined in the related model description of Chapter 4.3. The first approach

uses constant spatial positions for heat introduction and extraction. It is the basis for the results of Chapter 5.2.1. The second approach enforces ignition at a position $r_{m,\mathrm{in}}$ of constant local equivalence ratio ϕ_r (cf. Eq. (4.42)). Here, the effective local equivalence ratio is fixed to $\phi_r = 0.5$. The advantage is to ensure a safe ignition for all degrees of vaporization Ψ without receiving overlapping volumes of droplet and heat source, which can become crucial particularly at low values of Ψ. Since the heat source is distributed over a finite volume around $r_{m,\mathrm{in}}$, heat is also introduced at positions where $\phi_r > 0.5$. This ensures a safe ignition. The results of this second approach are discussed in the present chapter and compared with the previous results of Chapter 5.2.1.

For the heat extraction following a successful ignition, two different cases are considered: In the first case, a spatially fixed position of the heat extraction (i.e. the heat sink in Fig. 5.4) of $r_{m,\mathrm{ex}} = 1.4\times10^{-3}\,\mathrm{m}$ is used in combination with all ignition positions $r_{m,\mathrm{in}}$ (i.e. the heat source in Fig. 5.4). This case of heat extraction is termed “heat sink at fixed position”. In the second case, the position of the heat extraction $r_{m,\mathrm{ex}}$ is coupled to the (variable) ignition position $r_{m,\mathrm{in}}$ by the fixed distance of $0.6\times10^{-3}\,\mathrm{m}$. This latter case of heat extraction is termed “heat sink at fixed distance” [297].

Differences of the Approaches Applied for Ignition Modeling

The resulting mean positions of heat introduction, $r_{m,\mathrm{in}}$, and heat extraction, $r_{m,\mathrm{ex}}$, are depicted in Figure 5.4 as a function of pre-vaporization rate Ψ. The positions of $r_{m,\mathrm{in}}$ are marked with squares for heat sources, whereas the positions of $r_{m,\mathrm{ex}}$ are marked with circles for heat sinks. As introduced in Chapter 4.3 and Figure 4.3, the expansion of the respective volumes $V_{\mathrm{in/ex}}$ (Eq. (4.36)) is indicated in Figure 5.4 by vertical bars, ranging from r_{min} (Eq. (4.37)) to r_{max} (Eq. (4.38)). Even though these limiting minimum and maximum positions vary with Ψ, depending on the mean positions $r_{m,\mathrm{in/ex}}$, the effective volumes of heat introduction and extraction are of constant size. Starting from a low pre-vaporization rate of $\Psi = 0.15$, Figure 5.4 unveils a shift of the ignition position away from the droplet until a maximum is reached around $\Psi = 0.7$. Furthermore, an overlap can be identified between heat introduction and extraction volume in the range of $\Psi = 0.15$ to 0.4. For comparison, the fixed positions as employed in Chapter 5.2.1 are shown on the right hand side of Figure 5.4.

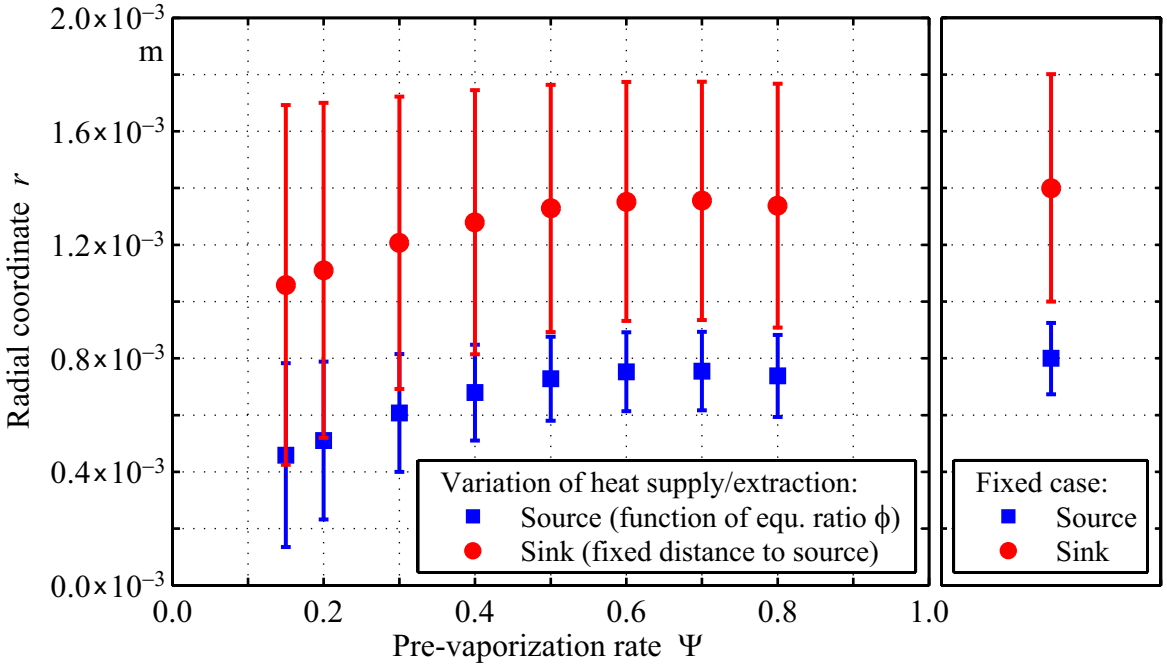

Figure 5.4: Position of Mean Radius for Ignition and Heat Extraction. The left hand side shows the parameters $r_{m,\mathrm{in}}$ and $r_{m,\mathrm{ex}}$ associated to the local equivalence ratio $\phi_r = 0.5$ as a function of the pre-vaporization rate Ψ. The fixed values used in Chapter 5.2.1 are plotted for comparison on the right-hand side [297].

Significance of Ignition Position to Pre-Vaporization and NO_x Formation

The position of the heat source $r_{m,\mathrm{in}}$ has to be carefully evaluated and, under certain circumstances, the amount of heat introduced, Q, may have to be adapted to achieve safe ignition. This becomes relevant particularly when changing geometry. However, changing $r_{m,\mathrm{in}}$ and Q has a significant influence on NO_x emissions. Therefore, this chapter is dedicated to the comparison of the two ignition approaches outlined here. To allow a direct comparison, droplets of a fixed size of $D_0 = 100\,\mu\mathrm{m}$ are considered here, and boundary as well as initial conditions are set identical to the previous ones of Chapter 5.2.1.

For both ignition approaches, the simulations conducted show a general decrease in NO_x formation with an increase in pre-vaporization rate Ψ (Fig. 5.5). Nevertheless, the results regarding flame stabilization and NO_x formation reveal a high sensitivity to the parameters of the ignition model. During the initial stages of droplet burning, the ignition position strongly dominates combustion including the flame stand-off ratio. On the other hand, the impact of

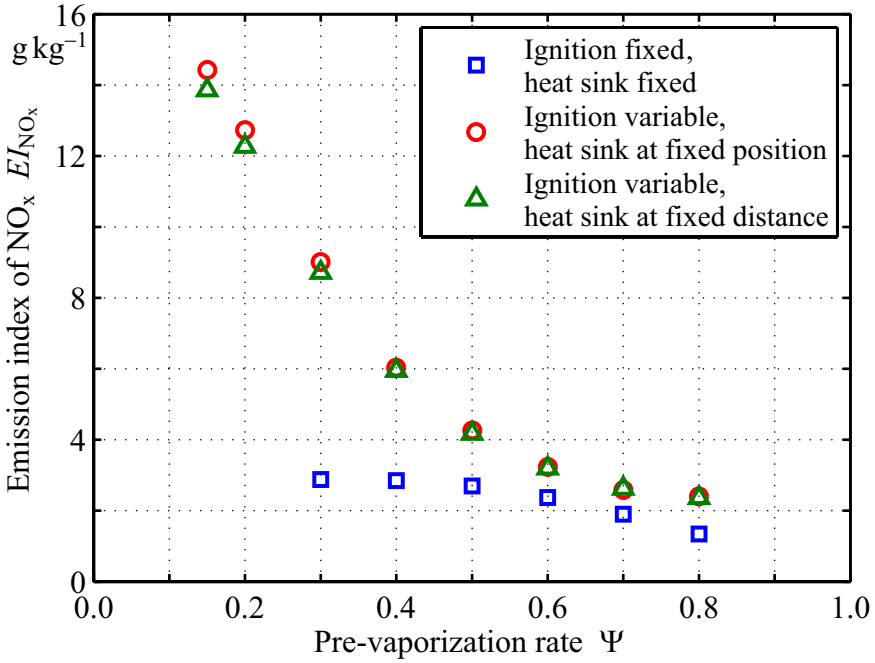

Figure 5.5: Emission Index of NO_x for Different Ignition Approaches. The emission index EI_{NO_x} is related to the initial droplet mass $m_{fuel,0}$ and shown as a function of pre-vaporization rate Ψ (cf. Fig. 5.3 and B.2). The initial droplet diameter, before pre-vaporization, is set to $D_0 = 100\,\mu m$ [297].

position and expansion of the heat extraction volume V_{ex} is marginal with regard to flame position and relative NO_x production. This is due to the larger radial distance of $r_{m,ex}$, the overall wide stretch of V_{ex}, and the low values of the volumetric heat sink $\dot{q}_v$ [297]. Figure 5.5 opposes the emission indices EI_{NO_x} calculated for the investigated methods of heat introduction and extraction to one another. Squares depict emissions for the case of heat introduction and extraction at the constant positions $r_{m,in} = 0.8\times10^{-3}\,m$ and $r_{m,ex} = 1.4\times10^{-3}\,m$, respectively. Circles show emissions for an ignition at $\phi_r = 0.5$ and a fixed heat extraction at $r_{m,ex} = 1.4\times10^{-3}\,m$ ("ignition variable, heat sink at fixed position"). Triangles also indicate emissions for an ignition position at $\phi_r = 0.5$ but a fixed heat extraction distance from this ϕ_r-position ("ignition variable, heat sink at fixed distance") [297].

A large difference emerges in the absolute values of EI_{NO_x} for the two different ignition approaches (Fig. 5.5). The emissions are significantly higher for the spatially variable ignition ($\phi_r = 0.5$), and an increase of fuel pre-vaporization results in continuous NO_x reduction. A significant NO_x reduction seems to be feasible in the range of $\Psi = 0.15$ to 0.6. However, the real potential for NO_x

abatement depends on the actual heat introduction and the correct modeling thereof. Figures 5.6 through 5.9 clarify the processes of ignition and NO_x formation, employing the maximum temperature T_{max} and the overall NO_x production rate $\dot{\omega}_{NO_x}$. T_{max} refers to the whole computational domain, and weighting of the NO_x production is realized according to the calculation of the emission index EI_{NO_x}. Comparing Figures 5.6 and 5.7, the different progress of T_{max} is apparent. It is due to the particular positions of $r_{m,in}$ but not to the choice of the respective ignition approach per se. While Figure 5.6 exposes a clear undershoot of T_{max} at $t = 0.5\times10^{-3}$ s for all curves of Ψ, this phenomenon diminishes to a lower deviation in Figure 5.7. In exchange for this, there is a more prominent peak of T_{max} in Figure 5.7 around $t = 0.4\times10^{-3}$ s. The difference ΔT_{max} between both figures at this point culminates in 1195 K for $\Psi = 0.3$. The radial position of heat introduction $r_{m,in}$ is responsible for these results. Here, it is the determining factor for the period of heat introduction as well as the initial stages of droplet burning until flame stabilization. Those results substantiate the assumption of different levels of ignition. In either case, heat introduction is sufficient to initiate ignition and maintain combustion. In Figure 5.6, however, the external heat introduction only triggers ignition by enforcing a kind of "pre-ignition" or first stage of ignition. The whole droplet regime is lifted to a higher energy level, fuel vaporization is accelerated, and fuel consumption is established. The automatic decrease of the heat flow $\dot{Q}_{in}$ towards the end of heat introduction after all causes a setback to this process. Still, the droplet is capable of maintaining combustion by itself due to the heat release and radical pool of its "pre-flame". As can be seen in Figure 5.6, the enforced pre-ignition and actual "main ignition" are well-balanced for all Ψ investigated. Conversely, ignition occurs completely without any time lag in Figure 5.7. The external heat introduction inflates the maximum temperature T_{max}, which rises 760 K above the adiabatic flame temperature of $C_{10}H_{22}$ ($T_{ad} = 2368$ K for $T_u = 500$ K) [300, 443]. As a result, droplet lifetime decreases and NO_x production escalates, with the latter being a major function of the thermal NO pathway [471, 472]. The approach of spatially fixed ignition only shows a minor peak of NO_x formation within the period of heat introduction (Fig. 5.8), whereas the one of spatially variable ignition unveils the main peak at this point (Fig. 5.9). The weighted NO_x production rate $\dot{\omega}_{NO_x}$ differs by almost three orders of magnitude, especially for $\Psi = 0.3$. This shifts the core of NO_x formation to the initial stages of droplet burning, and this is also reflected in the results of Figure 5.5.

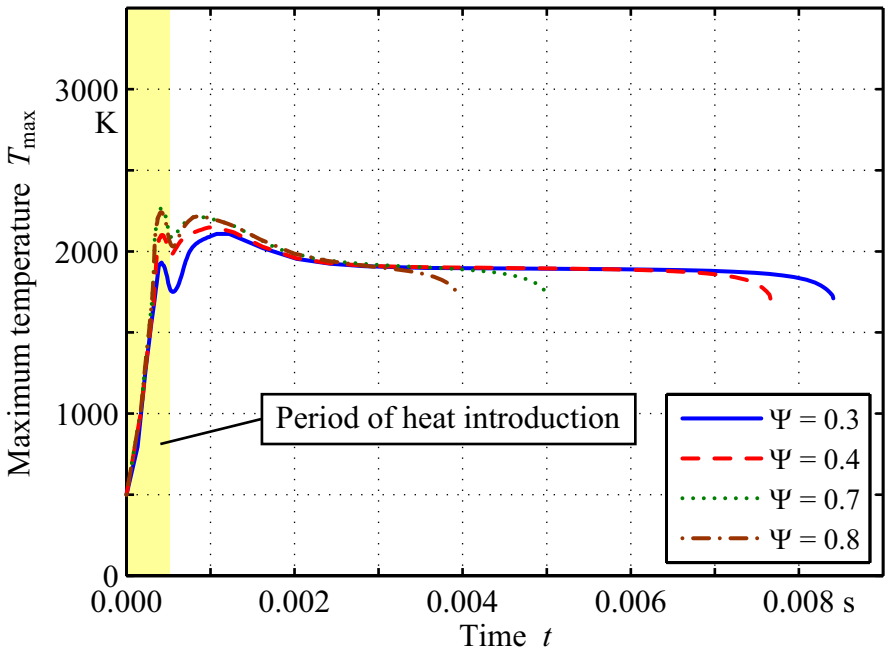

Figure 5.6: Evolution of Maximum Temperature for Spatially Fixed Ignition. The maximum temperature T_{max} is plotted against time t considering the whole computational domain. Heat introduction is performed at $r_{m,in} = 0.8 \times 10^{-3}$ m.

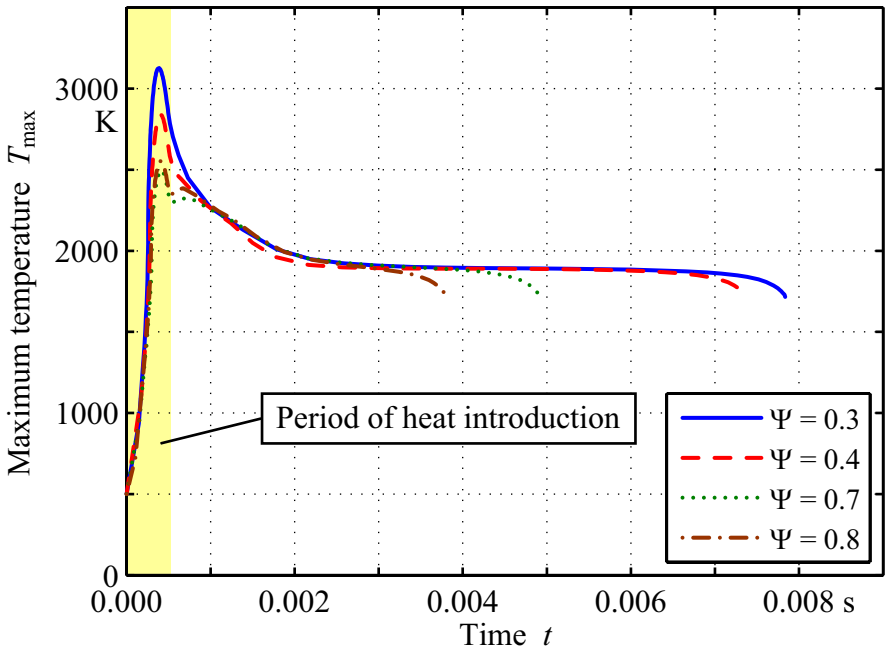

Figure 5.7: Evolution of Maximum Temperature for Spatially Variable Ignition. The maximum temperature T_{max} is depicted as in Figure 5.6 but based on the ignition method with a variable heat introduction $r_{m,in}$ at $\phi_r = 0.5$.

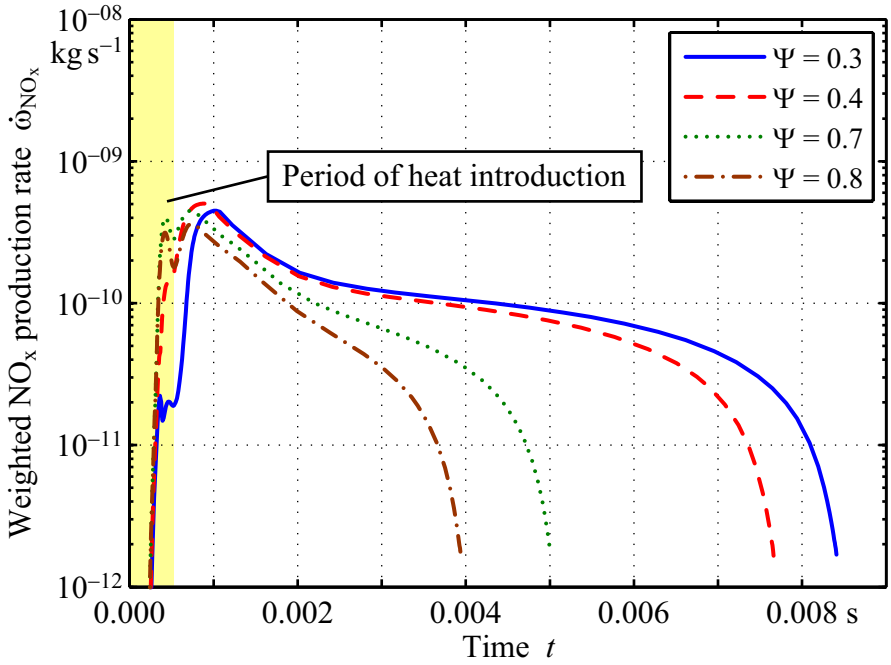

Figure 5.8: Evolution of Weighted NO_x Production for Spatially Fixed Ignition. Figure 5.6 shows the profile of the corresponding maximum temperature T_{max}. Here, the NO_x production rate $\dot{\omega}_{NO_x}$ is normalized with the molar mass of NO_2.

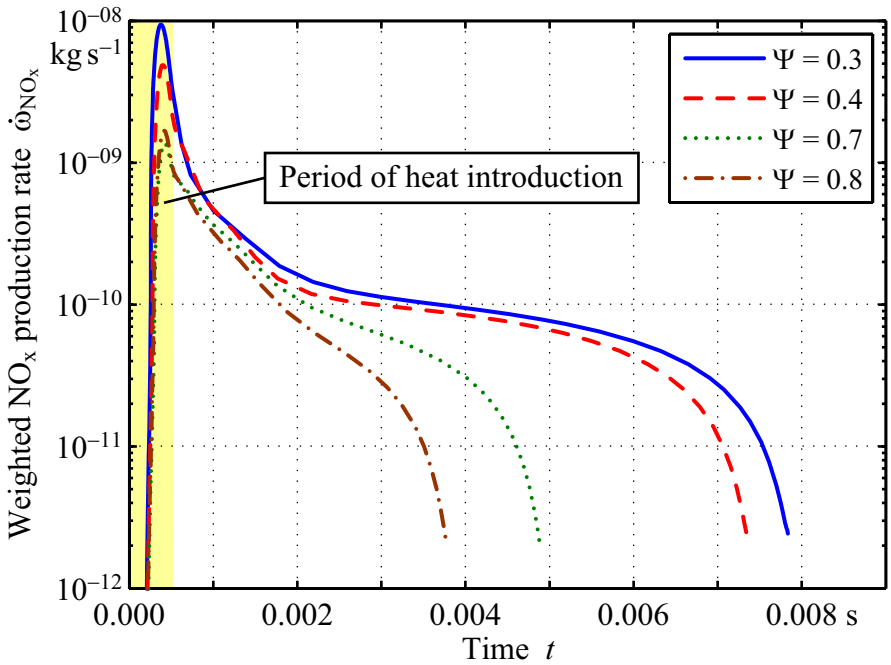

Figure 5.9: Evolution of Weighted NO_x Production for Spatially Variable Ignition. Figure 5.7 shows the associated profile of T_{max}. In line with Figure 5.8, the NO_x production rate $\dot{\omega}_{NO_x}$ is normalized with the molar mass of NO_2.

Even though the parameter set of $\phi_r = 0.5$, selected for the spatially variable heat introduction, yielded unrealistic NO_x values at lower degrees of droplet vaporization, the basic approach to couple $r_{m,\mathrm{in}}$ with the constant local equivalence ratio ϕ_r may still be adequate for combustion modeling including NO_x formation. The parameter ϕ_r could be set, for instance, to a lower value than 0.5. However, the decisive point in the end is the correlation between pre-vaporization Ψ and local equivalence ratio ϕ_r as depicted in Figure 4.4. As the amount of heat introduced for ignition, Q_{in}, and the associated volume V_{in} are kept constant here, the parameters $\Delta r_{m,\mathrm{in}}$ and $\dot{q}_{v,\max}$ vary with the mean position $r_{m,\mathrm{in}}$ according to the constraints of the ignition model (see also Fig. B.1). It is possible to analyze the variations of the mean radius $r_{m,\mathrm{in}}$, offset radius $\Delta r_{m,\mathrm{in}}$, maximum volumetric heat source $\dot{q}_{v,\max}$, and resulting emission index $EI_{\mathrm{NO_x}}$. The approach of spatially fixed ignition is used as the reference here (see Fig. 5.3 as well as Fig. 5.5, "ignition fixed, heat sink fixed"). Table 5.1 lists the respective deviations for different values of Ψ. Yet a small shift of $r_{m,\mathrm{in}}$ results in a considerably different NO_x production. Supposing a shift of the ignition position by 5.6 % towards the droplet ($\Psi = 0.7$) leads to an increase in $EI_{\mathrm{NO_x}}$ by 36.5 %. Consequently, forced ignition has to be realized at a position where stable droplet burning can be maintained but NO_x formation still remains at moderate levels.

Table 5.1: Impact of Ignition Approach on Ignition Key Parameters and Resulting NO_x Emissions. All ignition parameters and the calculated emission index $EI_{\mathrm{NO_x}}$ are given in relation to the results of spatially fixed heat introduction at $r_{m,\mathrm{in}} = 0.8\times10^{-3}$ m. The heat extraction position is consistent within this comparison with $r_{m,\mathrm{ex}} = 1.4\times10^{-3}$ m ("heat sink at fixed position").

Pre-vaporization rate Ψ	0.3	0.4	0.5	0.6	0.7	0.8
Relative variation of:						
Mean radius of heat introduction $r_{m,\mathrm{in}}$ in %	−24.1	−15.1	−9.0	−5.9	−5.6	−7.8
Offset radius $\Delta r_{m,\mathrm{in}}$ in %	68.4	36.9	20.0	12.5	11.9	17.0
Maximum volumetric heat source $\dot{q}_{v,\max}$ in ‰	13.4	5.3	2.4	1.6	1.4	2.0
Emission index $EI_{\mathrm{NO_x}}$ in %	213.4	113.0	58.0	36.9	36.5	78.3

Impact of Ignition Position on General Droplet Burning Behavior

The flame stand-off ratio, being a major characterization criterion of droplet burning, by itself is a key indicator for the quality of droplet combustion. Thus, it was also consulted in the verification of the present results. Cho and Dryer [74], for instance, identified four different stages of droplet burning. In order to compare the burning regimes of droplets of different sizes, the dimensionless flame stand-off ratio ζ is employed (Eq. (5.5)). It correlates the actual flame position r_f with the respective droplet radius R. In this context, the flame position r_f is associated with the maximum specific heat release of the reaction zone. The specific heat release, $\sum_{m=1}^{N} \dot{\omega}_m h_m^0$, in turn, is part of the energy conservation (Eq. (4.6) or (4.52)).

$$\zeta = \frac{r_f}{R} \tag{5.5}$$

Since the droplet combustion under consideration is initiated by forced ignition, heat introduction and extraction play an essential role. However, as a result of the verification process, both heat transfer processes only have a minor impact on the overall droplet burning behavior. This is essential for the general validity of the numerical results [297].

A representative evolution of the flame stand-off ratio ζ is plotted in Figure 5.10 for both ignition approaches and a pre-vaporization rate of $\Psi = 0.3$. It sheds light on the position of maximum specific heat release and its dependency on the ignition position $r_{m,\mathrm{in}}$. The absolute times and, thus, the progression of ζ are directly comparable in Figure 5.10. At the beginning, the flame is located at the position of heat introduction with $r_{m,\mathrm{in}}/R \approx 18$ for "ignition fixed" and $r_{m,\mathrm{in}}/R \approx 14$ for "ignition variable". However, the flame ignited closer to the droplet ("ignition variable") stabilizes more rapidly (cf. also Figs. 5.6 and 5.7). The accelerated ignition process in regions of increased flammability allows a fast movement of the flame to a stable position ζ. This faster flame stabilization, in turn, contributes to the radical difference in NO_x formation (cf. Figs. 5.8 and 5.9). After the two initial stages of vaporization and unsteady burning, the flame stabilizes at a virtually constant position in either case. Towards the end of droplet lifetime, the droplet shrinks more rapidly than the flame position r_f, which causes a rise of the flame stand-off ratio ζ.

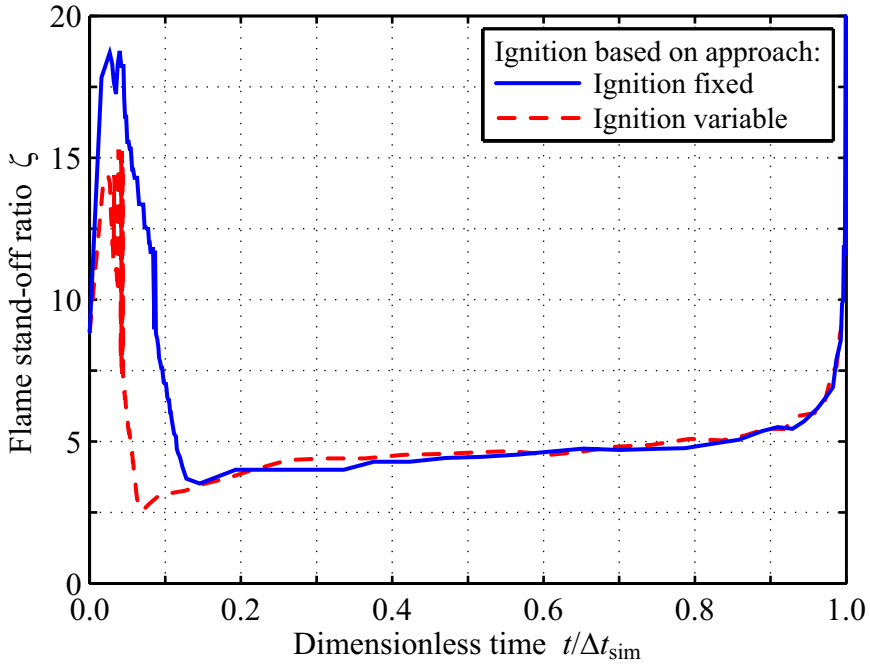

Figure 5.10: Flame Stand-off for Different Ignition Approaches. The flame stand-off ratio ζ is compared for a pre-vaporization rate of $\Psi = 0.3$ [297].

Figure 5.11 clarifies the impact of droplet pre-vaporization and heat extraction on the progress of ζ by showing data for pre-vaporization rates of $\Psi = 0.3$ and 0.7. Vertical auxiliary lines help in recognizing periods of heat introduction and extraction. Here, ignition is carried out with the position $r_{m,\mathrm{in}}$ set to the constant local equivalence ratio $\phi_r = 0.5$. Figure 5.11 also exposes the relative positions $r_{m,\mathrm{in}}/R$ and $r_{m,\mathrm{ex}}/R$ for heat introduction and heat extraction, respectively. Subject to the two different Ψ-values, these relative positions are non-congruent over the dimensionless time $t/\Delta t_{\mathrm{sim}}$. During heat introduction the flame position is close to the mean position $r_{m,\mathrm{in}}$ for both degrees of vaporization. This verifies a successful ignition at the spatial and temporal maxima of the sine profiles employed (Figs. 4.2 and 4.3). The parameter $r_{m,\mathrm{in}}$ can even be used for an exact positioning of the ignition kernel. When the heat Q_{ex} is extracted from the computational domain, the flame position remains unaffected. This confirms the correct choice of the heat extraction position $r_{m,\mathrm{ex}}$ and the size of the respective volume V_{ex}: It is reasonable to remove heat from the exhaust gas outside of the flame zone because the temperature level of these combustion products forces vaporization and ignition of neighboring droplets. Besides, the flame might extinguish if heat is taken directly from the flame zone [297].

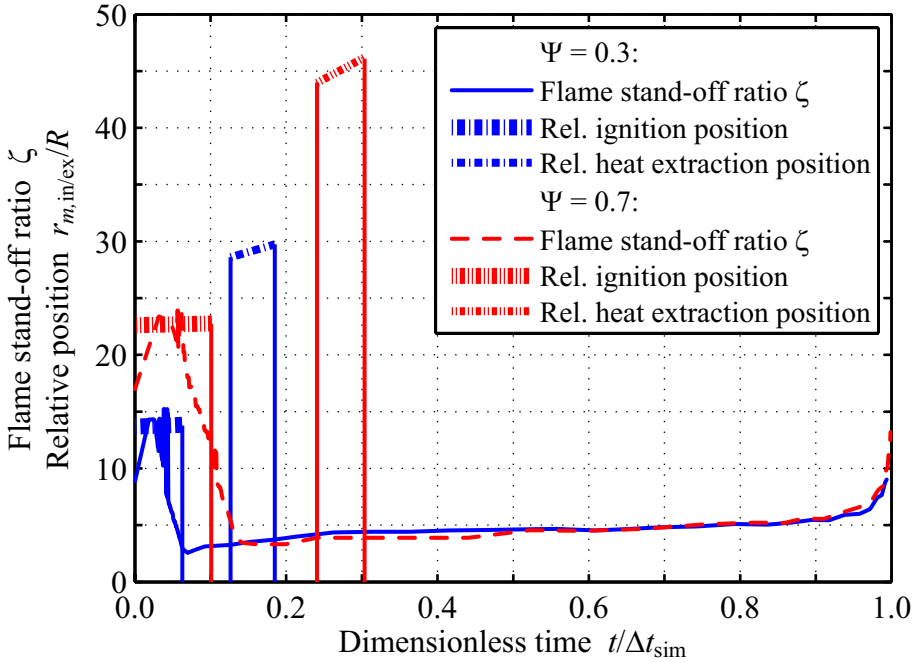

Figure 5.11: Correlation Between Flame Stand-off Ratio and the Positions of Heat Introduction and Extraction [297].

Final Remarks on the Impact of the Ignition Position

The correlations outlined for the initial stages of droplet combustion explain the discrepancies between the two ignition approaches and the NO_x emissions observed. The analysis of the maximum temperature T_{max}, weighted NO_x production rate $\dot{\omega}_{NO_x}$, and flame stand-off ratio ζ in conjunction with pre-vaporized droplets gives a more detailed insight into ignition modeling. It is important to apply the lessons learned from this study in order to obtain a well-founded modeling of droplet ignition within the combustion setup investigated here. The corresponding implementation procedure may require an iterative adaptation of the heat introduction parameters. They should be based on the findings for droplet burning and exhaust gas production. The dominance of the mean radius $r_{m,\mathrm{in}}$ is essential for the entire combustion process during the period of heat introduction. Subsequent to ignition and after a short period of flame stabilization, the impact of the ignition model decays.

5.2.3 Comparison with Microgravity Experiments on Droplet Arrays

There are severe technical limitations on experimental setups regarding the realization of a representative single droplet combustion, combining droplet pre-vaporization and NO_x formation. Thus, the experimental part of the study at hand was carried out to compare and, where possible, validate the numerical results on single droplets by resolving this issue on droplet arrays. Utilizing the environments of parabolic flight, drop tower, and sounding rocket flight, a significant number of experiments were conducted under microgravity conditions (see Tab. B.1). Figure 5.12 clarifies the difference in sequence between physical experiments and numerical simulation. Flame extinction and exhaust gas homogenization are not included in the simulation model, and thus production of thermal NO during this period is not accounted for.

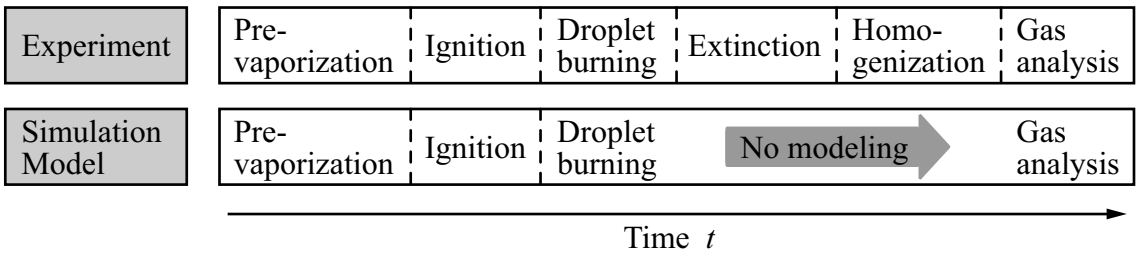

Figure 5.12: Combustion Sequence in Experiments and Numerical Simulation. This schematic is not to scale. The numerical simulations are stopped when the droplet diameter drops below the value $1/1000 D_0$.

A number of separate numerical simulations were conducted to include the heat loss of the combustion chamber induced by the insertion of the cold droplet array holder into the combustion chamber (see Chaps. 3.1.2 and 3.1.3) in the data post-processing. Their purpose is to relate the emission indices $EI_{NO_x}|_{exp,T_\infty=f(\Psi)}$, as measured with the actual temperature history of the experiments (Fig. D.4), to one single preheating level. This temperature level in turn is set to the reference temperature of $T_\infty = 500\,K$. The whole procedure helps to uncouple the effects of preheating on vaporization and NO_x formation. The approach is similar to the one outlined in Baessler et al. [31, 32] but different in that single droplet simulations are used instead of calculations of laminar premixed flames. Equations (5.6) and (5.7) provide the necessary link via the correction factor $f_{EI_{NO_x}}$. The single droplet model (Chapter 4.5) is used to determine $f_{EI_{NO_x}}$ from the full-scale droplet diameter D and the boundary

conditions taken from the experiment runs. Finally, the experimental results on NO_x formation are corrected by $f_{EI_{NO_x}}$, as far as applicable. As highlighted in Table 5.2, there is no linear correlation between pre-vaporization time t_Ψ, gas phase temperature, and NO_x formation. This effect stems from the spatial and, in particular, temporal overlap of the combustible gas region with the external heat supply.

$$f_{EI_{NO_x}} = \frac{EI_{NO_x}|_{sim,T_\infty=f(\Psi)}}{EI_{NO_x}|_{sim,T_\infty=500\,K}} \tag{5.6}$$

$$EI_{NO_x}|_{exp,T_\infty=500\,K} = \frac{EI_{NO_x}|_{exp,T_\infty=f(\Psi)}}{f_{EI_{NO_x}}} \tag{5.7}$$

Table 5.2: Correction Factors for NO Formation as Affected by the Heat Loss of the Combustion Chamber. The measurement readings of Figure D.4 are taken as boundary conditions for the underlying numerical simulations.

Pre-vaporization time t_Ψ in s	Correction factor $f_{EI_{NO_x}}$ ref. to	
	Reacting mass	Droplet mass
0	1.0000	1.0000
5	0.9255	0.9210
10	0.9706	1.0092
15	0.9738	1.1284
18	0.6456	0.9404

Figure 5.13 illustrates the NO_x and CO emissions as measured from the sounding rocket flight samples. In relation to Figure 2.5, the non-dimensional inter-droplet distance S/D_{ign} at ignition is in the range of 12 to 18. Since all precursor experiments included virtually no fuel pre-vaporization and, in addition, have a lower number S/D_0, they are not plotted in Figure 5.13. The CO emissions are given in ppm, as obtained by FT-IR spectroscopy via Standard No. 1 and No. 2 (Tabs. 3.7 and 3.8). The pre-vaporization times investigated were t_Ψ = 5, 10, and 18 s, corresponding to pre-vaporization rates of Ψ = 0.1695, 0.2728, and 0.5378 (cf. Tabs. D.1 through D.3, Method No. 2), when accounting for the density decrease due to droplet heat-up during the initial phase of droplet vaporization (cf. Eq. (5.4)). The raw data of these experiments were

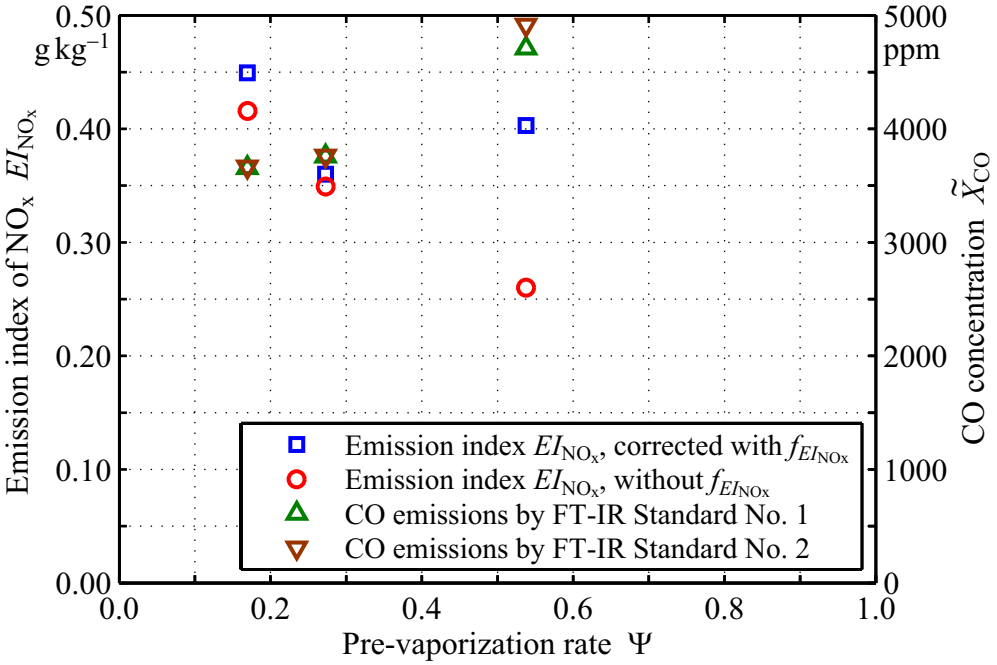

Figure 5.13: Correlation Between Droplet Pre-Vaporization and Emissions of Nitrogen Oxides and Carbon Monoxide. The raw data are published in Moesl et al. [296].

previously presented and discussed by Moesl et al. [296].[2] In addition to the heat loss of the combustion chamber, the secondary effect of fresh air entrainment into the combustion chamber is also accounted for.[3] It is corrected by the dilution factor that is calculated from the amount of carbon-containing species (i.e. CO_2 and CO) by the ratio of concentrations measured and values theoretically obtained at flame extinction. For this purpose, complete fuel consumption is presumed at the moment of flame extinction. In addition, the concentration profiles of the species under investigation are presumed to have a comparable spatial distribution at the moment of exhaust gas sampling. The latter assumption, in turn, necessitates coinciding regions of the exhaust gas formation of those species and/or an equal degree of mixing due

[2] The Ψ-values finally obtained from the sounding rocket flight turned out to be lower than the planned ones because of higher initial droplet diameters, $D_{0,\mathrm{exp}} > D_{0,\mathrm{nom}}$, and a lower, non-constant temperature level T_∞ inside the combustion chamber (see App. D). Consequently, pre-vaporization rates $\Psi \gg 0.5$ were missed by the experiments conducted.

[3] The emission level can also be expressed by the volumetric concentration in parts-per-million for a stated O_2 concentration of 15 %, for instance. This conversion would help in accounting for the effect of fresh air entrainment. However, on the one hand, the oxygen concentration could not be determined via the measurement approach employed, and on the other hand, the emission index $EI_{\mathrm{NO_x}}$ is more significant with respect to droplet combustion than volumetric concentrations (see also Eq. (2.25)).

to diffusion (i.e. during homogenization, Fig. 5.12) and convection (i.e. the gas sampling process).

Figure 5.13 depicts two trends of the NO_x emissions over the pre-vaporization rate Ψ: If the correction factor $f_{EI_{NO_x}}$ is taken into consideration, there is no straightforward linear correlation of the emission index EI_{NO_x} ($\Psi \leq 0.5378$), but it remains at a quasi-constant level. If the correction factor $f_{EI_{NO_x}}$ is not taken into consideration, an almost linear decrease of EI_{NO_x} can be observed with an increase of Ψ, which is in compliance with Moesl et al. [296]. Furthermore, the corrected values of the NO_x emissions are in good qualitative agreement with Figure 2.3 and 5.3 for sprays and single droplets, respectively. Thus, the experimental work at hand confirms the findings of the numerical simulations of Chapter 5.2: A substantial droplet pre-vaporization is required before NO_x emissions can be reduced.

The CO concentrations indicated by using the two FT-IR standards match perfectly for the lower Ψ-values and still very well for $\Psi = 0.5378$ (see also Fig. 5.13). This conformity was expected but is also an indication of high accuracy and data reproducibility of the exhaust gas analysis. The overall exponential increase in CO is due to the formation of a triple flame[4] with an increase in Ψ. The development of the triple flame is significantly triggered by the presence of a combustible gas phase along the droplet array and flame spread through this region as well as thermal expansion thereof. While the degree of fuel vaporization Ψ increases, fuel-rich regions are gradually formed along the droplet array. These rich regions are consumed by the approaching triple flame, and thus tend to be an excessive source of CO production [211, 253, 344, 452]. This particular development of the triple flame structure was also confirmed through visual observation of the flame spread sequence (Fig. 5.14) and numerical work conducted by Kikuchi and coworkers [206, 208].

Figure 5.14 shows sequences of flame spread associated with the emissions of the three experiment runs of Figure 5.13. The images are taken from high-speed recording and cover the field of view from the third to the fifth droplet. The flame front travels from left to right. In all cases, a dim blue flame marks the flame front, propagating into the unburned region. A yellow, luminous

[4] According to van Oijen and de Goey [452], a triple flame is a flame structure generated by flame propagation in a partially premixed system. Typical triple flames comprise a rich and lean premixed flame front and a diffusion flame, all of them intercepting in the triple point. Triple flames are also denoted as tribrachial flames.

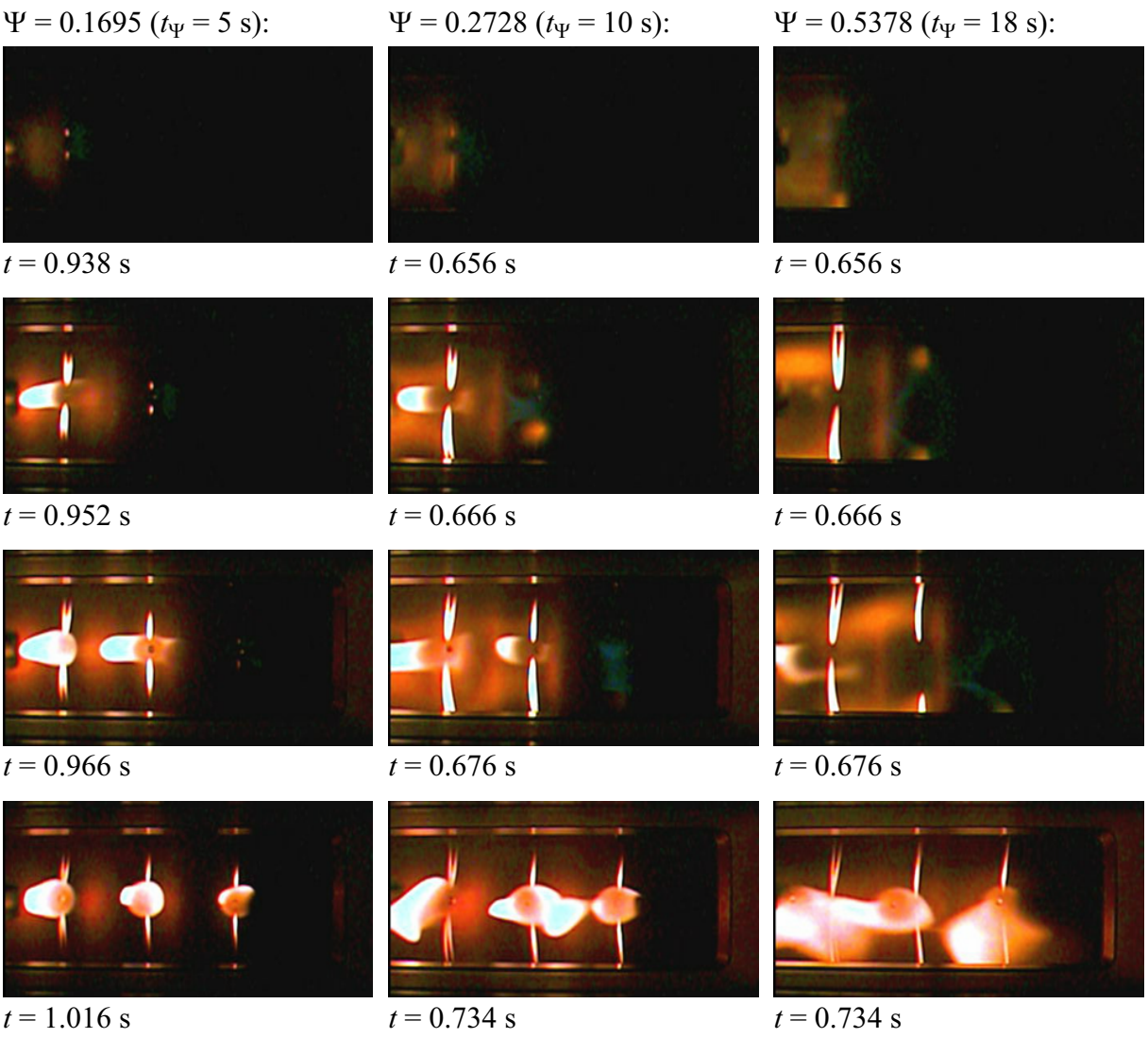

Figure 5.14: Flame Spread Sequence for Different Pre-Vaporization Rates. Flame spread occurs from left to right. Time $t = 0.000$ s corresponds to the start of ignition [208].

flame follows the blue flame region (cf. Chap. 2.1.1). The shape of this luminous flame around each droplet tends to change from a wake flame during its early phase to a quasi-spherical envelope flame for the rest of droplet burning. The observable flattening of the flames in the horizontal direction is a result of a decreased oxygen mass fraction [20]. If the droplets were moved closer, the individual flames would increase in size until they merge and form a common envelope flame or group flame with the droplets at the center simply vaporizing (see Chap. 2.1.3). The area of the visible blue flame is larger for larger pre-vaporization rates Ψ. On the other hand, the brightness of the blue flame appears to be lower for Ψ = 0.5378 than for the other conditions. Additionally,

the initial glowing points of each pair of SiC fibers shift outwards with an increase of Ψ. This indicates a broader width of the spreading flame front due to a further developed fuel vapor layer around the droplet array [208].

5.3 Influence of Ambient Preheating

In order to complement the results of Chapter 5.2, this section isolates the impact of ambient preheating on droplet vaporization and combustion, and furthermore on NO_x formation. Particularly Figures 5.15 and 5.16 provide a more detailed insight into the counteracting parameters of pre-vaporization and preheating within the field of NO_x formation. The curves of temperature with $T_\infty = 500\,K$ are identical to the ones in Figure 5.3 (i.e. the case "with heat extraction"). The temperature levels of 600 and 700 K are plotted in addition here. The results were obtained by numerical simulation.

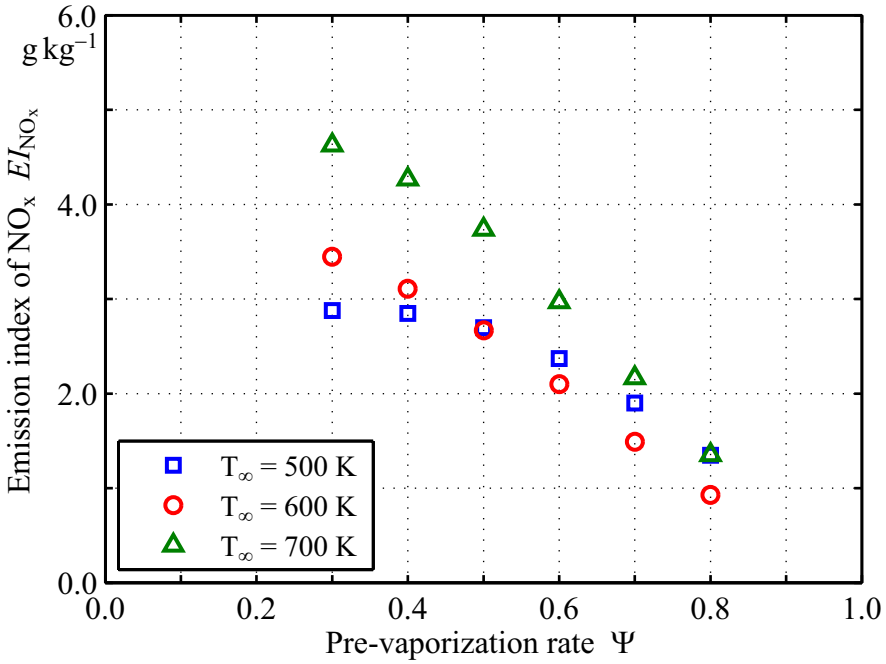

Figure 5.15: Impact of Ambient Preheating on NO_x Abatement Potential due to Pre-Vaporization by Referring to the Initial Droplet Mass. The positions of heat introduction and extraction are set to the constant values of $r_{m,\mathrm{in}} = 0.8\times10^{-3}\,m$ and $r_{m,\mathrm{ex}} = 1.4\times10^{-3}\,m$ (cf. Fig. 5.3).

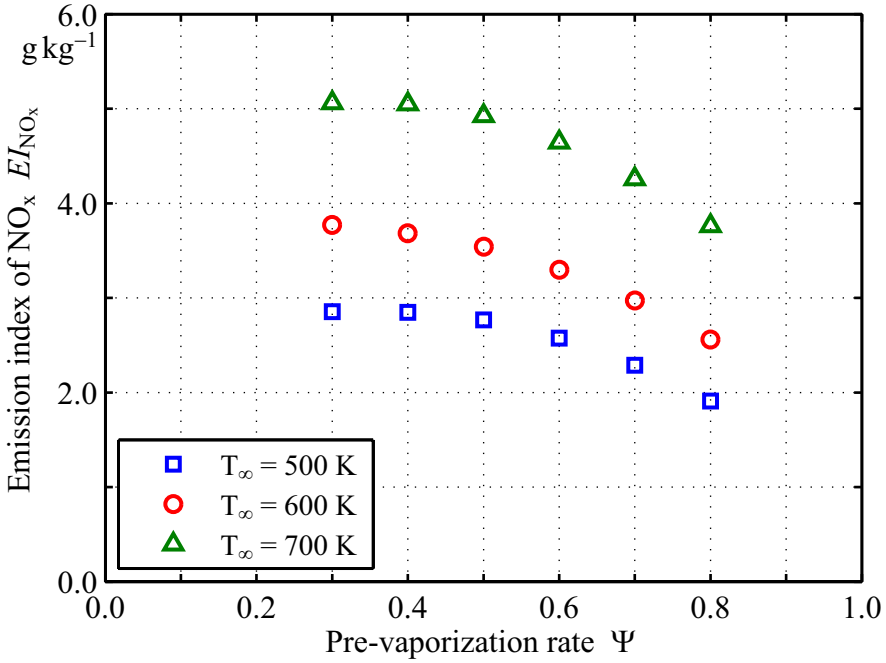

Figure 5.16: Impact of Ambient Preheating on NO_x Abatement Potential due to Pre-Vaporization by Referring to the Reacting Fuel Mass. The positions of heat introduction and extraction are set to the constant values of $r_{m,\mathrm{in}} = 0.8\times10^{-3}$ m and $r_{m,\mathrm{ex}} = 1.4\times10^{-3}$ m (cf. Fig. 5.3).

Emissions altogether are lower when relating the emission index EI_{NO_x} to the initial droplet mass (Fig. 5.15) than to the reacting fuel (Fig. 5.16). Despite the temperature difference of $\Delta T_\infty = 100$ and 200 K, pre-vaporization is capable of compensating the increased NO_x formation at $\Psi = 0.5$ and 0.8, respectively (Fig. 5.15). This is essential, as temperature level and pre-vaporization time are major design parameters that need to be weighed up against each other in the layout of many combustion systems. Furthermore, with an increase in T_∞, the process of obtaining lower NO_x emissions starts at lower degrees of vaporization. This is due to an increased diffusive transport at those higher temperature levels. As pointed out in Chapter 5.2, a certain amount of gaseous, unburned fuel remains in the outer region of the gas atmosphere. This fuel can be consumed in the further course of the combustion process within a technical application. For a preheating temperature of $T_\infty = 700$ K and a pre-vaporization rate of $\Psi = 0.8$, this fuel amount rises up to 278 % of the fuel consumed in the droplet flame. Figure 5.16 shows the NO_x emissions of the droplet after correcting the results for this influence. The trend is uniform for all three temperature levels. The offset of the individual curves alone

increases as a result of the exponential temperature dependency of thermal NO formation (cf. Chap. 2.2.3).

Recalling the results of Chapter 5.1, composition as well as temperature of the droplet atmosphere have a significant impact on the overall NO_x emissions. For this reason, droplets burning in an atmosphere of air are compared with droplets burning in exhaust at different initial temperatures $T_{g,0}$ (Fig. 5.17). Here, droplet combustion is initiated by auto-ignition and no supplementary ignition modeling needs to be employed. Even though this comparison is of a rather academic nature, it adds to the understanding of NO_x formation in droplet combustion[5]. Numerical simulation allows an initialization of the computational domains with identical temperatures for air and exhaust gas. Here, the temperature $T_{g,0}$ roughly ranges from 1690 to 2240 K (cf. Fig. 5.2). Since N_2, O_2, and H_2O are the only species appearing in the air atmosphere modeled, and as their concentration remains constant, temperature is the only parameter that has to be varied within the initial conditions. For droplet

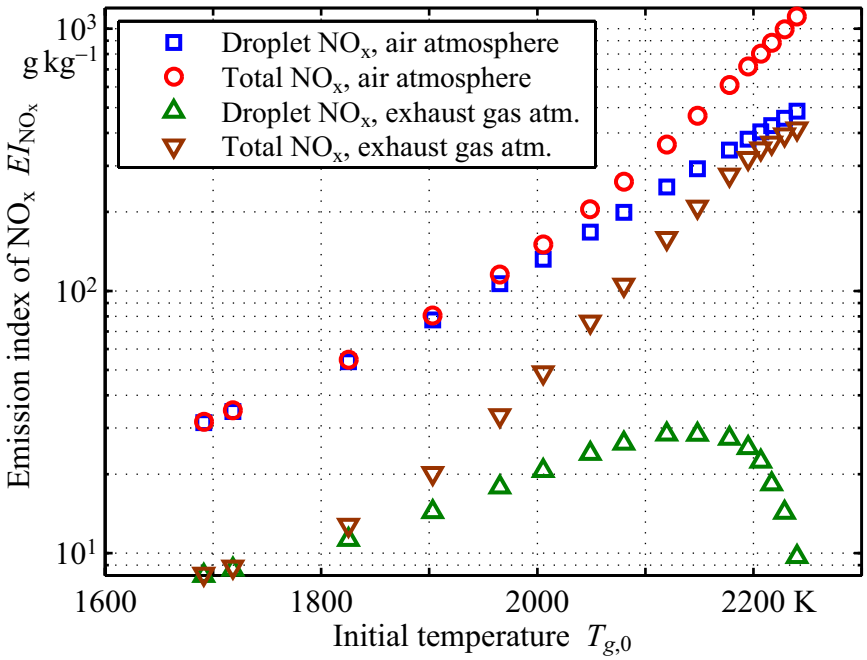

Figure 5.17: NO_x Emissions for Droplets Burning in Atmospheres of Air and Exhaust. The droplet-caused NO_x emissions "Droplet NO_x, exhaust gas atm." are taken from Figure 5.2 and included for comparison purposes.

[5] NO_x emissions in technical fuel sprays can be expected to be significantly lower than the ones of single droplets burning in regular air atmosphere.

combustion in exhaust gas, a set of exhaust gas concentrations and temperatures has to be used as an initial condition.

Figure 5.17 depicts NO_x emissions caused by the droplet exclusively (Eq. (5.1)) as well as the total NO_x emissions of the computational domain accounting for the absolute temperature level. These emissions are identical for both cases of air and exhaust gas atmosphere, as long as $T_{g,0}$ remains moderate ($T_{g,0} < 1800\,\mathrm{K}$). However, in either case the values of "Droplet NO_x" drop off from the ones of "Total NO_x" with an increase in $T_{g,0}$. The availability of the oxidant O_2 is one limiting factor of NO_x formation, too. A further resistance to NO_x formation is thermal ballast, resulting in depressed maximum temperatures (cf. Fig. 5.2). Consequently, the NO_x emissions of droplets burning in exhaust fall short of the ones burning in air of the same temperature.

As a reduction of droplet-caused NO_x in a technical application is a priori supposed to noticeably lower the total NO_x emissions, droplet-caused NO_x must be as a significant portion of the total NO_x emissions. The fraction of droplet emissions Γ_{EI} is a suitable measure in this context. According to Equation (5.8), it is the ratio of the droplet and total emission indices:

$$\Gamma_{EI} = \frac{EI_{\mathrm{NO_x,droplet}}}{EI_{\mathrm{NO_x,tot}}}. \tag{5.8}$$

Figure 5.18 depicts the fraction of droplet emissions Γ_{EI} as a function of the initial temperature $T_{g,0}$. Droplet emissions dominate in both atmospheres for temperatures up to 1800 K but decrease with increasing temperatures. While the fraction Γ_{EI} remains at a high level for air over the whole temperature range, it declines rapidly for exhaust gas around 2000 K. At an initial temperature of $T_{g,0} = 2178\,\mathrm{K}$, which corresponds to $\phi = 0.875$, it drops below 10 %. Hence, a reduction of droplet-caused NO_x in exhaust gas for $\phi > 0.875$ may be less important, when aiming for a reduction of the total NO_x emissions. Nonetheless, reducing NO_x emissions of droplets in exhaust gas for $\phi \leq 0.8$ tends to be efficient. The droplet emission index $EI_{\mathrm{NO_x}}$ is indicated in accordance with Figures 5.2 and 5.17 for comparison.

For the sake of completeness, the flame stand-off ratio ζ (Eq. (5.5)) is shown in Figure 5.19 for droplets burning in the two distinctive atmospheres. In the case of the exhaust atmosphere, extreme ϕ-values were selected for this plot (lean, rich, and maximum of NO_x production; cf. Fig. 5.2). The correspond-

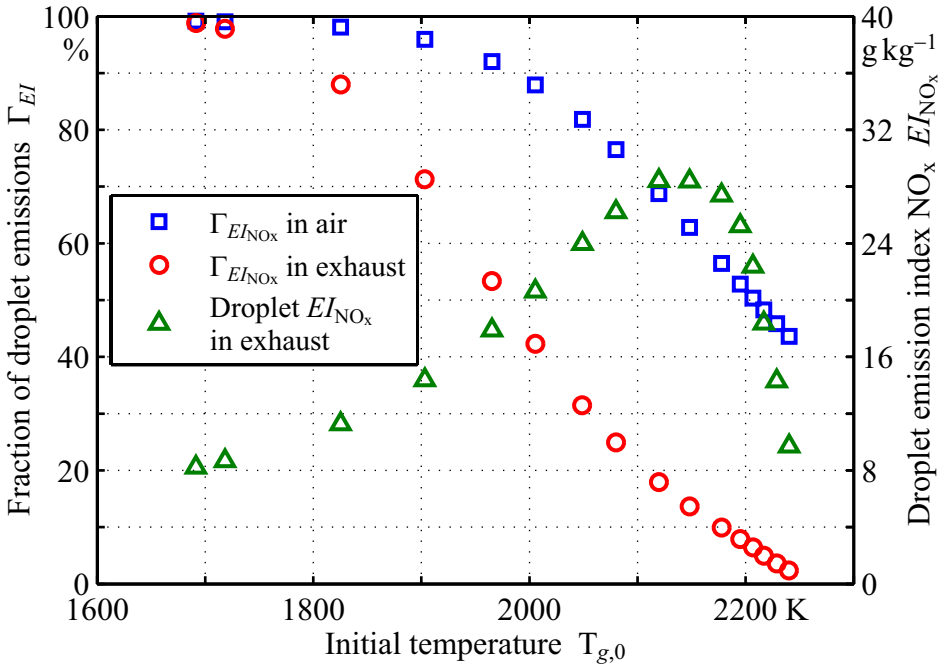

Figure 5.18: Impact of Gas Atmosphere on the Contribution of Droplet NO_x Production to the Overall NO_x Production. The droplet emission index EI_{NO_x} is indicated for comparison (cf. Figs. 5.2 and 5.17).

ing initial air temperatures $T_{g,0}$ were also selected for the case of the hot air atmosphere to allow a direct comparison. Droplet lifetime is related to the dimensionless time $t/\Delta t_{sim}$. The resulting flame stand-off ratio ζ shows similar characteristics for both cases. Deviations within each set of curves are small, which is due to a low impact of the temperature level. For $t/\Delta t_{sim}$ ranging from 0.0 to 0.1, the initial stages of unsteady droplet burning are observable (cf. Fig. 5.10). The stage of quasi-steady droplet burning appears subsequently until $t/\Delta t_{sim}$ reaches 0.8, and ζ remains almost constant with the flame position following the shrinking droplet. At the end of droplet lifetime ($t/\Delta t_{sim} > 0.8$), the droplet shrinks increasingly fast with the flame being unable to follow this trend, resulting in a rapid increase of ζ. However, the most essential aspect of Figure 5.19 with regard to NO_x formation is the discrepancy in the absolute values of ζ for air and exhaust gas. The time-averaged flame stand-off ratio $\overline{\zeta}$ of droplets burning in exhaust ranges from 48 to 70 % above the one of droplets burning in air. Figure 5.20 compares this parameter for the two cases, underlaid with the mole fraction X_{O_2} of excessive oxygen from the initial premixed flame. Assuming that the exhaust gas of this flame only consists of excessive oxygen and inert components, it can be regarded as a diluted

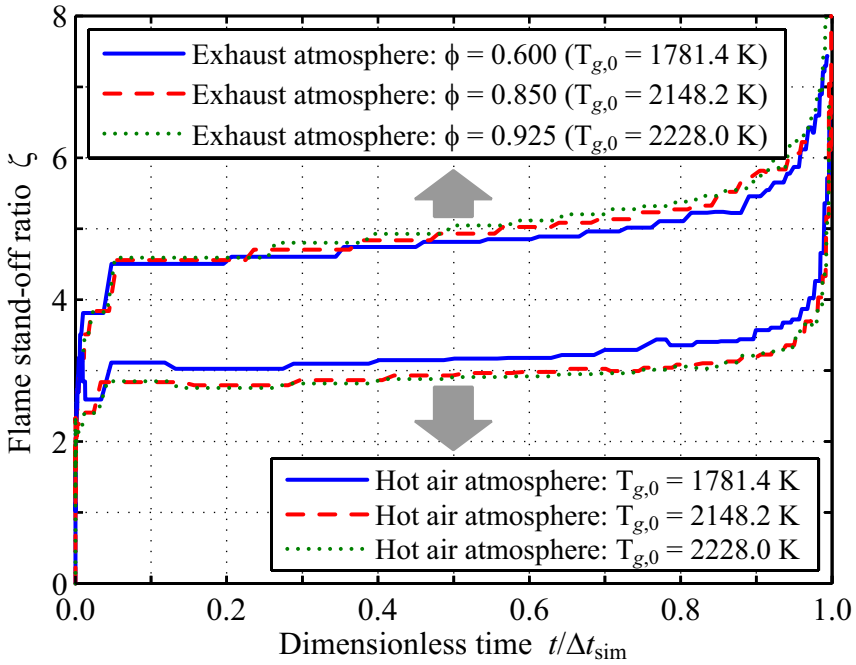

Figure 5.19: Progression of Flame Stand-off for Droplets Burning in Atmospheres of Air and Exhaust. The initial gas phase temperatures are chosen to be identical for the two depicted cases, and they correspond to the exhaust atmosphere of a premixed flame of the equivalence ratio ϕ = 0.600, 0.850, and 0.925.

oxygen atmosphere. As illustrated in Figure 5.20, a decrease of its oxygen concentration causes an increase in the time-averaged flame stand-off ratio $\overline{\zeta}$. On the other hand, an increase of $T_{g,0}$ only leads to a slight decrease of $\overline{\zeta}$ for air atmospheres with a constant concentration of oxygen. Thus, the decrease in oxygen dominates the parameter $\overline{\zeta}$ over the increase in temperature. Since the flame in this case is shifted away from the droplet surface, the droplet's influence on NO_x formation declines and the gas atmosphere gains predominance (cf. Fig. 5.18). Generally, the flame stand-off ratios of the present study are altogether consistent with literature. Similar results on the impact of atmosphere dilution are reported by Bae and Avedisian [30], Dietrich et al. [102], and Jin and Shaw [198]. For the influence of the initial temperature $T_{g,0}$, similar effects can be observed in the studies of Jackson and Avedisian [192], Xu et al. [465, 467], and Cuoci et al. [92], despite major variations of the initial droplet diameter.

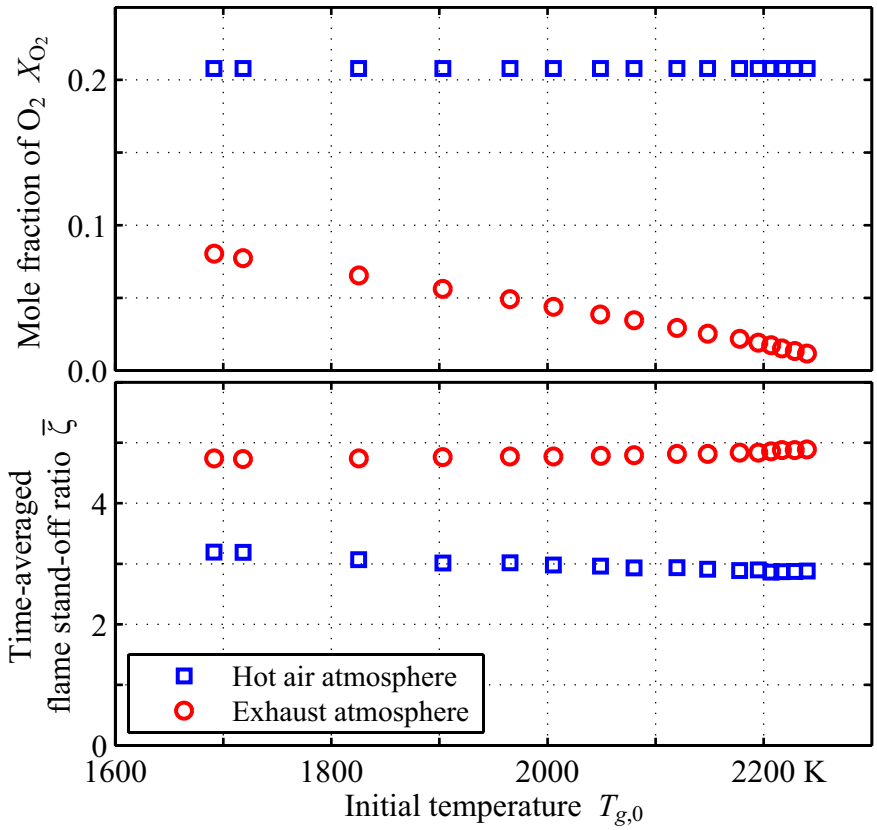

Figure 5.20: Dependence of Flame Stand-off on Temperature and Initial Oxygen Concentration. The time-averaged flame stand-off ratio $\overline{\zeta}$ indicates the flame position, and the initial mole fraction of oxygen X_{O_2} stands for the ratio of oxidant and inert gas.

5.4 Influence of Droplet Size

Generally, a practical spray can be regarded as a spectrum of droplets of different sizes. For technical atomizers, this spectrum typically ranges from a few micrometers up to around 500 µm [244]. Since the combustion characteristics of such a spray vary considerably with the prevailing mean droplet size and droplet size distribution, this section rounds off the parameters considered here and relevant to NO_x formation, that can be influenced by technical means. The results were obtained from numerical as well as experimental studies, and single droplets as well as droplet arrays were investigated.

Chapter 5.1 describes droplets burning in the atmosphere of hot exhaust gas of different equivalence ratios ϕ. The same numerical configuration is used to study the impact of the initial droplet diameter D_0 on NO_x formation, with

D_0 being varied between 25 and 200µm. The atmosphere composition utilized is again taken from the exhaust gas of a perfectly premixed flame with $\phi = 0.8$, leading to well-burned ambiance with sufficient oxygen remaining for the succeeding droplet combustion. Results of droplet-caused NO_x emissions are shown in Figure 5.21. These calculated values lie on a straight line through the origin of the plot. This tendency is in disagreement with the results of Bracco [55]. He hypothesized that the NO_x formation rate (normalized by the fuel burning rate) increases with the square of the droplet diameter. However, Bracco's results are based on a rudimentary combustion model and a number of simplifications (see also Chap. 2). The integral I of the NO source term $\dot{\omega}_{NO}$, for instance, is assumed by Bracco to be quasi-constant throughout droplet combustion. This assumption is fairly inaccurate. On the one hand, it is inconsistent with other assumptions and results of Bracco's own work. On the other hand, this approach would require the NO source term $\dot{\omega}_{NO}$ to balance the decrease of the droplet diameter squared due to vaporization and combustion [54, 55, 298].

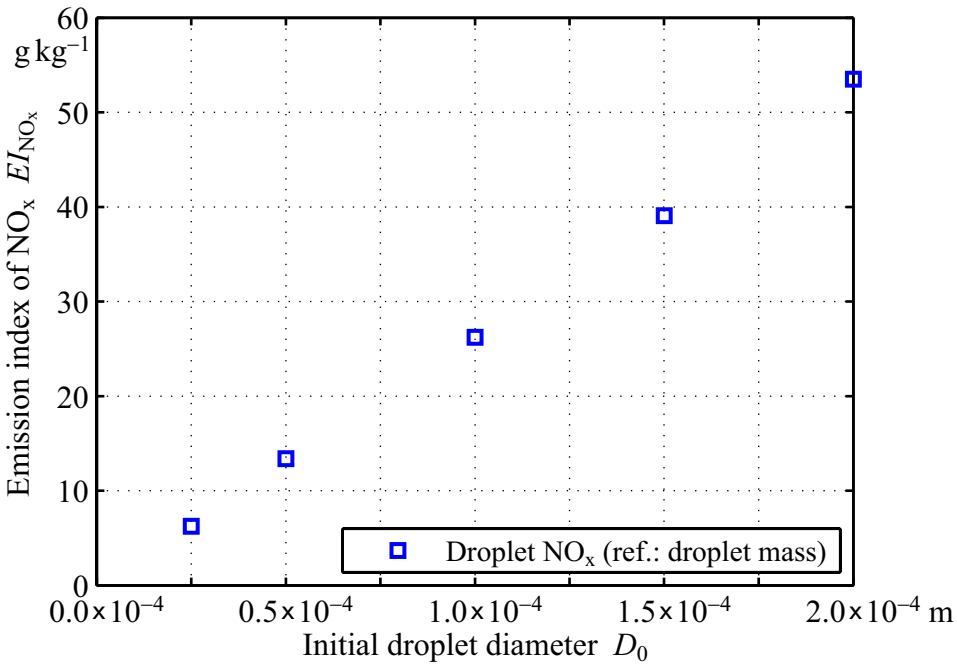

Figure 5.21: Emission Index of NO_x for an n-Decane Droplet in Hot Exhaust Gas as a Function of the Initial Droplet Diameter. The emission index EI_{NO_x} is calculated by referring to the initial mass of the fuel droplet [298].

The influence of droplet size on the emission index EI_{NO_x} can also be estimated analytically, based on the definition of EI_{NO_x}. Here, the mass of nitrogen oxides is given by

$$m_{NO_x} \propto \tau_v V_f \exp\left(-\frac{E_a}{RT}\right), \tag{5.9}$$

and the mass of fuel by

$$m_{C_{10}H_{22}} \propto D_0^3. \tag{5.10}$$

As stated in the D² law, the vaporization time τ_v is proportional to D_0^2, where D_0 is taken as characteristic length (Eq. (4.68)). The volume of the flame V_f depends on the area of a spherical shell ($\propto D_0^2$) and the thickness of the flame δ_f. The exponential factor results from the Arrhenius law (Eq. (4.18)). Assuming a constant thickness δ_f and neglecting differences in the temperature profile yields

$$EI_{NO_x} \propto \frac{D_0^2 D_0^2}{D_0^3} = D_0. \tag{5.11}$$

Hence, the estimated emission index goes linear with the initial droplet diameter D_0, which is consistent with the numerical results of Figure 5.21 [298].

These numerical and analytical findings are supported by the experimental results on droplet arrays (Fig. 5.22). The TEXNOX drop tower campaign allowed for a systematic variation of the initial droplet diameter D_0 in combination with the inter-droplet distance S, while keeping the total length of the droplet array fixed to $L = 72\,\text{mm}$ (cf. Tabs. 3.1 and B.1). Here, the linear trend of the NO_x emissions becomes apparent by varying the initial droplet diameter D_0. In addition to the relatively large database for $S = 4.5\,\text{mm}$, the other data fit in well, also indicating a linear trend. Furthermore, there is a consistent decrease in NO_x formation due to an increase in inter-droplet distance S. These different levels of NO_x formation are a result of a varying interaction of the sphere of influence of every droplet with its neighbors. If the parameter S is small, the specific energy density increases and the specific heat losses to the environment decrease. Thus, there will be a rise in temperature as well as in NO_x production. The absolute NO_x values are comparable for Figures 5.21 and 5.22, but the zero-intercept is different, which is due mainly to the significant heat losses of the combustion chamber during the experiment runs.

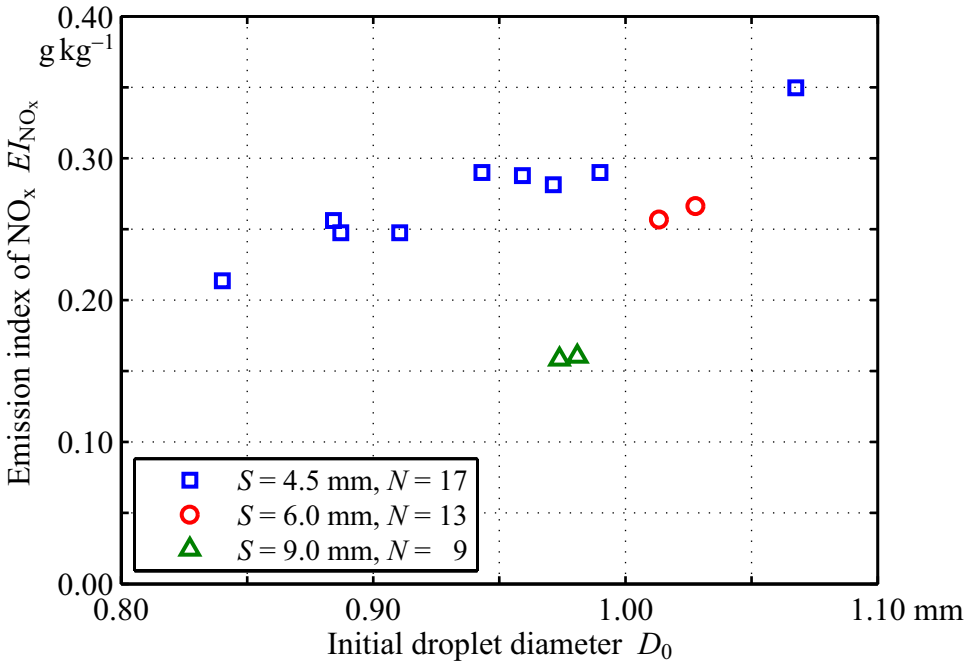

Figure 5.22: Emission Index of NO_x for Droplet Arrays of Different Initial Diameters. Inter-droplet distance S and number of droplets N are varied according to Tables 3.1 and B.1. The initial temperature of the gas phase is $T_{g,0} = 500\,\mathrm{K}$.

Figure 5.23 complements these results with regard to the preheating temperature of the air atmosphere. Since all data have an identical inter-droplet distance ($S = 4.5\,\mathrm{mm}$) but a different initial droplet diameter of $D_0 = 0.9$ or $1.0\,\mathrm{mm}$, the non-dimensional inter-droplet spacing S/D_0 differs between the two data series (cf. Fig. 2.5). An increase in the ratio S/D_0 results in a decrease in NO_x formation, which is in line with Figure 5.22. Furthermore, a relative minimum of NO_x formation can be deduced for an initial temperature $T_{g,0}$ between 300 and 400 K from the progress of both data sets.

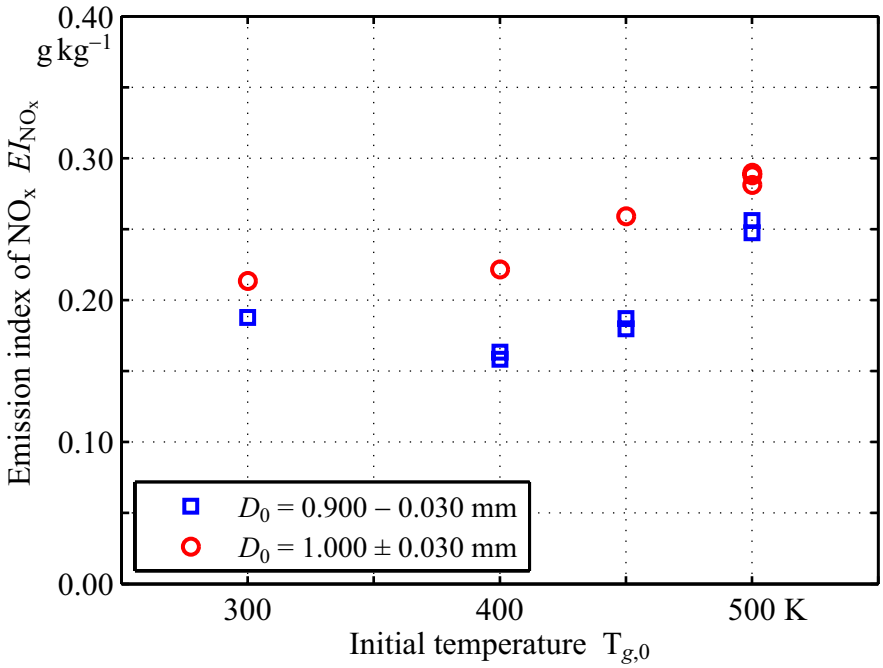

Figure 5.23: Impact of Initial Droplet Diameter and Preheating Temperature on NO_x Emissions for Droplet Arrays. All data displayed is obtained from droplet arrays with an inter-droplet distance of $S = 4.5$ mm and a number of $N = 17$ droplets [294].

5.5 Final Evaluation of Results

In particular, the extended microgravity duration of sounding rocket flight allowed for investigation of the pre-vaporization rate Ψ. The scientific quality of the results is very good and shows a high consistency with the precursor experiments from parabolic flight and drop tower, which were a substantial part of the present study. All these physical experiments comprise a temperature range of 300 to 500 K, initial droplet diameters in the range of 0.819 to 1.608 mm, droplet numbers from 5 to 17, and pre-vaporization time in the range of 0 to 18 s, resulting in pre-vaporization rates from 0.00 to 53.78 %. The experiment procedures, including those of exhaust gas sampling and analysis, were verified additionally by the values measured for CO_2, CO, and H_2O. These are in line with combustion theory. Particular combustion phenomena observed were predicted beforehand. These include the formation of a triple flame with an increase in pre-vaporization rate Ψ. All exhaust gas concentrations were corrected for secondary effects, such as fresh air entrainment into the combustion chamber and heat loss of the combustion chamber.

A twofold trend was observed for the NO_x signature of partially pre-vaporized droplet arrays: Emissions decrease almost linearly with an increase of Ψ if the heat loss of the combustion chamber is not taken into account. However, there is a quasi-constant correlation when employing the corresponding correction factors. Those final results obtained are in very good qualitative agreement with the spray experiments of Baessler [31], in which NO_x formation was investigated for the full range of Ψ. There is also good qualitative agreement between the experimental and numerical results within the present study, while the droplet burning regime differs slightly. Nonetheless, direct portability of the results to technical applications needs to be assessed carefully, in any case, on the basis of the specific burning regime. Since the available microgravity duration was still short within all experiment campaigns, the feasible pre-vaporization Ψ remained behind expectations.

The utilized single droplet model allowed for a trade-off between reproducing the real reaction kinetics and keeping the computational effort low to a reasonable extent. The governing equations for liquid and gas phase were solved fully coupled including detailed models for transport and vaporization as well as a moderately extensive reaction mechanism. An optimum combination of mechanisms could be isolated with the $C_{10}H_{22}$ kinetics of Zhao et al. [474] and the NO_x kinetics of Li and Williams [250] by the use of perfectly stirred reactors, laminar premixed flames, and diffusion flames. Since simplifications were justified in great detail within the model development, complexity is captured in an adequate way.

First, a series of numerical experiments were carried out to study the burning characteristics and NO_x formation mechanisms of droplets in hot exhaust gas. Initial composition and temperature of the respective droplet environment were selected according to the products of laminar premixed flames at different equivalence ratios ϕ. The key parameters covered in these computations were initial composition of the exhaust gas and initial droplet diameter. The computations show that a trade-off between ambient temperature and available oxygen determines NO_x formation. Maximum emissions are produced at $\phi = 0.825$. The initial droplet diameter has a linear effect on NO_x emissions in conjunction with a constant equivalence ratio of the ambient exhaust gas atmosphere. A simple analytical approach as well as the experiments conducted confirmed this observation.

Second, the combustion of partially pre-vaporized droplets was studied carrying out numerical experiments, too. Here, the atmosphere was air with an initial temperature in the range of 500 to 700 K. As this temperature is too low for auto-ignition, the droplets were ignited using an external energy source after the pre-vaporization time t_Ψ was reached. The energy introduced into the numerical domain was methodically re-extracted upon onset of reaction and before temperatures leading to substantial NO_x formation were attained. These numerical simulations yielded an almost constant NO_x production up to a pre-vaporization rate of around 50 %. If more than half of the droplet mass is vaporized before ignition takes place ($\Psi > 0.5$), lean, partially premixed areas develop and NO_x emissions decrease with an increase in Ψ. During the period of heat introduction, the droplet burning behavior is dominated by the influence of the volumetric heat source. Thus, it is crucial to choose energy and location of the ignition source in a way that the influence on total NO_x generation is negligible. Compared to previous studies, the precise supply and removal of energy by a source term turned out to be a beneficial feature to control ignition. As a result of improving the ignition method, the amount of heat introduced can be kept constant from case to case. This generic ignition procedure is energetically neutral. It allows to study NO_x formation without artificial, thermal effects stemming from ignition. Nonetheless, modeling ignition will remain a general problem in droplet combustion modeling. This becomes apparent when comparing different ignition approaches.

In summary, the overall agreement – in a qualitative manner – between experiments, numerical simulations, and analytical approximations is very good. There is also a very good reproducibility within the experimental results. The model, as employed in the numerical simulations, is in good agreement with literature. However, due to the different setups of spherically symmetric single droplets and linear droplet arrays, it is hard to develop correlations between numerical and experimental results. Significant heat losses in the experiment contribute to an absolute deviation in the NO_x values by a factor of 5 to 10. The strong coupling between droplet ignition and NO_x formation highlights the need for a reasonable modeling of the ignition position for pre-vaporized droplets. It is not possible to use the single droplet model for modeling the interaction of droplets in sprays.

5.6 Recommendations and Future Tasks

The study at hand is focused on the combustion of single droplets and droplet arrays under microgravity conditions. While studying these droplet setups under idealized conditions, the understanding of particular physical and chemical processes could be improved. Nevertheless, convective flow around the droplets also has a major influence on heat and mass transfer, and the interaction of droplets is significant in sprays. Both effects could, in part, be accounted for by the experimental part of this study. Besides, an extended, two-dimensional model was developed in cylindrical coordinates to accommodate those aspects. Its implementation into the software package Cosilab® and the multiphysics and reaction engineering environments of COMSOL® [80–83] was carried out successfully. However, neither implementation was capable of providing results comparable to those of the one-dimensional model with respect, in particular, to NO_x formation. This shortcoming was due to numerical instabilities, on the one hand, and combustion chemistry too complex for the CFD framework, on the other hand. In addition, droplet burnout within a droplet array is achieved at different instants, as the droplets vaporize and burn at different rates depending on their individual state of preheating and combustion. However, a droplet of zero radius cannot be represented by the numerical model, and thus calculations have to be stopped, once the size of a droplet drops below a certain threshold. Then, the interface conditions have to be changed before continuing simulation of the remaining droplets.

Nonetheless, such a two-dimensional model is capable of representing interactions in droplet arrays. The additional spatial dimension allows to model forced ignition even more realistically. It is also possible to study the influence of convective flow on single droplets or along a droplet array. Various droplet arrays can be investigated regarding droplet size and inter-droplet distance. Additional findings with regard to flame shape and temperature distribution can provide a deeper insight into the complex processes within spray flames.

In general, further work needs to be carried out to develop a comprehensive understanding of NO_x formation in partially pre-vaporized droplet and spray flames. It should focus on the ambient setting, including temperature, pressure, and atmospheric composition, as well as secondary effects of vapor-

ization and combustion, including droplet lifetime, ignition delay times, and peak temperature. The impact of the inter-droplet distance on the combustion process is also to be investigated, as it directly affects flame propagation and flame shape. Apart from modeling ignition by a well-defined volumetric heat source, it can also be achieved by convection of hot gas towards the first droplet. Research on reduced chemical kinetics as well as appropriate post-processing procedures is indispensable, provided that computational power remains moderately constant. This will help to reduce the number of species and elementary reactions represented in the calculations.

6 Summary and Conclusions

In times of depleting resources, processes involving the combustion of fossil fuels have to be highly efficient. Moreover, it is essential to develop novel combustion concepts that offer a high potential for improvement towards environmentally neutral combustion engines and low exhaust gas emissions. Especially in aero-engines, the NO_x emissions are seen to have a large potential for further reduction. In this respect, partial premixed combustion with a partial degree of liquid fuel vaporization aims at combining the advantages of lean premixed and nonpremixed combustion. The study at hand was undertaken to help resolve the issue of a possible effect of partial droplet vaporization on the overall NO_x production under idealized conditions. Against this background, the vaporization and combustion of single droplets and linear droplet arrays were investigated by experiments as well as modeled and numerically simulated.

The microgravity environment was utilized because it allows a detailed observation of the most essential phenomena in droplet combustion without the disturbance of natural convection. These experiments also provided a basis for the validation of an advanced model on droplet combustion. Linear droplet arrays of the hydrocarbon $C_{10}H_{22}$ were burned without relative velocity to the ambient gas. A sophisticated design and optimized control procedures were used to guarantee representative gas samples from the experiment runs and a reliable, subsequent gas analysis on the ground.

Numerical work was performed, studying the driving forces of NO_x generation in single droplet combustion based on a spherically symmetric 1D model. Microgravity conditions were applied correspondingly and detailed kinetics were used. Since none of the $C_{10}H_{22}$ mechanisms considered contains NO_x chemistry by default, an approach for combining chemical kinetics was established, and an energetically neutral ignition method was formulated within the droplet combustion model proposed. It was essential to provide a manageable combination of the fields of droplet vaporization, ignition, combus-

tion, and exhaust gas formation. Nitrogen oxide emissions of partially pre-vaporized droplets were finally studied, and the burning behavior was analyzed. Special attention was given to the interaction of both these aspects with the ignition model.

Recalling the findings of this research, pre-vaporization is beneficial to avoid NO_x formation. The major points observed are given as follows:

- Different stages of droplet burning could be confirmed, which is in line with results from literature. The ignition phase of a droplet is dominated by the ignition parameters and crucial to the overall NO_x production.
- After ignition, partially pre-vaporized droplets generally burn similarly to droplets in hot atmospheres. However, for high pre-vaporization rates, a significant amount of flammable premixed gas accumulates around the droplet. In this case, the flame burns in a rather premixed regime before it turns its mode into a diffusion flame.
- The accurate prediction of NO_x emissions is sensitive against heat introduction if an ignition model is required. Heat extraction from the exhaust gas regions of burning droplets shows only a minor impact on flame position and NO_x emissions.
- Within the burning regimes investigated, a minimum of 50 % droplet pre-vaporization is required to perceive a significant NO_x abatement.

Against this background, the influence of the most essential combustion parameters on NO_x formation shows:

- A strong dependence on the ambient temperature T_∞.
- A dominance of droplet-caused NO_x up to 1800 K, followed by a rapid decrease around 2000 K, and a dominance of the gas phase at higher T_∞.
- A linear dependence of droplet-caused NO_x for a variation of D_0 in a hot exhaust gas atmosphere.
- An overall similar progress for Ψ confirmed by experiments and numerical studies, as reported by Baessler [31] for sprays.

APPENDIX

A Chemical Mechanisms

All practical fuels are a mixture of a large number of different hydrocarbons. The combustion of each single hydrocarbon in reality involves hundreds of species and up to thousands of reaction steps (see Chap. 2.3). While Marchese et al. [271] were able to simulate the combustion of spherically symmetric droplets in combination with a mechanism involving 51 species, Sazhin [381] argues that even a mechanism with no more than 13 species did not prove applicable for realistic multi-dimensional models (cf. Chap. 5.6).

In numerical modeling, a scalar transport equation must be solved for each species. However, the system of differential equations is commonly very stiff due to discrepancies in the timescales of the reactions involved [341, 443]. Implicit time-integration schemes have to be employed that are computationally expensive [43, 157]. In order to overcome the issues of a stiff system of equations and a large number of degrees of freedom, several strategies have been suggested in combustion modeling, of which some are highlighted in the following paragraphs. Still, the focus of NO_x formation modeling is kept in mind.

A.1 Global Kinetics

Global reaction kinetics can be used for first estimates of temperature and the major species in flames. These mechanisms consist of only a few species and one or a few nonelementary reactions. Thus, computational cost remains low. The conversion of fuel and oxidizer is described by either a single reaction or a few reactions with some intermediate species. There is no explicit correlation to the elementary reactions, and reaction equations as well as rate coefficients for reactions are determined from measurements. This is typically done by obtaining appropriate values for the adiabatic flame temperature T_{ad} and flame propagation velocity S_L to fit the experimental data in a limited field of application.

The earliest approaches to combustion modeling were based on global one-step or simple multi-step mechanisms. A popular single-step mechanism for $C_{10}H_{22}$ is the one of Westbrook and Dryer [459], which is trimmed to predict correct flame speeds for premixed flames over a range of different mixtures. The global reaction equation reads:

$$C_{10}H_{22} + 15.5\,O_2 \rightarrow 10\,CO_2 + 11\,H_2O. \tag{A.1}$$

Westbrook and Dryer [459] also present a two-step mechanism for hydrocarbons, in which an intermediate step accounts for the existence of CO.

$$C_{10}H_{22} + 10.5\,O_2 \rightarrow 10\,CO + 11\,H_2O \tag{A.2}$$

$$CO + 0.5\,O_2 \rightleftharpoons CO_2 \tag{A.3}$$

The reaction rate parameters of the forward and backward reaction of Equation (A.3) are given separately and not correlated via equilibrium.

Figure A.1 compares temperature profiles of a premixed flame with an equivalence ratio of $\phi = 1.0$ using different reaction kinetics (cf. Fig. 2.11). The single- and two-step mechanisms deviate from the more detailed mechanisms in the temperature of the post-flame zone. Apart form the detailed, skeletal mechanism of Zhao et al. [474] (Chap. 2.3.1), a quasi-global mechanism is consulted, too. The latter is a one-step fuel breakdown reaction (Eq. (A.4)) in combination with a detailed CO–H_2–O_2 mechanism [459].

$$C_{10}H_{22} + 5\,O_2 \rightarrow 10\,CO + 11\,H_2 \tag{A.4}$$

The reaction of Equation (A.4) is extended with 21 elementary reactions of the CO–H_2–O_2 system, yielding a mechanism of 12 species and 22 reactions altogether [116, 117, 459]. This quasi-global mechanism shows good agreement with the detailed chemistry in terms of temperature and exhaust gas composition in the post-flame region. However, the location of the reaction zone is predicted wrongly. Nevertheless, the quasi-global mechanism includes species, such as the radicals OH, H, and O, that are involved in NO_x production by the Zeldovich mechanism. The mass fraction profiles of these species agree reasonably well with the reference values in the post-flame region, whereas deviations of about 20 % occur in the flame zone itself. The formation of NO_x via other pathways (e.g. prompt NO) is not feasible, as the species required are not included in the quasi-global mechanism.

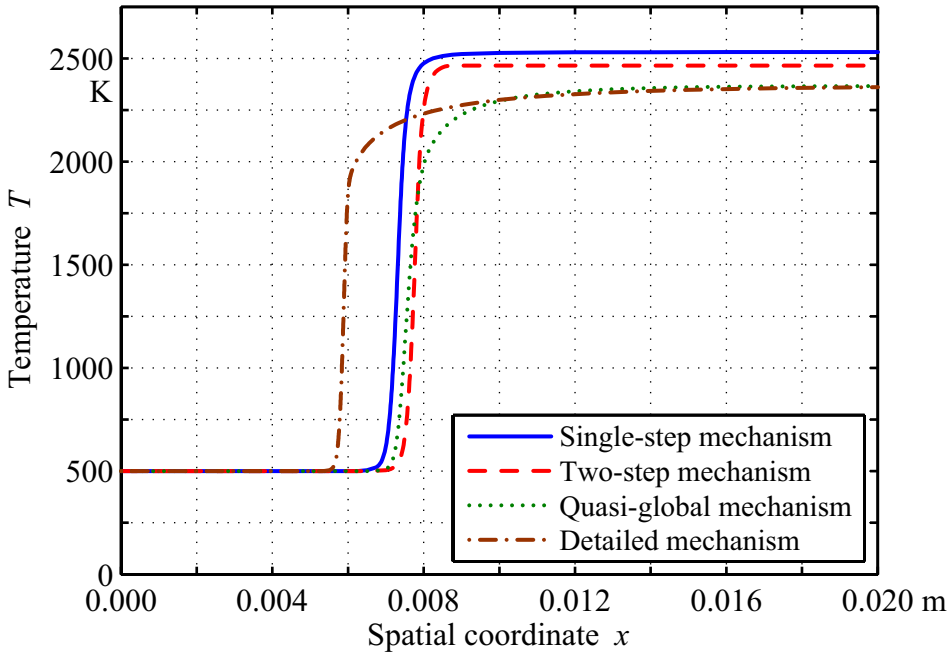

Figure A.1: Temperature Profile of a Laminar Premixed Flame for Reaction Mechanisms with Different Degrees of Abstraction. n-Decane is burned at stoichiometric conditions ($\phi = 1.0$). The inlet temperature is $T = 500\,\mathrm{K}$ at a pressure of 1.0 bar.

With respect to liquid-fueled gas turbines, Lefebvre [243] points out that chemical reaction rates vary only slightly between the various hydrocarbon fractions of the fuel. This is due to only marginal differences in adiabatic flame temperature of the particular fuels, on the one hand, and extensive pyrolysis of all fuel fractions before entering the true reaction zone, on the other hand. The major pyrolysis products are CH_4, other 1-2 carbon atom hydrocarbons, and H_2. Consequently, the reactant composition in the reaction zone is virtually independent of the parent fuel. Duterque et al. [106] also provided quasi-global schemes for methane, propane, benzene, and iso-octane with an initial transformation of the hydrocarbon into CO and H_2 by one or two[1] global stages, similar to Equation (A.4). In the mechanism developed by Hautman et al. [172], intermediates are generally represented by ethene (C_2H_4), regardless of the actual main reactants. Unlike the quasi-global reaction schemes discussed so far, the one by Jones and Lindstedt [199] involves two competing fuel breakdown reactions. Oxygen as well as water are considered to be involved in the global fuel oxidation step. However, this set of reactions was

[1] Duterque et al. [106] consider individual intermediate species for different hydrocarbons.

only deduced to describe the high temperature oxidation of gaseous alkane hydrocarbons up to butane (C_4H_{10}).

Ennetta et al. [124] compare the four-step, quasi-global mechanism of Jones and Lindstedt [199] and a single-step kinetic of Duterque et al. [106] with the detailed GRI 3.0 mechanism [408] for methane combustion. The authors conclude that global mechanisms can provide results that are in good agreement with more detailed mechanisms with regard to particular engineering applications. However, the reduced mechanisms are incapable of predicting pollutant emissions. The major drawback of all global mechanisms is that they do not account for chain branching reactions involving radicals [381, 474]. These are essential for auto-ignition at low temperatures. Still, utilization of the above mechanisms may well be an option for high temperature applications, when the limiting factor for ignition is thermal feedback rather than reproduction of the chain branching reactions. In contrast, Sazhin [381] refers to the Shell model [167, 168, 385] as the most commonly employed mechanism accounting for auto-ignition in automotive applications. This model captures the essential features of the combustion process, such as chain branching and intermediate species, but it does not reproduce the actual physics and chemistry. It is an eight-step scheme incorporated into four processes, employing generic species with chemical reaction constants deduced from experiments.

A.2 Concepts of Kinetics Reduction

Apart from global kinetics presented in Chapter A.1, there are various concepts to obtain user-specific mechanisms consisting of a lower number of species and reactions. In comparison with detailed mechanisms, reduced mechanisms typically are free of the fastest timescales but still able to reproduce the most essential features of the problem under investigation.

Conventional reduction methods require the selection and elimination of particular species and reactions by the user. Starting from detailed mechanisms, reduced kinetics are derived assuming reactions in partial equilibrium and species at quasi-steady state. Comparing the timescales of different reactions, the combustion process is limited by the slower reactions, while the fast ones are in partial equilibrium [149, 336, 443]. In order to save computational

power, the net reaction rates of the latter can be set to zero, leading to algebraic relations. The steady-state approximation searches for species whose production and consumption cancel out immediately. By doing so, many intermediate species can be eliminated from a detailed mechanism if their net production rates tend towards zero. In practice, species are regarded as quasi-steady if their net production rate is small compared to their respective production and consumption rates [11, 43, 336]. This process of analyzing the timescales was successfully automated, resulting in the so-called computer assisted reduction method (CARM). It evaluates reaction rates and automatically eliminates species at quasi-steady state on the basis of results obtained from perfectly stirred reactor models, employing more or less detailed mechanisms [67, 90, 299].

The computational singular perturbation (CSP) method investigates the dynamics of the source term vector and tries to find the directions in which it will rapidly reach steady-state. Eigenvalues and eigenvectors of the Jacobian matrix of the source term represent chemical timescales and reaction groups, respectively [11, 43, 256].

The intrinsic low-dimensional manifold (ILDM) method was presented by Maas and Pope [262] in 1992. Similar to the CSP method, the ILDM method tries to find directions in state space in which the source term rapidly reaches steady-state. The method is based on the assumption that a combustion system follows certain trajectories in state space during the combustion process. However, these trajectories are not associated with any particular species or reaction. Since the steady-state assumption is applied locally, different reaction paths can be captured. The common part of all trajectories can be described as a parameterized curve of only a single progress variable. Assuming all but two processes to be in steady-state results in a surface parameterized by two variables and so on. This process generally leads to intrinsic low-dimensional manifolds, in which the number of dimensions represents the number of slow processes. However, the higher the number of dimensions, the more rapidly the trajectories through state space will approach the manifold. As time approaches infinity and independently of the initial conditions, all solution trajectories of stable systems will approach the same equilibrium point. Thus, movement along the ILDM corresponds to the evolution of the predefined slow processes, and the equilibrium point effectively would be a zero-dimensional manifold [191, 262, 399, 400].

Another, very recent approach to reduce kinetics is the path flux analysis (PFA) developed by Sun et al. [426]. The PFA method reduces a chemical mechanism by removing species and reactions that have a minor influence on the conversion of reactants to products. It is possible to specify certain target species, as for instance the oxides of nitrogen, which are kept in the reduced mechanism in any case. Since this is a promising approach to obtain a compact mechanism that can also predict NO_x formation, a sensitivity analysis was conducted on this method, starting from the combination "n-Decane (Princeton) + NO_x (Li)" discussed in Chapter 2.3.3.

As a starting point it is necessary to consider a reacting system, such as a perfectly stirred reactor, that is representative for the particular application. This system is run with a number of elementary reactions and their associated net reaction rates $\dot{\omega}_m$. The so-called flux of one species S_m to another species S_n is the basis for finding the significance of species. The reduction process begins with a set of preselected species A. The significance of all other species B to the conversion of the preselected species is determined by the interaction coefficient r_{AB}. Using the total production fluxes P_A and the total consumption fluxes C_A of a particular species A (Eqs. (A.5) and (A.6)), the PFA method evaluates the interaction coefficient between the selected species A and any other species B. The stoichiometric coefficient of species A in the l-th reaction and the respective net production rate are represented by ν_{Al} and $\dot{\omega}_{Al}$. The number of elementary reactions is identified by L [426]:

$$P_A = \sum_{l=1}^{L} \max(\nu_{Al}\dot{\omega}_{Al}, 0)\,, \tag{A.5}$$

$$C_A = \sum_{l=1}^{L} \max(-\nu_{Al}\dot{\omega}_{Al}, 0)\,. \tag{A.6}$$

The determination of the interaction coefficient r_{AB} further requires the production and consumption fluxes of A due to the presence of B:

$$P_{AB} = \sum_{l=1}^{L} \max\left(\nu_{Al}\dot{\omega}_{Al}\delta_B^l, 0\right), \tag{A.7}$$

$$C_{AB} = \sum_{l=1}^{L} \max\left(-\nu_{Al}\dot{\omega}_{Al}\delta_B^l, 0\right), \tag{A.8}$$

$$\delta_B^l = \begin{cases} 1 & \text{if the } l\text{-th elementary reaction involves species } B, \\ 0 & \text{otherwise.} \end{cases} \tag{A.9}$$

Taking into account only the direct influence of B on A, interaction coefficients of the "first generation" are defined as

$$r_{AB}^{\text{prod,1st}} = \frac{P_{AB}}{\max(P_A, C_A)}, \tag{A.10}$$

$$r_{AB}^{\text{con,1st}} = \frac{C_{AB}}{\max(P_A, C_A)}. \tag{A.11}$$

If the influence of intermediate species has to be captured as well, reaction coefficients of a higher generation are employed. For instance, B affects the conversion of S_o, and S_o in turn is involved in the conversion of A. This particular case represents the "second generation" with the additional coefficients:

$$r_{AB}^{\text{prod,2nd}} = \sum_{S_o \neq A,B}^{N} \left(r_{AS_o}^{\text{prod,1st}} r_{S_oB}^{\text{prod,1st}} \right), \tag{A.12}$$

$$r_{AB}^{\text{con,2nd}} = \sum_{S_o \neq A,B}^{N} \left(r_{AS_o}^{\text{con,1st}} r_{S_oB}^{\text{con,1st}} \right). \tag{A.13}$$

The overall reaction coefficient r_{AB} is defined as the sum of Equations (A.10) through (A.13) and is finally used to determine the relevance of species B to species A in the reacting system:

$$r_{AB} = r_{AB}^{\text{prod,1st}} + r_{AB}^{\text{con,1st}} + r_{AB}^{\text{prod,2nd}} + r_{AB}^{\text{con,2nd}}. \tag{A.14}$$

In combination with the user-defined threshold ε, the calculated value of r_{AB} delivers a criterion for the reduction of the reaction mechanism. If $r_{AB} \geq \varepsilon$, species B is selected for the reduced mechanism. However, if $r_{AB} < \varepsilon$, species B can be neglected and is removed. Furthermore, reactions including removed species are no more relevant either, and thus are removed from the original mechanism as well.

Hence, extent and quality of the reduction are determined by the threshold ε of the interaction coefficient, the input set of the production rates $\dot{\omega}_{Al}$, and the preselected species A. For the set of production rates, values should represent

the reactions appearing in the particular field of application as accurately as possible. The set of preselected species A also has to be chosen to fit the later field of application, which is not trivial and requires a priori knowledge about the overall reactions of the system.

Sun et al. [157, 256, 426] provide a set of tools along with their method to carry out the whole process of kinetics reduction. The procedure implemented in the PFA reduction tools uses a general method to capture species production rates from a wide range of reaction phenomena. This method presumes that all phenomena dominating reactions appear during ignition and extinction of the flame. Ignition is modeled by a perfectly stirred, closed adiabatic reactor at constant pressure, available in the software package Senkin [259, 348]. Here, a homogeneous mixture is investigated at temperatures of $T_0 \geq 1000\,\mathrm{K}$. The ensuing species net production rates are captured at fixed time intervals until the mixture ignites, with ignition delay time t_{ign} being defined as

$$T(t_{\mathrm{ign}}) = T_0 + 400\,\mathrm{K}. \tag{A.15}$$

To obtain species production rates of the extinction phenomena, a perfectly stirred reactor (PSR) is used. More precisely, this is an open, adiabatic constant mass flow reactor at constant pressure. A mixture at low temperatures is inserted into this reactor at a progressive rate with $T_{\mathrm{in}} = 300\,\mathrm{K}$. Here, the species production rates are captured while the mass flow rate is increased until flame blowout. Finally, all species production rates from the Senkin and PSR calculations are combined in one library. For execution of the actual PFA method, values of $\dot{\omega}_{Al}$ are taken from this library.

This set of PFA tools was employed to reduce the combined kinetics "n-Decane (Princeton) + NO_x (Li)" with an initial number of 99 species and 693 reactions. The goal was to deliberately provide and evaluate a reduction by about one third. Thus, the threshold ε was trimmed to obtain a reduced mechanism with 64 species. For the Senkin and PSR calculations, the initial mixture properties were varied to obtain the optimum with respect to an application in droplet combustion. As illustrated in Table A.1, these properties included the range of equivalence ratios ϕ, range of temperatures T_0, and different sets of preselected species A. The species $C_{10}H_{22}$, N_2, O_2, CO_2, and H_2O were considered to be essential for the combustion process in general and were therefore preselected in any case. The different parameter sets were varied systematically: Only one parameter was changed, while the two remaining ones were

Table A.1: Accuracy of Reduced Mechanisms as Controlled by Path Flux Parameters.

Preselected path flux parameter: Equivalence ratio ϕ				
Mech. ID	Scope of ϕ	$\epsilon_{NO_x,pre}$ in %	$\epsilon_{NO_x,diff}$ in %	$\epsilon_{t_{ign}}$ in %
P1	1.00	4.22	17.14	0.81
P2	0.75, 1.00, 1.25	1.98	4.19	0.81
P3	0.60, 0.75, 0.90, 1.00, 1.10, 1.25, 1.40	1.98	4.19	0.81
Preselected path flux parameter: Temperature T_0 in K				
Mech. ID	Scope of T_0	$\epsilon_{NO_x,pre}$ in %	$\epsilon_{NO_x,diff}$ in %	$\epsilon_{t_{ign}}$ in %
T1	1500, 1800	1.52	2.60	172.85
T2	1200, 1500, 1800, 2000	2.65	4.74	78.22
T3	1000, 1200, 1500, 1800, 2000, 2200	1.98	4.19	0.81
Preselected path flux parameter: NO_x species				
Mech. ID	Scope of NO_x species	$\epsilon_{NO_x,pre}$ in %	$\epsilon_{NO_x,diff}$ in %	$\epsilon_{t_{ign}}$ in %
S1	–	1.98	4.19	0.81
S2	NO	1.98	4.19	0.81
S3	NO, NO_2, N_2O	1.98	4.19	0.81
S4	Total NO_x chemistry [250]	1.79	7.82	3.09

kept constant. For each of these parameter variations, a reduced mechanism was calculated, at which the threshold ε was trimmed to retain a number of 64 species. Moreover, the integral of the local relative error ϵ (Eqs. (2.26) and (2.27)) was used as a measure for the deviation between original and reduced kinetics. Quality criteria were the NO_x mass fractions in stoichiometric premixed flames and diffusion flames, as well as ignition delay time. For preselection of the parameter ϕ, a medium range of values (P2) is beneficial to reduce errors (Tab. A.1). On the other hand, the range of the parameter T_0 turns out to be very important. Preselection of the species N_2 alone is sufficient to capture NO_x kinetics (S1 to S3). Consequently, NO_x formation must be a dominant contributor for the production and consumption of N_2. Hence, the final reduced mechanism with 64 species and 443 reactions reproduces the emission indices EI_{NO_x} of Figures 5.2 and 5.3 with a maximum relative error of 6.3 % and 7.0 %, respectively.

B Investigated Conditions

There are a number of parameters and conditions having a major impact on the quality of scientific results as presented in the thesis at hand. For instance, it is essential to provide an equal and reproducible pre-vaporization rate Ψ (Fig. 3.1). Producing equally sized droplets of the diameter D_0 is most important in achieving this constraint in experiments. If there is a spatially uniform temperature T_∞, the droplet size at ignition D_{ign} shows as a function of pre-vaporization time t_Ψ only [294]. As far as the numerical part of this research is concerned, the spatial position of the ignition source is most crucial for the overall NO_x production. Besides, different values of the emission index EI_{NO_x} are likely to be obtained by relating the raw values of NO_x formation to the reacting fuel instead of the initial droplet mass [297]. Hence, this chapter gives a supplementary overview of investigated conditions and sensitive parameters.

B.1 Experiment Operation Conditions for Droplet Array Combustion

The microgravity environment, as employed in the experiments of this study, provided ideal conditions for achieving a reproducible degree of droplet vaporization by avoiding the disturbing effects of natural convection (cf. Fig. 1.2). This allowed the study of the interacting phenomena of multi-phase flow, thermodynamics, and chemical kinetics [208, 293, 294, 296].

Systematic Experiment Approach

Flame propagation in the investigated linear droplet arrangement (Fig. 3.1) has an "averaging" effect on combustion temperature and exhaust gas production. The experimentally obtained, averaged production of NO_x can therefore be considered as representing the NO_x quantities of what a single droplet

produces as a link in an infinite droplet array. Nevertheless, gas exchange during the combustion and gas sampling processes needs to be accounted for.

Since the sounding rocket flight of TEXUS-46 originally comprised only four combustion cycles, a statistical evaluation of the procedures for gas sampling and analysis became indispensable. Furthermore, diversification of the experiment parameters was essential for the scientific output. Consequently, parabolic flight and drop tower experiments were conducted as precursor experiments to investigate the reference case for the sounding rocket experiments as well as to gain additional knowledge about various technical aspects of the experiment.[1]

As mentioned above, the main focus of the study at hand was the degree of fuel vaporization Ψ. The extended microgravity duration of sounding rocket flight allowed to investigate larger values of Ψ compared to parabolic flight and drop tower. However, further experiment parameters were studied within the drop tower campaign to achieve a more complete understanding of droplet combustion and NO_x formation. They included the preheating temperature T_∞, initial droplet diameter D_0, inter-droplet distance S, and total droplet number N. Table B.1 gives an overview of all experiments conducted under microgravity conditions. The reason for investigating such large droplets (0.840 – 1.608 mm) was to provide large spatial and temporal scales, and thus well-defined droplet combustion regimes. This approach in particular helped to restrain the relative deviations within fuel vapor formation around the droplets. Experimental errors in the initial droplet diameter D_0 and/or pre-vaporization time t_Ψ can be caused by the fuel-dosing pump, the fine glass tubes, the ignition system, and the hysteresis of the system itself.

Precursor Experiments

Parabolic flight experiments typically provide a microgravity level of $1\times10^{-2}\,g_0$ for approximately 20 s. Major advantages of parabolic flight are direct access to the experiment by the scientist, multiple experiment runs within one campaign, absence of negative impact loads, minor restrictions in weight and power consumption, and moderate costs. However, the aircraft can normally

[1] In the meantime, Nomura et al. [318] and Oyagi et al. [327] were making efforts to investigate the combustion of moving droplets and droplet clusters, which is the next step towards the systematic investigation of complex sprays.

Table B.1: Experiment Overview of Droplet Array Combustion Under Microgravity. In Figure 2.5, the experiments are classified according to the flame propagation mode.

Experiment run	Ambient temperature T_∞ in K	Droplet diameter D_0 in mm	Droplet diameter D_{ign} in mm	Pre-vap. time t_Ψ in s	Droplet number N	Inter-droplet distance S in mm
JAXA PFC Exp. 1	500	1.2	–	0	8	10
JAXA PFC Exp. 2	500	1.2	–	3	8	10
JAXA PFC Exp. 3	500	1.2	–	0	8	10
JAXA PFC Exp. 4	500	1.2	–	3	8	10
TEXNOX Exp. 00	500	0.9269	–	0	17	4.5
TEXNOX Exp. 01	500	0.9431	–	0	17	4.5
TEXNOX Exp. 02	500	1.0675	–	0	17	4.5
TEXNOX Exp. 03	500	0.9899	–	0	17	4.5
TEXNOX Exp. 04	500	0.9899	–	0	17	4.5
TEXNOX Exp. 05	500	0.9714	–	0	17	4.5
TEXNOX Exp. 06	500	0.9105	–	0	17	4.5
TEXNOX Exp. 07	500	0.8871	–	0	17	4.5
TEXNOX Exp. 08	500	0.8401	–	0	17	4.5
TEXNOX Exp. 09	500	0.8842	–	0	17	4.5
TEXNOX Exp. 10	300	1.0283	–	0	17	4.5
TEXNOX Exp. 11	400	0.9783	–	0	17	4.5
TEXNOX Exp. 12	300	0.8871	–	0	17	4.5
TEXNOX Exp. 13	400	0.8800	–	0	17	4.5
TEXNOX Exp. 14	450	0.8800	–	0	17	4.5
TEXNOX Exp. 15	450	0.8471	–	0	17	4.5
TEXNOX Exp. 16	400	0.8941	–	0	17	4.5
TEXNOX Exp. 17	450	0.8909	–	0	17	4.5
TEXNOX Exp. 18	500	0.9591	–	0	17	4.5
TEXNOX Exp. 19	500	1.0278	–	0	13	6.0
TEXNOX Exp. 20	500	0.8805	–	0	13	6.0
TEXNOX Exp. 21	500	0.8186	–	(1)	17	4.5
TEXNOX Exp. 22	500	0.8800	–	1	17	4.5
TEXNOX Exp. 23	500	0.8800	–	1	17	4.5
TEXNOX Exp. 24	500	0.8493	–	0	9	9.0
TEXNOX Exp. 25	500	0.9809	–	0	9	9.0
TEXNOX Exp. 26	500	0.9738	–	0	9	9.0
TEXNOX Exp. 27	500	0.8800	–	1	9	9.0
TEXNOX Exp. 28	500	0.8800	–	1	9	9.0
TEXNOX Exp. 29	(500)	–	–	(0)	(17)	(4.5)
TEXNOX Exp. 30	500	1.0206	–	0	17	4.5
TEXUS Exp. 1	500	1.6084	1.3190	18	5	18.0
TEXUS Exp. 2	500	1.6010	1.5271	10	5	18.0
TEXUS Exp. 3	500	1.5972	1.5924	5	5	18.0
TEXUS Exp. 4	(500)	–	–	(15)	(5)	(18.0)

not be controlled precisely enough to follow a perfect free-fall trajectory. Thus, buoyant motion and other accelerative disturbances are usually not entirely suppressed. On the other hand, sophisticated drop tower facilities can provide a microgravity level of 1×10^{-4} to $1\times10^{-6}\,g_0$ for 2 to 10 s of experiment time [66, 235].

Hence, the engineering module (EM) of the experimental unit was used in parabolic flight for initial tests in the microgravity environment. For this purpose, a parabolic flight campaign (PFC) was conducted with Diamond Air Service (DAS) in Nagoya, Japan, in October 2007. The campaign consisted of two flight days with ten parabolas each. The main novelty was the integration of the EGS system into the former DCU (see Figs. 3.2 and 3.9). In order to ensure relevance and comparability, the total amount of fuel and the overall length of the droplet array were kept constant to the final sounding rocket setup. The results of the PFC were satisfying in qualitative and quantitative terms. All control systems were operable, and the measurement units produced useful results and could be adjusted regarding range and resolution [294].

The drop tower campaign was conducted at the facility of ZARM (Zentrum für angewandte Raumfahrttechnologie und Mikrogravitation) in Bremen, Germany, in July 2008. It comprised 30 drops nominally. The EM was used again, and the campaign itself was termed "TEXNOX", which is derived from TEXUS and NO_x. Here, the precursor experiments included preheating of the combustion chamber in the range of 300 to 500 K and droplet arrays consisting of 9 to 17 droplets (cf. Tab. B.1). Microgravity time was 4.74 s. Apart from generating a basis of scientific results, all operational parameters and procedures were reevaluated and recommendations given for the subsequent sounding rocket campaign [294].

PHOENIX Experiment on TEXUS-46

Sounding rocket flights provide a microgravity time of 200 to 900 s at a typical microgravity level of $1\times10^{-4}\,g_0$ [66, 235]. Main advantage is the extended microgravity time in the range of several minutes combined with a very good microgravity quality. On the downside of the sounding rocket environment are limited remote access by telecommand, severe restrictions in weight, dimensions and power consumption, long preparation and qualification phases,

high mechanical loads on the experimental setup, and very high costs. Key data regarding payload and rocket operation is given in Chapter C.1 for sounding rocket flights in general and the PHOENIX mission in particular.

Despite the limitations and additional effort, the "Japanese Combustion Module" (JCM) was retrofit and customized for sounding rocket flight. This was due to the scientific experiments requiring microgravity in excess of 40 s for every single combustion run. These extended microgravity times alone allowed for an in-depth investigation of the degree of fuel pre-vaporization in droplet combustion. The TEXUS sounding rocket system was chosen for this purpose, and the flight of the associated PHOENIX mission was finally performed on TEXUS-46 in Kiruna, Sweden, in November 2009.

B.2 Supplementary Data on Numerical Simulations

In order to enforce ignition of partially pre-vaporized droplets, a volumetric heat source is applied in the gas phase (cf. Figs. 4.2 and 4.3). Figure B.1 shows the maximum volumetric heat release $\dot{q}_{v,\max}$ of this external heat source. Here,

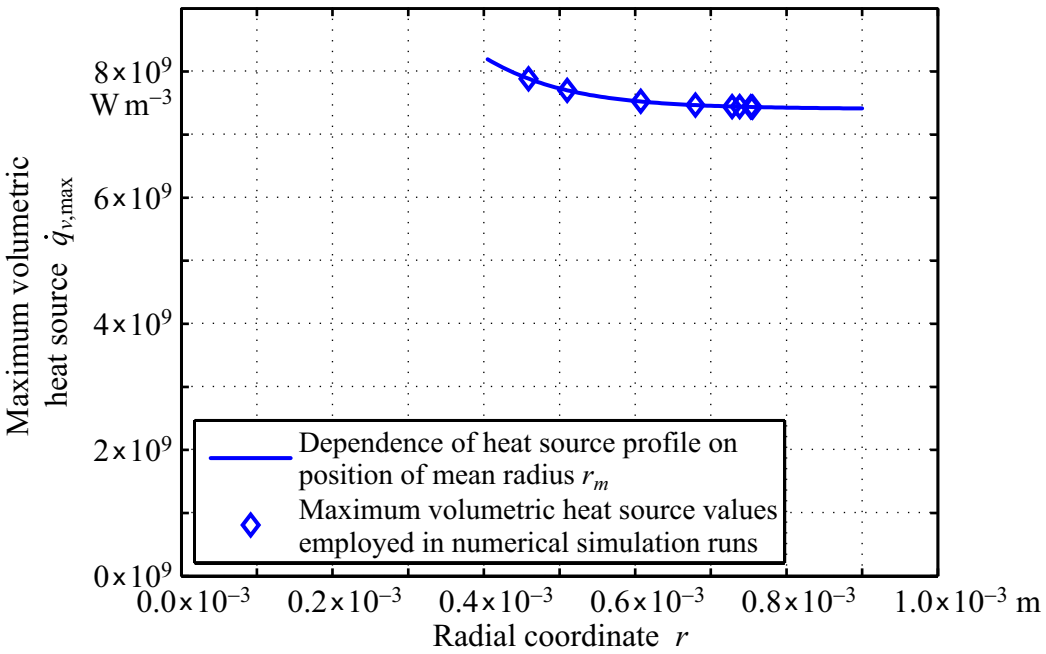

Figure B.1: Maximum Value of Volumetric Heat Source in Relation to its Radial Position.

it is shown in relation to an ignition position that is coupled with the local equivalence ratio ϕ_r (see Fig. 5.4). In the case of a spatially fixed ignition position of $r_{m,\mathrm{in}} = 0.8\times10^{-3}\,\mathrm{m}$, the respective value is $\dot{q}_v = 7.43\times10^{9}\,\mathrm{W\,m^{-3}}$ (cf. Fig. 4.3), which is also the asymptotic value in Figure B.1 for $r \to \infty$.

In Figure 5.5, the initial mass of the fuel droplet $m_{\mathrm{fuel},0}$ is used as the basis for the calculation of the emission index $EI_{\mathrm{NO_x}}$. Different values are obtained when relating the $\mathrm{NO_x}$ emissions to the reacting fuel mass $m_{\mathrm{fuel,reac}}$ instead. Figure B.2 illustrates the relative deviation between these two relations by $\Delta EI_{\mathrm{NO_x}}$. The overall trends are similar. At low degrees of vaporization Ψ, the emission indices are nearly identical and $\Delta EI_{\mathrm{NO_x}}$ is close to zero. With an increase of Ψ, the difference increases between the two calculation approaches. It reaches its maximum at $\Psi = 0.8$ with the relative deviation of $\Delta EI_{\mathrm{NO_x}} = 42\,\%$ or an absolute value of $EI_{\mathrm{NO_x}} = 0.98\,\mathrm{g_{NO_x}/kg_{fuel}}$ [297].

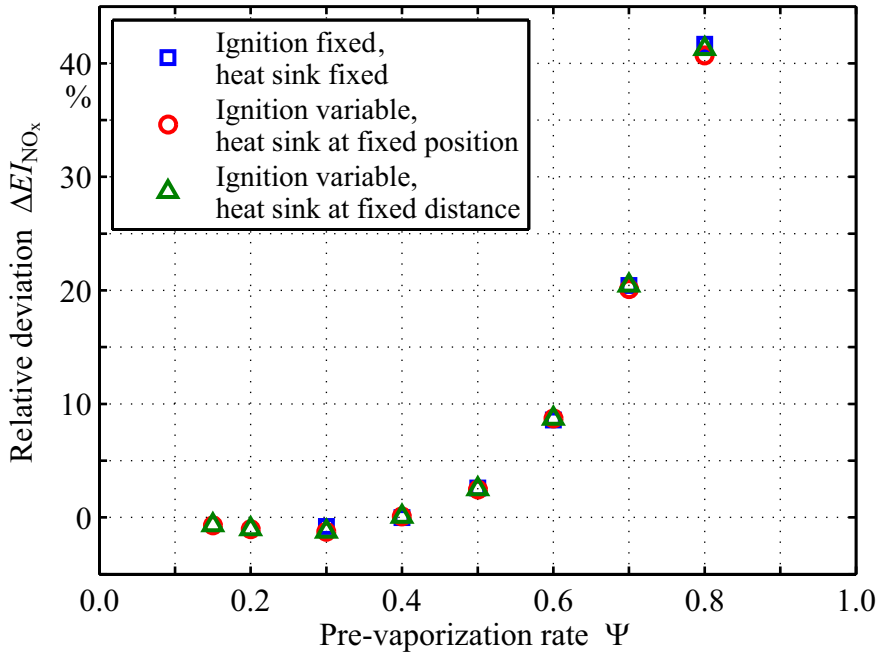

Figure B.2: Relative Deviation of Emission Index by Relating $\mathrm{NO_x}$ Emissions to Different Fuel Masses. Relating the emission index $EI_{\mathrm{NO_x}}$ to the reacting fuel mass $m_{\mathrm{fuel,reac}}$ instead of the initial droplet mass $m_{\mathrm{fuel},0}$ results in a relative deviation of $\Delta EI_{\mathrm{NO_x}}$ (cf. Fig. 5.5) [297].

C Design Details of Experiment Equipment

An intrusive concept was chosen for the crucial steps of exhaust gas sampling during/after microgravity [293, 294, 296]. This gas sampling process was complemented by a gas analysis on the ground. The related exhaust gas sampling (EGS) setup is arranged in a compact manner on the fifth DCU platform (see Fig. 3.2, **F**).

C.1 Key Data of Experimental Setup

In addition to the general outline of the experiment, Table C.1 provides a systematic overview of weight and dimensions of the experimental setup broken down at the JCM and DCU levels. The DCU technically is the upper part of the "experiment deck", which itself is the lowest circular baseplate [196, 208].

Table C.1: Weight and Dimensions of Experimental Setup. The overview shows the functional units hierarchically structured, as integrated in the TEXUS environment. The weight of the DCU is indicated including the "experiment deck" (i.e. common baseplate of JCM and DCU), which has a mass of 5 kg itself. The inner diameter of the DCU vacuum protection is 377 mm with a radial clearance of 2.5 mm.

	Mass m in kg	Height h in mm	Diameter d in mm
TEXUS-46 total payload	393.7	4979	438
TEXUS-46 scientific payload (all experiments)	291.0	3143	438
TEXUS nominal maximum scientific payload	270.0	3300	438
Japanese Combustion Module (JCM)	103.0	1290	403
Droplet Array Combustion Unit (DCU)	42.0	813	372

Depending on these figures and the rocket motor of the particular sounding rocket mission, the achievable apogee height is approximately 250 km with an available microgravity time of 6 min. For the TEXUS-46 mission, launched on November, 22nd, 2009, an apogee height of 252.3 km and a microgravity time of 388 s could be reached.

Telemetry/Telecommand Parameters

Table C.2 provides an overview of the telemetry/telecommand setup of the TEXUS-46 mission. The scan transmitter was used for self-configuration of the hook antennas that were mounted to the TEXUS service module.

Table C.2: Overview of Telemetry/Telecommand System on TEXUS-46.

Scan transmitter		S-band	2295.0 MHz
TV downlink		S-band	2361.5 MHz
Telemetry downlink		S-band	2292.5 MHz
Telemetry uplink			449.96 MHz
2	RS-232	9.6 kBd	
32	Analog channels	3 × 500 Hz (16 bit), 29 × 5 Hz (16 bit)	
30	Digital channels		
12	Discrete telecommands with JCM		

A special approach needed to be pursued for the video data of the cameras CCD1, CCD2, and CCD3 (see Chap. 3.2.3) with the sounding rocket setup. This was due to a limitation of TV downlink channels and in favor of redundancy. Figure C.1 shows the video/image flow scheme of the JCM. While all four camera images were channeled through umbilical cable during testing and flight preparation on the ground by switching the two RF relays (TVR1 and TVR2), only the signal of TVR1 was transmitted via TV downlink during sounding rocket flight. Therefore, a DV recorder documented the alternating video data of the cameras CCD3 and HSV directly on MiniDV tape. In the case of the HSV data, this was a backup solution, as the high-speed raw data was also kept in the volatile DRAM of the camera until payload recovery [196].

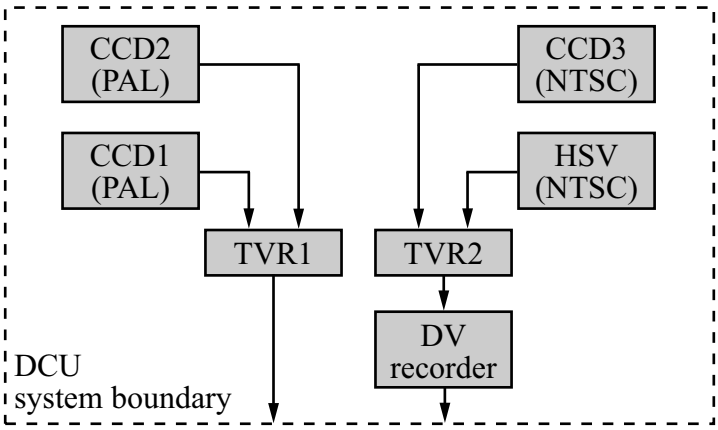

Figure C.1: Schematic of TV Signal Interface for Sounding Rocket Flight. The TV relays TVR1 and TVR2 are operated by subsequencer, and no multiplexing is used [196].

As far as the drop tower setup is concerned, the video data was recorded on three separate MiniDV recorders (Fig. 3.11, **E**). During post-processing of every drop, the video clips were copied from the recorders by FireWire (IEEE 1394). The Kodak HSV recorder, on the other hand, had an internal memory of 5.46 s at 500 Hz.

Mechanical Loads

In the case of drop tower experiments, only deceleration of the drop capsule is critical. It happens in the deceleration container at the end of the microgravity period. As can be seen in Figure C.2, the deceleration lasts for about 200 ms and is of a quasi-steady type. Its average is 25 g_0, but the peak value can reach up to 50 g_0 (<11 ms). In order to keep the experiment operational over a longer campaign period, its hardware was designed to withstand acceleration loads up to 100 g_0. Furthermore, all elements were fit together as rigidly as possible, and damping elements were avoided because they might lead to an amplification of the acceleration. Damping is performed by polystyrene grain inside the deceleration container [66, 104].

In the case of sounding rocket experiments, the mechanical and thermal loads are generally higher and more complex than in the drop tower environment. The Brazilian VSB-30 sounding rocket vehicle was employed to launch the PHOENIX experiment on the TEXUS-46 campaign. It is a rail-launched, spin stabilized, unguided, two-stage rocket vehicle, consisting of a S-31 first stage

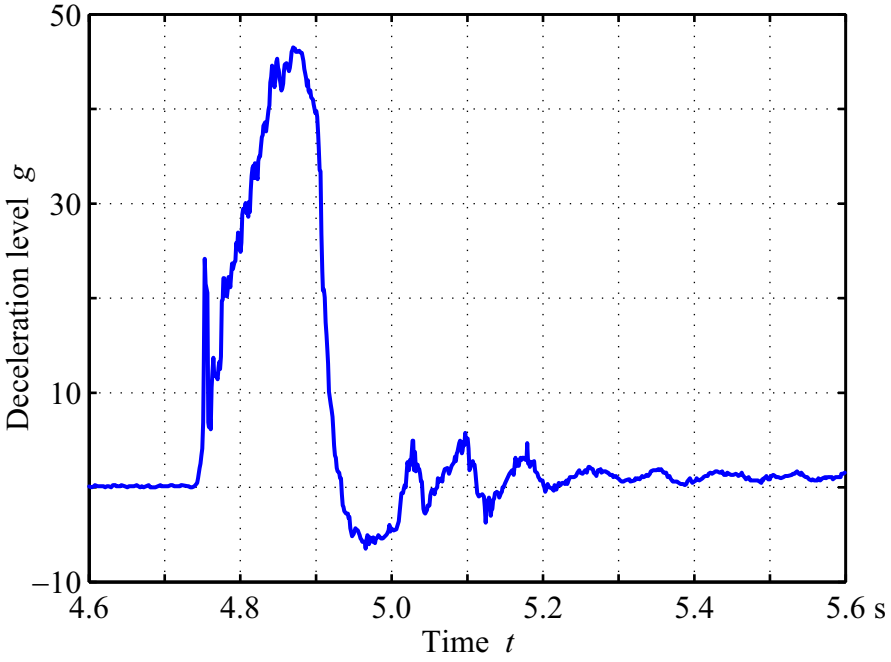

Figure C.2: Deceleration of Drop Capsule Inside Deceleration Container (reprinted from Ref. [104]). Time t is indicated with t_0 referring to the capsule release. The nominal microgravity time of the ZARM drop tower is 4.74 s. The catapult operation mode was not used here [104].

solid propellant booster, boost adapter, S-30 second stage booster, payload, and service system. Figure C.3 shows a typical acceleration profile of the VSB-30 vehicle. Spin stabilization is achieved by using canted fins with a boost motor, resulting in a roll rate of up to 3.0 rps at burnout. De-spin is started 56 s after lift-off by a yo-yo mechanism (cf. Fig. C.3, x- and y-axis) and normally stops 64 s after lift-off. The static loads caused by the spin of 3 Hz can be calculated based on the radial distance of the experiment components from the z-axis [143, 272]. The vibrational loads inside the experimental payload remain below an integrated RMS value of $3\,g_0$ in the spectrum of 15 to 2000 Hz. Nonetheless, the payload components as well as the whole experiment module are designed for $7.5\,g_0$ RMS for qualification and for $5.6\,g_0$ RMS for acceptance on all three axes [66, 143, 196, 272].

Re-entry loads are generated during the re-entry phase of the sounding rocket module (Figure C.4). The static loads during this phase can reach up to $50\,g_0$ in each direction depending on the re-entry conditions of the payload at an altitude of about 40 km and the center of gravity (COG). Against this background, the design load for static acceleration should be in the range of 50 to $60\,g_0$. The

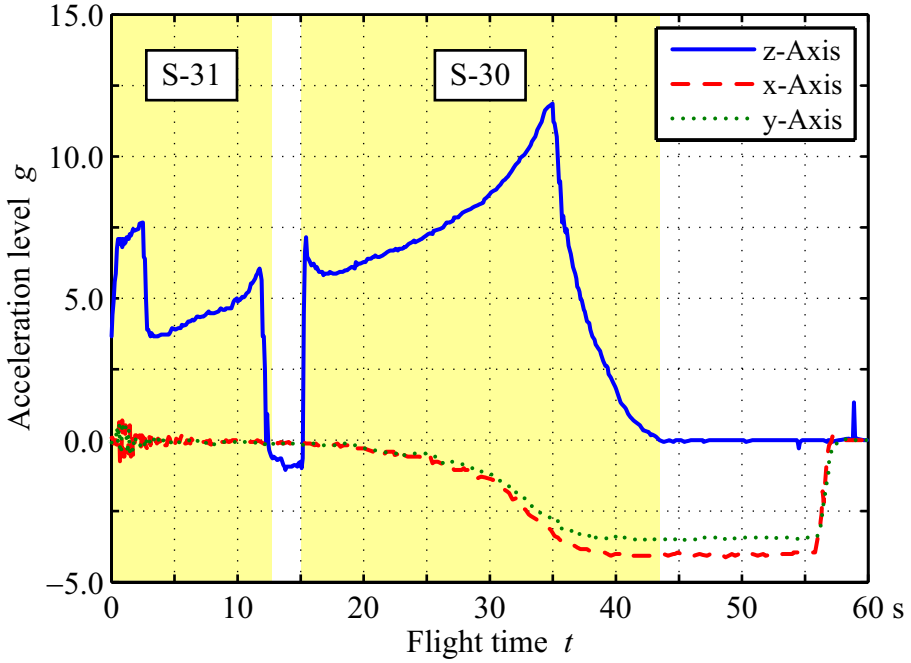

Figure C.3: Acceleration of VSB-30 Sounding Rocket Vehicle During Launch (reprinted from Refs. [196, 272]). At motor ignition, a shock load of 20 g_0 is generated for approximately 15 ms. The following initial acceleration reaches 7.7 g_0 in the longitudinal direction (z-axis) within the first few seconds, and maximum acceleration occurs at 32.0 s during burning of the second stage (S-30) with a value of 11.9 g_0 [66, 196, 272].

final touchdown shock level strongly depends on the ground conditions. Provided an intact parachute, the touchdown velocity is in the order of 10 m s^{-1}, and the shock loads during impact can reach 50 to 60 g_0. In the worst case, the touchdown may generate a shock of 250 g_0 on the payload at an effective time of 7 to 10 ms. This exceptionally high stress level was also considered for the design of the module employed here because such a hard landing occurred on the prior TEXUS-41 [66, 109, 196].

Pressure Loads

The DCU is pressurized during all phases including experiment preparation and execution in the drop tower as well as the sounding rocket environment. In the case of the JCM sounding rocket module, a separate vacuum dome is installed for this purpose (Fig. 3.10, **D**). Consequently, pressure loads on the experimental setup are negligible. However, there are pressure loads on the

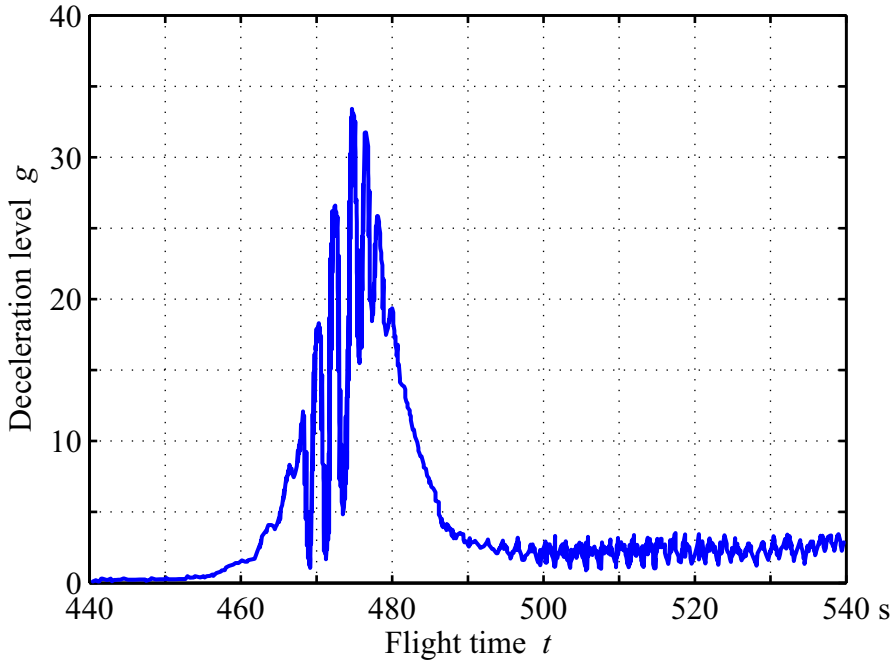

Figure C.4: Deceleration of Sounding Rocket Module During Re-Entry (reprinted from Refs. [109, 196]). Here, the maximum deceleration during re-entry is shown for TEXUS-40. Microgravity time was from $t = 75$ to 432 s [109, 196, 272].

outer vacuum protection. During the sounding rocket flight, the vacuum protection experiences pressure in the range of 1×10^{-7} to 1.5 bar due to evacuation through venting holes and a possible pressurization caused by atmospheric drag [66, 196].

Thermal Loads

Thermal loads are marginal in the drop tower environment. Thus, physical provision could be omitted, apart from the nominal cooling system used to maintain the ambient temperature of the DCU during combustion chamber preheating (Fig. 3.10, **G**).

However, the DCU was exposed to different ambient temperatures during transportation, preparation, and countdown as well as to aerodynamic heating during the ascent and re-entry phase of the sounding rocket flight. Additionally, the whole TEXUS payload was exposed to the environmental winter temperature of North Sweden after touchdown until recovery of the module by helicopter. A temperature range of −20 to 20 °C typically prevails for trans-

portation and 18 °C for preparation at the launch site. During rocket ascent the skin temperature of the outer structure rises up to 140 °C, and during reentry it reaches approximately 200 °C. Nevertheless, the temperature of the DCU within the vacuum dome was in the order of 19 to 33 °C during the experimental phase of the TEXUS-46 flight. A temperature increase of the experiment deck of about 6 K, due to radiation and suppression of convective cooling, was taken into account for the experiment design. An increase from 29 to 32 °C was finally measured for the vicinity of the droplet array generation device. Depending on the winter season in North Sweden, an environmental temperature of −30 °C is probable, but the payload temperature after touchdown does not drop below 0 °C in normal recovery operation, which was the case for the TEXUS-46 mission.

C.2 Construction and Manufacturing Details

Apart from the microgravity environment itself, special design features were incorporated in the experimental setup to provide high quality results. Special attention was given to the droplet array generation system (Fig. 3.2, **D**) to realize equal vapor distribution around each droplet as well as a symmetrical fuel vapor layer around the axis of the droplet array.

Manufacturing of Fine Glass Tubes

The manufacturing process of the fine glass tubes that are integrated into the fuel supply block (Fig. 3.4) can be summarized as follows. Commercially obtainable glass tubes of 1 mm outer diameter are narrowed down to pairs of micropipettes with an outer tip diameter of approximately 40 µm by a pipette generator:

- Thin-walled glass capillaries of standard borosilicate glass are sorted for outer diameters of 0.990±0.002 mm. Their nominal outer and inner diameter is 1 mm and 0.75 mm, respectively. Their length is 90 mm.
- A puller is used to vertically stretch the selected glass capillaries into pipettes by applying heat and using the gravitational force. If the heater

coil is positioned correctly, a symmetric pair of raw pipettes can be generated this way, both of which can be used as fuel supply tubes later on.

- Both raw pipettes are cut to identical lengths with a simple glass cutter.
- Each raw pipette is finished with a microforge[1] to provide a well-defined and sharp orifice diameter. The "cutting" function of the microforge is used for this purpose, as pictured in Figure C.5. The raw pipette is positioned with an overlap of 0.5 to 1.0 mm over the glass bead, whose heater temperature is initially set to zero. After the pipette is brought into contact with the glass bead, the heater temperature is turned up slowly and thermal expansion shifts the glass bead to the left (cf. Fig. C.5). Pipette and glass bead start fusing. As soon as this fusing is observed, heating is interrupted. By the loss of temperature, the glass bead moves back to the right, and the pipette is separated at the fusing location [310].
- The orifice area of the final micropipette is determined by a metallurgical microscope, since it is the decisive parameter for the pressure drop over the orifice and, thus, for the volume of the generated droplet. As not all glass tubes have an absolutely circular orifice, the major and minor axes of the orifice are measured assuming an elliptical shape. The final orifice area is typically in the range of 800 to 1000 μm^2.

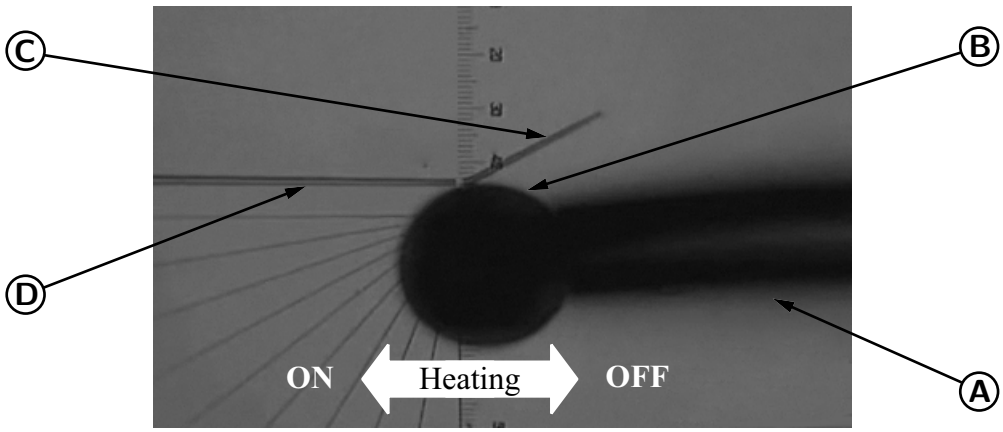

Figure C.5: Cutting of Micropipette with Microforge. This microscope image illustrates the cutting process with the MF-900 microforge of NARISHIGE [310]. **A**: heatable filament, **B**: glass bead, **C**: fused/cut-off piece of raw pipette, **D**: final micropipette.

[1] All instruments and tools are made by NARISHIGE [310]. These are glass tubes of type G-100, puller PC-10, and microforge MF-900.

Performance of Surface Coating

The exhaust gas samples are withdrawn from the combustion chamber via four symmetrically aligned, uncooled fine-orifice probes (see Chaps. 3.1.3 and 3.1.4). Even though critical flow through the probe orifices was not achieved here, the cooling rate of the products was assumed to be sufficient to quench the NO forming reactions, which themselves require a high activation energy. Chemical transformations of NO_x in the temperature range of 300 to 700 K are of special interest here, since moderate temperature probing is encountered and the sample has an extended residence time at lower temperatures while undergoing transport and storage in the EGS system. Figure C.6 shows the stability of hydrogen sulfide (H_2S) when Sulfinert® coating is applied. It offers inertness for active compounds, including polar and volatile organic compounds (VOCs). Sample collection and storage of sulfur, nitrogen, and mercury containing species are reliable at ppb levels [351, 406, 407]. In Figure C.6, the concentration stability of H_2S at 11 ppb is illustrated for dry and humid conditions.

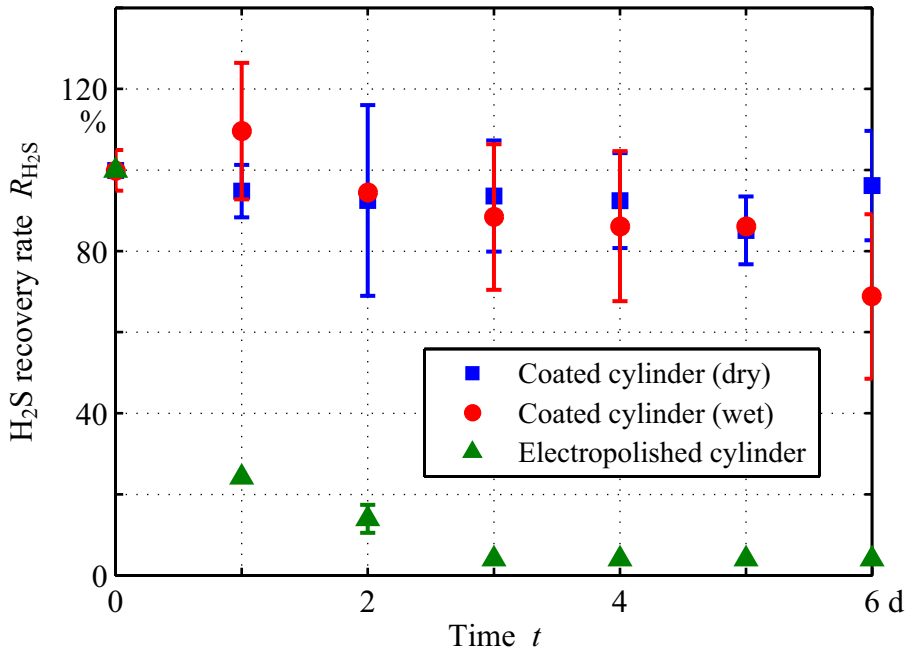

Figure C.6: Stability of Hydrogen Sulfide in Sample Cylinder (reprinted from Refs. [351, 407]).

D Raw Data of Microgravity Experiments

Figures D.1 through D.3 show measurement data of the three combustion runs conducted on TEXUS-46 with $t_\Psi = 5$, 10, and 18 s. Recalling Figure 3.20 and the trigger logic introduced for exhaust gas sampling, there is a discrepancy between the predefined/indicated time limits t_{min} and t_{max} and the actual start of the gas sampling process. This delay is due to a misinterpretation of the ignition duration within the gas sampling process. Still, the overall combustion and gas sampling process was run nominally, and the systematic delay of 1.4 to 1.8 s has no negative impact on the scientific quality of the experimental results. Reproducibility is not affected either.

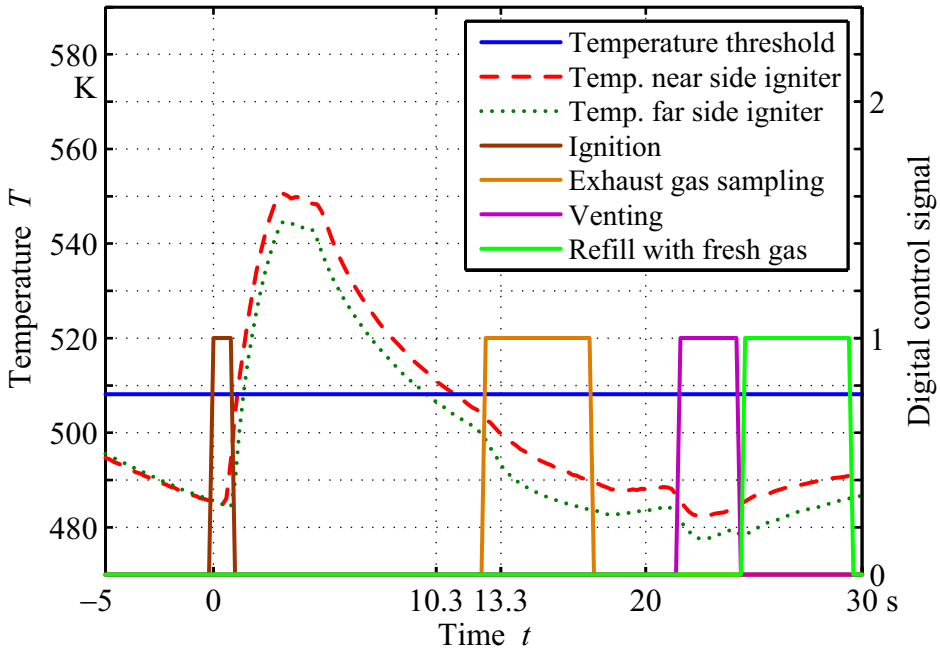

Figure D.1: Temperature and Event Data of PHOENIX Experiment ($t_\Psi = 5$ s). Based on the burnout time calculated for $t_\Psi = 5$ s, the time limits for exhaust gas sampling are indicated at $t_{min} = 10.3$ s and $t_{max} = 13.3$ s.

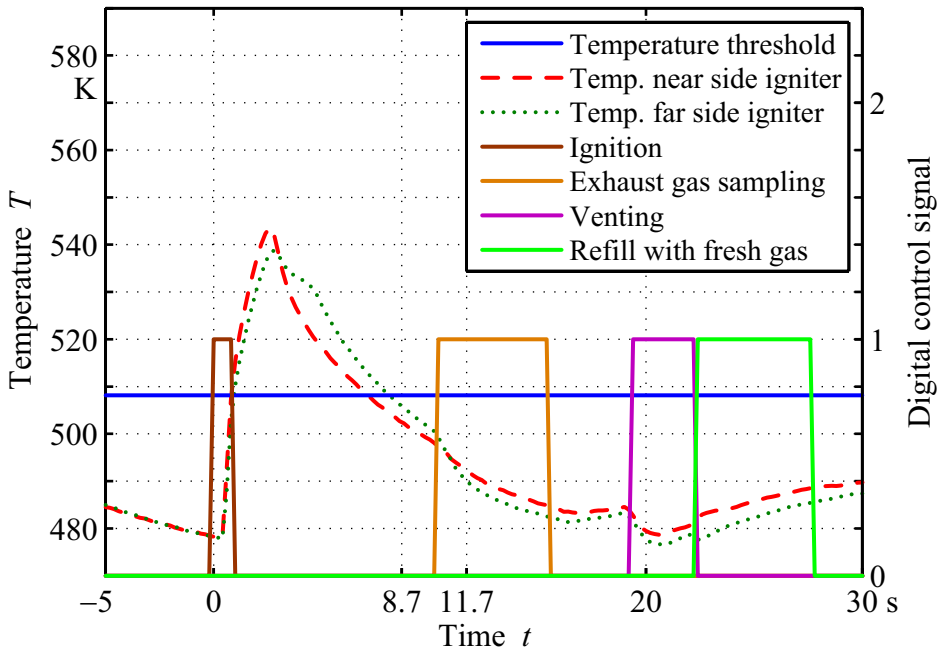

Figure D.2: Temperature and Event Data of PHOENIX Experiment ($t_\Psi = 10\,\mathrm{s}$). Based on the burnout time calculated for $t_\Psi = 5\,\mathrm{s}$, the time limits for exhaust gas sampling are indicated at $t_{\min} = 8.7\,\mathrm{s}$ and $t_{\max} = 11.7\,\mathrm{s}$.

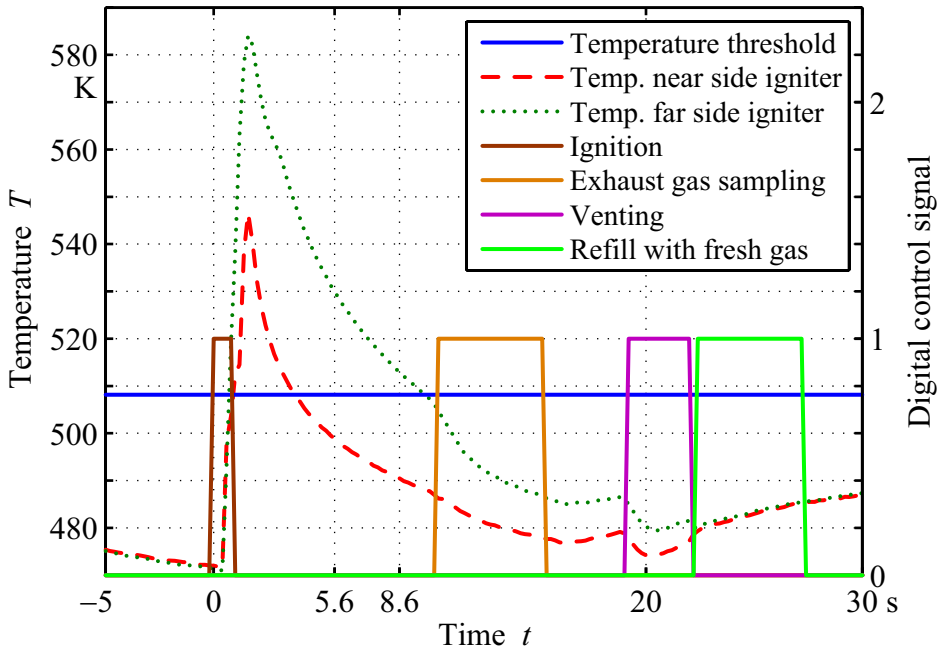

Figure D.3: Temperature and Event Data of PHOENIX Experiment ($t_\Psi = 18\,\mathrm{s}$). Based on the burnout time calculated for $t_\Psi = 5\,\mathrm{s}$, the time limits for exhaust gas sampling are indicated at $t_{\min} = 5.6\,\mathrm{s}$ and $t_{\max} = 8.6\,\mathrm{s}$.

Heat Loss of Combustion Chamber

Figure D.4 shows measurements of the heat loss of the combustion chamber, which is induced by the insertion of the cold droplet array holder into the combustion chamber (see Chap. 3.1.3). In general, all experiment runs unveil an identical cool-down curve. Data is again taken from the combustion runs conducted on TEXUS-46. Operational commands as well as microswitches control the operation of the motors and valves involved. Here, $\Delta t = 2.2\,\mathrm{s}$ passes between the indication of "shutter open" and "lifting device up". The event "lifting device up", in turn, initiates the start of droplet pre-vaporization ($t_\Psi = 0.0\,\mathrm{s}$). The time between indication of "lifting device up" and ignition is $\Delta t = t_\Psi + 0.8\,\mathrm{s}$, subject mainly to the heat-up of the ignition wire. The associated time between indication of the heat loss and ignition is $\Delta t = t_\Psi + 1.4\,\mathrm{s}$ (i.e. 6.4, 11.4, and 19.4 s). As illustrated in Figure D.4, temperature starts to drop with the droplet array holder reaching the interior of the combustion chamber. The mere opening of the combustion chamber shutter does not result in a detectable temperature drop.

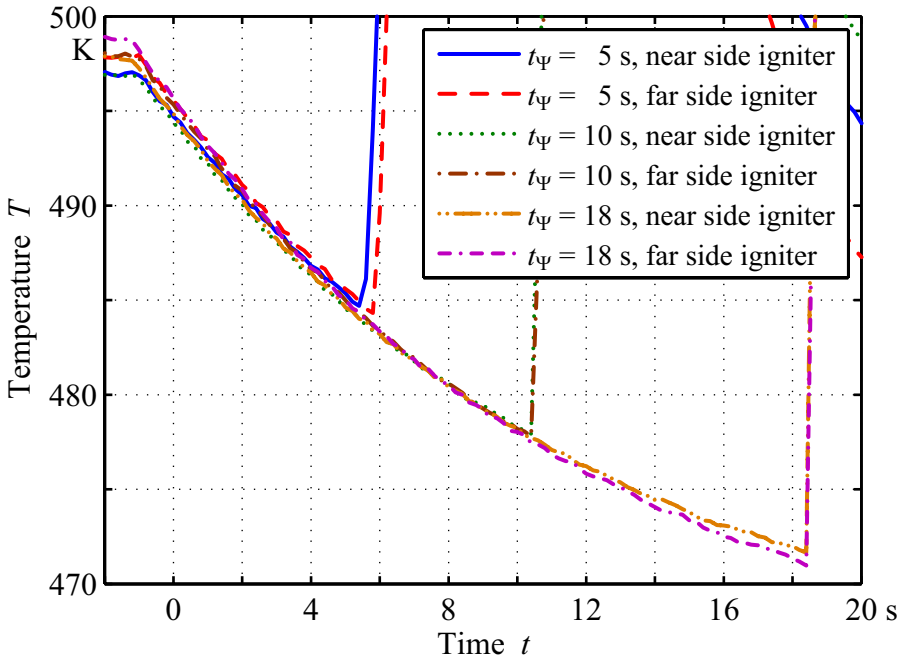

Figure D.4: Heat Loss of Combustion Chamber During Droplet Pre-Vaporization. The measurement readings of the PHOENIX experiment are plotted here. Time $t = t_0$ corresponds to the start of droplet pre-vaporization ($t_\Psi = 0.0\,\mathrm{s}$).

Data on Droplet Vaporization

Tables D.1 through D.3 list the equivalent droplet diameter measured for the combustion runs on TEXUS-46. These data are evaluated on a 1.0 Hz basis. Struk et al. [424] examine various methods of determining such an equivalent droplet diameter of a droplet that is distorted in shape due to fiber suspension (see Chap. 3.1.2). In accordance with the work of Nomura et al. [317, 318, 319], the droplet diameter $D(t_\Psi)$ of this research work is determined via the equiv-

Table D.1: Progression of Droplet Vaporization ($t_\Psi = 5\,s$). Method No. 1 is employed in the work of Kikuchi et al. [208]. Method No. 2 uses the same raw data but a different filter [317–319].

Pre-vaporization time t_Ψ in s	Droplet diameter $D(t_\Psi)$ in mm		Pre-vaporization rate Ψ (Eq. (1.1))	
	Method No. 1	Method No. 2	Method No. 1	Method No. 2
0	1.5501	1.5972	0.0000	0.0000
1	1.5483	1.6144	0.0034	−0.0328
2	1.5559	1.6153	−0.0114	−0.0345
3	1.5515	1.6146	−0.0028	−0.0332
4	1.5461	1.6039	0.0076	−0.0126
5	1.5298	1.5924	0.0388	0.0089

Table D.2: Progression of Droplet Vaporization ($t_\Psi = 10\,s$) [208, 317–319].

Pre-vaporization time t_Ψ in s	Droplet diameter $D(t_\Psi)$ in mm		Pre-vaporization rate Ψ (Eq. (1.1))	
	Method No. 1	Method No. 2	Method No. 1	Method No. 2
0	1.5544	1.6010	0.0000	0.0000
1	1.5583	1.6177	−0.0075	−0.0317
2	1.5577	1.6183	−0.0064	−0.0329
3	1.5544	1.6151	0.0000	−0.0268
4	1.5573	1.6078	−0.0056	−0.0129
5	1.5393	1.6022	0.0288	−0.0023
6	1.5360	1.5951	0.0351	0.0109
7	1.5242	1.5837	0.0572	0.0320
8	1.5028	1.5658	0.0963	0.0644
9	1.4903	1.5514	0.1187	0.0900
10	1.4638	1.5271	0.1648	0.1321

Table D.3: Progression of Droplet Vaporization ($t_\Psi = 18\,\mathrm{s}$) [208, 317–319].

Pre-vaporization time t_Ψ in s	Droplet diameter $D(t_\Psi)$ in mm		Pre-vaporization rate Ψ (Eq. (1.1))	
	Method No. 1	Method No. 2	Method No. 1	Method No. 2
0	1.5500	1.6084	0.0000	0.0000
1	1.5633	1.6225	−0.0260	−0.0266
2	1.5510	1.6268	−0.0020	−0.0347
3	1.5642	1.6288	−0.0277	−0.0386
4	1.5557	1.6227	−0.0110	−0.0270
5	1.5484	1.6164	0.0030	−0.0150
6	1.5371	1.5981	0.0248	0.0191
7	1.5362	1.5864	0.0265	0.0404
8	1.5065	1.5710	0.0819	0.0681
9	1.4938	1.5528	0.1048	0.1001
10	1.4792	1.5359	0.1308	0.1292
11	1.4437	1.5128	0.1920	0.1679
12	1.4267	1.4892	0.2202	0.2063
13	1.4072	1.4653	0.2517	0.2439
14	1.3780	1.4343	0.2974	0.2908
15	1.3500	1.4076	0.3393	0.3297
16	1.3346	1.3773	0.3616	0.3720
17	1.3173	1.3502	0.3862	0.4084
18	1.2983	1.3190	0.4124	0.4485

alent droplet diameter, defined by $(a^2 b)/3$, where a and b are the minor and major axis of the droplet, respectively. The major difference between "Method No. 1" and "Method No. 2" is the filter that distinguishes between droplet and background. The droplet diameter $D(t_\Psi)$ increases during the first 2 to 3 s, and the associated Ψ-value appears to be negative for up to 5 s due to the thermal expansion of the droplet.[1] This is a well-documented behavior for the initial period of droplet heating [210, 307, 309, 312, 465]. The droplet diameter squared increases accordingly, as illustrated in Figure D.5. Considering data fluctuation and reproducibility as well as the deviation from pre-estimated figures, Method No. 2 shows a higher consistency than Method No. 1. Hence, it is chosen for data analysis throughout this work. The vaporization rate for steady-state conditions ($t_\Psi \geq 7\,\mathrm{s}$) calculates to $k = 0.075 \pm 0.025\,\mathrm{mm^2\,s^{-1}}$. Figure D.6 shows corresponding results from the drop tower campaign.

[1] The experimental results discussed in Chapter 5 are compensated for this effect according to Equation (5.4). In this context, Chin and Lefebvre [70] studied the role of the heat-up period in droplet evaporation in an analytical way.

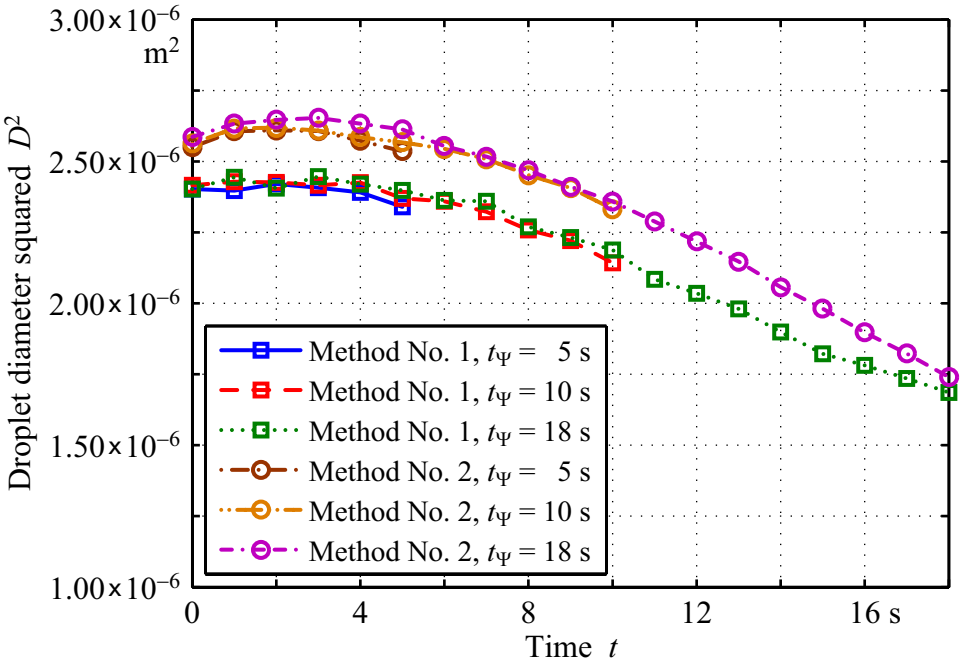

Figure D.5: Time Histories of Droplet Diameter Squared for Vaporizing Droplets. The data are analyzed at intervals of 1.0 Hz, corresponding to Tables D.1 through D.3.

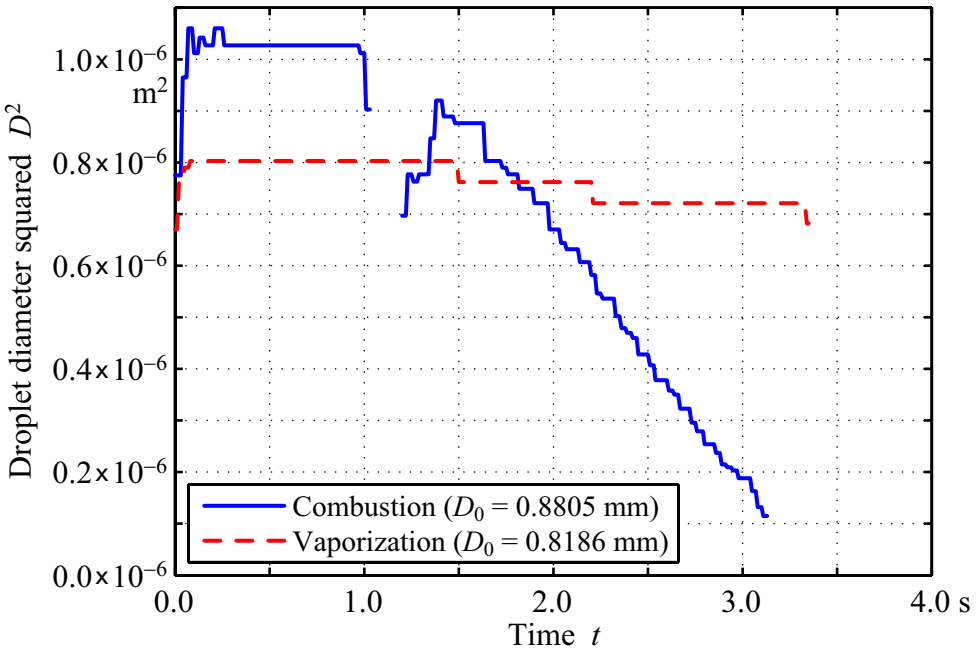

Figure D.6: Time Histories of Droplet Diameter Squared for Vaporizing and Burning Droplets. Measurement data are taken from the TEXNOX drop tower campaign. For combustion: Exp. 20, for vaporization: Exp. 21 (see also Tab. B.1).

Supervised Theses

Im Rahmen dieser Dissertation entstanden am Lehrstuhl für Thermodynamik in den Jahren 2005 bis 2012 unter wesentlicher wissenschaftlicher, fachlicher und inhaltlicher Anleitung des Autors die im Folgenden aufgeführten studentischen Arbeiten. In ihnen wurden verschiedene Fragestellungen zur Verbrennungswissenschaft und -technik sowie zur Abgasentstehung und -analyse untersucht. Ergebnisse aus diesen Arbeiten sind in Teilen in das vorliegende Dokument eingeflossen. Der Autor dankt hiermit nochmals explizit allen ehemals betreuten Studenten für ihr Engagement bei der Unterstützung des hier behandelten Forschungsprojekts sowie der damit verknüpften Dissertation.

Associated with the research under discussion, there are a number of different “student theses” (Semesterarbeiten, Diplomarbeiten, Bachelor theses, or Master theses). This students’ contribution was prepared at the Lehrstuhl für Thermodynamik in the years 2005 through 2012 under the close supervision of the author of this Ph.D. thesis with regard to all academic, professional, and context-related concerns. Various issues were investigated contributing to combustion science and particular applications as well as to exhaust gas formation and exhaust gas analysis. Finally, the author would like to express his sincere gratitude to all formerly supervised students for their commitment and support of this research project and of the Ph.D. thesis at hand.

Student	Thesis
Sebastian Bomberg	*Optimierung eines Modells zur Tropfenverbrennung mittels stabilisierter Finiter Elemente* (in German), Semesterarbeit, filed in December 2009.
Sebastian Bomberg	*Comparison and Evaluation of Different Modelling Approaches of the Nitrogen Oxide Emissions from the Combustion of Single Droplets and Droplet Arrays* (in English), Diplomarbeit, filed in July 2010. Partially integrated in Chapter 1 and 2, Chapter 4 through 6, and Appendix A.
Matthias Bühner	*Modifikation des Abgasentnahmesystems eines TEXUS-Experiments zur Tropfenverbrennung für dessen Einsatz im Parabelflug* (in German), Semesterarbeit, filed in January 2008.
Biyuan Chen	*Aufbau und Inbetriebnahme eines Abgasanalysesystems für geringe Gasmengen am FTIR* (in German), Semesterarbeit, filed in December 2006.
Micha Dirmeier	*Identifizierung von Divergenzen bei Verdunstungsemissionsmessungen an verschiedenen Standorten der BMW Group und Optimierung der bestehenden Prozesse* (in German), Diplomarbeit, filed in November 2007.
Wolfgang J. Fenninger	*Implementation and Evaluation of Different Modeling Approaches of the Nitrogen Oxide Emissions in Droplet Combustion* (in English), Semesterarbeit, filed in January 2011. Partially integrated in Chapter 1 and 2, Chapter 4 through 6, and Appendix A.
Philipp Hack	*Numerische Simulation der Strömungs- und Verbrennungsvorgänge in einer Versuchsbrennkammer* (in German), Semesterarbeit, filed in September 2008. Partially integrated in Chapter 3.
Matthias Huber	*Preparation and Conduction of a Droplet Combustion Experiment for Drop Tower in a Multi-National Research Environment* (in English), Semesterarbeit, filed in May 2009. Partially integrated in Chapter 3 and 5.

Andreas Kollmannsberger	*Evaluation and Implementation of the Safety Measures of a Combustion Experiment for Parabolic Flight* (in English), Semesterarbeit, filed in July 2008.
Le Liu	*Evaluation eines begasten Rührkessels unter Schwerelosigkeit* (in German), Semesterarbeit, filed in June 2008.
Andreas Sachsenhauser	*Konstruktion eines Reaktors zur Aufoxidation von NO zu NO_2* (in German), Semesterarbeit, filed in March 2012.
Christian Schinkel	*Aufbau und Inbetriebnahme eines Abgasanalysesystems für Sprayflammen unter Schwerelosigkeit* (in German), Diplomarbeit, filed in May 2006.
Felix Schröder	*Evaluation of a 125cc High-Performance Two-Stroke Engine by 1D Simulation* (in English), Semesterarbeit, filed in August 2006.
Nicola Schwentner	*Entwicklung und Implementierung einer Versuchssteuerung mit Messdatenerfassung für zeitkritische Verbrennungsprozesse unter Schwerelosigkeitsbedingungen* (in German), Semesterarbeit, filed in January 2007.
Joachim E. Schwing	*Modeling and Simulation of Nitrogen Oxide Emissions from Combustion of Single Droplets and Droplet Arrays* (in English), Diplomarbeit, filed in April 2009. Partially integrated in Chapter 1, Chapter 2, and Chapter 4 through 6.
Klaus G. Vollmer	*Untersuchung verschiedener Zündsystemkonzepte in Verbrennungsprozessen mit Sprayeindüsung und idealer Gasvormischung* (in German), Master thesis, filed in March 2007.
Ruize Xu	*Überarbeitung eines Brennstoffdosiersystems für ein Verbrennungsexperiment unter Schwerelosigkeitsbedingungen* (in German), Semesterarbeit, filed in January 2007.

References

[1] J.A. Aardenne van, G.R. Carmichael, H. Levy II, D. Streets, and L. Hordijk. Anthropogenic NOx Emissions in Asia in the Period 1990 – 2020. *Atmospheric Environment*, 33:633–646, 1999.

[2] B. Abramzon and S.S. Sazhin. Droplet Vaporization Model in the Presence of Thermal Radiation. *International Journal of Heat and Mass Transfer*, 48:1868–1873, 2005.

[3] B. Abramzon and S.S. Sazhin. Convective Vaporization of Fuel Droplet with Thermal Radiation Absorption. *Fuel*, 85:32–46, 2006.

[4] B. Abramzon and W.A. Sirignano. Droplet Vaporization Model for Spray Combustion Calculations. *International Journal of Heat and Mass Transfer*, 32:1605–1618, 1989.

[5] ACARE Strategy Review Group. Aeronautics and Air Transport: Beyond Vision 2020 (Towards 2050). Background document, Advisory Council for Aeronautics Research in Europe (ACARE), June 2010.

[6] M.D. Ackerman, R.O. Colantonio, R.K. Crouch, F.L. Dryer, J.B. Haggard Jr., G.T. Linteris, A.J. Marchese, V. Nayagam, J.E. Voss, F.A. Williams, and B.L. Zhang. A Treatment of Measurements of Heptane Droplet Combustion Aboard MSL-1. Technical memorandum NASA/TM–2003-212553, National Aeronautics and Space Administration (NASA), 2003.

[7] AeroSpace and Defence Industries Association of Europe (Brussels, Belgium). ASD Facts and Figures 2010. Report, September 2011.

[8] S.K. Aggarwal and H.C. Mongia. Multicomponent and High-Pressure Effects on Droplet Vaporization. *Journal of Engineering for Gas Turbines and Power*, 124:248–255, 2002.

[9] S.K. Aggarwal, A.Y. Tong, and W.A. Sirignano. A Comparison of Vaporization Models in Spray Calculations. *AIAA Journal*, 22:1448–1457, 1984.

[10] S.K. Aggarwal, G. Chen, T.A. Jackson, and G.L. Switzer. Vaporization Behavior of Fuel Droplets in a Hot Air Stream. *International Journal of Heat and Mass Transfer*, 34:2669–2673, 1991.

[11] R. Aglave. *CFD Simulation of Combustion Using Automatically Reduced Reaction Mechanisms: A Case for Diesel Engine*. Ph.D. diss., Rupertus-Carola University of Heidelberg, 2007.

[12] I. Aharon and B.D. Shaw. Estimates of Liquid Species Diffusivities from Experiments on Reduced-Gravity Combustion of Heptane-Hexadecane Droplets. *Combustion and Flame*, 113:507–518, 1998.

[13] M. Aigner, A. Mayer, P. Schiessel, and W. Strittmatter. Second-Generation Low-Emission Combustors for ABB Gas Turbines: Test Under Full-Engine Conditions. In *Gas Turbine and Aeroengine Congress*, number 90-GT-308, Brussels, Belgium, 1990.

[14] J.D. Allen. A Review of Methods of Analysis for Oxides of Nitrogen. *Journal of the Institute of Fuel*, 46:123–133, 1973.

[15] J.D. Allen. Probe Sampling of Oxides of Nitrogen from Flames. *Combustion and Flame*, 24:133–136, 1975.

[16] J.D. Allen, J. Billingsley, and J.T. Shaw. Evaluation of the Measurement of Oxides of Nitrogen in Combustion Products by the Chemiluminescence Method. *Journal of the Institute of Fuel*, 47:275–280, 1974.

[17] R.A. Altenkirch, S.M. Shahed, and R.F. Sawyer. Nitric Oxide Formation Around Droplets Burning at Elevated Pressures. *Combustion Science and Technology*, 5:147–154, 1972.

[18] D.N. Anderson. Effect of Premixing on Nitric Oxide Formation . Technical memorandum NASA/TM-X-68220, National Aeronautics and Space Administration (NASA), 1973.

[19] K. Annamalai and I.K. Puri. *Combustion Science and Engineering*. CRC Press, 2007.

[20] K. Annamalai and W. Ryan. Interactive Processes in Gasification and Combustion. Part I: Liquid Drop Arrays and Clouds. *Progress in Energy and Combustion Science*, 18:221–295, 1992.

[21] ANSYS, Inc. (Canonsburg, PA, USA). *ANSYS CFX-Solver Theory Guide – ANSYS CFX Release 11.0*, December 2006.

[22] ANSYS, Inc. (Canonsburg, PA, USA). *ANSYS CFX-Solver Modeling Guide – ANSYS CFX Release 11.0*, December 2006.

[23] J.P. Appleton and J.B. Heywood. The Effects of Imperfect Fuel-Air Mixing in a Burner on NO Formation from Nitrogen in the Air and the Fuel. *Fourteenth Symposium (International) on Combustion*, pages 777–786, 1973.

[24] Arbeitsgemeinschaft Energiebilanzen e.V. (Berlin/Köln, Germany). Evaluation Tables on the Energy Balance for the Federal Republic of Germany – 1990 to 2010, July 2011.

[25] R. Atkinson, A.C. Lloyd, and L. Winges. An Updated Chemical Mechanism for Hydrocarbon/NOx/SO_2 Photooxidations Suitable for Inclusion in Atmospheric Simulation Models. *Atmospheric Environment*, 16:1341–1355, 1982.

[26] M.P. Auer, C. Gebauer, K.G. Moesl, C. Hirsch, and T. Sattelmayer. Active Instability Control: Feedback of Combustion Instabilities on the Injection of Gaseous Fuel. *Journal of Engineering for Gas Turbines and Power*, 127:748–754, 2005.

[27] C.T Avedisian. Recent Advances in Soot Formation from Spherical Droplet Flames at Atmospheric Pressure. *Journal of Propulsion and Power*, 16:628–635, 2000.

[28] C.T. Avedisian and B.J. Callahan. Experimental Study of Nonane/Hexanol Mixture Droplet Combustion Without Natural or Forced Convection. *Proceedings of the Combustion Institute*, pages 991–997, 2000.

[29] C.T. Avedisian, J.C. Yang, and C.H. Wang. On Low-Gravity Droplet Combustion. *Proceedings of the Royal Society of London. Series A*, 420:183–200, 1988.

[30] J.H. Bae and C.T. Avedisian. Experimental Study of the Effect of Helium/Nitrogen Concentration and Initial Droplet Diameter on Nonane Droplet Combustion with Minimal Convection. *Proceedings of the Combustion Institute*, 31:2157–2164, 2007.

[31] S. Baessler. *Einfluss des Vorverdampfungsgrades auf die Stickoxidbildung in Sprayflammen*. Ph.D. diss., Technische Universität München, 2008.

[32] S. Baessler, K.G. Moesl, and T. Sattelmayer. NOx Emissions of a Premixed Partially Vaporized Kerosene Spray Flame. *Journal of Engineering for Gas Turbines and Power*, 129:695–702, 2007.

[33] R.S. Barlow, A.N. Karpetis, J.H. Frank, and J.-Y. Chen. Scalar Profiles and NO Formation in Laminar Opposed-Flow Partially Premixed Methane/Air Flames. *Combustion and Flame*, 127:2102–2118, 2001.

[34] J.C. Barnes and A.M. Mellor. Quantifying Unmixedness in Lean Premixed Combustors Operating at High Pressure, Fired Conditions. In *International Gas Turbine & Aeroengine Congress & Exhibition*, number 97-GT-73, Orlando, FL, USA, 1997.

[35] J.C. Barnes and A.M. Mellor. Effects of Unmixedness in Piloted-Lean Premixed Gas Turbine Combustors. In *International Gas Turbine & Aeroengine Congress & Exhibition*, number 97-GT-206, Orlando, FL, USA, 1997.

[36] F. Battin-Leclerc. Detailed Kinetic Models for the Low-Temperature Combustion of Hydrocarbons with Application to Gasoline and Diesel Fuel Surrogates. *Progress in Energy and Combustion Science*, 34:440–498, 2008.

[37] F. Battin-Leclerc, R. Fournet, P.A. Glaude, B. Judenherc, V. Warth, G.M. Côme, and G. Scacchi. Modeling of the Gas-Phase Oxidation of n-Decane from 550 to 1600 K. *Proceedings of the Combustion Institute*, 28:1597–1605, 2000.

[38] C.H. Beck. *Analyse der Stickoxidbildung in mageren Sprayflammen mit partieller Vorverdunstung*. Ph.D. diss., Universität Karlsruhe, 2009.

[39] C.H. Beck, R. Koch, and H.-J. Bauer. Investigations of the Effect of Incomplete Droplet Prevaporization on NOx Emissions in LDI Combustion Systems. *Journal of Engineering for Gas Turbines and Power*, 130: 051504/1–8, 2008.

[40] C.H. Beck, R. Koch, and H.-J. Bauer. Identification of Droplet Burning Modes in Lean, Partially Prevaporized Swirl-Stabilized Spray Flames. *Proceedings of the Combustion Institute*, 32:2195–2203, 2009.

[41] C.H. Beck, R. Koch, and H.-J. Bauer. Numerical Investigation of the Time Scales of Single Droplet Burning. *Flow, Turbulence and Combustion*, 82: 571–598, 2009.

[42] J. Becker and C. Hassa. Breakup and Atomization of a Kerosene Jet in Crossflow at Elevated Pressure. *Atomization and Sprays*, 11:49–67, 2002.

[43] G. Bikas. *Kinetic Mechanisms for Hydrocarbon Ignition*. Ph.D. diss., Rheinisch-Westfälische Technische Hochschule Aachen, 2001.

[44] G. Bikas and N. Peters. Kinetic Modelling of n-Decane Combustion and Autoignition. *Combustion and Flame*, 126:1456–1475, 2001.

[45] R.B. Bird, W.E. Stewart, and E.N. Lightfoot. *Transport Phenomena*. John Wiley & Sons, 1960.

[46] F.M. Black and J.E. Sigsby Jr. Chemiluminescent Method for NO and NOx (NO + NO_2) Analysis. *Environmental Science & Technology*, 8:149–152, 1974.

[47] T. Bolik, O. Essmann, C. Eigenbrod, and H.J. Rath. Experimental Study of the Autoignition in a Two-Droplet Arrangement at JAMIC and ZARM. In *Drop Tower Days*, Sapporo, Japan, 1998.

[48] J.A. Bolt and M.A. Saad. Combustion Rates of Freely Falling Fuel Drops in a Hot Atmosphere. *Sixth Symposium (International) on Combustion/The Combustion Institute*, pages 717–725, 1957.

[49] R. Bounaceur, P.A. Glaude, R. Fournet, F. Battin-Leclerc, S. Jay, and A. Pires da Cruz. Kinetic Modeling of a Surrogate Diesel Fuel Applied to 3D Auto-Ignition in HCCI Engines. Technical paper, Département de Chimie Physique des Réactions, Nancy, France, 2007.

[50] C.T. Bowman. Kinetics of Nitric Oxide Formation in Combustion Processes. *Fourteenth Symposium (International) on Combustion/The Combustion Institute*, pages 729–738, 1973.

[51] C.T. Bowman. Control of Combustion-Generated Nitrogen Oxide Emissions: Technology Driven by Regulation. *Twenty-Forth Symposium (International) on Combustion/The Combustion Institute*, pages 859–878, 1992.

[52] C.T. Bowman, R.K. Hanson, D.F. Davidson, W.C. Gardiner Jr., V.V. Lissianski, G.P. Smith, D.M. Golden, M. Frenklach, and M. Goldenberg. GRI-Mech 2.11, June 2009. URL `http://www.me.berkeley.edu/gri_mech/`.

[53] J.W. Bozzelli, A.Y. Chang, and A.M. Dean. Analysis of the Reactions H+N_2O and NH+NO: Pathways and Rate Constants over a Wide Range of Temperature and Pressure. *Twenty-Fifth Symposium (International) on Combustion/The Combustion Institute*, pages 965–974, 1994.

[54] F.V. Bracco. "NO" Formation in Droplet Diffusion Flames. In *Western States Section/The Combustion Institute, Fall Meeting*, Irvine, CA, USA, 1971.

[55] F.V. Bracco. Nitric Oxide Formation in Droplet Diffusion Flames. *Fourteenth Symposium (International) on Combustion/The Combustion Institute*, pages 831–842, 1973.

[56] J.H. Bromly, F.J. Barnes, and L.H. Little. The Effect of Low Levels of CO, H_2 and Hydrocarbons on NO_2/NO Ratios in Heated Gases. *Journal of the Institute of Energy*, 61:89–97, 1988.

[57] J.R. Brückner-Kalb. *Sub-ppm-NOx-Verbrennungsverfahren für Gasturbinen*. Ph.D. diss., Technische Universität München, 2008.

[58] T.A. Brzustowski, E.M. Twardus, S. Wojcicki, and A. Sobiesiak. Interaction of Two Burning Fuel Droplets of Arbitrary Size. *AIAA Journal*, 17: 1234–1242, 1979.

[59] T.A. Brzustowski, A. Sobiesiak, and S. Wojcicki. Flame Propagation Along an Array of Liquid Fuel Droplets at Zero Gravity. *Eighteenth Symposium (International) on Combustion/The Combustion Institute*, pages 265–273, 1981.

[60] F. Buda, R. Bounaceur, V. Warth, P.A. Glaude, R. Fournet, and F. Battin-Leclerc. Progress Toward a Unified Detailed Kinetic Model for the Autoignition of Alkanes from C_4 to C_{10} Between 600 and 1200 K. *Combustion and Flame*, 142:170–186, 2005.

[61] S.P. Burke and T.E.W. Schuhmann. Diffusion Flames. *Industrial and Engineering Chemistry*, 20:998–1004, 1928.

[62] H.F. Calcote. Mechanisms of Soot Nucleation in Flames – A Critical Review. *Combustion and Flame*, 42:215–242, 1981.

[63] G.S. Canada and G.M. Faeth. Fuel Droplet Burning Rates at High Pressures. Contractor report NASA/CR–126666, National Aeronautics and Space Administration (NASA), 1972.

[64] L.S. Caretto. Modeling Pollutant Formation in Combustion Processes. *Fourteenth Symposium (International) on Combustion*, pages 803–816, 1973.

[65] V.P. Carey. *Liquid-Vapor Phase-Change Phenomena*. Taylor & Francis, 2007.

[66] E. Ceglia. *European Users Guide to Low Gravity Platforms*. Erasmus User Center and Communication Office (HME-HE), European Space Agency (ESA), Noordwijk, The Netherlands, September 2005.

[67] J.-Y. Chen. Development of Reduced Mechanisms for Numerical Modelling of Turbulent Combustion. In *Workshop on "Numerical Aspects of Reduction in Chemical Kinetics"*, Cite Descartes - Champus sur Marne, France, 1997.

[68] R.-H. Chen. Some Characteristics of NOx Emission of Turbulent Nonpremixed Hydrogen-Air Flames Stabilized by Swirl-Generated Flow Recirculation. *Combustion Science and Technology*, 110:443–460, 1995.

[69] R.-H. Chen and J.F. Driscoll. Nitric Oxide Levels of Jet Diffusion Flames: Effects of Coaxial Air and Other Mixing Parameters. *Twenty-Third Symposium (International) on Combustion/The Combustion Institute*, pages 281–288, 1990.

[70] J.S. Chin and A.H. Lefebvre. The Role of the Heat-up Period in Fuel Drop Evaporation. *International Journal of Turbo and Jet Engines*, 2:315–325, 1985.

[71] H.H. Chiu. Dynamics of Deformation of Liquid Drops. *Astronautica Acta*, 15:199–213, 1970.

[72] H.H. Chiu and T.M. Liu. Group Combustion of Liquid Droplets. *Combustion Science and Technology*, 17:127–142, 1977.

[73] H.H. Chiu, H.Y. Kim, and E.J. Croke. Internal Group Combustion of Liquid Droplet. *Nineteenth Symposium (International) on Combustion/The Combustion Institute*, pages 971–980, 1982.

[74] S.Y. Cho and F.L. Dryer. A Numerical Study of the Unsteady Burning Behaviour of n-Heptane Droplets. *Combustion Theory and Modelling*, 3:267–280, 1999.

[75] S.Y. Cho, M.Y. Choi, and F.L. Dryer. Extinction of a Free Methanol Droplet in Microgravity. *Twenty-Third Symposium (International) on Combustion/The Combustion Institute*, pages 1611–1617, 1990.

[76] M.Y. Choi, F.L. Dryer, and J.B. Haggard Jr. Observations on Slow Burning Regime for Hydrocarbon Droplets: n-Heptane/Air Results. *Twenty-Third Symposium (International) on Combustion/The Combustion Institute*, pages 1597–1604, 1990.

[77] M.Y. Choi, F.L. Dryer, J.M. Card, F.A. Williams, J.B. Haggard Jr., and B.A. Borowski. Microgravity Combustion of Isolated n-Decane and n-Heptane Droplets. In *30th Aerospace Sciences Meeting & Exhibit*, number AIAA-92-0242, Reno, NV, USA, 1992.

[78] M.Y. Choi, F.L. Dryer, G.J. Green, and J.J. Sangiovanni. Soot Agglomeration in Isolated Free Droplet Combustion. In *31th Aerospace Sciences Meeting & Exhibit*, number AIAA-93-0823, Reno, NV, USA, 1993.

[79] M.Y. Choi, A. Yozgatligil, A. Kazakov, F.L. Dryer, and P. Ferkul. Sooting and Radiation Effects in Microgravity Droplet Combustion. In *AIAA Conference & Exhibit on International Space Station Utilization*, number AIAA-2001-5045, Cape Canaveral, FL, USA, 2001.

[80] Comsol AB (Stockholm, Sweden). *COMSOL Multiphysics User's Guide (COMSOL 3.5)*, September 2008.

[81] Comsol AB (Stockholm, Sweden). *COMSOL Multiphysics Modeling Guide (COMSOL 3.5)*, September 2008.

[82] Comsol AB (Stockholm, Sweden). *COMSOL Reaction Engineering Lab User's Guide (COMSOL 3.5a)*, November 2008.

[83] Comsol AB (Stockholm, Sweden). *Chemical Engineering Module User's Guide (COMSOL 3.5a)*, November 2008.

[84] C.S. Cooper and N.M. Laurendeau. Quantitative Measurements of Nitric Oxide Concentration in High-Pressure, Swirl-Stabilized Spray Flames. Contractor report NASA/CR–2000-210365, National Aeronautics and Space Administration (NASA), 2000.

[85] C.S. Cooper and N.M. Laurendeau. Quantitative Measurements of Nitric Oxide in High-Pressure (2-5 atm), Swirl-Stabilized Spray Flames via Laser-Induced Fluorescence. *Combustion and Flame*, 123:175–188, 2000.

[86] L.P. Cooper. Effect of Degree of Fuel Vaporization upon Emissions for a Premixed Partially Vaporized Combustion System. Technical paper 1582, National Aeronautics and Space Administration (NASA), 1980.

[87] L.P. Cooper. Analysis of Effect of Flameholder Characteristics on Lean, Premixed, Partially Vaporized Fuel-Air Mixture Quality and Nitrogen Oxides Emissions. Technical paper 1842, National Aeronautics and Space Administration (NASA), 1981.

[88] S.M. Correa. A Review of NOx Formation Under Gas-Turbine Combustion Conditions. *Combustion Science and Technology*, 87:329–362, 1993.

[89] R.A. Cox and J.A. Cole. Chemical Aspects of the Autoignition of Hydrocarbon-Air Mixtures. *Combustion and Flame*, 60:109–123, 1985.

[90] M.A. Cremer, C.J. Montgomery, D.H. Wang, M.P. Heap, and J.-Y. Chen. Development and Implementation of Reduced Chemistry for Computational Fluid Dynamics Modeling of Selective Non-Catalytic Reduction. *Proceedings of the Combustion Institute*, 28:2427–2434, 2000.

[91] A. Crespo and A. Liñán. Unsteady Effects in Droplet Evaporation and Combustion. *Combustion Science and Technology*, 11:9–18, 1975.

[92] A. Cuoci, M. Mehl, G. Buzzi-Ferraris, T. Faravelli, D. Manca, and E. Ranzi. Autoignition and Burning Rates of Fuel Droplets Under Microgravity. *Combustion and Flame*, 143:211–226, 2005.

[93] P. Dagaut. Kinetics of Jet Fuel Combustion over Extended Conditions: Experimental and Modeling. *Journal of Engineering for Gas Turbines and Power*, 129:394–403, 2007.

[94] P. Dagaut and M. Cathonnet. The Ignition, Oxidation, and Combustion of Kerosene: A Review of Experimental and Kinetic Modeling. *Progress in Energy and Combustion Science*, 32:48–92, 2006.

[95] P. Dagaut, P. Glarborg, and M.U. Alzueta. The Oxidation of Hydrogen Cynide and Related Chemistry. *Progress in Energy and Combustion Science*, 34:1–46, 2008.

[96] J.M. Daisey. Organic Compounds in Urban Aerosols. *Annals of the New York Academy of Sciences*, 338:50–69, 1980.

[97] S.P. Davis, M.C. Abrams, and J.W. Brault. *Fourier Transform Spectroscopy*. Academic Press, 2001.

[98] K.L. Demerjian, J.A. Kerr, and J.G. Calvert. *The Mechanism of Photochemical Smog Formation*, volume 4 of *Advances in Environmental Science and Technology*. John Wiley & Sons, 1974.

[99] R.A. Dickman, W.J. Dodds, and E.E. Ekstedt. Lean, Premixed-Prevaporized (LPP) Combustor Conceptual Design Study. Final report NASA/CR–159629, General Electric Company, 1979.

[100] L.A. Diehl. Measurement of Gaseous Emissions from an Afterburning Turbojet Engine at Simulated Altitude Conditions. Technical memorandum NASA/TM-X-2726, National Aeronautics and Space Administration (NASA), 1973.

[101] D.L. Dietrich, J.B. Haggard Jr., F.L. Dryer, V. Nayagam, B.D. Shaw, and F.A. Williams. Droplet Combustion Experiments in Spacelab. *Twenty-Sixth Symposium (International) on Combustion/The Combustion Institute*, pages 1201–1207, 1996.

[102] D.L. Dietrich, P.M. Struk, M. Ikegami, and G. Xu. Single Droplet Combustion of Decane in Microgravity: Experiments and Numerical Modelling. *Combustion Theory and Modelling*, 9:569–585, 2005.

[103] J. Dignon and S. Hameed. Global Emissions of Nitrogen and Sulfur Oxides from 1860 to 1980. *Journal of Air Pollution Control Association (JAPCA)*, 39:180–186, 1989.

[104] Drop Tower Operation and Service Company ZARM FABmbH (Bremen, Germany). *ZARM Drop Tower Bremen User Manual*, November 2007.

[105] F.L. Dryer, A. Kazakov, and B.D. Urban. Some Recent Observations on the Burning of Isolated n-Heptane and Alcohol Droplets. In *Sixth International Microgravity Combustion Workshop*, number NASA/CP–2001-210826, pages 233–236, Cleveland, OH, USA, 2001.

[106] J. Duterque, R. Borghi, and H. Tichtinsky. Study of Quasi-Global Schemes for Hydrocarbon Combustion. *Combustion Science and Technology*, 26:1–15, 1981.

[107] H.A. Dwyer and B.R. Sanders. Calculations of Unsteady Reacting Droplet Flows. *Twenty-Second Symposium (International) on Combustion/The Combustion Institute*, pages 1923–1929, 1988.

[108] H.A. Dwyer, P. Stapf, and R. Maly. Unsteady Vaporization and Ignition of a Three-Dimensional Droplets Array. *Combustion and Flame*, 121: 181–194, 2000.

[109] EADS Astrium GmbH (Bremen, Germany). Schlussbericht TEXUS-40. Final report, 2003.

[110] Eastman Kodak (San Diego, CA, USA). *KODAK Motion Corder Analyzer, User's Manual SR-Series*, September 1999.

[111] Eco Physics AG (Dürnten, Switzerland). *CLD 700 EL ht*, Januar 1997.

[112] Eco Physics AG (Dürnten, Switzerland). *CLD 700 AL*, February 2002.

[113] Eco Physics AG (Dürnten, Switzerland). Prospekt CLD 700 EL ht, September 2005.

[114] Eco Physics AG (Dürnten, Switzerland). Prospekt CLD 700 LEV ht, September 2005.

[115] Eco Physics AG (Dürnten, Switzerland). Brochure EFT 700, September 2005.

[116] R.B. Edelman and O.F. Fortune. A Quasi-Global Chemical Kinetic Model for the Finite Rate Combustion of Hydrocarbon Fuels with Application to Turbulent Burning and Mixing in Hypersonic Engines and Nozzles. In *AIAA 7th Aerospace Sciences Meeting*, number AIAA-69-86, New York, NY, USA, 1969.

[117] R.B. Edelman and P.T. Harsha. Laminar and Turbulent Gas Dynamics in Combustors – Current Status. *Progress in Energy and Combustion Science*, 4:1–62, 1978.

[118] F.N. Egolfopoulos. METRANS Research Project 08-01: Combustion and Emission Characteristics of Biofuels Used for Transportation. Final report, National Center for Metropolitan Transportation Research, 2009.

[119] C.T. Eichler and T. Sattelmayer. Experiments on Flame Flashback in a Quasi-2D Turbulent Wall Boundary Layer for Premixed Methane-Hydrogen-Air Mixtures. *Journal of Engineering for Gas Turbines and Power*, 133:011503/1–7, 2011.

[120] C.T. Eichler, G. Baumgartner, and T. Sattelmayer. Experimental Investigation of Turbulent Boundary Layer Flashback Limits for Premixed Hydrogen-Air Flames Confined in Ducts. *Journal of Engineering for Gas Turbines and Power*, 134:011502/1–8, 2012.

[121] C. Eigenbrod, O. Moriue, P. Weilmuenster, and H.J. Rath. Development of a Simple Model Fuel for Kerosene Droplet Ignition. In *28th International Annual Conference of Fraunhofer Institut Chemische Technologie*, pages 42/1–14, Karlsruhe, Germany, 1997.

[122] C. England, J. Houseman, and D.P. Teixeira. Sampling Nitric Oxide from Combustion Gases. *Combustion and Flame*, 20:439–442, 1973.

[123] V.S. Engleman, W. Bartok, J.P. Longwell, and R.B. Edelman. Experimental and Theoretical Studies of NOx Formation in a Jet-Stirred Reactor. *Fourteenth Symposium (International) on Combustion/The Combustion Institute*, pages 755–765, 1973.

[124] R. Ennetta, M. Hamdi, and R. Said. Comparison of Different Chemical Kinetic Mechanisms of Methane Combustion in an Internal Combustion Engine Configuration. *Thermal Science*, 12:43–51, 2008.

[125] A. Eroglu, K. Döbbeling, F. Joos, and P. Brunner. Vortex Generators in Lean-Premix Combustion. *Journal of Engineering for Gas Turbines and Power*, 123:41–49, 2001.

[126] G.M. Faeth. Current Status of Droplet and Liquid Combustion. *Progress in Energy and Combustion Science*, 3:191–224, 1977.

[127] G.M. Faeth. Evaporation and Combustion of Sprays. *Progress in Energy and Combustion Science*, 9:1–76, 1983.

[128] G.M. Faeth. Priorities for Microgravity Combustion Research and Goals for Workshop Discussions. In *Second International Microgravity Combustion Workshop*, number NASA/CP–1992-10013, Cleveland, OH, USA, 1992.

[129] G.M. Faeth, D.P. Dominicis, J.F. Tulpinsky, and D.R. Olson. Supercritical Bipropellant Droplet Combustion. *Twelfth Symposium (International) on Combustion/The Combustion Institute*, pages 9–18, 1969.

[130] T. Farouk and F.L. Dryer. Microgravity Droplet Combustion: Effect of Tethering Fiber on Burning Rate and Flame Structure. *Combustion Theory and Modelling*, 15:487–515, 2011.

[131] C.P. Fenimore. Formation of Nitric Oxide in Premixed Hydrocarbon Flames. *Thirteenth Symposium (International) on Combustion/The Combustion Institute*, pages 373–380, 1971.

[132] C.P. Fenimore. The Ratio NO_2/NO in Fuel-Lean Flames. *Combustion and Flame*, 25:85–90, 1975.

[133] C.P. Fenimore and G.W. Jones. Nitric Oxide Decomposition at 2200 – 2400 °K. *The Journal of Physical Chemistry*, 61:654–657, 1957.

[134] C.P. Fenimore and G.W. Jones. Rate of Reaction in Hydrogen, Nitrous Oxide and in Some Other Flames. *The Journal of Physical Chemistry*, 63: 1154–1158, 1959.

[135] C.P. Fenimore and G.W. Jones. Rate of the Reaction, O + $N_2O \rightarrow 2\,NO$. *Eighth Symposium (International) on Combustion/The Combustion Institute*, pages 127–133, 1961.

[136] D. Fitz and W.A. Welch. Quantification of Uncertainties in Continuous Measurement Systems for Low NOx Emissions from Stationary Sources. Final report 01-AP-18491-01-DFR, College of Engineering-Center for Environmental Research and Technology, University of California, 2001.

[137] R.S. Fletcher and J.B. Heywood. A Model for Nitric Oxide Emissions from Aircraft Gas Turbine Engines. In *AIAA 9th Aerospace Sciences Meeting*, number AIAA-71-123, New York, NY, USA, 1971.

[138] R. Friedman and E. Burke. Measurement of Temperature Distribution in a Low Pressure Flat Flame. *The Journal of Chemical Physics*, 22:824–830, 1954.

[139] J. Fritz. *Flammenrückschlag durch verbrennungsinduziertes Wirbelaufplatzen*. Ph.D. diss., Technische Universität München, 2003.

[140] A. Frohn and N. Roth. *Dynamics of Droplets*. Springer-Verlag, 2000.

[141] N. Frössling. Über die Verdunstung fallender Tropfen. *Gerlands Beiträge zur Geophysik*, 52:170–216, 1938.

[142] N. Fuchs. Über die Verdampfungsgeschwindigkeit kleiner Tröpfchen in einer Gasatmosphäre. *Physikalische Zeitschrift der Sowjetunion*, 6:224–243, 1934.

[143] M. García-Fernández, M. Markgraf, and O. Montenbruck. Spin Rate Estimation of Sounding Rockets Using GPS Wind-up. *GPS Solutions*, 12: 155–161, 2008.

[144] F.-J. Gärtner. *Vergleich der Bildung von Stickstoffoxid in Methanol/Luft- und Kohlenwasserstoff/Luft-Flammen*. Ph.D. diss., Technische Hochschule Darmstadt, 1982.

[145] M. Gautam. Testing of Volatile and Nonvolatile Emissions from Advanced Technology Natural Gas Vehicles. Final report, Center for Alternative Fuels, Engines & Emissions, West Virginia University, 2011.

[146] A.G. Gaydon and H.G. Wolfhard. *Flames – Their Structure, Radiation and Temperature*. Chapman and Hall, 1979.

[147] V. Giovangigli. *Multicomponent Flow Modeling*. Birkhäuser Boston, 1999.

[148] I. Glassman. Soot Formation in Combustion Processes. *Twenty-Second Symposium (International) on Combustion/The Combustion Institute*, pages 295–311, 1988.

[149] I. Glassman and R.A. Yetter. *Combustion*. Academic Press, 2008.

[150] S. Gluck, C. Glenn, T. Logan, B. Vu, M. Walsh, and P. Williams. Evaluation of NOx Flue Gas Analyzers for Accuracy and Their Applicability for Low-Concentration Measurements. *Journal of the Air & Waste Management Association*, 53:749–758, 2003.

[151] G.A.E Godsave. Combustion of Droplets in a Fuel Spray. *Nature*, 164: 708–709, 1949.

[152] G.A.E. Godsave. Studies of the Combustion of Drops in a Fuel Spray – The Burning of Single Drops of Fuel. *Fourth Symposium (International) on Combustion/The Combustion Institute*, pages 818–830, 1953.

[153] G. Gogos, S. Soh, and D.N. Pope. Effects of Gravity and Ambient Pressure on Liquid Fuel Droplet Evaporation. *International Journal of Heat and Mass Transfer*, 46:283–296, 2003.

[154] M. Goldsmith. *The Burning of Single Drops of Fuel in Oxidizing Atmospheres*. Ph.D. diss., California Institute of Technology, 1955.

[155] M. Goldsmith. Experiments on the Burning of Single Drops of Fuel. *Jet Propulsion*, 26:172–178, 1956.

[156] D. Goodwin. Cantera, January 2009. URL `http://sourceforge.net/projects/cantera`.

[157] X. Gou, W. Sun, Z. Chen, and Y. Ju. A Dynamic Multi-Timescale Method for Combustion Modeling with Detailed and Reduced Chemical Kinetic Mechanisms. *Combustion and Flame*, 157:1111–1121, 2010.

[158] H. Günzler and H.-U. Gremlich. *IR-Spektroskopie*. Wiley-VCH Verlag, 2003.

[159] S.C. Gupta. *The Classical Stefan Problem – Basic Concepts, Modelling, and Analysis*, volume 45 of *North-Holland Series in Applied Mathematics and Mechanics*. Elsevier, 2003.

[160] N. Hadjiconstantinou, K. Min, and J.B. Heywood. Relation Between Flame Propagation Characteristics and Hydrocarbon Emissions Under Lean Operating Conditions in Spark-Ignition Engines. *Twenty-Sixth Symposium (International) on Combustion/The Combustion Institute*, pages 2637–2644, 1996.

[161] J.B. Haggard Jr., M.H. Brace, J.L. Kropp, and F.L Dryer. Droplet Combustion Experiment Drop Tower Tests Using Models of the Space Flight Apparatus. In *27th Aerospace Sciences Meeting*, number AIAA-89-0501, Reno, NV, USA, 1989.

[162] J.B. Haggard Jr., M.H. Brace, F.L. Dryer, M.Y. Choi, F.A. Williams, and J. Card. n-Decane-Air Droplet Combustion Experiments in the NASA-Lewis 5 Second Zero-Gravity Facility. In *28th Aerospace Sciences Meeting*, number AIAA-90-0649, Reno, NV, USA, 1990.

[163] J.B. Haggard Jr., B.A. Borowski, F.L. Dryer, M.Y. Choi, F.A. Williams, and J. Card. n-Decane Droplet Combustion in the NASA-Lewis 5 Second Zero-Gravity Facility: Results in Test Gas Environments Other Than Air. In *29th Aerospace Sciences Meeting*, number AIAA-91-0720, Reno, NV, USA, 1991.

[164] A.R. Hall and J. Diederichsen. An Experimental Study of the Burning of Single Drops of Fuel in Air at Pressures up to Twenty Atmospheres. *Fourth Symposium (International) on Combustion/The Combustion Institute*, pages 837–846, 1953.

[165] C.J. Halstead, G.H. Nation, and L. Turner. The Determination of Nitric Oxide and Nitrogen Dioxide in Flue Gases – Part I: Sampling and Colorimetric Determination. *Analyst*, 97:55–63, 1972.

[166] C.J. Halstead, G.H. Nation, and L. Turner. The Determination of Nitric Oxide and Nitrogen Dioxide in Flue Gases - Part II: Continuous Instrumental Methods. *Analyst*, 97:64–69, 1972.

[167] M.P. Halstead, L.J. Kirsch, A. Prothero, and C.P. Quinn. A Mathematical Model for Hydrocarbon Autoignition at High Pressures. *Proceedings of the Royal Society of London. Series A*, 346:515–538, 1975.

[168] M.P. Halstead, L.J. Kirsch, and C.P. Quinn. The Autoignition of Hydrocarbon Fuels at High Temperatures and Pressures – Fitting of a Mathematical Model. *Combustion and Flame*, 30:45–60, 1977.

[169] D. Hänel. *Molekulare Gasdynamik*. Springer-Verlag, 2004.

[170] H. Hara and S. Kumagai. Experimental Investigation of Free Droplet Combustion Under Microgravity. *Twenty-Third Symposium (International) on Combustion/The Combustion Institute*, pages 1605–1610, 1990.

[171] J.E. Harrington, G.P. Smith, P.A. Berg, A.R. Noble, J.B. Jeffries, and D.R. Crosley. Evidence for a New NO Production Mechanism in Flames. *Twenty-Sixth Symposium (International) on Combustion/The Combustion Institute*, pages 2133–2138, 1996.

[172] D.J. Hautman, F.L. Dryer, K.P. Schug, and I. Glassman. A Multiple-Step Overall Kinetic Mechanism for the Oxidation of Hydrocarbons. *Combustion Science and Technology*, 25:219–235, 1981.

[173] A.N. Hayhurst and E.M. Hutchinson. Evidence for a New Way of Producing NO via NNH in Fuel-Rich Flames at Atmospheric Pressure. *Combustion and Flame*, 114:274–279, 1998.

[174] B.S. Haynes and H.G. Wagner. Soot Formation. *Progress in Energy and Combustion Science*, 7:229–273, 1981.

[175] T.J. Held, A.J. Marchese, and F.L. Dryer. A Semi-Empirical Reaction Mechanism for n-Heptane Oxidation and Pyrolysis. *Combustion Science and Technology*, 123:107–146, 1997.

[176] J.C. Hewson and M. Bollig. Reduced Mechanisms for NOx Emissions from Hydrocarbon Diffusion Flames. *Twenty-Sixth Symposium (International) on Combustion/The Combustion Institute*, pages 2171–2180, 1996.

[177] J.B. Heywood. Gas Turbine Combustor Modeling for Calculating Nitric Oxide Emissions. In *AIAA/SAE 7th Propulsion Joint Specialist Conference*, number AIAA-71-712, Salt Lake City, UT, USA, 1971.

[178] J.B. Heywood and T. Mikus. Parameters Controlling Nitric Oxide Emissions from Gas Turbine Combustors. In *41st Meeting of the AGARD Propulsion and Energetics Panel on "Atmospheric Pollution by Aircraft Engines"*, pages 21/1–14, London, UK, 1973.

[179] J.C. Hilliard and R.W. Wheeler. Catalysed Oxidation of Nitric Oxide to Nitrogen Dioxide. *Combustion and Flame*, 29:15–19, 1977.

[180] J.O. Hirschfelder, C.F. Curtiss, and R.B. Bird. *Molecular Theory of Gases and Liquids*. John Wiley & Sons, 1966.

[181] J. Hoffmann. *Messen nichtelektronischer Grössen – Grundlagen der Praxis*. VDI-Verlag, 1996.

[182] S. Honnet, K. Seshadri, U. Niemann, and N. Peters. A Surrogate Fuel for Kerosene. *Proceedings of the Combustion Institute*, 32:485–492, 2009.

[183] M. Hori, N. Matsunaga, P.C. Malte, and N.M. Marinov. The Effect of Low-Concentration Fuels on the Conversion of Nitric Oxide to Nitrogen Dioxide. *Twenty-Fourth Symposium (International) on Combustion/The Combustion Institute*, pages 909–916, 1992.

[184] G.L. Hubbard, V.E. Denny, and A.F. Mills. Droplet Evaporation: Effects of Transients and Variable Properties. *International Journal of Heat and Mass Transfer*, 18:1003–1008, 1975.

[185] K.J. Hughes, A.S. Tomlin, E. Hampartsoumian, W. Nimmo, I.G. Zsély, M. Ujvári, T. Turányi, A.R. Clague, and M.J. Pilling. An Investigation of Important Gas-Phase Reactions of Nitrogenous Species from the Simulation of Experimental Measurements in Combustion Systems. *Combustion and Flame*, 124:573–589, 2001.

[186] K.J. Hughes, T. Turányi, A. Clague, and M.J. Pilling. Development and Testing of a Comprehensive Chemical Mechanism for the Oxidation of Methane. *International Journal of Chemical Kinetics*, 33:513–538, 2001.

[187] K.J. Hughes, T. Turányi, and M.J. Pilling. The Leeds Methane Oxidation Mechanism 1.5, July 2011. URL `http://garfield.chem.elte.hu/Combustion/Combustion.html`.

[188] K.J. Hughes, T. Turányi, M.J. Pilling, and A.S. Tomlin. The Leeds Nitrogen Chemistry Mechanism 2.0, July 2011. URL `http://garfield.chem.elte.hu/Combustion/Combustion.html`.

[189] I.E. Idelchik. *Handbook of Hydraulic Resistance*. Jaico Publishing House, 2008.

[190] International Organization for Standardization (Genève, Switzerland). ISO 3977-2: Gas turbines – Procurement – Part 2: Standard reference conditions and ratings. Norm, June 1997.

[191] A. Ishmurzin, B. Schramm, D. Lebiedz, and J. Warnatz. Reduction of Detailed Reaction Mechanisms for Large Hydrocarbons Combustion by the ILDM Method. In *Proceedings of the European Combustion Meeting*, Orléans, France, 2003.

[192] G.S. Jackson and C.T. Avedisian. The Effect of Initial Diameter in Spherically Symmetric Droplet Combustion of Sooting Fuels. *Proceedings of the Royal Society of London. Series A*, 446:255–276, 1994.

[193] P. Jansohn. *Bildung und Abbau N-haltiger Verbindungen, insbesondere von HCN, NH_3 und NO, in turbulenten Diffusionsflammen*. Ph.D. diss., Universität Karlsruhe, 1991.

[194] P. Jansohn, T. Ruck, C. Steinbach, H.-P. Knöpfel, and T. Sattelmayer. Development of the Advanced EV (AEV) Burner for the ABB GTX100 Gas Turbine. In *ASME Asia 97 – International Gas Turbine Conference*, number 97-AA-139, Singapore, 1997.

[195] Japan Aerospace Exploration Agency. Experimental Plan of JAXA-ESA Cooperative Microgravity Combustion Experiment "PHOENIX" for TEXUS-46. Technical report, September 2009.

[196] Japan Aerospace Exploration Agency and EADS Astrium GmbH. Hardware/Software Interface Control Document (ICD) – Technical Experiment Module - Japanese Combustion Module (TEM-JCM). Technical report, March 2009.

[197] Japan Aerospace Exploration Agency and EADS Astrium GmbH. Operations Requirements Document – Technical Experiment Module - Japanese Combustion Module (TEM-JCM). Technical report, March 2009.

[198] Y. Jin and B.D. Shaw. Computational Modeling of n-Heptane Droplet Combustion in Air-Diluent Environments Under Reduced-Gravity. *International Journal of Heat and Mass Transfer*, 53:5782–5791, 2010.

[199] W.P. Jones and R.P. Lindstedt. Global Reaction Schemes for Hydrocarbon Combustion. *Combustion and Flame*, 73:233–249, 1988.

[200] D.D. Joseph and Y.Y. Renardy. *Fundamentals of Two-Fluid Dynamics*. Springer-Verlag, 1993.

[201] J.R. Kalb and T. Sattelmayer. Lean Blowout Limit and NOx-Production of a Premixed Sub-ppm NOx Burner with Periodic Recirculation of Combustion Products. *Journal of Engineering for Gas Turbines and Power*, 128:247–254, 2006.

[202] J. Kanevsky. Interference During Burning in Air for Nine Stationary Fuel Droplets Arranged in a Body-Centered Cubic Lattice. *Jet Propulsion*, 26: 788, 1956.

[203] S. Kato, H. Mizuno, H. Kobayashi, and T. Niioka. Experiments on Flame Spread of a Fuel Droplet Array in a High-Pressure Ambience. *JSME International Journal - Series B - Fluids and Thermal Engineering*, 41:322–330, 1998.

[204] A.S. Kesten. Analysis of NO Formation in Single Droplet Combustion. *Combustion Science and Technology*, 6:115–123, 1972.

[205] M. Kikuchi, Wakashima Y., S. Yoda, and M. Mikami. Numerical Study on Flame Spread of an n-Decane Droplet Array in Different Temperature Environment Under Microgravity. *Proceedings of the Combustion Institute*, 30:2001–2009, 2005.

[206] M. Kikuchi, S. Yamamoto, S. Yoda, Y. Wakashima, and M. Mikami. Effect of Ambient Temperature on Flame Spread of an n-Decane Droplet Array Under Microgravity. In *56th International Astronautical Congress*, number IAC-05-A2.7.04, Fukuoka, Japan, 2005.

[207] M. Kikuchi, N. Sugano, S. Yoda, and M. Mikami. Effects of Pre-Vaporization on Flame Spread of a Linear Fuel Droplet Array in Microgravity. In *6th Asia-Pacific Conference on Combustion*, pages 639–642, Nagoya, Japan, 2007.

[208] M. Kikuchi, S. Yamamoto, S. Yoda, M. Mikami, H. Nomura, O. Moriue, A. Umemura, Y. Hisashi, N. Sugano, K.G. Moesl, T. Sattelmayer, C. Eigenbrod, and O. Minster. Japan-Europe Collaborative Droplet Array Combustion Experiment in Microgravity Onboard TEXUS-46 – Technical Achievements and Preliminary Scientific Results. In *Proceedings of the 20th ESA Symposium on European Rocket and Balloon Programmes and Related Research*, volume ESA SP-700, Hyères, France, 2011.

[209] M.K. King and H.D. Ross. Overview of the NASA Microgravity Combustion Program. *AIAA Journal*, 36:1337–1345, 1998.

[210] R. Kneer. *Grundlegende Untersuchungen zur Sprühstrahlausbreitung in hochbelasteten Brennräumen: Tropfenverdunstung und Sprühstrahlcharakterisierung*. Ph.D. diss., Universität Karlsruhe, 1993.

[211] E. Knudsen and H. Pitsch. A Validation Study of the Flamelet Approach's Ability to Predict Flame Structure when Fluid Mechanics are Fully Resolved. In *Center for Turbulence Research Annual Research Briefs*, pages 185–197, 2009.

[212] H. Kobayashi, J. Park, T. Iwahashi, and T. Niioka. Microgravity Experiments on Flame Spread of an n-Decane Droplet Array in a High-Pressure Environment. *Proceedings of the Combustion Institute*, 29: 2603–2610, 2002.

[213] M.N. Kogan. Molecular Gas Dynamics. *Annual Review of Fluid Mechanics*, 5:383–404, 1973.

[214] J. Kolar. *Stickstoffoxide und Luftreinhaltung - Grundlagen, Emissionen, Transmission, Immission, Wirkungen*. Springer-Verlag, 1990.

[215] A.A. Konnov, G. Colson, and J. De Ruyck. The New Route Forming NO Via NNH. *Combustion and Flame*, 121:548–550, 2000.

[216] M. Kono, K. Ito, T. Niioka, T. Kadota, and J. Sato. Current State of Combustion Research in Microgravity. *Twenty-Sixth Symposium (International) on Combustion/The Combustion Institute*, 26:1189–1199, 1996.

[217] J.C. Kramlich and P.C. Malte. Modeling and Measurement of Sample Probe Effects on Pollutant Gases Drawn from Flame Zones. *Combustion Science and Technology*, 18:91–104, 1978.

[218] M. Kröner. *Einfluss lokaler Löschvorgänge auf den Flammenrückschlag durch verbrennungsinduziertes Wirbelaufplatzen*. Ph.D. diss., Technische Universität München, 2003.

[219] S. Kumagai. Combustion of Fuel Droplets in a Falling Chamber with Special Reference to the Effect of Natural Convection. *Jet Propulsion*, 26:786, 1956.

[220] S. Kumagai. Combustion of Fuel Sprays. *Sixth Symposium (International) on Combustion/The Combustion Institute*, pages 668–674, 1956.

[221] S. Kumagai and H. Isoda. Combustion of Fuel Droplets. *Nature*, 166: 1111, 1950.

[222] S. Kumagai and H. Isoda. Combustion of Fuel Droplets in a Falling Chamber. *Sixth Symposium (International) on Combustion/The Combustion Institute*, pages 726–731, 1956.

[223] S. Kumagai, T. Sakai, and S. Okajima. Combustion of Free Fuel Droplets in a Freely Falling Chamber. *Thirteenth Symposium (International) on Combustion/The Combustion Institute*, pages 779–785, 1970.

[224] P.K. Kundu and I.M. Cohen. *Fluid Mechanics*. Elsevier Academic Press, 2004.

[225] K.K. Kuo. *Principles of Combustion*. John Wiley & Sons, 1986.

[226] V.N. Kurdyumov and A. Liñán. Structure of a Flame Front Propagating Against the Flow Near a Cold Wall. *International Journal of Bifurcation and Chaos*, 12:2547–2555, 2002.

[227] M. Labowsky. Calculation of the Burning Rates of Interacting Fuel Droplets. *Combustion Science and Technology*, 22:217–226, 1980.

[228] J.C. Lasheras, A.C. Fernandez-Pello, and F.L. Dryer. On the Disruptive Burning of Free Droplets of Alcohol/n-Paraffin Solutions and Emulsions. *Eighteenth Symposium (International) on Combustion/The Combustion Institute*, pages 293–305, 1981.

[229] N.M. Laurendeau. Fast Nitrogen Dioxide Reactions: Significance During NO Decomposition and NO_2 Formation. *Combustion Science and Technology*, 11:89–96, 1975.

[230] C.K. Law. Asymptotic Theory for Ignition and Extinction in Droplet Burning. *Combustion and Flame*, 24:89–98, 1975.

[231] C.K. Law. Unsteady Droplet Combustion with Droplet Heating. *Combustion and Flame*, 26:17–22, 1976.

[232] C.K. Law. Multicomponent Droplet Combustion with Rapid Internal Mixing. *Combustion and Flame*, 26:219–233, 1976.

[233] C.K. Law. Recent Advances in Droplet Vaporization and Combustion. *Progress in Energy and Combustion Science*, 8:171–201, 1982.

[234] C.K. Law. Combustion in Microgravity: Opportunities, Challenges, and Progress. In *28th Aerospace Sciences Meeting*, number AIAA-90-0120, Reno, NV, USA, 1990.

[235] C.K. Law and G.M. Faeth. Opportunities and Challenges of Combustion in Microgravity. *Progress in Energy and Combustion Science*, 20:65–113, 1994.

[236] C.K. Law and W.A Sirignano. Unsteady Droplet Combustion with Droplet Heating - II: Conduction Limit. *Combustion and Flame*, 28:175–186, 1977.

[237] C.K. Law and F.A. Williams. Kinetics and Convection in the Combustion of Alkane Droplets. *Combustion and Flame*, 19:393–405, 1972.

[238] C.K. Law, S.H. Chung, and N. Srinivasan. Gas-Phase Quasi-Steadiness and Fuel Vapor Accumulation Effects in Droplet Burning. *Combustion and Flame*, 38:173–198, 1980.

[239] A. Lee and C.K. Law. An Experimental Investigation on the Vaporization and Combustion of Methanol and Ethanol Droplets. *Combustion Science and Technology*, 86:253–265, 1992.

[240] J.C.Y. Lee, P.C. Malte, and M.A. Benjamin. Low NOx Combustion for Liquid Fuels: Atmospheric Pressure Experiments Using a Staged Prevaporizer-Premixer. *Journal of Engineering for Gas Turbines and Power*, 125:861–871, 2003.

[241] A.H. Lefebvre. *Gas Turbine Combustion*. Hemisphere Publishing, 1983.

[242] A.H. Lefebvre. Fuel Effects on Gas Turbine Combustion-Liner Temperature, Pattern Factor, and Pollutant Emissions. *Journal of Aircraft*, 21: 887–898, 1984.

[243] A.H. Lefebvre. Fuel Effects on Gas Turbine Combustion – Ignition, Stability, and Combustion Efficiency. *Journal of Engineering for Gas Turbines and Power*, 107:24–37, 1985.

[244] A.H. Lefebvre. *Atomization and Sprays*. Hemisphere Publishing, 1989.

[245] A.H. Lefebvre. The Role of Fuel Preparation in Low-Emission Combustion. *Journal of Engineering for Gas Turbines and Power*, 117:617–654, 1995.

[246] A.H. Lefebvre (ed.). Lean Premixed/Prevaporized Combustion. Conference proceedings NASA/CP–1977-2016, National Aeronautics and Space Administration (NASA), Cleveland, OH, USA, 1977.

[247] G. Leippe, B. Lenzen, P. Spurk, W. Fabinski, M. Moede, H. Pongratz, W. Schindler, and E. Schiefer. Neues System zur Messung von Stickstoffkomponenten im Einsatz an SCR-Katalysatoren. *MTZ*, 65:392–399, 2004.

[248] A. Levy. Unresolved Problems in SOx, NOx, Soot Control in Combustion. *Nineteenth Symposium (International) on Combustion/The Combustion Institute*, pages 1223–1242, 1982.

[249] B. Lewis and G. von Elbe. *Combustion, Flames and Explosions of Gases*. Academic Press, New York, NY, USA, 1951.

[250] S.C. Li and F.A. Williams. NOx Formation in Two-Stage Methane-Air Flames. *Combustion and Flame*, 118:399–414, 1999.

[251] S.C. Li, N. Ilincic, and F.A. Williams. Reduction of NOx Formation by Water Sprays in Strained Two-Stage Flames. *Journal of Engineering for Gas Turbines and Power*, 119:836–843, 1997.

[252] T. Lieuwen, Y. Neumeier, and B.T. Zinn. The Role of Unmixedness and Chemical Kinetics in Driving Combustion Instabilities in Lean Premixed Combustors. *Combustion Science and Technology*, 135:193–211, 1998.

[253] A. Liñán and F.A. Williams. *Fundamental Aspects of Combustion*. The Oxford Engineering Science Series 34. Oxford University Press, 1993.

[254] R.P. Lindstedt and L.Q. Maurice. Detailed Chemical-Kinetic Model for Aviation Fuels. *Journal of Propulsion and Power*, 16:187–195, 2000.

[255] A.J. Lock, R. Ganguly, I.K. Puri, S.K. Aggarwal, and U. Hegde. Gravity Effects on Partially Premixed Flames: An Experimental-Numerical Investigation. *Proceedings of the Combustion Institute*, 30:511–518, 2005.

[256] T. Lu, Y. Ju, and C.K. Law. Complex CSP for Chemistry Reduction and Analysis. *Combustion and Flame*, 126:1445–1455, 2001.

[257] A. Luch. *Molekulare Mechanismen der Kanzerogenese: Untersuchungen am Beispiel des Umweltschadstoffes Dibenzo[a,l]pyren*. Habil. thesis, Technische Universität München, 1999.

[258] D.E. Ludwig, F.V. Bracco, and D.T. Harrje. Nitric Oxide and Composition Measurements Within Diffusion Flames Around Simulated Ethanol and Ethanol-Pyridine Droplets. *Combustion and Flame*, 25:107–120, 1975.

[259] A.E. Lutz, R.J. Kee, and J.A. Miller. Senkin: A Fortran Program for Predicting Homogeneous Gas Phase Chemical Kinetics with Sensivity Analysis. Report SAND87-8248, Sandia National Laboratories, 1997.

[260] K.H. Lyle, L.K. Tseng, J.P. Gore, and N.M. Laurendeau. A Study of Pollutant Emission Characteristics of Partially Premixed Turbulent Jet Flames. *Combustion and Flame*, 116:627–639, 1999.

[261] V.J. Lyons. Effect of Fuel-Air-Ratio Nonuniformity on Emissions of Nitrogen Oxides. Technical paper 1798, National Aeronautics and Space Administration (NASA), 1981.

[262] U. Maas and S.B. Pope. Simplifying Chemical Kinetics: Intrinsic Low-Dimensional Manifolds in Composition Space. *Combustion and Flame*, 88:239–264, 1992.

[263] G. Maier and S. Wittig. Fuel Preparation and Emission Characteristics of a Pressure Loaded LPP Combustor. In *30th AIAA Fluid Dynamics Conference*, number AIAA-99-3774, Norfolk, VA, USA, 1999.

[264] G. Maier, M. Willmann, and S. Wittig. Development and Optimization of Advanced Atomizers for Application in Premix Ducts. In *International Gas Turbine & Aeroengine Congress & Exhibition*, number 97-GT-56, Orlando, FL, USA, 1997.

[265] E.-F. Mallard and H.L. Le Chatelier. Recherches Experimentales et Théoriques sur la Combustion des Mélanges Gazeux Explosifs – Troisième Mémoire. Sur les Températures de Combustion et les Chaleurs Spécifiques des Gaz aux Températures Élevées. *Annales des Mines*, 4:379–568, 1883.

[266] P.C. Malte and J.C. Kramlich. Further Observations of the Effect of Sample Probes on Pollutant Gases Drawn from Flame Zones. *Combustion Science and Technology*, 22:263–269, 1980.

[267] S.L. Manzello, M.Y. Choi, A. Kazakov, F.L. Dryer, R. Dobashi, and T. Hirano. The Burning of Large n-Heptane Droplets in Microgravity. *Proceedings of the Combustion Institute*, 28:1079–1086, 2000.

[268] C. Maqua, G. Castanet, and F. Lemoine. Bi-Component Droplets Evaporation: Temperature Measurements and Modelling. *Fuel*, 87:2932–2942, 2008.

[269] A.J. Marchese and F.L. Dryer. Science Support for Space-Based Droplet Combustion: Drop Tower Experiments and Detailed Numerical Modeling. In *4th International Microgravity Conference*, Cleveland, OH, USA, 1997.

[270] A.J. Marchese, F.L. Dryer, and R.O. Colantonio. Radiative Effects in Space-Based Methanol/Water Droplet Combustion Experiments. *Twenty-Seventh Symposium (International) on Combustion/The Combustion Institute*, pages 2627–2634, 1998.

[271] A.J. Marchese, F.L. Dryer, and V. Nayagam. Numerical Modeling of Isolated n-Alkane Droplet Flames: Initial Comparisons with Ground and Space-Based Microgravity Experiments. *Combustion and Flame*, 116: 432–459, 1999.

[272] M. Markgraf. VSB30 Phoenix GPS Tracking System. Flight report, Space Flight Technology, German Space Operations Center (GSOC), Deutsches Zentrum für Luft- und Raumfahrt (DLR) e.V., May 2005.

[273] R.D. Matthews, R.F. Sawyer, and R.W. Schefer. Interferences in Chemiluminescent Measurement of NO and NO_2 Emissions from Combustion Systems. *Environmental Science & Technology*, 11:1092–1096, 1977.

[274] N. McElwee. *Oil Creek... the Beginning: A History and Guide to the Early Oil Industry in Pennsylvania.* Oil Creek Press, 2001.

[275] H. Meinel and T. Just. Measurement of NOx Exhaust Emissions by a New NDUV Analyzer. In *14th Aerospace Sciences Meeting*, number AIAA-76-137, Washington, D.C., USA, 1976.

[276] Merck KGaA. Safety Data Sheet – n-Decane ($C_{10}H_{22}$), April 2007. URL `http://www.chemdat.info`.

[277] H.J. Merk. The Macroscopic Equations for Simultaneous Heat and Mass Transfer in Isotropic, Continuous and Closed Systems. *Journal of Applied Sciences Research*, 8:73–99, 1958.

[278] M. Mikami, M. Kono, J. Sato, D.L. Dietrich, and F.A. Williams. Combustion of Miscible Binary-Fuel Droplets at High Pressure Under Microgravity. *Combustion Science and Technology*, 90:111–123, 1993.

[279] M. Mikami, O. Habara, M. Kono, J. Sato, D.L. Dietrich, and F.A. Williams. Pressure Effects in Droplet Combustion of Miscible Binary Fuels. *Combustion Science and Technology*, 124:295–309, 1997.

[280] M. Mikami, M. Kono, J. Sato, and D.L. Dietrich. Interactive Effects in Two-Droplet Combustion of Miscible Binary Fuels at High Pressure. *Twenty-Seventh Symposium (International) on Combustion/The Combustion Institute*, pages 2643–2649, 1998.

[281] M. Mikami, S. Miyamoto, and N. Kojima. Counterflow Diffusion Flame with Polydisperse Sprays. *Proceedings of the Combustion Institute*, 29: 593–599, 2002.

[282] M. Mikami, H. Oyagi, N. Kojima, M. Kikuchi, Y. Wakashima, and S. Yoda. Microgravity Experiments on Flame Spread Along Fuel-Droplet Arrays Using a New Droplet-Generation Technique. *Combustion and Flame*, 141:241–252, 2005.

[283] M. Mikami, H. Oyagi, N. Kojima, Y. Wakashima, M. Kikuchi, and S. Yoda. Microgravity Experiments on Flame Spread Along Fuel-Droplet Arrays at High Temperatures. *Combustion and Flame*, 146:391–406, 2006.

[284] V.A. Mikhel'son. *On the Normal Ignition Rate of Fulminating Gas Mixtures* (О нормальной скорости воспламенения гремучих газовых смесей). Ph.D. thesis (in Collected Works, Vol. 1, pp. 87-161, Новый Агроном Press, Moscow, 1930), Lomonosov Moscow State University, 1889.

[285] V.A. Mikhel'son. Über die normale Entzündungsgeschwindigkeit explosiver Gasgemische. *Annalen der Physik und Chemie*, 273:1–24, 1889.

[286] V.A. Mikhel'son. On the Normal Ignition Rate of Fulminating Gas Mixtures (О нормальной скорости воспламененiя гремучихъ газовыхъ смѣсей). Ученыя записки Императорскаго Московскаго университета, Отдѣлъ физико-математическiй, 10:1–92, 1893.

[287] T. Mikus and J.B. Heywood. The Automotive Gas Turbine and Nitric Oxide Emissions. *Combustion Science and Technology*, 4:149–158, 1971.

[288] T. Mikus, J.B. Heywood, and R.E. Hicks. Nitric Oxide Formation in Gas Turbine Engines: A Theoretical and Experimental Study. Contractor report NASA/CR–2977, National Aeronautics and Space Administration (NASA), 1978.

[289] J.A. Miller and C.T. Bowman. Mechanism and Modeling of Nitrogen Chemistry in Combustion. *Progress in Energy and Combustion Science*, 15:287–338, 1989.

[290] J.A. Miller, R.J. Kee, and C.K. Westbrook. Chemical Kinetics and Combustion Modeling. *Annual Review of Physical Chemistry*, 41:345–387, 1990.

[291] J.A. Miller, S.J. Klippenstein, and P. Glarborg. A Kinetic Issue in Reburning: The Fate of HCNO. *Combustion and Flame*, 135:357–362, 2003.

[292] K. Miyasaka and C.K. Law. Combustion of Strongly-Interacting Linear Droplet Arrays. *Eighteenth Symposium (International) on Combustion/The Combustion Institute*, pages 283–292, 1981.

[293] K.G. Moesl, T. Sattelmayer, M. Kikuchi, and S. Yoda. Preparations of the NOx Measurements for the Combustion of an n-Decane Droplet Array Under Microgravity Conditions. *Journal of The Japan Society of Microgravity Application (JASMA)*, 25:361–366, 2008.

[294] K.G. Moesl, T. Sattelmayer, M. Kikuchi, and S. Yoda. NOx Measurements in the Combustion of an n-Decane Droplet Array Under Microgravity Conditions on TEXUS-46. In *19th ESA Symposium on European Rocket and Balloon Programmes and Related Research*, volume ESA SP-671, Bad Reichenhall, Germany, 2009.

[295] K.G. Moesl, K.G. Vollmer, T. Sattelmayer, J. Eckstein, and H. Kopecek. Experimental Study on Laser-Induced Ignition of Swirl-Stabilized Kerosene Flames. *Journal of Engineering for Gas Turbines and Power*, 131:021501/1–8, 2009.

[296] K.G. Moesl, T. Sattelmayer, C. Eigenbrod, M. Kikuchi, S. Yamamoto, S. Yoda, M. Mikami, H. Nomura, O. Moriue, A. Umemura, Y. Hisashi, and N. Sugano. The Study of Droplet Array Combustion on TEXUS-46 – Preliminary Scientific Results of the Nitrogen Oxide Production. In *20th ESA Symposium on European Rocket and Balloon Programmes and Related Research*, volume ESA SP-700, Hyères, France, 2011.

[297] K.G. Moesl, J.E. Schwing, W.J. Fenninger, and T. Sattelmayer. Influence of Heat and Mass Transfer on the Ignition and NOx Formation in Single Droplet Combustion. *Heat and Mass Transfer*, 47:1065–1076, 2011.

[298] K.G. Moesl, J.E. Schwing, and T. Sattelmayer. Modelling NOx Emissions of Single Droplet Combustion. *Combustion Theory and Modelling*, 16: 107–141, 2012.

[299] C.J. Montgomery, M.A. Cremer, J.-Y. Chen, C.K. Westbrook, and L.Q. Maurice. Reduced Chemical Kinetic Mechanisms for Hydrocarbon Fuels. *Journal of Propulsion and Power*, 18:192–198, 2002.

[300] C. Morley. Gaseq – Chemical Equilibria in Perfect Gases, January 2005. URL `http://www.gaseq.co.uk`.

[301] E.J. Mularz. Lean, Premixed, Prevaporized Combustion for Aircraft Gas Turbine Engines. Technical memorandum NASA/TM–79148, National Aeronautics and Space Administration (NASA), 1979.

[302] NAC Image Technology, Inc. (Tokyo, Japan). *NAC's Memrecam Ci/RX-2 Digital High-Speed Video System*, July 1999.

[303] S. Naha and S.K. Aggarwal. Fuel Effects on NOx Emissions in Partially Premixed Flames. In *42nd Aerospace Sciences Meeting & Exhibit*, number AIAA-2004-145, Reno, NV, USA, 2004.

[304] S. Naha and S.K. Aggarwal. Fuel Effects on NOx Emissions in Partially Premixed Flames. *Combustion and Flame*, 139:90–105, 2004.

[305] M. Nakamura, F. Akamatsu, R. Kurose, and M. Katsuki. Combustion Mechanism of Liquid Fuel Spray in a Gaseous Flame. *Physics of Fluids*, 17:1–14, 2005.

[306] K. Nakanishi, T. Kadota, and H. Hiroyasu. Effect of Air Velocity and Temperature on the Soot Formation by Combustion of a Fuel Droplet. *Combustion and Flame*, 40:247–262, 1981.

[307] S. Nakaya, Y. Nagashima, K. Takase, D. Segawa, and T. Kadota. Effects of Carbon Dioxide on Unsteady Combustion of Isolated Fuel Droplet in Microgravity. In *27th International Symposium on Space Technology and Science*, Tsukuba, Japan, 2009.

[308] S. Nakaya, M. Tsue, O. Imamura, S. Nishida, K. Yamashita, D. Segawa, and M. Kono. Effects of Fuel Vapor in Ambience on Spontaneous Ignition of Isolated Fuel Droplet. *Combustion Science and Technology*, 181: 1464–1479, 2009.

[309] S. Nakaya, D. Segawa, T. Kadota, Y. Nagashima, and T. Furuta. Combustion Behaviors of Isolated n-Decane and Ethanol Droplets in Carbon Dioxide-Rich Ambience Under Microgravity. *Proceedings of the Combustion Institute*, 33:2031–2038, 2011.

[310] NARISHIGE Group (Tokyo, Japan). MF-900: Microforge – Cutting, October 2011. URL `http://narishige-group.com/movie/MF-900_cutting/index.html`.

[311] National Institute of Standards and Technology (NIST). NIST Chemistry WebBook, November 2008. URL `http://webbook.nist.gov/chemistry/`.

[312] V. Nayagam, J.B. Haggard Jr., R.O. Colantonio, A.J. Marchese, F.L. Dryer, B.L. Zhang, and F.A. Williams. Microgravity n-Heptane Droplet Combustion in Oxygen-Helium Mixtures at Atmospheric Pressure. *AIAA Journal*, 36:1369–1378, 1998.

[313] Q.-V. Nguyen. Measurements of Equivalence Ratio Fluctuations in a Lean Premixed Prevaporized (LPP) Combustor and its Correlation to Combustion Instability. In *ASME Turbo Expo*, number GT-2002-30060, Amsterdam, The Netherlands, 2002.

[314] M. Nishioka, S. Nakagawa, Y. Ishikawa, and T. Takeno. NO Emission Characteristics of Methane-Air Double Flame. *Combustion and Flame*, 98:127–138, 1994.

[315] A.A. Nizami and N.P. Cernansky. NOx Formation in Monodisperse Fuel Spray Combustion. *Seventeenth Symposium (International) on Combustion/The Combustion Institute*, pages 475–483, 1979.

[316] A.A. Nizami, S. Singh, and N.P. Cernansky. Formation of Oxides of Nitrogen in Monodisperse Spray Combustion of Hydrocarbon Fuels. *Combustion Science and Technology*, 28:97–106, 1982.

[317] H. Nomura, Y. Ujiie, H.J. Rath, J. Sato, and M. Kono. Experimental Study on High-Pressure Droplet Evaporation Using Microgravity Conditions. *Twenty-Sixth Symposium (International) on Combustion/The Combustion Institute*, 26:1267–1273, 1996.

[318] H. Nomura, Y. Suganuma, A. Setani, M. Takahashi, M. Mikami, and H. Hara. Microgravity Experiments on Droplet Motion During Flame Spreading Along Three-Fuel-Droplet Array. *Proceedings of the Combustion Institute*, 32:2163–2169, 2009.

[319] H. Nomura, H. Iwasaki, Y. Suganuma, M. Mikami, and M. Kikuchi. Microgravity Experiments of Flame Spreading Along a Fuel Droplet Array in Fuel Vapor-Air Mixture. *Proceedings of the Combustion Institute*, 33: 2013–2020, 2011.

[320] J.C. Oefelein and S.K. Aggarwal. Toward a Unified High-Pressure Drop Model for Spray Simulations. In *Proceedings of the Summer Program*, pages 193–205. Center for Turbulence Research (Stanford/NASA-AMES), 2000.

[321] F. Oehme, U. Gerlach-Meyer, V. Leonhard, M. Josowicz, U. Löffler, A. Nauber, and K. Rümler. *Chemische Sensoren heute und morgen – Anforderungen, Fertigungstechniken, Entwicklungstrend*. Sensorik. expert verlag, 1994.

[322] H. Oertel Jr., M. Böhle, and U. Dohrmann. *Strömungsmechanik*. Friedr. Vieweg & Sohn Verlag, 2006.

[323] Oil Heritage Alliance of Business, Industry, and Tourism. History of the Oil Region, October 2010. URL `http://www.oilheritage.org/history/history.htm`.

[324] S.T. Omaye. Metabolic Modulation of Carbon Monoxide Toxicity. *Toxicology*, 180:139–150, 2002.

[325] E.S. Oran and J.P. Boris. Detailed Modelling of Combustion Systems. Memorandum report 4371, Naval Research Laboratory (NRL), 1980.

[326] Y. Otsuka and T. Niioka. On the Deviation of the Flame from the Stagnation Point in Opposed-Jet Diffusion Flames. *Combustion and Flame*, 19: 171–179, 1972.

[327] H. Oyagi, H. Shigeno, M. Mikami, and N. Kojima. Flame-Spread Probability and Local Interactive Effects in Randomly Arranged Fuel-Droplet Arrays in Microgravity. *Combustion and Flame*, 156:763–770, 2009.

[328] S. Palle, C. Nolan, and R.S. Miller. On Molecular Transport Effects in Real Gas Laminar Diffusion Flames at Large Pressure. *Physics of Fluids*, 17: 103601/1–19, 2005.

[329] J. Park, H. Kobayashi, and T. Niioka. A Study of Flame Spread Along a Droplet Array at Elevated Pressures up to a Supercritical Pressure. *International Journal of Energy Research*, 23:813–826, 1999.

[330] PCB Piezotronics, Inc. (Depew, NY, USA). *Model 422E12, In-Line Charge Converter, Installation and Operating Manual*, November 2006.

[331] PCB Piezotronics, Inc. (Depew, NY, USA). *Model 422E02, In-Line Charge Converter, Installation and Operating Manual*, April 2007.

[332] PCB Piezotronics, Inc. (Depew, NY, USA). *Model 112A05, Charge Output Dynamic Pressure Sensor, Installation and Operating Manual*, October 2008.

[333] PCB Piezotronics, Inc. (Depew, NY, USA). *Model 422E36, In-Line Charge Converter, Installation and Operating Manual*, October 2010.

[334] D. Peitz, A. Bernhard, M. Elsener, and O. Kröcher. Laboratory Test Reactor for the Investigation of Liquid Reducing Agents in the Selective Catalytic Reduction of NOx. *Review of Scientific Instruments*, 82:084101/1–8, 2011.

[335] A. Perronace, C. Leppla, F. Leroy, B. Rousseau, and S. Wiegand. Soret and Mass Diffusion Measurements and Molecular Dynamics Simulations of n-Pentane–n-Decane Mixtures. *Journal of Chemical Physics*, 116:3718–3729, 2002.

[336] N. Peters and B. Rogg, editors. *Reduced Kinetic Mechanisms for Applications in Combustion Systems*. Number m 15 in Lecture Notes in Physics. Springer-Verlag, 1993.

[337] U. Pfahl, K. Fieweger, and G. Adomeit. Self-Ignition of Diesel-Related Hydrocarbon-Air Mixtures Under Engine Conditions. *Twenty-Sixth Symposium (International) on Combustion/The Combustion Institute*, pages 781–789, 1996.

[338] Pfeiffer Vacuum (Asslar, Germany). *SingleGauge™ Single-Channel Measurement and Control Unit for Compact Gauges TPG 261, Operating Instructions*, August 2004.

[339] Pfeiffer Vacuum (Asslar, Germany). *Compact FullRange™ Gauge PKR 251, Operating Instructions*, August 2005.

[340] W.J. Pitz, C. Westbrook, O. Herbinet, and E. Silke. Chemical Kinetic Research on HCCI & Diesel Fuels. Technical paper, Lawrence Livermore National Laboratory, 2008.

[341] T.J. Poinsot and D. Veynante. *Theoretical and Numerical Combustion*. R.T. Ewards, 2005.

[342] F. Pompei and J.B. Heywood. The Role of Mixing in Burner-Generated Carbon Monoxide and Nitric Oxide. *Combustion and Flame*, 19:407–418, 1972.

[343] A.E. Potter Jr. and J.N. Butler. A Novel Combustion Measurement Based on the Extinguishment of Diffusion Flames. *ARS Journal (AIAA)*, 29:54–56, 1959.

[344] X. Qin, I.K. Puri, and S.K. Aggarwal. Characteristics of Lifted Triple Flames Stabilized in the Near Field of a Partially Premixed Axisymmetric Jet. *Proceedings of the Combustion Institute*, 29:1565–1572, 2002.

[345] R.V. Ravikrishna and N.M. Laurendeau. Laser-Induced Fluorescence Measurements and Modeling of Nitric Oxide in Methane-Air and Ethane-Air Counterflow Diffusion Flames. *Combustion and Flame*, 120: 372–382, 2000.

[346] R.V. Ravikrishna and N.M. Laurendeau. Laser-Induced Fluorescence Measurements and Modeling of Nitric Oxide in Counterflow Partially Premixed Flames. *Combustion and Flame*, 122:474–482, 2000.

[347] A.R. Ravishankara, J.S. Daniel, and R.W. Portmann. Nitrous Oxide (N_2O): The Dominant Ozone-Depleting Substance Emitted in the 21st Century. *Science*, 326:123–125, 2009.

[348] Reaction Design, Inc. (San Diego, CA, USA). *Senkin: A Program for Predicting Homogeneous Gas-Phase Chemical Kinetics in a Closed System with Sensivity Analysis*, July 1999.

[349] R. Reichenbach, D. Squires, and S.S. Penner. Flame Propagation in Liquid-Fuel Droplet Arrays. *Eighth Symposium (International) on Combustion/The Combustion Institute*, pages 1068–1073, 1961.

[350] M. Renksizbulut, M. Bussmann, and X. Li. A Droplet Vaporization Model for Spray Calculations. *Particle & Particle Systems Characterization*, 9: 59–65, 1992.

[351] Restek Corporation (Bellefonte, PA, USA). Specification for Coating Silcosteel and Sulfinert, July 2009.

[352] J.F. Rex, A.E. Fuhs, and S.S. Penner. Interference Effects During Buring in Air for Stationary n-Heptane, Ethyl Alcohol, and Methyl Alcohol Droplets. *Jet Propulsion*, 26:179–187, 1956.

[353] K.K. Rink and A.H. Lefebvre. Pollutant Formation in Heterogeneous Mixtures of Fuel Drops and Air. *Journal of Propulsion and Power*, 3:5–10, 1987.

[354] N.K. Rizk and J.S. Chin. Modeling of NOx Formation in Diffusion Flame Combustors. In *38th AIAA/ASME/SAE/ASEE Joint Propulsion Conference & Exhibit*, number AIAA 2002-3713, Indianapolis, IN, USA, 2002.

[355] N.K. Rizk, J.S. Chin, A.W. Marshall, and M.K. Razdan. Predictions of NOx Formation Under Combined Droplet and Partially Premixed Reaction of Diffusion Flame Combustors. *Journal of Engineering for Gas Turbines and Power*, 124:31–38, 2002.

[356] P.D. Ronney. Understanding Combustion Processes Through Microgravity Research. *Twenty-Seventh Symposium (International) on Combustion/The Combustion Institute*, pages 2485–2506, 1998.

[357] P.D. Ronney, M.S. Wu, H.G. Pearlman, and K.J. Weiland. Structure of Flame Balls at Low Lewis-Number (SOFBALL): Preliminary Results from the STS-83 Space Flight Experiments. *AIAA Journal*, 36:1361–1368, 1998.

[358] F.G. Roper. The Prediction of Laminar Jet Diffusion Flame Sizes: Part I. Theoretical Model. *Combustion and Flame*, 29:219–226, 1977.

[359] F.G. Roper. Laminar Diffusion Flame Sizes for Curved Slot Burners Giving Fan-Shaped Flames. *Combustion and Flame*, 31:251–259, 1978.

[360] F.G. Roper, C. Smith, and A.C. Cunningham. The Prediction of Laminar Jet Diffusion Flame Sizes: Part II. Experimental Verification. *Combustion and Flame*, 29:227–234, 1977.

[361] D.E. Rosner, R.S. Israel, and B. La Mantia. "Heavy" Species Ludwig-Soret Transport Effects in Air-Breathing Combustion. *Combustion and Flame*, 123:547–560, 2000.

[362] ROTEXO GmbH & Co. KG – SoftPredict (Bad Zwischenahn, Germany). *Cosilab®: Single Drop*, June 2005.

[363] ROTEXO GmbH & Co. KG – SoftPredict (Bad Zwischenahn, Germany). *Cosilab®: Gasphase Chemistry*, October 2006.

[364] ROTEXO GmbH & Co. KG – SoftPredict (Bad Zwischenahn, Germany). *Cosilab®: Two-Phase Flames*, September 2006.

[365] ROTEXO GmbH & Co. KG – SoftPredict (Bad Zwischenahn, Germany). *Cosilab®: Thermodynamics & Transport*, September 2006.

[366] N. Roth, A. Karl, K. Anders, and A. Frohn. Flame Propagation in Planar Droplet Arrays and Interaction Phenomena Between Neighboring Droplet Streams. *Twenty-Sixth Symposium (International) on Combustion/The Combustion Institute*, pages 1697–1703, 1996.

[367] T. Rutar and P.C. Malte. NOx Formation in High-Pressure Jet-Stirred Reactors with Significance to Lean-Premixed Combustion Turbines. *Journal of Engineering for Gas Turbines and Power*, 124:776–783, 2002.

[368] T. Rutar, S.M. Martin, D.G. Nicol, P.C. Malte, and D.T. Pratt. Effects of Incomplete Premixing on NOx Formation at Temperature and Pressure Conditions of LP Combustion Turbines. In *International Gas Turbine & Aeroengine Congress & Exhibition*, number 97-GT-335, Orlando, FL, USA, 1997.

[369] T. Rutar, J.C.Y. Lee, P. Dagaut, P.C. Malte, and A.A. Byrne. NO_x Formation Pathways in Lean-Premixed-Prevapourized Combustion of Fuels with Carbon-to-Hydrogen Ratio Between 0.25 and 0.88. *Proceedings of the Institution of Mechanical Engineers, Part A: Journal of Power and Energy*, 221:387–398, 2007.

[370] SAE Aerospace. ARP1533 Revision A, Procedure for the Analysis and Evaluation of Gaseous Emissions from Aircraft Engines. Technical report, 2004.

[371] G.S. Samuelsen and J.N. Harman III. Chemical Transformations of Nitrogen Oxides While Sampling Combustion Products. *Journal of Air Pollution Control Association*, 27:648–655, 1977.

[372] C. Sanchez Tarifa, P. Perez del Notario, and F. Garcia Moreno. Combustion of Liquid Monopropellants and Bipropellants in Droplets. *Eighth Symposium (International) on Combustion/The Combustion Institute*, pages 1035–1056, 1961.

[373] T. Sano. NO_2 Formation in Laminar Flames. *Combustion Science and Technology*, 29:261–275, 1982.

[374] T. Sano. NO_2 Formation in the Mixing Region of Hot Burned Gas with Cool Air. *Combustion Science and Technology*, 38:129–144, 1984.

[375] D.A. Santavicca, R.L. Steinberger, K.A. Gibbons, J.V. Citeno, and S. Mills. The Effect of Incomplete Fuel-Air Mixing on the Lean Limit and Emissions Characteristics of a Lean Prevaporized Premixed (LPP) Combustor. In *AGARD Meeting on 'Fuels and Combustion Technology for Advanced Aircraft Engines'*, volume 536, Fiuggi, Italy, 1993.

[376] J. Sato, M. Tsue, M. Niwa, and M. Kono. Effects of Natural Convection on High-Pressure Droplet Combustion. *Combustion and Flame*, 82:142–150, 1990.

[377] T. Sattelmayer. Influence of the Combustor Aerodynamics on Combustion Instabilities from Equivalence Ratio Fluctuations. *Journal of Engineering for Gas Turbines and Power*, 125:11–19, 2003.

[378] T. Sattelmayer and W. Polifke. Assessments of Methods for the Computation of the Linear Stability of Combustors. *Combustion Science and Technology*, 175:453–476, 2003.

[379] T. Sattelmayer and W. Polifke. A Novel Method for the Computation of the Linear Stability of Combustors. *Combustion Science and Technology*, 175:477–497, 2003.

[380] T. Sattelmayer, W. Polifke, D. Winkler, and K. Döbbeling. NOx-Abatement Potential of Lean-Premixed GT Combustors. *Journal of Engineering for Gas Turbines and Power*, 120:48–59, 1998.

[381] S.S. Sazhin. Advanced Models of Fuel Droplet Heating and Evaporation. *Progress in Energy and Combustion Science*, 32:162–214, 2006.

[382] S.S. Sazhin, P.A. Krutitskii, W.A. Abdelghaffar, E.M. Sazhina, S.V. Mikhalovsky, S.T. Meikle, and M.R. Heikal. Transient Heating of Diesel Fuel Droplets. *International Journal of Heat and Mass Transfer*, 47:3327–3340, 2004.

[383] S.S. Sazhin, W.A. Abdelghaffar, P.A. Krutitskii, E.M. Sazhina, and M.R. Heikal. New Approaches to Numerical Modelling of Droplet Transient Heating and Evaporation. *International Journal of Heat and Mass Transfer*, 48:4215–4228, 2005.

[384] S.S. Sazhin, A. Elwardany, P.A. Krutitskii, G. Castanet, F. Lemoine, E.M. Sazhina, and M.R. Heikal. A Simplified Model for Bi-Component Droplet Heating and Evaporation. *International Journal of Heat and Mass Transfer*, 53:4495–4505, 2010.

[385] E.M. Sazhina, S.S. Sazhin, M.R. Heikal, and C.J. Marooney. The Shell Autoignition Model: Applications to Gasoline and Diesel Fuels. *Fuel*, 78: 389–401, 1999.

[386] R.W. Schefer, W.J. McLean, and R.F. Sawyer. Dispersion in Combustion Gas Sampling Probes. *Combustion and Flame*, 19:267–274, 1972.

[387] E. Schiefer, W. Schindler, and H. Schimpl. Study of Interferences for ULEV-CVS Measurement, Related to the Complete Measuring System, Discussion of Error Sources, Cross-Sensitivity and Adsorption. In *SAE 2000 World Congress*, Detroit, MI, USA, 2000.

[388] A. Schlegel, M. Streichsbier, R. Mongia, and R. Dibble. A Comparison of the Influence of Fuel/Air Unmixedness on NOx Emissions in Lean Premixed, Non-Catalytic and Catalytically Stabilized Combustion. In *International Gas Turbine & Aeroengine Congress & Exhibition*, number 97-GT-306, Orlando, FL, USA, 1997.

[389] H. Schlichting. *Grenzschicht-Theorie*. Verlag G. Braun, 1982.

[390] A. Schöne. *Messtechnik*. Springer-Verlag, 1997.

[391] J.H. Seinfeld. *Atmospheric Chemistry and Physics of Air Pollution*. John Wiley & Sons, 1986.

[392] B.D. Shaw and V. Dee. Influence of the Gas Phase Inert on Reduced-Gravity Combustion of Decane/Hexadecane Droplets. *Microgravity Science and Technology*, 16:26–34, 2005.

[393] B.D. Shaw, F.L. Dryer, F.A. Williams, and N. Gat. Interactions Between Gaseous Electrical Discharges and Single Liquid Droplets. *Combustion and Flame*, 74:233–254, 1988.

[394] B.D. Shaw, F.L. Dryer, F.A. Williams, and J.B. Haggard Jr. Sooting and Disruption in Spherically Symmetrical Combustion of Decane Droplets in Air. *Acta Astronautica*, 17:1195–1202, 1988.

[395] A.T. Shih and C.M. Megaridis. Suspended Droplet Evaporation Modeling in a Laminar Convective Environment. *Combustion and Flame*, 102: 256–270, 1995.

[396] H. Sigloch. *Technische Fluidmechanik*. Springer-Verlag, 2012.

[397] J.E. Sigsby Jr., F.M. Black, T.A. Bellar, and D.L. Klosterman. Chemiluminescent Method for Analysis of Nitrogen Compounds in Mobile Source Emissions (NO, NO_2, and NH_3). *Environmental Science & Technology*, 7: 51–54, 1973.

[398] R.F. Simmons and H.G. Wolfhard. Some Limiting Oxygen Concentrations for Diffusion Flames in Air Diluted with Nitrogen. *Combustion and Flame*, 1:155–161, 1957.

[399] S. Singh, S. Paolucci, and J.M. Powers. Reactive Flow Calculations with Intrinsic Low Dimensional Manifold Corrections for Convection and Diffusion. In *18th International Colloquium on the Dynamics of Explosions and Reactive Systems*, Seattle, WA, USA, 2001.

[400] S. Singh, Y. Rastigejev, S. Paolucci, and J.M. Powers. Viscous Detonation in H_2-O_2-Ar Using Intrinsic Low-Dimensional Manifolds and Wavelet Adaptive Multilevel Representation. *Combustion Theory and Modelling*, 5:163–184, 2001.

[401] W.A. Sirignano. Theory of Multicomponent Fuel Droplet Vaporization. *Archiwum Termodynamiki i Spalania (Archives of Thermodynamics and Combustion)*, 9:231–247, 1978.

[402] W.A. Sirignano. Fuel Droplet Vaporization and Spray Combustion Theory. *Progress in Energy and Combustion Science*, 9:291–322, 1983.

[403] W.A. Sirignano. An Integrated Approach to Spray Combustion Model Development. *Combustion Science and Technology*, 58:231–251, 1988.

[404] W.A Sirignano. *Fluid Dynamics and Transport of Droplets and Sprays*. Cambridge University Press, 1999.

[405] W.A. Sirignano and C.K. Law. Transient Heating and Liquid-Phase Mass Diffusion in Fuel Droplet Vaporization. *Advances in Chemistry: Evaporation-Combustion of Fuels*, 166:3–26, 1978.

[406] D.A. Smith and Restek Corporation (Bellefonte, PA, USA). Surface Modification of Solid Supports Through the Thermal Decomposition and Functionalization of Silanes. Patent US 6,444,326, 2002.

[407] D.A. Smith, D. Shelow, and G. Barone. Instrument and Sampling Equipment Passivation Requirements to Meet Current Demands for Low-Level Sulfur Analysis. In *Gulf Coast Conference*, Galveston, TX, USA, 2001.

[408] G.P. Smith, D.M. Golden, M. Frenklach, N.W. Moriarty, B. Eiteneer, M. Goldenberg, C.T. Bowman, R.K. Hanson, S. Song, W.C. Gardiner Jr., V.V. Lissianski, and Z. Qin. GRI-Mech 3.0, June 2009. URL `http://www.me.berkeley.edu/gri_mech/`.

[409] S.W. Smith. *The Scientist and Engineer's Guide to Digital Signal Processing*. California Technical Publishing, 1999.

[410] Sony Corp. (Tokyo, Japan). *CCD Black-and-White Video Camera Module XC-ES50, Technical Manual*, January 2006.

[411] Sony Corp. (Tokyo, Japan). *CCD Color Video Camera Module XC-555P, Operating Instructions*, April 2010.

[412] D.B. Spalding. Combustion of Liquid Fuels. *Nature*, 165:160, 1950.

[413] D.B. Spalding. Combustion of Liquid Fuels in a Gas Stream – I. *Fuel*, 29: 2–7, 1950.

[414] D.B. Spalding. Combustion of Liquid Fuels in a Gas Stream – II. *Fuel*, 29: 25–32, 1950.

[415] D.B. Spalding. The Combustion of Liquid Fuels. *Fourth Symposium (International) on Combustion/The Combustion Institute*, pages 847–864, 1953.

[416] D.B. Spalding. Experiments on the Burning and Extinction of Liquid Fuel Spheres. *Fuel*, 32:169–185, 1953.

[417] D.B. Spalding. Theory of Mixing and Chemical Reaction in the Opposed-Jet Diffusion Flame. *ARS Journal (AIAA)*, 31:763–771, 1961.

[418] D.B. Spalding. *Combustion and Mass Transfer*. Pergamon Press, 1979.

[419] J.H. Spurk. *Strömungslehre*. Springer-Verlag, 2004.

[420] J. Staab. *Industrielle Gasanalyse*. R. Oldenburg Verlag, 1994.

[421] Statistisches Bundesamt (Wiesbaden, Germany). Datenreport 2008 – ein Sozialbericht für die Bundesrepublik Deutschland, November 2008.

[422] C. Steinbach, T. Ruck, J. Lloyd, P. Jansohn, K. Döbbeling, T. Sattelmayer, and T. Strand. ABB's Advanced EV Burner – A Dual Fuel Dry Low NOx Burner for Stationary Gas Turbines. In *International Gas Turbine & Aeroengine Congress & Exhibition*, number 98-GT-519, Stockholm, Sweden, 1998.

[423] S. Steinbach. *Einfluss der Transportvorgänge auf die Effizienz von Harnstoffkatalysatoren in SCR-Abgasanlagen*. Ph.D. diss., Technische Universität München, 2007.

[424] P.M. Struk, M.D. Ackerman, V. Nayagam, and D.L. Dietrich. On Calculating Burning Rates During Fiber Supported Droplet Combustion. *Microgravity Science and Technology*, 10:144–151, 1998.

[425] Y. Suganuma, H. Nomura, Y. Ujiie, M. Kikuchi, S. Yamamoto, S. Yoda, and M. Mikami. Flame Spread of a Fuel Droplet Array in a Fuel Vapor-Air Mixture. In *56th International Astronautical Congress*, number IAC-05-A2.7.01, Fukuoka, Japan, 2005.

[426] W. Sun, Z. Chen, X. Gou, and Y. Ju. A Path Flux Analysis Method for the Reduction of Detailed Chemical Kinetic Mechanisms. *Combustion and Flame*, 157:1298–1307, 2010.

[427] T. Suzuki and H.H. Chiu. Multi-Droplet Combustion of Liquid Propellants. In *International Symposium on Space Technology and Science*, pages 145–154, 1971.

[428] G. Sybon. *Untersuchungen zur Bildung und Emission von NOx und N_2O bei brennstoffgestufter Verbrennungsführung*. Ph.D. diss., Universität Karlsruhe, 1994.

[429] M. Takei, H. Kobayashi, and T. Niioka. Ignition Experiment of a Blended-Fuel Droplet in a Microgravity Field. *Microgravity Science and Technology*, 6:184–187, 1993.

[430] R. Tal (Thau), D.N. Lee, and W.A. Sirignano. Hydrodynamics and Heat Transfer in Sphere Assemblages - Cylindrical Cell Models. *International Journal of Heat and Mass Transfer*, 26:1265–1273, 1983.

[431] M. Tanabe, M. Kono, J. Sato, J. and. Koenig, C. Eigenbrod, and H.J. Rath. Effects of Natural Convection on Two Stage Ignition of an n-Dodecane Droplet. *Twenty-Fifth Symposium (International) on Combustion/The Combustion Institute*, pages 455–461, 1994.

[432] M. Tanabe, M. Kono, J. Sato, J. Koenig, C. Eigenbrod, F. Dinkelacker, and H.J. Rath. Two Stage Ignition of n-Heptane Isolated Droplets. *Combustion Science and Technology*, 108:103–119, 1995.

[433] M. Tanabe, T. Bolik, C. Eigenbrod, H.J. Rath, J. Sato, and M. Kono. Spontaneous Ignition of Liquid Droplets from a View of Non-Homogeneous Mixture Formation and Transient Chemical Reactions. *Twenty-Sixth Symposium (International) on Combustion/The Combustion Institute*, pages 1637–1643, 1996.

[434] Thermo Electron Corporation (Madison, WI, USA). *Gas Cell User's Guide*, 2003.

[435] Thermo Electron Corporation (Madison, WI, USA). *OMNIC® User's Guide*, 2006.

[436] Thermo Nicolet Corporation (Madison, WI, USA). *OMNIC® QuantPad User's Guide*, 1995.

[437] Thermo Scientific (Madison, WI, USA). The Use of FT-IR to Analyze NOx Gases in Automobile Exhaust. Application note 50649, 2007.

[438] Thermo Scientific (Madison, WI, USA). FT-IR Sampling Parameters for Exhaust Gas Measurements. Application note 50650, 2007.

[439] R.J. Tidona, A.A. Nizami, and N.P. Cernansky. Reducing Interference Effects in the Chemiluminescent Measurement of Nitric Oxides from Combustion Systems. *Journal of the Air Pollution Control Association*, 38:806–811, 1988.

[440] G. Tiné. *Gas Sampling and Chemical Analysis in Combustion Processes*. NATO Advisory Group for Aeronautical Research and Development: AGARDograph. Pergamon Press, 1961.

[441] J.S. Tsai and A.M. Sterling. The Combustion of Linear Droplet Arrays. *Twenty-Third Symposium (International) on Combustion/The Combustion Institute*, pages 1405–1411, 1990.

[442] H. Tsuji. Counterflow Diffusion Flames. *Progress in Energy and Combustion Science*, 8:93–119, 1982.

[443] S.R. Turns. *An Introduction to Combustion – Concepts and Applications*. McGraw-Hill Higher Education, 2000.

[444] T. Ueda, O. Imamura, K. Okai, M. Tsue, M. Kono, and J. Sato. Combustion Behavior of Single Droplets for Sooting and Non Sooting Fuels in Direct Current Electric Fields Under Microgravity. *Proceedings of the Combustion Institute*, 29:2595–2601, 2002.

[445] A. Umemura. A Theoretical Study on the Unsteady, Interactive Combustion of a Linear Fuel Droplet Stream. *Twenty-Third Symposium (International) on Combustion/The Combustion Institute*, pages 1445–1453, 1990.

[446] A. Umemura. Flame Propagation Along a Linear Array of Liquid Droplets Under Micro-Gravity Condition (1st & 2nd Report, Inter-Droplet Flame Propagation Map, in Japanese). *Transactions of the Japan Society of Mechanical Engineers. B*, 68:2422–2436, 2002.

[447] A. Umemura and M. Uchida. Flame Propagation Along a Linear Array of Liquid Droplets Under Micro-Gravity Condition (3rd Report, Inter-Droplet Flame Propagation Map, in Japanese). *Transactions of the Japan Society of Mechanical Engineers. B*, 68:2636–2642, 2002.

[448] A. Umemura, A. Ogawa, and N. Oshiwa. Analysis of the Interaction Between Two Burning Droplets. *Combustion and Flame*, 41:45–55, 1981.

[449] Umweltbundesamt. Emission Trends for Germany Since 1990, March 2011. URL `http://www.umweltbundesamt.de/emissionen/publikationen.htm`.

[450] U.S. Energy Information Administration (Washington, D.C., USA). Annual Energy Review (AER) 2010, October 2011. URL `http://www.eia.gov/aer`.

[451] U.S. Environmental Protection Agency (Washington, D.C., USA). Air Quality Criteria for Oxides of Nitrogen. Report EPA600/8-91/049aF-cF, August 1993.

[452] J.A. van Oijen and L.P.H. de Goey. A Numerical Study of Confined Triple Flames Using a Flamelet-Generated Manifold. *Combustion Theory and Modelling*, 8:141–163, 2004.

[453] Verein Deutscher Ingenieure, VDI-Gesellschaft Verfahrenstechnik und Chemieingenieurwesen (GVC), editor. *VDI-Wärmeatlas – Berechnungsblätter für den Wärmeübergang*. VDI-Verlag, 1994.

[454] G. Vermes, L.E. Barta, and J.M. Beér. Low NOx Emission from an Ambient Pressure Diffusion Flame Fired Gas Turbine Cycle (APGC). *Journal of Engineering for Gas Turbines and Power*, 125:46–50, 2003.

[455] H.G. Wagner. Soot Formation in Combustion. *Seventeenth Symposium (International) on Combustion/The Combustion Institute*, pages 3–19, 1979.

[456] Y. Wakashima, S. Yamamoto, M. Kikuchi, S. Yoda, M. Mikami, and A. Umemura. Numerical and Experimental Study on Flame Propagating Mechanism of a Fuel Droplet Array. *Microgravity Science and Technology*, 16:338–341, 2005.

[457] G.B. Wallis. *One-Dimensional Two-Phase Flow*. McGraw-Hill, 1969.

[458] J. Warnatz, R.W. Dibble, and U. Maas. *Verbrennung*. Springer-Verlag, 2001.

[459] C.K. Westbrook and F.L. Dryer. Simplified Reaction Mechanism for the Oxidation of Hydrocarbon Fuels in Flames. *Combustion Science and Technology*, 27:31–43, 1981.

[460] G. Wiegleb, U. Demisch, G. Horner, J. Kiesewetter, O. Kiesewetter, D. Kitzelmann, M. Unruh, M. Weber, and D. Wenker. *Industrielle Gassensorik – Messverfahren, Signalverarbeitung, Anwendungstechnik, Prüfkriterien*. Sensorik. expert verlag, 2001.

[461] F.A. Williams. *Combustion Theory*. The Benjamin/Cummings Publishing Company, 1985.

[462] S.-C. Wong, A.-C. Lin, and H.-Y. Chi. Effects of Surfactant on the Evaporation, Shell Formation and Disruptive Behavior of Slurry Droplets. *Twenty-Third Symposium (International) on Combustion/The Combustion Institute*, pages 1391–1397, 1990.

[463] J. Xin and C.M. Megaridis. Modeling of Multiple Droplet Streams in Close Spacing Configurations and Sprays. *Atomization and Sprays*, 7: 267–294, 1997.

[464] T.Y. Xiong, C.K. Law, and M. Miyasaka. Interactive Vaporization and Combustion of Binary Droplet Systems. *Twentieth Symposium (International) on Combustion/The Combustion Institute*, pages 1781–1787, 1984.

[465] G. Xu, M. Ikegami, S. Honma, K. Ikeda, X. Ma, H. Nagaishi, D.L. Dietrich, and P.M. Struk. Inverse Influence of Initial Diameter on Droplet Burning Rate in Cold and Hot Ambiences: A Thermal Action of Flame in Balance with Heat Loss. *International Journal of Heat and Mass Transfer*, 46: 1155–1169, 2003.

[466] G. Xu, M. Ikegami, S. Honma, K. Ikeda, D.L. Dietrich, and P.M. Struk. Interactive Influences of Convective Flow and Initial Droplet Diameter on Isolated Droplet Burning Rate. *International Journal of Heat and Mass Transfer*, 47:2029–2035, 2004.

[467] G. Xu, M. Ikegami, S. Honma, Ikeda K., D. L. Dietrich, and P.M. Struk. Sooting Characteristics of Isolated Droplet Burning in Heated Ambients Under Microgravity. *International Journal of Heat and Mass Transfer*, 47:5807–5821, 2004.

[468] H. Xue and S.K Aggarwal. Effects of Reaction Mechanisms on Structure and Extinction of Partially Premixed Flames. *AIAA Journal*, 39:637–645, 2001.

[469] H. Xue and S.K. Aggarwal. NOx Emissions in n-Heptane/Air Partially Premixed Flames. *Combustion and Flame*, 132:723–741, 2003.

[470] J.C. Yang, G.S. Jackson, and C.T. Avedisian. Combustion of Unsupported Methanol/Dodecanol Mixture Droplets at Low Gravity. *Twenty-Third Symposium (International) on Combustion/The Combustion Institute*, pages 1619–1625, 1990.

[471] Ya.B. Zel'dovich. The Oxidation of Nitrogen in Combustion and Explosions. *Acta Physicochimica U.R.S.S.*, 21:577–628, 1946.

[472] Ya.B. Zel'dovich, P.Ya. Sadonikov, and D.A. Frank-Kamenetskii. *Oxidation of Nitrogen in Combustion* (Окисление азота при горении). USSR Academy of Sciences (Академия Наук СССР), 1947.

[473] S.P. Zeppieri, S.D. Klotz, and F.L. Dryer. Modeling Concepts for Larger Carbon Number Alkanes: A Partially Reduced Skeletal Mechanism for n-Decane Oxidation and Pyrolysis. *Proceedings of the Combustion Institute*, 28:1587–1595, 2000.

[474] Z. Zhao, J. Li, A. Kazakov, F.L. Dryer, and S.P. Zeppieri. Burning Velocities and a High Temperature Skeletal Kinetic Model for n-Decane. *Combustion Science and Technology*, 177:89–106, 2005.

[475] V.P. Zhukov. Kinetic Modelling of n-Decane Ignition at High Pressure. In *22nd International Colloquium on the Dynamics of Explosions and (ICDERS)*, Poitiers, France, 2007.

[476] V.P. Zhukov. Kinetic Model of Alkane Oxidation at High Pressure from Methane to n-Heptane. *Combustion Theory and Modelling*, 13:427–442, 2009.

[477] V.P. Zhukov. About Kinetic Modelling of n-Decane Autoignition. *Combustion and Flame*, 156:1674–1676, 2009.